The role and evolution of CO, CO_2 and H_2O in star forming regions.

Jennifer A. Noble

Department of Physics; Scottish Universities Physics Alliance

A thesis presented in fulfilment of the requirements for the degree of

Doctor of Philosophy

2011

This thesis is the result of the author's original research. It has been composed by the author and has not been previously submitted for examination which has led to the award of a degree.

The copyright of this thesis belongs to the author under the terms of the United Kingdom Copyright Acts as qualified by University of Strathclyde Regulation 3.50. Due acknowledgement must always be made of the use of any material contained in, or derived from, this thesis.

Signed:

Date:

To August

赤々と出来揃けり雲の峰

shining bright
one and all
the billowing clouds

Matsuo Bashō

Abstract

This thesis presents a study of the abundances, distribution and evolution of solid phase molecular species in icy mantles on the surface of dust grains in molecular clouds, by a unique combination of both observational and experimental results. In particular, it addresses the development of high resolution ice mapping as a tracer and probe of chemical and physical conditions, and the formation of CO_2 in quiescent regions.

Observations of molecular clouds were made using the AKARI satellite, utilising its slitless spectroscopy mode to observe multiple lines of sight in a single pointing. A dedicated data reduction pipeline was written to analyse these data, and 30 spectra towards 22 field stars behind the clouds and eight embedded young stellar objects were successfully extracted. Abundances of molecular species, including H_2O, CO_2, CO, CH_3OH, $^{13}CO_2$, OCN^-, and, tentatively HDO, were calculated using a component analysis method. Towards four fields of view, 2D ice abundance maps were constructed, probing resolutions as low as 650 AU; results indicate that chemistry in a molecular cloud is very localised, and that ice mapping is a powerful tool to identify local variations in abundance.

Experiments on the desorption behaviour and reactions of interstellar molecules were performed at very low surface coverages. From a series of desorption experiments, a model was constructed to describe the desorption characteristics of CO, O_2 and CO_2 from H_2O and silicate surfaces, encompassing sub-monolayer to multilayer coverages. It was determined that sub-monolayer behaviour and surface morphology are vital to describing interstellar desorption. A study of the non-energetic CO_2 formation route CO + OH successfully produced CO_2 and, from a model of the reaction kinetics, relative reaction rates and a tentative energy barrier to the reaction were derived for the first time.

This thesis illustrates that by combining laboratory and observational studies, key insights are made into interstellar chemistry.

CONTENTS

LIST OF FIGURES

List of Tables

CHAPTER 1

INTRODUCTION

1.1 Molecular clouds

Around 1784, while compiling a catalogue of deep sky objects, the astronomer Sir William Herschel noted, of a region apparently devoid of stars, "Hier ist wahrhaftig ein Loch im Himmel" ("Here is truly a hole in the sky", Houghton [1942]). It was not until the 20^{th} Century that these regions were identified, not as holes, but rather as matter present between the Earth and the stars. A catalogue of 182 "dark markings in the sky" was compiled by Barnard [1919], in which he postulated that at least some of the objects must be composed of matter, rather than being voids. A proof for extinction was published by Trumpler [1930], explaining the dark appearance of the "holes" in the sky as clouds of an absorbing medium; these clouds were later identified as regions of star formation [Bok & Reilly, 1947; Bok, 1948; Spitzer, 1941].

Nowadays, molecular clouds (or dark clouds, dense clouds), such as the one in Figure 1.1, are known to be stellar nurseries; vast clouds of dust and gas within which stars and their associated planetary systems form. Their dark appearance on the sky is the result of extinction of the light from background stars due to absorption and scattering by interaction with the dust particles. These regions are of particular interest to astrochemists, due to the plethora of molecular species found both in the gas phase but also as icy mantles on the dust grain surfaces. Grain surfaces are crucial in catalysing a complex network of chemical reactions, which are otherwise highly improbable in the vacuum

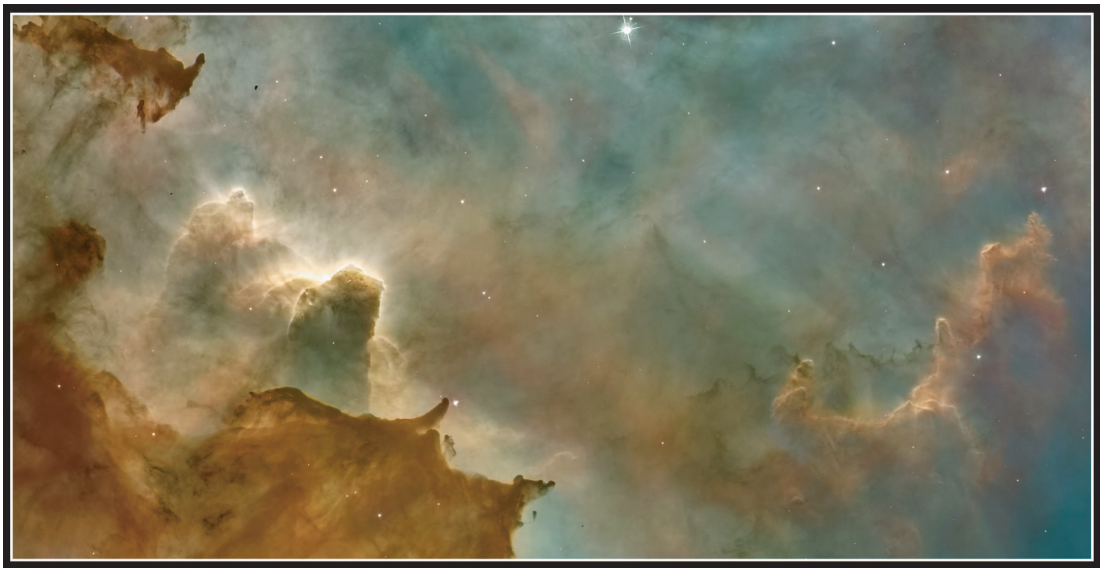

Figure 1.1. An image of part of a molecular cloud in the Carina Nebula. The image was produced by combining Hubble Space Telescope (HST) and Cerro-Tololo Interamerican Observatory (CTIO) observations using the following filters: CTIO [O III] 501nm – blue; CTIO Hα+[N II] 658nm – green; CTIO [S II] 672+673nm – red; and HST ACS F656N Hα+[N II] – luminosity. Image credit: NASA, ESA, N. Smith (University of California, Berkeley), NOAO/AURA/NSF, and The Hubble Heritage Team (STScI/AURA).

of space.

This thesis is a study of just some of these molecular species; their abundances, formation pathways, and distribution in molecular clouds. Despite much valuable study over the past two to three decades, many fundamental questions remain unanswered in astrochemistry. The formation of solid phase molecular species is widely believed to occur, for the most part, in the icy mantles on the surface of dust grains. However, many of the reaction pathways and the chemical and physical processes governing the chemistry in molecular clouds remain obscure and unexplained. Thus, determining the physical and chemical behaviour of molecules and their interactions with dust grains is necessary. The combination of laboratory and observational data is central to this thesis and to developing answers to the big questions in astrochemistry.

In order to interpret the evolution of the chemical networks present throughout the star formation cycle, it is critical to appropriately benchmark the chemistry at each stage. How much of the extensive chemical network present in

more evolved environments, such as protostellar disks, or planetary systems, can be attributed to simple reactions occurring on dust grains in quiescent molecular clouds? In this thesis, the formation, abundances, and distribution of key molecular species are examined, using both observational and experimental approaches, with a view to providing answers to some of these questions. Observations of solid phase molecular species in molecular clouds is key to this aim, as quiescent regions of molecular clouds are the starting point for the chemistry, yet can prove relatively difficult to observe and interpret. Ice mapping, the technique of quantifying ice abundances spatially distributed across a two dimensional region of an interstellar environment, has the potential to reveal intricacies of molecular distribution which are not apparent from traditional single line of sight observational spectroscopic studies. In particular, the formation of CO_2 is addressed in this thesis, by the combined approach of observing its abundance in multiple quiescent molecular clouds, and experimentally studying potential formation pathways in the laboratory.

1.1.1 Star formation cycle

Molecular clouds represent a critical stage in the formation of low mass stars and their planetary systems, a process which is illustrated by the schematic diagram in Figure 1.2.

Matter in the InterStellar Medium (ISM) consists of around 99 % gas (70 % atomic and molecular hydrogen, 28 % helium, 1 % heavier elements) and 1 % dust particles, by mass. Regions of the ISM are generally characterised by temperature, density and hydrogen state [e.g. Tielens, 2005]. The majority of the volume of the ISM contains ionised hydrogen at high temperatures and is thus devoid of molecular chemistry. Molecular clouds, regions of dense (density of hydrogen atoms, $n_H \sim 10^3 - 10^4\ cm^{-3}$), cold (10 – 50 K) dust, form gravitationally from the dust and gas present in cold, neutral regions of the ISM. The most dense parts ($n_H > 2 \times 10^4\ cm^{-3}$) of molecular clouds, distributed non-uniformly throughout the cloud, are defined as molecular cores [Williams, 2005]. These cores are the regions of star formation in the cloud; there is a strong correlation between the distribution of young stellar objects (YSOs) and that of molecular cores [Evans, 2008]. Prior to the gravitational collapse that

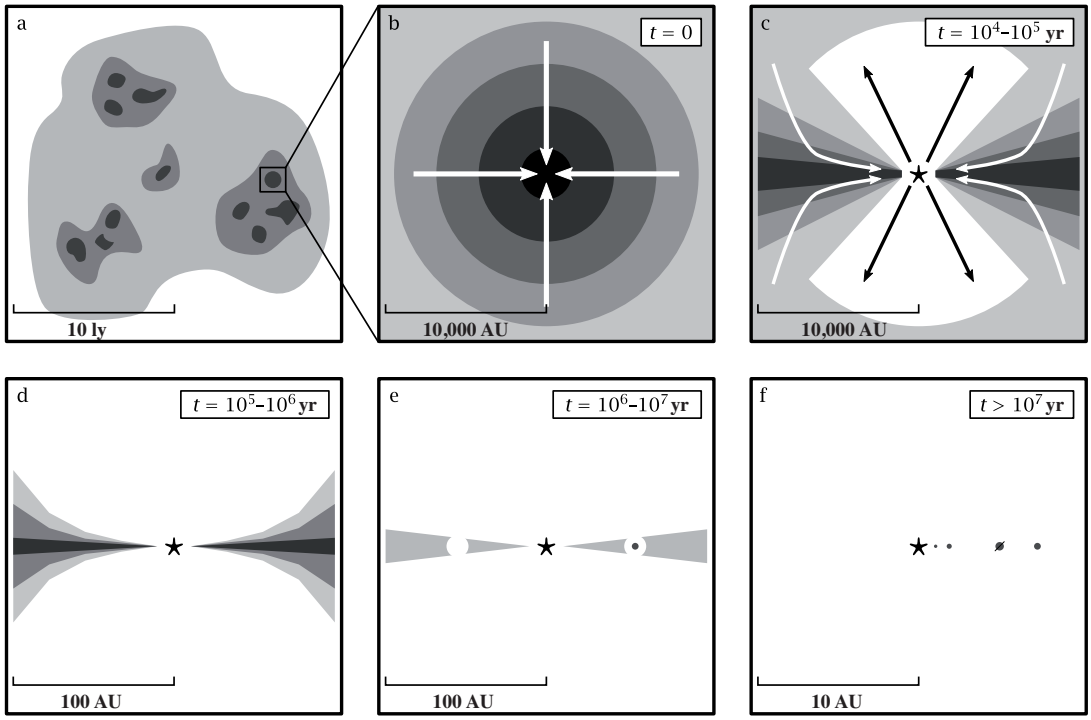

Figure 1.2. Stages of the low mass star formation cycle. (a) In the diffuse ISM, molecular clouds of dust and gas form gravitationally. Within these clouds, more dense cores are present. (b) Collapse of a core is triggered when the density is high enough for gravity to overcome the turbulent or magnetic forces supporting the core. (c) YSO class 0/I – material from the cloud falls inward to create a circumstellar disk around the forming star, while matter is expelled through bipolar outflows. (d) YSO class II – the outflows stop and star formation is complete; the circumstellar disk remains. (e) Material in the protoplanetary disk begins to accumulate into larger aggregates, which sweep out their orbital paths. (f) When all of the disk has been swept out, a planetary system is evident around the newly formed star. In this figure, ly is light year and AU is astronomical unit. Figure adapted from Visser [2009].

precipitates protostellar formation, molecular cores host important chemical reactions, and it is for this reason that these objects and their precursors are so widely studied by astrochemists.

Low mass star formation occurs over four stages, known as class 0, I, II, III [Shu et al., 1987; Lada, 1987; Andre et al., 1993; Andre & Montmerle, 1994]. Gravitationally bound molecular clouds are stabilised over timescales of $\sim 10^7$ years due to turbulent forces and magnetic pressure. Gradual loss of these supporting forces, in combination with increasing core density, precipitates gravitational collapse of the cloud core (Class 0, Figure 1.2b). The central protostar accretes matter from a rotating circumstellar disk, formed by the collapse of

the cloud. Rotation preserves the angular momentum of the cloud, and both star and disk are surrounded by a cold envelope (Class I, Figure 1.2c). During this stage, a bipolar outflow perpendicular to the disk plane disperses the envelope. When the star and disk become visible, following depletion of the envelope, the source is defined as Class II (Figure 1.2d). Strong UV and X-ray radiation from the protostar removes gas from the disk surface, and at the same time dust particles in the disk combine and grow, settling into a thin disk in the midplane (Class III, Figure 1.2e). The growth of dust particles leads to larger particles and planetesimals which can eventually 'sweep out' their orbits of any remaining dust and gas to form a planetary system around the YSO (Figure 1.2f). The YSO joins the main sequence when its temperature is high enough to initiate the nuclear fusion of hydrogen atoms into helium.

The star formation cycle is completed upon the death of the star, when its matter is returned to the ISM, enriching it with dust and heavy elements.

1.1.2 Interstellar dust

Dust grains are formed in the atmospheres of evolved stars and are present throughout the ISM. The formation of dust in stellar atmospheres is seemingly similar to soot production in a candle flame, although neither process is currently well understood [Williams & Herbst, 2002]. In stars whose atmospheres become cool and dense enough, solid nuclei form. Solid particles then form by the deposition of supersaturated atoms and molecules onto these nuclei. Stellar radiation pressure pushes the newly formed dust out into the ISM. Generally, carbonaceous grains are produced in carbon rich outflows, while siliceous grains are produced in oxygen rich outflows. In addition to stellar atmospheres, another source of interstellar dust is stellar explosions, novae and supernovae, in which dust forms from elements produced in the star. An interplanetary dust grain retrieved from the stratosphere is shown in Figure 1.3a.

Dust grains evolve by various processes, including coagulation, evaporation and shattering during grain-grain collisions, photolysis and sputtering. They are destroyed by shock waves with shock speed $v_s \geq 200$ km s^{-1} [Draine & Murdin, 2000], e.g. in supernovae, but survive in cold, dark clouds where they are protected from sputtering and shock waves. Following its evaporation

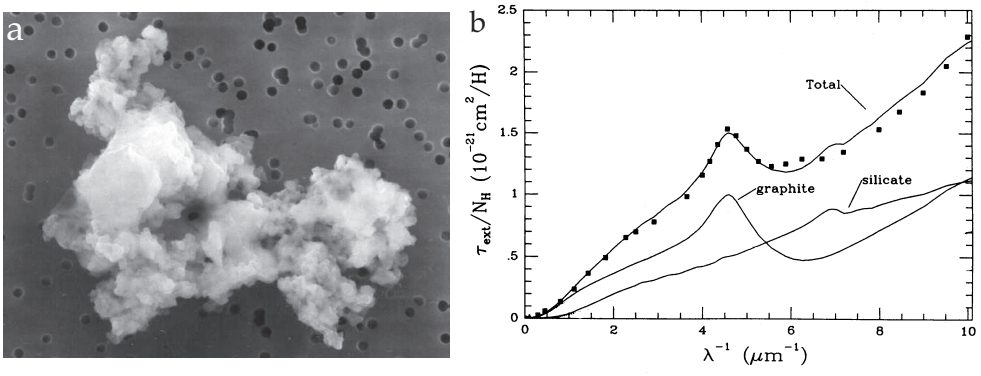

Figure 1.3. Interstellar dust. Part a) is an interplanetary dust grain collected in the stratosphere by NASA. This particle is $\sim$ 10 μm in diameter, and composed of glass, carbon and silicates. Reproduced from http://stardust.jpl.nasa.gov/science/sci2.html. Part b) is an interstellar extinction curve for our galaxy, adapted from Draine & Lee [1984], Figure 7. The graph plots extinction with wavenumber, with observational data plotted as points. Overplotted as lines are the model contributions of silicates and graphite to the extinction, and the overall modelled extinction curve. A combination of graphite and silicates is a reasonable model to fit the observed data, although the carbonaceous contribution could also be due to polyaromatic hydrocarbons.

by a shock wave, dust recondenses out of the gas phase. The particle size is believed to vary from a few nm up to 1 μm, with larger grains porous, or 'fluffy', in nature due to their formation by aggregation [Williams & Herbst, 2002].

Estimates of the timescales of grain formation ($\tau_{formation} \sim 3 \times 10^9$ years) and destruction ($\tau_{destruction} \sim 5 \times 10^8$ years) vary by an order of magnitude, implying that, since there is a high abundance of dust in the ISM, it must be regenerated within the ISM. The residence time of dust grains in the ISM is $\sim 3 \times 10^8$ years [Draine & Salpeter, 1979; Jones et al., 1994].

Up to 15 % of the silicates in outflows are crystalline, but in the ISM, grains are $\sim$ 95 % amorphous in nature due to cosmic ray processing [Li & Draine, 2002]. Various minerals, including siliceous olivines ($Mg_{2x}Fe_{2-2x}SiO_4$), siliceous pyroxenes ($Mg_xFe_{1-x}SiO_3$), and metallic oxides have been postulated as constituents of dust grains, with the amorphous olivine $MgFeSiO_4$ showing the best approximation to interstellar observations [Sofia & Meyer, 2001]. It is also believed that polycyclic aromatic hydrocarbons (PAHs), diamond and graphite are present.

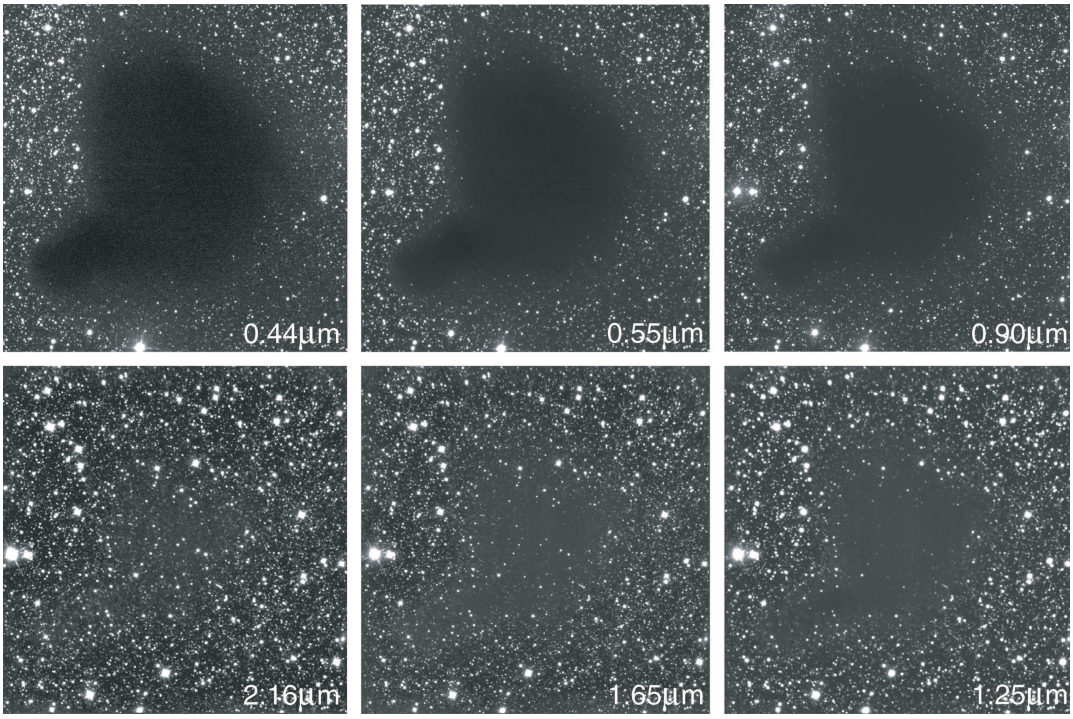

Figure 1.4. Extinction by interstellar dust. Barnard 68 is imaged in six different wavebands, from 0.44 μm in the top left, clockwise to 2.16 μm in the bottom left. It is clear that extinction decreases redward, as the light from background stars is less obscured by the dust in the molecular cloud. Image credit: ESO PR Image eso9934b.

Although interstellar dust constitutes only ~ 1 % of the mass of the ISM, it has a large impact on its physics and chemistry. One of the main ways to study dust derives from the property first noted by Herschel - its propensity for extinction. Dust scatters, absorbs and reflects light at wavelengths comparable to its dimensions; most extinction is seen in the optical region, but in the infrared, light is less affected by interactions with dust particles. This is illustrated in Figure 1.4, where the same molecular cloud is imaged at various wavelengths. At 0.44 μm, it appears dark due to extinction, but at 2.16 μm the light from stars behind the cloud is not extincted by the dust to the same degree, and the cloud is much less apparent on the sky. The interstellar extinction curve, illustrated in Figure 1.3b, is a measure of optical depth as a function of wavelength. By modelling the extinction curve, particle size distribution, composition and abundance can be estimated [Draine, 2003].

Dust grains are known to align within molecular clouds, causing polarisation

of the light from reddened stars. The degree of polarisation (only a few percent, as the orientation of grains changes due to rotation and collision) suggests that grains are ellipsoidal in shape. The alignment of grains suggests they are magnetically susceptible, possibly due to the presence of iron and oxides in their composition [Draine, 2003].

Light associated with dust grains is observed in the form of far-infrared emission peaks (luminescence), microwave emission (rotational electric dipole emission), infrared (thermal) emission, and reflection nebulae and X-ray haloes (scattered light) [Draine & Murdin, 2000]. The depletion or under abundance of certain elements in the gas phase (e.g. Fe, Si, Mg and C) relative to solar abundances, suggests that a large fraction of these elements are in the solid phase i.e. grains, rather than remaining in the gas phase. However, it should be noted that these calculations assume that solar abundances would not otherwise differ from interstellar abundances, which is not necessarily a safe assumption [Snow, 2000].

One final indirect method of observing dust grains in molecular clouds is by observing the absorption bands of solid phase molecular species that form on grain surfaces.

1.1.3 Icy mantles

Spectroscopic studies in the infrared have revealed that dust grains in molecular clouds are covered in a mantle of solid phase molecular species, predominantly H_2O. One such infrared spectrum is shown in Figure 1.5. Due to the low temperatures and (relatively) high pressures of molecular clouds, gas phase atomic and molecular species condense onto the surface of dust grains, forming an icy mantle. The mantle composition evolves due to various processes, including the catalysed formation of molecular species in or on the ice, desorption of these species into the gas phase, and the processing of the ices by UV radiation and cosmic rays. Thus the final ice composition is very different to that of the gas phase [van Dishoeck & Blake, 1998]. Ice mantle formation and evolution occurs on a timescale far shorter than that of the astrophysical processes involved in star formation (§ 1.1.1), and therefore the chemistry of molecular clouds has the potential to be a useful indicator of shorter term

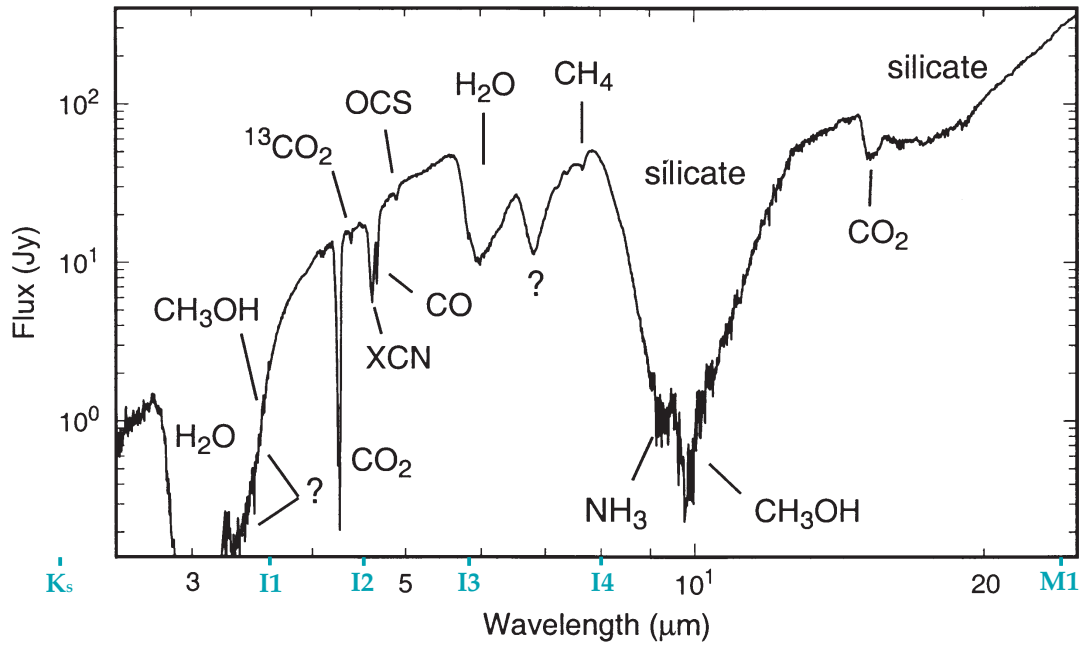

Figure 1.5. Infrared spectrum of massive protostar W 33A, illustrating the absorption bands of molecular species in dust grains in the region 2.4 – 25 μm. Absorption features are labelled in black and several photometric bands, relevant to the data in this thesis, are plotted in light blue on the wavelength axis. The full list of photometric bands discussed in this thesis includes: J (1.25 μm, not shown here), H (1.65 μm, not shown here), K_S (2.17 μm), IRAC1–4 (3.6, 4.5, 5.8, 8.0 μm, labelled I), MIPS1 (24 μm, labelled M), SCUBA (450, 850 μm, not shown here). Figure adapted from Gibb et al. [2000], Figure 1.

physical and chemical processes in these regions.

The composition of icy mantles, as derived from observational evidence, is discussed in § 1.2, while laboratory studies of the characteristics and formation mechanisms are discussed in § 1.4.

1.1.4 Interstellar molecules

The first molecule detected in space was CH [Adams, 1941]; to date, around 170 interstellar molecules have been identified (see Table 1.1). In astrochemical terms, as distinct from terrestrial chemistry, both ions and radicals are considered to be molecular species. By far the most abundant molecule in the ISM is H_2. Interstellar gas, which has a mean density of $\sim$ 1 atom cm^{-3}, is composed of $\sim$ 90 % hydrogen by number density, or $\sim$ 75 % by mass

[Dyson & Williams, 1997], and the vast majority of the identified interstellar molecules reside in the gaseous phase. Gas phase observations are traditionally performed in the microwave or radiofrequency regions, where the rotational transitions of molecules occur. Solid phase observations are performed in the infrared, where the molecules are identified via the stretching and bending vibrational modes of their functional groups.

Molecules are important in astronomy as they can be used as probes or tracers of astrophysical conditions. Traditionally, only gas phase molecules have been utilised in this way. At lower densities ($n_H < 10^2$ cm^{-3}), most hydrogen is in its atomic form. H can be observed via its spin-flip transition at 21 cm (in the radio region), and thus the physical properties and kinematics of low density gas can be traced [Ewen & Purcell, 1951]. In molecular clouds, however, almost all hydrogen is in its molecular form. H_2 has no dipole, and thus has no (allowed) rotational transitions with which to trace it in a cold gas. Thus rotational transitions of CO, the second most abundant species in molecular clouds (H_2/CO = 10^4 – 10^5), are used as a cold gas tracer. Some molecules, such as N_2H^+, NH_3, H_2D^+, HC_5N and CS, only become excited at high densities, so are used to probe interstellar gas density in various environments [Little et al., 1978; Walmsley & Ungerechts, 1983; Taylor et al., 1996; Roberts & Millar, 2007].

Some recent attempts have been made to determine the links between the gas phase and solid phase abundances of molecular species in molecular clouds [Öberg et al., 2009]. By observing the molecules CH_3OH and HNCO, which can reside in either the gaseous or solid phases, Öberg et al. [2009] hoped to determine a link between their gas phase and solid phase abundances, and thus establish a benchmark for using gas phase abundances as a diagnostic of the solid phase abundances in molecular clouds. As it is, in many respects, more complex to observe and interpret the spectra of solid phase molecules than those in the gas phase, the establishment of such relationships between solid phase and gas phase abundances would be an important step in quantifying the abundances of solid phase molecular species, particularly those with low abundances. Although studies to date have proven relatively inconclusive, with the high resolution gas phase observations of Herschel and ALMA telescopes, this type of investigation is becoming more feasible from an observational point of view.

Table 1.1. Molecules in the Interstellar Medium.[a,b]

2 atoms	3 atoms	4 atoms	5/6 atoms	7/8/9 atoms	10+ atoms
H_2	C_3^*	c-C_3H	C_5^*	C_6H	CH_3C_5N
AlF	C_2H	l-C_3H	C_4H	CH_2CHCN	$(CH_3)_2CO$
AlCl	C_2O	C_3N	C_4Si	CH_3C_2H	$(CH_2OH)_2$
C_2^{**}	C_2S	C_3O	l-C_3H_2	HC_5N	CH_3CH_2CHO
CH, CH^+	CH_2	C_3S	c-C_3H_2	CH_3CHO	HC_9N
SH^+	HCN, HNC	$C_2H_2^*$	H_2CCN	CH_3NH_2	CH_3C_6H
CN, CN^-	HCO	NH_3	CH_4^*	c-C_2H_4O	C_2H_5OCHO
CO	HCO^+	HCCN	HC_3N	H_2CCHOH	$C_6H_6^*$
CO^+	HCS^+	$HCNH^+$	HC_2NC	C_6H^-	$C_2H_5OCH_3$?
CP	HOC^+	HNCO	HCOOH	CH_3C_3N	n-C_3H_7CN
SiC	H_2O	HNCS	H_2CNH	$HC(O)OCH_3$	$HC_{11}N$
HCl	H_2S	$HOCO^+$	H_2C_2O	CH_3COOH	C_{60}^*
KCl	H_2Cl^+	H_2CO	H_2NCN	C_7H	C_{70}^*
NH	HNO	H_2CN	HNC_3	H_2C_6	
NO	MgCN, MgNC	H_2CS	SiH_4^*	CH_2OHCHO	
NS	FeCN	H_3O^+	H_2COH^+	l-HC_6H^*	
NaCl	N_2H^+	c-SiC_3	C_4H^-	CH_2CHCHO ?	
OH	N_2O	CH_3^*	HC(O)CN	CH_2CCHCN	
PN	NaCN	C_3N^-	C_5H	H_2NCH_2CN	
SO, SO^+	OCS	PH_3 ?	l-H_2C_4	CH_3C_4H	
OH^+	SO_2	HCNO	$C_2H_4^*$	CH_3CH_2CN	
SiN	c-SiC_2	HOCN	CH_3CN	$(CH_3)_2O$	
SiO	CO_2^*	HSCN	CH_3NC	CH_3CH_2OH	
SiS	NH_2	H_2O_2	CH_3OH	HC_7N	
CS	H_3^{+*}		CH_3SH	C_8H	
HF	H_2D^+, HD_2^+		HC_3NH^+	$CH_3C(O)NH_2$	
HD	SiCN, KCN		HC_2CHO	C_8H^-	
FeO ?	AlNC		NH_2CHO	C_3H_6	
O_2	SiNC		C_5N, C_5N^-		
CF^+	HCP		l-HC_4H^*		
SiH ?	CCP		l-HC_4N		
PO	AlOH		c-H_2C_3O		
AlO	H_2O^+		H_2CCNH ?		

[a] Table reproduced from The Cologne Database for Molecular Spectroscopy http://www.astro.uni-koeln.de/cdms/molecules

[b] All molecules have been detected (also) by rotational spectroscopy in the radiofrequency to far-infrared regions unless indicated otherwise. * indicates molecules that have been detected by their rotation-vibration spectrum. ** indicates molecules that have been detected by electronic spectroscopy only. Tentative detections are indicated by ?

This thesis is focussed on the molecular species present in the icy mantles on the surface of dust grains. By combining observational evidence with laboratory studies, as well as chemical models, the abundances, formation mecha-

nisms and evolution of these species can be determined.

1.2 Observations of interstellar ices

In the 1930s, it was conjectured that interstellar water ice existed because it seemed fitting that interstellar clouds were analogous to "common" atmospheric clouds [Eddington, 1937]. Water ice was finally observed in the 1970s via its 3.1 μm OH stretch absorption band, alongside a 10 μm absorption feature assigned to silicates in the dust grain [Gillett & Forrest, 1973]. Since then, observational evidence for the presence of a complex network of molecular species and their chemistry has been published, and interstellar ices are now known to contain numerous species, including CO_2, CO, CH_3OH, CH_4, NH_3, H_2CO, HCOOH, SO_2 and OCS [e.g. Gerakines et al., 1999; Nummelin et al., 2001; Pontoppidan et al., 2003; Gibb et al., 2004; Knez et al., 2005; Boogert et al., 2008; Öberg et al., 2008; Pontoppidan et al., 2008; Zasowski et al., 2009]. Typical ice abundances in molecular clouds, around low mass YSOs, and around high mass YSOs are shown in Table 1.2.

Whereas gas phase observations rely only upon the presence of gaseous atoms or molecules with observable transitions, and are made in emission, solid phase species are observed as absorption features superimposed upon the blackbody radiation curve of a star, and thus can only be detected along a line of sight towards an embedded object or a star behind a molecular cloud. Observations of solid phase molecules are made in the near- to mid-infrared region, where absorption bands result from vibrational excitation of functional groups in the molecules. This region of the spectrum is difficult to observe from the ground due to telluric absorptions, primarily by gaseous H_2O and CO_2, restricting observation to certain atmospheric windows.

Despite the restrictions, early ground based observations detected ices on interstellar grains, predominantly via observation of the OH stretching vibration at $\sim$ 3.1 μm [Merrill et al., 1976; Capps et al., 1978]. CO was first observed towards the massive protostar W 33A via its stretching vibration at $\sim$ 4.6 μm [Soifer et al., 1979; Lacy et al., 1984].

The advent of space based infrared spectroscopy vastly accelerated the rate

Table 1.2. Molecular ice abundances in quiescent molecular clouds, and towards low mass YSOs and high mass YSOs, relative to H_2O.[a]

Molecule	Molecular cloud	Low mass YSO	High mass YSO
H_2O	1	1	1
CO_2	0.24	0.22	0.14
CO	0.26	0.20	0.08
NH_3	< 0.08	0.06	0.15
CH_3OH	< 0.02	0.06	0.15
NH_4^+	0.05	0.06	0.08
CH_4	< 0.03	0.05	0.02
H_2CO	$\cdots$	0.06	0.03
HCOOH	< 0.01	0.03	0.05
OCN^-	< 0.02	< 0.01	0.02

[a]Abundances relate to objects Elias 16, HH 46, and W 33A, respectively. Values taken from Chiar et al. [1995]; Boogert et al. [2004]; Gibb et al. [2004]; Knez et al. [2005]; Pontoppidan et al. [2008]; Boogert et al. [2008]; Bottinelli et al. [2010]; Öberg et al. [2008]; van Broekhuizen et al. [2005]

of ice observations. Due to atmospheric absorptions, it is not possible to observe CO_2 from the ground via either its 4.27 μm stretching mode or its 15.2 μm bending mode. The first observations of CO_2 were made with the InfraRed Astronomical Satellite, IRAS [D'Hendecourt & Jourdain de Muizon, 1989], with confirmation from the superior spectral resolution of the Infrared Space Observatory, ISO, a few years later [de Graauw et al., 1996; Nummelin et al., 2001]. ISO also revealed the presence of CH_4 [Boogert et al., 1996], NH_3 [Gibb et al., 2000], HCOOH and H_2CO [Keane et al., 2001] in interstellar ices.

The first space based studies of low mass protostars were performed with *Spitzer*. Much examination was made of the CO_2 bending mode at 15.2 μm [Pontoppidan et al., 2008; Whittet et al., 2009; Zasowski et al., 2009], and it was determined that the profile of this band towards quiescent regions showed none of the signs of processing seen towards YSOs [Knez et al., 2005]. Large surveys also investigated H_2O [Boogert et al., 2008] and CH_4 [Öberg et al., 2008]. Most recently, the AKARI satellite has allowed the observation of the three most abundant solid phase molecular species (H_2O, CO_2 and CO) con-

currently, in the 2.5 – 5.0 μm region [Shimonishi et al., 2008, 2010], although no spectra have yet been published of objects in this galaxy.

Addressing primarily the molecules and the environments investigated in this thesis, observations to date reveal some interesting results. H_2O was the first ice to be identified in quiescent molecular clouds [Whittet et al., 1983] and, as in other interstellar environments, is the most abundant species, at $\sim$ 70 % of the total ice (see Table 1.2). CO_2, first observed using ISO [Whittet et al., 1998], exists in two environments – a H_2O-rich phase and a CO-rich phase – and is unprocessed [Knez et al., 2005]. CO is also present at high abundances and is unprocessed in molecular clouds, typically existing as pure CO or CO in a H_2O-rich mixture [Chiar et al., 1994, 1995].

Molecular clouds were believed to contain neither OCN^- nor CH_3OH [Tegler et al., 1995; Chiar et al., 1996] but more recent observations reveal upper limits of a few percent on both of these species [Knez et al., 2005; Boogert et al., 2008]. Limitations of infrared absorption spectroscopy include the overlap of absorption features which may mask the observation of minor species, the scattering of light, the potential presence of material from different environments in the line of sight, and the dependence upon a high oscillator strength to detect low abundance species. Thus, species with abundances below a few percent relative to water are very difficult to detect [Dartois et al., 2002]. Other low abundance detections include HCOOH [Boogert et al., 2008], NH_3, CH_4 [Knez et al., 2005], OCS [Gibb et al., 2004], as detailed in Table 1.2.

Low mass YSOs also have high abundances of H_2O [Boogert et al., 2008], CO_2 [Pontoppidan et al., 2008] and CO [Pontoppidan et al., 2003]. Due to energetic processing, higher abundances of species such as HCOOH [Boogert et al., 2008] and CH_3OH [Bottinelli et al., 2010] are observed, as well as the presence of H_2CO [Boogert et al., 2008]. Typical abundance values for a low mass YSO are presented in Table 1.2. Other signs of processing include the evolution of the absorption profiles of species such as CO_2 and CO [Pontoppidan et al., 2008] and the varying ratios of pure and H_2O-rich CO ices [Pontoppidan et al., 2003].

O_2, one of the molecules studied in Chapter 6, is a homonuclear diatomic and thus infrared inactive. O is the most abundant cosmic atomic species (after

H and He) and O_2 is predicted to form on dust grain surfaces in molecular clouds, with abundances comparable to CO [Tielens & Hagen, 1982]. Studies of gas phase O_2 have determined that the gaseous O_2 concentration is lower than anticipated [Goldsmith et al., 2000; Pagani et al., 2003; Liseau & O_2din Team, 2005], suggesting that O_2 is frozen out on grain surfaces. However, studies into solid O_2 abundance have proved inconclusive. It was suggested that, for sufficiently high abundances, O_2 could be detected via the 6.45 μm absorption feature when present in a H_2O matrix [Ehrenfreund et al., 1992]. Such a study towards two protostars provided tentative upper limits on O_2 abundance, suggesting that less than 6 % of interstellar O was contained in solid O_2, but these values were calculated by analysing the profile of the CO band, as the 6.45 μm band was not detected [Vandenbussche et al., 1999]. The question of the 'missing' oxygen remains an important topic for further study, currently being addressed by the Herschel Oxygen Project [Goldsmith et al., 2011].

Observations in the infrared towards individual lines of sight have revealed a lot about the molecules present in molecular clouds. In order to understand the complex chemical networks underpinning these abundances, it is necessary to determine the spatial distribution of these species and relate this to pressure, temperature and the abundance of other molecules in the cloud.

1.3 Ice mapping

Ice mapping aims to determine the spatial distribution of solid phase molecular species within a molecular cloud, and from this distribution, gain a better understanding of the chemical links between species. As discussed in § 1.1.4, certain molecules in the gas phase can be observed in emission, in order to trace the abundance and distribution of that molecular species across the cloud. Mapping in the solid phase, however, relies upon the serendipitous positioning of stars directly behind the cloud to provide lines of sight that can be probed.

The density of the dust in a cloud can be measured by calculating the visual extinction (A_V) towards field stars behind the cloud. As dust density increases, so does the observed A_V, and by comparing molecular abundances to extinc-

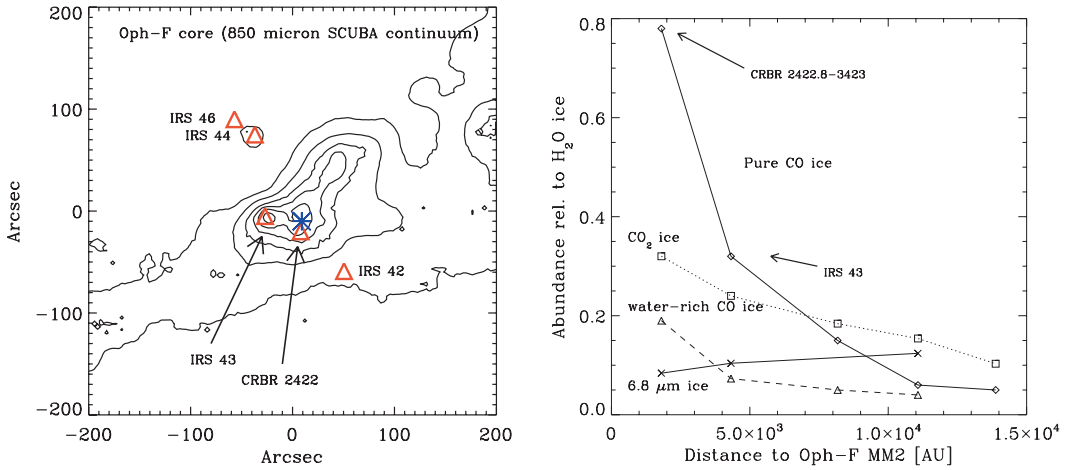

Figure 1.6. Left: the 850 μm SCUBA map of the Oph-F core, with observed lines of sight marked as red triangles and the core centre marked with a blue asterisk. Right: the variation of molecular abundance as a function of distance from the centre of the core. Reproduced from [Pontoppidan, 2006], Figures 2 & 3.

tion, some interesting links are apparent. H_2O is the solid phase molecular species that forms at the lowest densities (earliest times) and is linearly correlated with extinction above a critical A_V of ~ 3 [Smith et al., 1993]. CO, believed to be the only observed solid phase species to form in the gas phase and condense onto the grain, is a highly abundant gas phase molecule in molecular clouds, but catastrophically freezes out into the solid phase, beginning at a critical A_V of ~ 7 [Chiar et al., 1994; Pontoppidan et al., 2003; Whittet et al., 2010]. CO_2 first appears at an A_V critical of ~ 4 [Whittet et al., 2010], and thus some CO_2 must be formed before CO freezes out onto the grain surface.

Studies of more than one molecular species provide even greater insight. H_2O, CO_2 and CO observed towards five YSOs in the Ophiuchus-F star forming core imply that CO_2 formation occurs in two distinct periods: concurrently with H_2O at low extinctions, observed in a H_2O-rich ice formed on the grain surface; and during freeze-out of CO, observed in a CO-rich overlayer [Pontoppidan, 2006], as illustrated in Figure 1.6.

A spatially resolved map of H_2O and CH_3OH ice abundances showed that, while H_2O ice abundances remain constant over a range of densities, CH_3OH ice abundances increase by at least a factor of ten towards the class 0 protostar SMM 4 in the Serpens star forming cloud [Pontoppidan et al., 2004]. The

CH_3OH is likely forming from CO frozen out on dust grains at high densities.

Other ice mapping studies include the partial observation of the 3 μm H_2O stretching absorption band towards 50 stars behind the Taurus molecular cloud complex [Murakawa et al., 2000]. The optical depth at 3.1 μm was found to correlate well with a gas phase $C^{18}O$ map; as $C^{18}O$ traces relatively dense regions of the CO gas, this suggests that H_2O ice abundance increases with the density of the cloud. A study of ice abundances of CO_2 and H_2O towards the Cepheus A East star-forming region, was performed using *Spitzer* [Sonnentrucker et al., 2008]. Abundances of the molecular species were calculated by fitting laboratory spectra to the bending mode absorption bands at 15 μm (CO_2) and 6 μm (H_2O). The results of this study suggested that CO_2 and H_2O were formed on dust grains, somewhat concurrently, across the region sampled, while peak abundances are found in regions close to an embedded protostar. This type of study provides evidence that processing in one region of a star-forming region facilitates a different chemistry in that local region, but not necessarily throughout the surrounding areas.

Considering both the abundances and spatial distributions of key ice species provides insight into chemical networks in molecular clouds, including the links between the solid and gas phases. Chapter 4 presents spatially resolved ice maps of H_2O, CO_2 and CO towards molecular clouds. As well as observational evidence, laboratory astrochemistry and surface science are key to furthering understanding of molecular abundances and distributions in molecular clouds. While observations can sometimes provoke questions rather than providing answers, the more controlled environment of a laboratory allows the study of a particular chemical reaction or molecular species under standard conditions, thus allowing a larger degree of interpretation and analysis.

1.4 Chemistry on dust grains

1.4.1 The formation of molecules on surfaces

Of the molecular species detected in the icy mantles on interstellar dust grains, only CO is believed to form in the gas phase. All other species form on the

dust grain or ice surface, upon which atoms and molecules accreting from the gas phase can meet and react, and which acts as an energy sink, removing excess reaction energy from the newly formed molecule [Tielens, 2005]. The formation of water ice on dust grain surfaces was first postulated in the 1940s [van de Hulst, 1946], and more recent chemical models predict that the reactions of O, C, N and H, condensed out of the gas phase, form molecular species such as CO_2 and NH_3 [Tielens & Hagen, 1982; Ruffle & Herbst, 2001]. At low densities ($< 10^{-4}$ cm^{-3}), H is the dominant reaction partner, and thus hydrogenated species prevail, but at higher densities, hydrogen is predominantly in the form H_2 – it forms on grain surfaces and desorbs into the gas phase, but is somewhat shielded from cosmic rays and photons, limiting its destruction – and hydrogenation plays little role [Tielens, 2005].

The formation of molecular hydrogen, for example, is catalysed by dust grains, which dissipate the energy released by the formation reaction. H_2 is the most abundant molecule in the universe, an abundance significantly higher than that predicted by gas phase models. As H_2 is a homonuclear diatomic, it has no dipole moment and thus can not radiate away excess energy. Therefore, were it to form by radiative recombination in the ISM, the energy of formation would dissociate the molecule into H atoms. To explain the abundance of this molecule in molecular clouds, a solid phase formation route is necessary.

In order to participate in surface chemistry, an atom or molecule must first accrete out of the gas phase. The probability of a gaseous atom colliding with the grain surface and remaining there is defined by the sticking coefficient. The probability depends on several parameters, including the kinetic energy of the incident atom or molecule, its binding energy on the surface, surface morphology and surface temperature [Govers et al., 1980]; at 10 K, the value of the sticking coefficient for most species is close to unity (with the exception of He and H_2). At densities of $\sim 10^4$ cm^{-3}, atoms and molecules accrete from the gas phase at a rate of around one per day [Ehrenfreund & Charnley, 2000].

Adsorption, the process by which a gas phase atom or molecule becomes bonded to the grain surface, can be a chemical bond (chemisorption) or a physical interaction (physisorption). Chemisorption is characterised by a strong interaction, such as a covalent or ionic bond, between the atom or molecule and the surface, on the order of ~ 1 eV. Chemisorption sites on a grain surface are very energet-

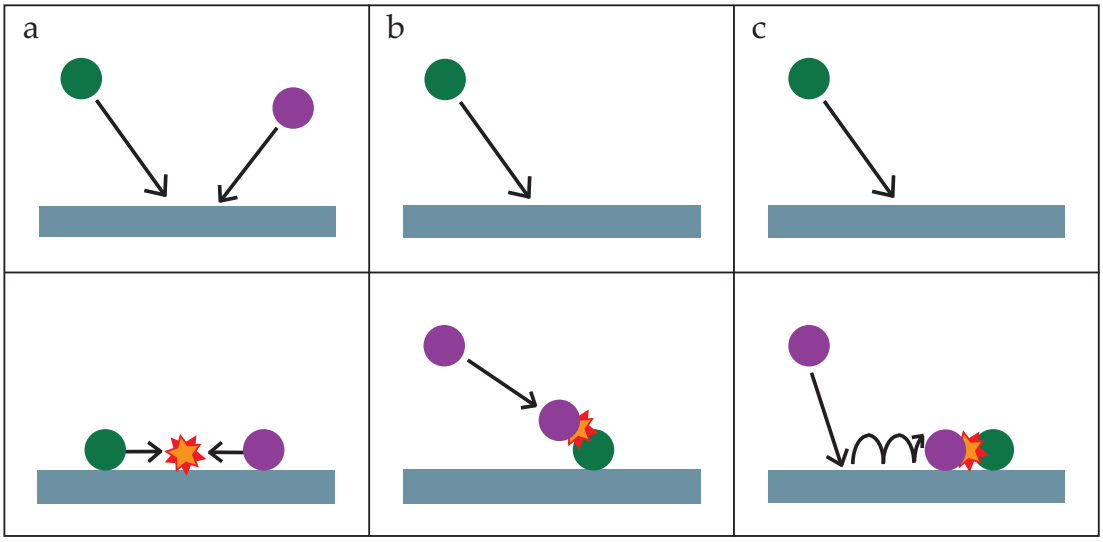

Figure 1.7. Molecular formation mechanisms. In all cases one atom (green) adsorbs on the surface. a) Langmuir-Hinshelwood. The second atom (purple) also adsorbs on the surface. Both atoms diffuse around the surface and react to form a molecule when they both share a binding site. b) Eley-Rideal. The second atom, in the gas phase, collides directly with the first. c) Harris-Kasemo. The second atom lands on the grain and hops several times before meeting and reacting with the first.

ically favourable and are therefore quickly occupied by solid phase molecules. They are typically unavailable for atomic or molecular adsorption from the gas due to the high energy barrier to chemisorption. Physisorption, weak Van der Waals interactions between the gas and the solid, has much shallower potential energy wells in the range 0.01 – 0.2 eV, and is the dominant interaction force for adsorbing species.

Atomic species are mobile on the grain surface and can diffuse between adsorption sites. Most atoms diffuse across the surface by thermal hopping, while hydrogen can also migrate rapidly by quantum mechanical tunnelling [Goodman, 1978]. Evaporation of atomic species occurs due to vibrations in the bond with the surface, but at low temperatures the timescale of evaporation is large compared to the diffusion timescale, so atoms are likely to visit all available bonding sites before desorbing. In reality, some adsorption sites on a grain will be unavailable to an atom or molecule (e.g. those on a different facet), and so low coverage regimes are important models of grain surface chemistry.

The formation of molecules occurs via two principle mechanisms: the Langmuir-

Hinshelwood (LH) or the Eley-Rideal (ER) mechanisms, illustrated in Figure 1.7. In LH, two atoms or molecules adsorbed on (and at thermal equilibrium with) the dust grain surface encounter one another on a binding site and react to form a molecule, which may then desorb. In ER, the collision of an atom or molecule from the gas phase with another atom or molecule adsorbed on the grain surface leads to the formation of a molecule. Activation barriers and reaction energies of LH and ER generally differ as the effect of the surface is different in the two mechanisms. A third formation mechanism which can overcome higher activation barriers is the Harris-Kasemo or 'hot atom' mechanism. An atom with a high kinetic temperature lands on the grain surface, hopping several times and losing some energy before meeting and reacting with another atom. This scenario has a reaction frequency of virtually zero in molecular clouds, as atoms are likely to be in the ground energy state, but may occur in the laboratory.

Astrochemists' understanding of the basic chemical mechanisms in the interstellar medium is complemented and enhanced by laboratory experiments under astrophysically relevant conditions of temperature and pressure.

1.4.2 Laboratory astrochemistry

Solid phase laboratory astrochemistry is concerned with the formation and evolution of astrophysically relevant ices and ice species, the dust upon which they reside, and the identification and interpretation of absorption features in infrared observations. These two types of study can provide complementary information about interstellar ices in a controlled, reproducible manner.

Laboratory experiments are carried out under conditions as close as possible to those in the interstellar medium. Temperatures of 10 – 20 K are typically used to mimic molecular clouds; the lowest experimental pressures available are $\sim 10^{-10}$ mbar – a density of $\sim 10^{6}$ cm^{-3} – which is significantly higher than those in molecular clouds ($\sim 10^{4}$ cm^{-3} [Williams & Herbst, 2002]). However, the low pressure does reduce surface contamination by molecular species (particularly H_2O) which have high abundances in air. Experiments are performed on a surface, traditionally a well characterised metal surface [e.g. Watanabe & Kouchi, 2002; Fuchs et al., 2006] or a metal coated in a thick layer of wa-

ter ice [e.g. Collings et al., 2004], but increasingly a dust grain mimic such as silicates [Pirronello et al., 1997; Noble et al., 2011], amorphous carbon [Pirronello et al., 1999], graphite [Bolina et al., 2005], zeolites [Fraser et al., 2005] or meteorite sample [Mautner et al., 2006]. It is not possible to work on astronomical timescales, nor at astronomical fluxes; the lifetime of a dense core is 10^5 – 10^6 years, while the typical deposition rate of atoms onto a dust grain surface is one per day, as mentioned above. Thus, experimental data on formation mechanisms, desorption kinetics and ice processing must be modelled before being compared to empirical astrophysical data.

As discussed in § 1.2, observations of interstellar ices consist of infrared spectra containing absorption bands. In order to identify and quantify the molecular species responsible for these absorptions, reference spectra of pure, layered, and mixed ice species are measured in the laboratory. From comparison with experiments, ices in molecular clouds are believed to exist in mantles 50 – 100 monolayers thick, composed predominantly of H_2O, with CO_2, CO, CH_3OH, NH_3, CH_4 and HCOOH components.

In gas phase infrared spectroscopy, molecules absorb light at specific frequencies, the frequencies of the vibrating chemical bonds in their structure. Gas phase absorption features are well resolved, appearing as sharp, narrow peaks in the ro-vibrational spectrum, with separation between bands on the order of 10 cm^{-1} and the width of the bands a few tenths of 1 cm^{-1}. In the solid phase, these absorption features can shift in frequency and become broadened by the interactions of the molecules with one another and (in the case of molecules on a surface) the surface they are deposited on. Rotational transitions are severely restricted and the width of the spectral feature is of the order of at least a few times 10 cm^{-1}. Thus, the spectroscopy of even pure ice samples is far more complex than that of gases, as there are fewer features, they are harder to reproduce, and derive from general functional group absorptions (rather than molecule-specific transitions).

The spectra of mixed and layered ices are particularly important, as they highlight the effect that ice components have on the profiles of other species. The 3.1 μm OH stretch of H_2O was the first ice absorption feature identified in the ISM (§ 1.2). Investigations of the profile of this band in pure H_2O and in mixtures reveal that the profile of the band is altered due to the overlap of

features from other molecules [Hagen et al., 1980]. In order to compare astronomical spectra with laboratory spectra, an understanding of the changing profiles of ice bands is vital to prevent misinterpretation of features. Attempts have been made to calculate the profile distortions caused by interactions of different species, but it is a very complex relationship [Mate et al., 2008]. In observational spectra, the effects of mixing, temperature, pressure, structure and surface all modify the profile and position of absorption features with respect to those measured in the laboratory.

Other surface science techniques are also used to characterise the physical properties of molecular ices. Desorption studies can reveal information about the effects that molecules have on each other in mixtures, and are used to calculate desorption energies and reaction rates for integration into chemical models. Molecules deposited on the surface of H_2O, or co-deposited as a mixture, desorb with altered desorption characteristics compared to pure samples of the molecule [Collings et al., 2003, 2004; Gálvez et al., 2007; Burke et al., 2008].

The properties of H_2O deposited on a surface change with variables like the deposition method, angle of deposition and surface temperature [Stevenson et al., 1999; Fraser et al., 2001; Kimmel et al., 2001; Gálvez et al., 2007]. In interstellar environments, H_2O exists mainly as amorphous solid water (ASW); it forms in the laboratory at temperatures of < 130 K [Merrill et al., 1976; Klinger, 1983; Kouchi et al., 1994]. High density, porous ASW is formed when the surface temperature is low (~ 10 K), and low density, non-porous ASW is formed above ~ 70 K [Jenniskens & Blake, 1994]. Recent experiments suggest that although H_2O forms on dust grains at ~ 10 K, H atom recombinations compact the ice, destroying any porosity, and thus suggesting that a large fraction of interstellar H_2O ice is in the form of non-porous ASW [Accolla et al., 2011]. Observationally, the collapse of pores over time is seen, but this could be due to time or temperature, rather than H atom recombinations. H_2O deposited above 140 K is in a crystalline form, such as that seen in regions which have undergone thermal processing e.g. circumstellar disks [Schegerer & Wolf, 2010] and solar system bodies [Newman et al., 2008]. Reliable analysis of observational spectra relies on the knowledge gleaned from laboratory experiments, as well as laboratory spectra.

Another complication in the 3.1 μm absorption band of H_2O ice is the extended

red wing of the feature, not apparent in laboratory spectra. This feature has more than one contribution and, to date, has not been fully explained. As light passes through a molecular cloud, it is not only absorbed by dust grains and their mantles, but can also be scattered by grains whose dimensions are comparable to the wavelength of the light. In the near infrared, this scattering effect is most apparent in H_2O, as it is the most abundant molecule and also its absorption band is at a wavelength susceptible to scattering. Theoretical models of grain shape effects have been proposed, and application of these modelled scattering effects to laboratory spectra before analysis of observational data is routine [Ehrenfreund et al., 1997]. Other contributions to the red wing of the H_2O band include the absorption bands of CH_3OH at 3.53 μm [Pontoppidan et al., 2003] and PAHs, aliphatic hydrocarbons, or hydrogenated carbonaceous grains at 3.4 μm [Sandford et al., 1991; Mennella, 2008]. This is further discussed in Chapter 4.

Laboratory experiments have been extensively utilised to study formation scenarios for various molecular species. The formation of CO_2 is of particular interest, due to its high abundances and complex observational absorption profiles. As described in § 1.2, CO_2 is observed in two distinct environments in a molecular cloud: roughly two thirds in a water-rich ice layer, where CO_2 likely forms concurrently with H_2O, and a later CO-rich layer formed after the freeze-out of CO [Boogert et al., 2004; Bergin et al., 2005; Pontoppidan, 2006; Pontoppidan et al., 2008]. The identification of these environments was made possible by laboratory studies of CO_2 in mixtures and layers [Gerakines et al., 1995; Ehrenfreund et al., 1997; Elsila et al., 1997; Ehrenfreund et al., 1999; van Broekhuizen et al., 2006].

Theoretical and experimental studies suggest various potential formation routes to CO_2, including energetic routes in regions subject to UV or cosmic ray processing. The UV processing of pure CO ice (at very high energies) [Loeffler et al., 2005], pure CO ice under high vacuum [Gerakines et al., 1996], mixed H_2O:CO ices [Ehrenfreund et al., 1997; Watanabe & Kouchi, 2002; Cottin et al., 2003] and more complex mixtures [D'Hendecourt et al., 1986] yields CO_2. Irradiation of ices with cosmic ray mimics such as H^+, He^+ and electrons also yields high abundances of CO_2 [Palumbo et al., 1998; Loeffler et al., 2005; Jamieson et al., 2006; Bennett et al., 2009; Ioppolo et al., 2009]. It has also been

suggested that irradiation of the carbonaceous grain itself by photons [Mennella et al., 2006] or ions [Mennella et al., 2004] can yield CO_2. Surface science experiments have shown that the oxidation of CO at temperatures of around 150 K is catalysed by the presence of H_2O [Bergled et al., 2001].

The abundance of CO_2 in quiescent regions of molecular clouds has been explained in models by a series of cold solid phase reaction mechanisms [Tielens & Hagen, 1982; Ruffle & Herbst, 2001; Stantcheva & Herbst, 2004; Goumans et al., 2008]. The reaction CO + O $\rightarrow$ CO_2 is the simplest mechanism, but experimentally has been shown to have a very high activation barrier, and is effectively impossible under conditions in molecular clouds [Grim & D'Hendecourt, 1986; Roser et al., 2001; Madzunkov et al., 2006; Oba et al., 2010]. The reaction can proceed via tunnelling, but at such low rates that it does not contribute a significant fraction of CO_2 [Goumans & Andersson, 2010]. The reaction CO + OH has been shown to proceed at 10 K theoretically [Goumans et al., 2008] and experimentally [Oba et al., 2010; Ioppolo et al., 2011; Noble et al., 2011] and is the subject of Chapter 7.

It is clear that the integration of observations, theoretical studies and experiments is key to fully explaining all observations in astrochemistry.

1.5 This thesis

The central theme of this thesis is the complexity of the chemical networks present in molecular clouds, even when considering only the most abundant and simple molecular species. In particular, the thesis focusses on the relationship between the abundances of H_2O, CO_2 and CO, and the formation of CO_2 in quiescent molecular clouds. The work is divided into two sections of three chapters each. The first section of this thesis is concerned with observations of molecular clouds using the AKARI satellite, and the analysis of these data. The second section pertains to experiments performed using the FORMOLISM setup at the Université de Cergy-Pontoise.

Chapters 2, 3 & 4 detail observational results. Chapter 2 introduces the AKARI infrared satellite, detailing its technical specifications and describing its data products. Observations were made with AKARI as part of the IMAPE pro-

gramme to study the abundances of key solid phase molecular species in molecular clouds. Chapter 3 introduces the observations and details a data reduction pipeline written to analyse these data, producing spectra of lines of sight towards stars both embedded in and located behind molecular clouds. In Chapter 4, the spectra are analysed to calculate the abundance of multiple molecular species towards each line of sight. The key correlations between these species are discussed and, for some of the clouds, 2D ice maps of molecular abundance are created.

Chapters 5, 6 & 7 detail experimental results. Over the course of a year, experiments were performed on the FORMOLISM setup at the Université de Cergy-Pontoise. Chapter 5 describes the FORMOLISM experiment in detail. In Chapter 6, a study of the desorption characteristics of various small interstellar-relevant molecules from different types of surface is described. Chapter 7 presents experiments on the formation of CO_2 by the non-energetic formation route CO + OH, and discusses the relevance of this formation route to quiescent molecular clouds.

References

Accolla, M., et al. 2011, PCCP, 13, 8037

Adams, W. S. 1941, ApJ, 93, 11

Andre, P., Ward-Thompson, D., & Barsony, M. 1993, ApJ, 406, 122

Andre, P., & Montmerle, T. 1994, ApJ, 420, 837

Barnard, E. E. 1919, ApJ, 49, 1

Bennett, C. J., Jamieson, C. S., & Kaiser, R. I. 2009, ApJS, 182, 1

Bergeld, J., Kasemo, B., & Chakarov, D. V. 2001, Surface Science, 495, L815

Bergin, E. A., Melnick, G. J., Gerakines, P. A., Neufeld, D. A., & Whittet, D. C. B. 2005, ApJL, 627, L33

Bok, B. J., & Reilly, E. F. 1947, ApJ, 105, 255

Bok, B. J. 1948, Harvard Observatory Monographs, 7, 53

Bolina, A. S., Wolff, A. J., & Brown, W. A., 2005, J. Chem. Phys., 122, 044713

Boogert, A. C. A., et al. 1996, A&A, 315, L377

Boogert, A. C. A., et al. 2004, ApJS, 154, 359

Boogert, A. C. A., et al. 2008, ApJ, 678, 985

Bottinelli, S., et al. 2010, ApJ, 718, 1100

Burke, D. J., Wolff, A. J., Edridge, J. L., & Brown, W. A. 2008, PCCP, 10, 4956

Capps, R. W., Gillett, F. C., & Knacke, R. F. 1978, ApJ, 226, 863

Chiar, J. E., Adamson, A. J., Kerr, T. H., & Whittet, D. C. B. 1994, ApJ, 426, 240

Chiar, J. E., Adamson, A. J., Kerr, T. H., & Whittet, D. C. B. 1995, ApJ, 455, 234

Chiar, J. E., Adamson, A. J., & Whittet, D. C. B. 1996, ApJ, 472, 665

Collings, M. P., Dever, J. W., Fraser, H. J., & McCoustra, M. R. S. 2003, Ap&SS, 285, 633

Collings, M. P., Anderson, M. A., Chen, R., Dever, J. W., Viti, S., Williams, D. A., & McCoustra, M. R. S. 2004, MNRAS, 354, 1133

Cottin, H., Moore, M. H., & Bénilan, Y. 2003, ApJ, 590, 874

Dartois, E., d'Hendecourt, L., Thi, W., Pontoppidan, K. M., & van Dishoeck, E. F. 2002, A&A, 394, 1057

de Graauw, T., et al. 1996, A&A, 315, L345

D'Hendecourt, L. B., Allamandola, L. J., Grim, R. J. A., & Greenberg, J. M. 1986, A&A, 158, 119

D'Hendecourt, L. B., & Jourdain de Muizon, M. 1989, A&A, 223, L5

Draine, B. T. 2003, ARA&A, 41, 241

Draine, B. T., & Lee, H. M. 1984, ApJ, 285, 89

Draine, B., & Murdin, P. 2000, "Encyclopedia of Astronomy and Astrophysics", Institute of Physics Publishing, Bristol.

Draine, B. T., & Salpeter, E. E. 1979, ApJ, 231, 438

Dyson, J. E., & Williams, D. A. 1997, "The physics of the interstellar medium. 2nd ed.", Institute of Physics Publishing, Bristol.

Eddington, A. S. 1937, The Observatory, 60, 99

Ehrenfreund, P., Breukers, R., D'Hendecourt, L., & Greenberg, J. M. 1992, A&A, 260, 431

Ehrenfreund, P., Boogert, A. C. A., Gerakines, P. A., Tielens, A. G. G. M., & van Dishoeck, E. F. 1997, A&A, 328, 649

Ehrenfreund, P., et al. 1999, A&A, 350, 240

Ehrenfreund, P., & Charnley, S. B. 2000, ARA&A, 38, 427

Elsila, J., Allamandola, L. J., & Sandford, S. A. 1997, ApJ, 479, 818

Evans, N. J., II 2008, Pathways Through an Eclectic Universe, 390, 52

Ewen, H. I., & Purcell, E. M. 1951, Nature, 168, 356

Fraser, H. J., Collings, M. P., McCoustra, M. R. S., & Williams, D. A. 2001, MNRAS, 327, 1165

Fraser, H. J., Bisschop, S. E., Pontoppidan, K. M., Tielens, A. G. G. M., & van Dishoeck, E. F. 2005, MNRAS, 356, 1283

Fuchs, G. W., et al. 2006, Faraday Discussions, 133, 331

Gálvez, O., Ortega, I. K., Maté, B., Moreno, M. A., Martín-Llorente, B., Herrero, V. J., Escribano, R., & Gutiérrez, P. J. 2007, A&A, 472, 691

Gerakines, P. A., Schutte, W. A., Greenberg, J. M., & van Dishoeck, E. F. 1995, A&A, 296, 810

Gerakines, P. A., Schutte, W. A., & Ehrenfreund, P. 1996, A&A, 312, 289

Gerakines, P. A., et al. 1999, ApJ, 522, 357

Gibb, E. L., et al. 2000, ApJ, 536, 347

Gibb, E. L., et al. 2004, ApJS, 151, 35

Gillett, F. C., & Forrest, W. J. 1973, ApJ, 179, 483

Goldsmith, P. F., et al. 2000, ApJL, 539, L123

Goldsmith, P. F., et al. 2011, IAU Symposium 280: The Molecular Universe

Goodman, F. O. 1978, ApJ, 226, 87

Goumans, T. P. M., Uppal, M. A., & Brown, W. A. 2008, MNRAS, 384, 1158

Goumans, T. P. M., & Andersson, S. 2010, MNRAS, 406, 2213

Govers, T. R., Mattera, L., & Scoles, G. 1980, J. Chem. Phys., 72, 5446

Grim, R. J. A., & D'Hendecourt, L. B. 1986, A&A, 167, 161

Hagen, W., Allamandola, L. J., & Greenberg, J. M. 1980, A&A, 86, L3

Houghton, H. E. 1942, Monthly Notes of the Astronomical Society of South Africa, 1, 107

Ioppolo, S., Palumbo, M. E., Baratta, G. A., & Mennella, V. 2009, A&A, 493, 1017

Ioppolo, S., van Boheemen, Y., Cuppen, H. M., van Dishoeck, E. F., & Linnartz, H. 2011, MNRAS, 413, 2281

Jamieson, C. S., Mebel, A. M., & Kaiser, R. I. 2006, ApJS, 163, 184

Jenniskens, P., & Blake, D. F. 1994, Science, 265, 753

Jones, A. P., Tielens, A. G. G. M., Hollenbach, D. J., & McKee, C. F. 1994, ApJ, 433, 797

Keane, J. V., Tielens, A. G. G. M., Boogert, A. C. A., Schutte, W. A., & Whittet, D. C. B. 2001, A&A, 376, 254

Kimmel, G. A., Stevenson, K. P., Dohnalek, Z., Smith, R. S., & Kay, B. D. 2001, J. Chem. Phys., 114, 5284

Klinger, J., 1983, J. Phys. Chem., 87, 4209

Knez, C., et al. 2005, ApJL, 635, L145

Kouchi, A., Yamamoto, T., Kozasa, T., Kuroda, T., & Greenberg, J. M. 1994, A&A, 290, 1009

Lacy, J. H., Baas, F., Allamandola, L. J., van de Bult, C. E. P., Persson, S. E., McGregor, P. J., Lonsdale, C. J., & Geballe, T. R. 1984, ApJ, 276, 533

Lada, C. J. 1987, IAU Symposium 115: Star Forming Regions, 115, 1

Li, A., & Draine, B. T. 2002, ApJ, 564, 803

Liseau, R., & O_2din Team 2005, Astrochemistry: Recent Successes and Current Challenges, 231, 301

Little, L. T., MacDonald, G. H., Riley, P. W., & Matheson, D. N. 1978, MNRAS, 183, 45P

Loeffler, M. J., Baratta, G. A., Palumbo, M. E., Strazzulla, G., & Baragiola, R. A. 2005, A&A, 435, 587

Madzunkov, S., Shortt, B. J., Macaskill, J. A., Darrach, M. R., & Chutjian, A. 2006, Phys. Rev. A, 73, 020901

Mate, B., Galvez, O., Martin-Llorente, B., Moreno, M. A., Herrero, V. J., Escribano, R., & Artacho, E. 2008, J. Phys. Chem. A, 112, 457

Mautner, M. N., Abdelsayed, V., El-Shall, M. S., Thrower, J. D., Green, S. D., Collings, M. P., & McCoustra, M. R. S. 2006, Faraday Discussions, 133, 103

Mennella, V., Palumbo, M. E., & Baratta, G. A. 2004, ApJ, 615, 1073

Mennella, V., Baratta, G. A., Palumbo, M. E., & Bergin, E. A. 2006, ApJ, 643, 923

Mennella, V. 2008, ApJL, 82, L101

Merrill, K. M., Russell, R. W., & Soifer, B. T. 1976, ApJ, 207, 763

Molster, F. J., et al. 1999, Nature, 401, 563

Murakawa, K., Tamura, M., & Nagata, T. 2000, ApJS, 128, 603

Newman, S. F., Buratti, B. J., Brown, R. H., Jaumann, R., Bauer, J., & Momary, T. 2008, Icarus, 193, 397

Noble, J. A., Dulieu, F., Congiu, E., & Fraser, H. J. 2011, ApJ, 735, 121

Nummelin, A., Whittet, D. C. B., Gibb, E. L., Gerakines, P. A., & Chiar, J. E. 2001, ApJ, 558, 185

Oba, Y., Watanabe, N., Kouchi, A., Hama, T., & Pirronello, V. 2010, ApJL, 712, L174

Öberg, K. I., Boogert, A. C. A., Pontoppidan, K. M., Blake, G. A., Evans, N. J., Lahuis, F., & van Dishoeck, E. F. 2008, ApJ, 678, 1032

Öberg, K. I., Bottinelli, S., & van Dishoeck, E. F. 2009, A&A, 494, L13

Pagani, L., et al. 2003, A&A, 402, L77

Palumbo, M. E., Baratta, G. A., Brucato, J. R., Castorina, A. C., Satorre, M. A., & Strazzulla, G. 1998, A&A, 334, 247

Pirronello, V., Biham, O., Liu, C., Shen, L., & Vidali, G. 1997, ApJL, 483, L131

Pirronello, V., Liu, C., Roser, J. E., & Vidali, G. 1999, A&A, 344, 681

Pontoppidan, K. M., Dartois, E., van Dishoeck, E. F., Thi, W.-F., & d'Hendecourt, L. 2003, A&A, 404, L17

Pontoppidan, K. M., et al. 2003, A&A, 408, 981

Pontoppidan, K. M., van Dishoeck, E. F., & Dartois, E. 2004, A&A, 426, 925

Pontoppidan, K. M. 2006, A&A, 453, L47

Pontoppidan, K. M., et al. 2008, ApJ, 678, 1005

Roberts, H., & Millar, T. J. 2007, A&A, 471, 849

Roser, J. E., Vidali, G., Manicò, G., & Pirronello, V. 2001, ApJL, 555, L61

Ruffle, D. P., & Herbst, E. 2001, MNRAS, 324, 1054

Sandford, S. A., Allamandola, L. J., Tielens, A. G. G. M., Sellgren, K., Tapia, M., & Pendleton, Y. 1991, ApJ, 371, 607

Schegerer, A. A., & Wolf, S. 2010, A&A, 517, A87

Shimonishi, T., Onaka, T., Kato, D., Sakon, I., Ita, Y., Kawamura, A., & Kaneda, H. 2008, ApJL, 686, L99

Shimonishi, T., Onaka, T., Kato, D., Sakon, I., Ita, Y., Kawamura, A., & Kaneda, H. 2010, A&A, 514, A12

Shu, F. H., Adams, F. C., & Lizano, S. 1987, ARA&A, 25, 23

Smith, R. G., Sellgren, K., & Brooke, T. Y. 1993, MNRAS, 263, 749

Snow, T. P. 2000, J. Geophys. Res., 105, 10239

Sofia, U. J., & Meyer, D. M. 2001, ApJL, 554, L221

Soifer, B. T., Puetter, R. C., Russell, R. W., Willner, S. P., Harvey, P. M., & Gillett, F. C. 1979, ApJL, 232, L53

Sonnentrucker, P., Neufeld, D. A., Gerakines, P. A., Bergin, E. A., Melnick, G. J., Forrest, W. J., Pipher, J. L., & Whittet, D. C. B. 2008, ApJ, 672, 361

Spitzer, L., Jr. 1941, ApJ, 94, 232

Stantcheva, T., & Herbst, E. 2004, A&A, 423, 241

Stevenson, K. P., Kimmel, G. A., Dohnalek, Z., Smith, R. S., Kay, B. D. 1999, Science, 283, 1505

Taylor, S. D., Morata, O., & Williams, D. A. 1996, A&A, 313, 269

Tegler, S. C., Weintraub, D. A., Rettig, T. W., Pendleton, Y. J., Whittet, D. C. B., & Kulesa, C. A. 1995, ApJ, 439, 279

Tielens, A. G. G. M., & Hagen, W. 1982, A&A, 114, 245

Tielens, A. G. G. M. 2005, "The Physics and Chemistry of the Interstellar Medium", Cambridge University Press, Cambridge.

Trumpler, R. J. 1930, PASP, 42, 214

Vandenbussche, B., et al. 1999, A&A, 346, L57

van Broekhuizen, F. A., Pontoppidan, K. M., Fraser, H. J., & van Dishoeck, E. F. 2005, A&A, 441, 249

van Broekhuizen, F. A., Groot, I. M. N., Fraser, H. J., van Dishoeck, E. F., & Schlemmer, S. 2006, A&A, 451, 723

van de Hulst, H. C. 1946, Recherches Astronomiques de l'Observatoire d'Utrecht, 11, 2

van Dishoeck, E. F., & Blake, G. A. 1998, ARA&A, 36, 317

Visser, R. 2009, Ph.D. Thesis, Leiden Observatory, Leiden University.

Walmsley, C. M., & Ungerechts, H. 1983, A&A, 122, 164

Watanabe, N., & Kouchi, A. 2002, ApJ, 567, 651

Whittet, D. C. B., Bode, M. F., Baines, D. W. T., Longmore, A. J., & Evans, A. 1983, Nature, 303, 218

Whittet, D. C. B., et al. 1998, ApJL, 498, L159

Whittet, D. C. B., Cook, A. M., Chiar, J. E., Pendleton, Y. J., Shenoy, S. S., & Gerakines, P. A. 2009, ApJ, 695, 94

Whittet, D. C. B., Goldsmith, P. F., & Pineda, J. L. 2010, ApJ, 720, 259

Williams, D., & Herbst, E. 2002, Surface Science, 500, 823

Williams, D. A. 2005, Journal of Physics Conference Series, 6, 1

Zasowski, G., Kemper, F., Watson, D. M., Furlan, E., Bohac, C. J., Hull, C., & Green, J. D. 2009, ApJ, 694, 459

CHAPTER 2

THE AKARI SATELLITE

2.1 Synopsis

This chapter introduces the infrared satellite AKARI. The satellite was launched in 2006 and observed in the 1.7 – 180 μm range. AKARI was primarily an imaging satellite, but also carried filters allowing spectroscopy to be carried out in the 1.8 – 25.7 μm range. In particular, the dispersion method and detector design allowed for the simultaneous slitless spectroscopy of all objects across two fields of view with dimensions $9.5' \times 10'$ and $1' \times 1'$. Specifically, this chapter describes the technical details of the AKARI satellite and the observations it made.

2.2 Overview of the AKARI spacecraft

AKARI, the first Japanese Aerospace Exploration Agency (JAXA) dedicated infrared satellite, was launched on 22^{nd} February 2006. AKARI carried two instruments: the Far Infrared Surveyor (FIS) and the InfraRed Camera (IRC). FIS was designed to carry out AKARI's primary mission – to perform an all-sky survey at infrared (IR) wavelengths. The first all-sky survey in the IR was performed by IRAS, the first infrared astronomical satellite, launched in 1983 [Ipac, 1994]. The AKARI all-sky survey was intended to surpass that of IRAS due to superior sensitivity, spatial resolution and wider wavelength coverage

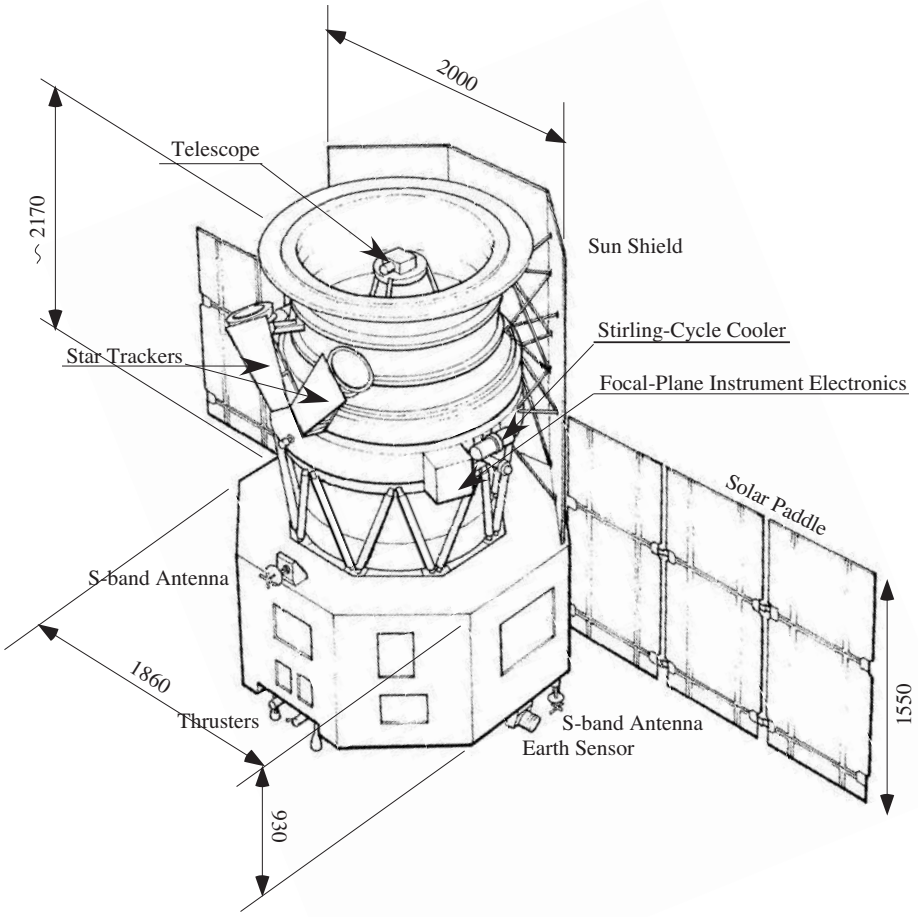

Figure 2.1. The AKARI spacecraft. Dimensions are in mm. The AKARI spacecraft was 3.7 m tall, weighing 960 kg on launch, and consisted of two sections, the cryostat (upper) and the bus module (lower). Reproduced from ASTRO-F User Support Team [2005], Figure 2.2.1.

[Pearson et al., 2004]. IRC was designed for deep imaging from 1.8 – 25.5 μm in pointed observation mode, and also allowed observations using a spectroscopic mode. Only the IRC was used to produce the data presented in this thesis.

AKARI (pre-launch name ASTRO-F) had a 68.5 cm telescope cooled down to 6 K, observing in the range 1.7 – 180 μm. The satellite design, shown in Figure 2.1, consisted of two main sections, the cryostat and the bus module. The bus module contained subsystems that controlled electrical power, propulsion,

positioning, data acquisition and telecommunications.

2.2.1 Cryogenics

The telescope was cooled using two sets of Stirling-cycle coolers and liquid helium (170 L on launch). During the helium cooled period, the telescope was held at 5.8 K while, after helium boil-off, the temperature was maintained at $\sim$ 40 K by the mechanical coolers. The coolers were positioned symmetrically, in such a way that their momentum was cancelled out to prevent interference with the satellite attitude.

The Sun shield (Figure 2.1) was always directed towards the Sun, and the cryostat was coated in a silver film to reflect visible light. The telescope, FIS and IRC were shielded by two layers of helium cooled 'Vapour Cooled Shield'.

Liquid helium boiled off on 26^{th} August 2007 [AKARI User Support Team, 2009].

2.2.2 Telescope

The telescope was an F/6.1 Ritchey-Chrétien system (Figure 2.2) with a primary mirror of effective diameter 685 mm and a focal length of 4200 mm (and thus a focal ratio of 6.1). In order to save weight, the primary and secondary mirrors were constructed from silicon carbide (SiC), the first of their kind to be used in a space cryogenic application [Kaneda et al., 2003]. The material is a sandwich construction with a core of porous SiC and a coating of SiC applied by chemical vapour deposition. The diffraction limit for imaging was reached at 7.3 μm.

2.2.3 Attitude and operation

AKARI orbited in a solar-synchronous near-Earth polar orbit along the twilight zone, at an altitude of 745 km and with a period of 100 minutes. This position was maintained throughout the helium cooled period, with no adjustments to the orbit, in order to prevent contamination by thruster gas.

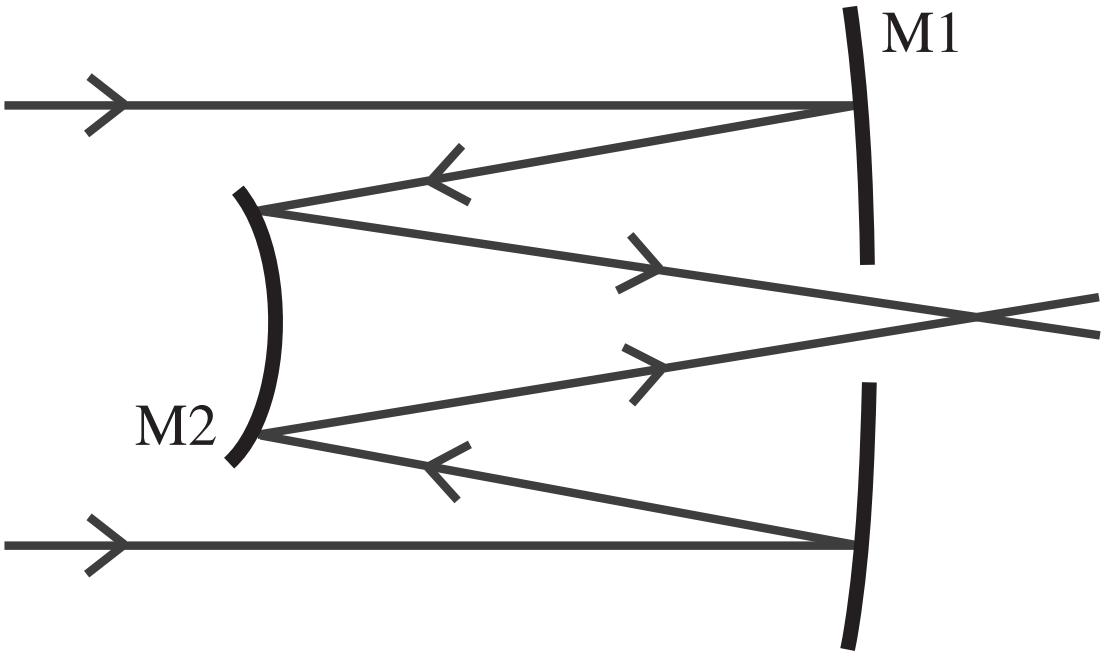

Figure 2.2. A Ritchey-Chrétien system. M1 and M2 are the primary and secondary mirrors.

The spacecraft pointed in the direction perpendicular to the Sun-Earth line, with the Sun shield facing the Sun, rotating once per orbit. As one side of the satellite faced the sun at all times, the design of the heat shield was simplified. This orbit is illustrated in Figure 2.3a.

The attitude and orbit were established and controlled by a series of sensors. The Inertial Reference Unit (IRU, gyroscope) measured the satellite's motion; the Two-dimensional Fine Sun Sensor (TFSS) was intended to monitor the position of the Sun in two dimensions perpendicular to the Sun-satellite direction, correcting any signal drift from the IRU; two Star Trackers (STT) observed the attitude along the third axis and determined satellite roll angle and any change in alignment between the cryostat and bus modules. Following launch it was discovered that the TFSS could not detect the Sun, so attitude control was instead heavily reliant upon the STTs.

The sensor input was analysed by a dedicated computer, the Attitude and Orbit Control Unit (AOCU), which determined the satellite's attitude. A series of reaction wheels and magnetic torque rods controlled the attitude, with an absolute pointing accuracy of 30 arcseconds and a pointing stability of < 1 arc-

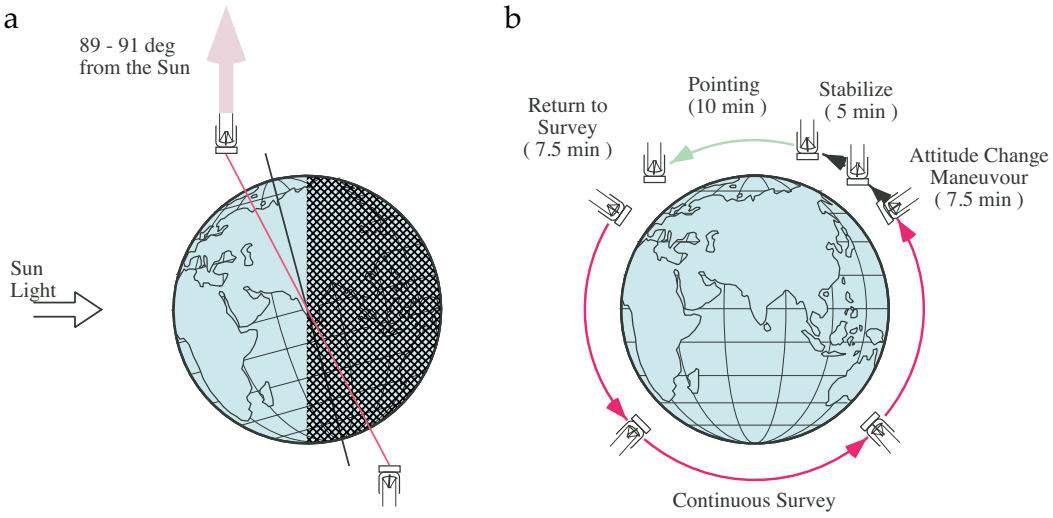

Figure 2.3. The in-orbit attitude of AKARI. Reproduced from Lorente et al. [2007], Figure 3.1.1.

sec min^{-1}.

2.3 The Infrared Camera (IRC)

IRC was designed for deep imaging from 1.8 – 25.5 μm in pointed observations, primarily functioning as an imaging instrument; in addition, low-resolution slitless spectroscopy of the imaging field of view (FoV) was possible due to the interchangeability of transmission-type disperser elements (prism and grism) with the filter optics. A diagram of the IRC instrument is shown in Figure 2.4.

During its initial observational phase, the IRC worked in three channels, near IR (NIR, 2 – 5 μm), short wavelength mid IR (MIR-S, 5 – 13 μm) and long wavelength mid IR (MIR-L, 13 – 26 μm). The properties of these channels are described in Table 2.1.

The NIR camera had a 512 $\times$ 412 pixel InSb detector array (SBRC-189), corresponding to 391 $\times$ 412 in a 9.5 $\times$ 10.0 arcmin^2 FoV and 121 $\times$ 412 for slit spectroscopy. Each MIR camera had a 256 $\times$ 256 pixel Si:As array (CRC-744), with FoV 9.1 $\times$ 10.0 and 10.3 $\times$10.2 arcmin^2 for MIR-S and MIR-L, respectively.

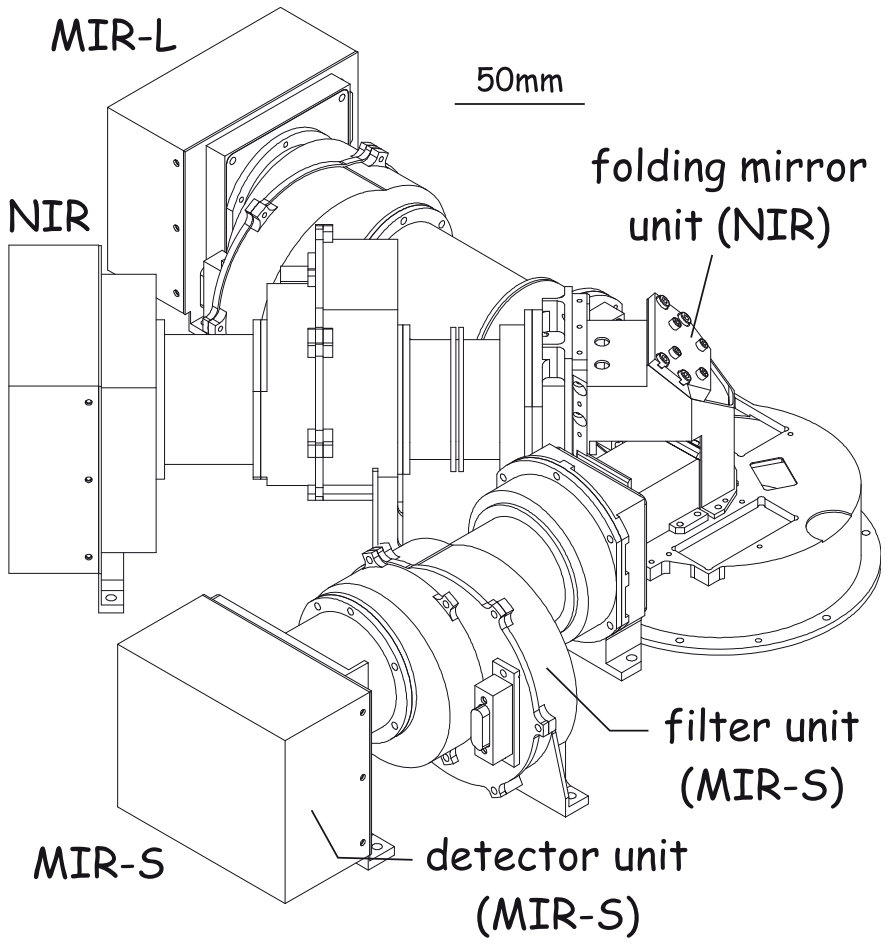

Figure 2.4. The InfraRed Camera on AKARI. The NIR channel operated in the 2 – 5 micron region, the MIR-S channel covered 5 – 12 micron and the MIR-L channel worked in the 12 – 26 micron region. Reproduced from Lorente et al. [2007], Figure 2.0.1.

All detectors were provided by Raytheon IRCoE.

Figure 2.5 details the relative position and size of the fields of view in the three wavelength channels. Full technical specifications for the IRC can be found in e.g. Ohyama et al. [2007]; Lorente et al. [2007]. Light from the telescope was split by a germanium beam splitter in the MIR-S channel, before being focussed through a series of silicon and germanium lenses in the NIR, which had an off-axis refractive optical system. Thus, observations in the NIR and MIR-S channels were obtained simultaneously for every pointing. Only the NIR channel observational data was analysed in this thesis. The NIR channel

Table 2.1. Characteristics of IRC filters and dispersion elements. Reproduced from Lorente et al. [2007], Table 2.0.1.

Channel	Name	Type	λ_{ref}[a] μm	Wavelength μm	λ_C[b] μm	$\Delta\lambda$[c] μm/pixel	Dispersion μm/pixel
NIR	N2	filter	2.4	1.9–2.8	2.34	0.71	—
	N3	filter	3.2	2.7–3.8	3.19	0.87	—
	N4	filter	4.1	3.6–5.3	4.33	1.53	—
	NP	prism	—	1.8–5.2	—	—	0.06 @ 3.5 μm
	NG[d]	**grism**	**—**	**2.5–5.0**	**—**	**—**	**0.0097**
MIR-S[e]	S7	filter	7.0	5.9–8.4	7.12	1.75	—
	S9W	filter	9.0	6.7–11.6	8.61	4.10	—
	S11	filter	11.0	8.5–13.1	10.45	4.12	—
	SG1	grism	—	5.4–8.4	—	—	0.057
	SG2	grism	—	7.5–12.9	—	—	0.099
MIR-L[e]	L15	filter	15.0	12.6-19.4	15.58	5.98	—
	L18W	filter	18.0	13.9-25.6	18.39	9.97	—
	L24	filter	24.0	20.3-26.5	22.89	5.34	—
	LG2[f]	grism	—	17.5-25.7	—	—	0.175

[a]Reference wavelength of the optical element.

[b]Isophotal wavelength of the filter band.

[c]Effective bandwidth.

[d]The spectroscopic mode used for the observations in this thesis, as presented in Chapters 3 & 4.

[e]Not available during Phase 3.

[f]Originally, MIR-L contained a second dispersion element, LG1, with wavelength range 11 – 19 μm, but this element was not available in orbit as it was degraded during ground tests [Ohyama et al., 2007].

is shown in Figure 2.6.

The filters and dispersion elements (summarised in Table 2.1), as well as a blind mask, were located in a filter wheel at the camera iris. Using either the filter or dispersion elements, all light in the FoV was transmitted or dispersed onto the detector. In the NIR, in addition to the main imaging 9.5′ × 10′ FoV, a 'slit' region consisting of three parts was available (see Figure 2.5). Closest to the imaging FoV was a 5″ slit, 'Ns'; next was a 1′ × 1′ square, 'Np', designed for spectroscopy of point sources; finally, a 3″ slit, 'Nh', was designed for spectroscopy of diffuse radiation. Spectra were dispersed parallel to the scan direction (Figure 2.5), producing spectral data in a 2D array, rather than the traditional 3D data cube format.

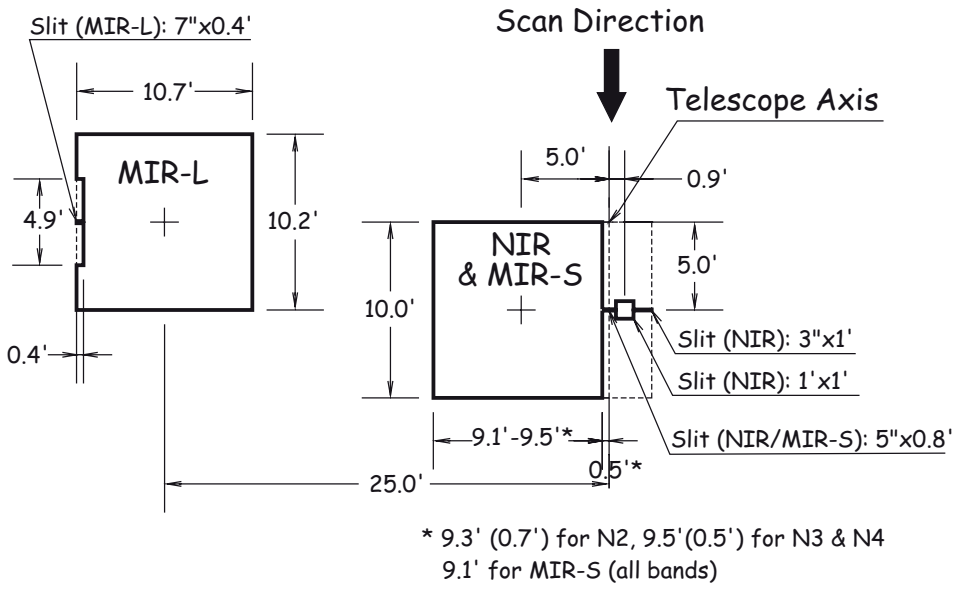

Figure 2.5. Effective field of view location on the sky of the three channels of the IRC. The NIR used a 512 $\times$ 412 format InSb array and MIR-S and MIR-L both employed 256 $\times$ 256 format Si:As impurity band conduction arrays. NIR and MIR-S shared the same FoV by employment of a beam splitter. The NIR detector had a 9.5′ $\times$ 10′ area, as well as a 1′ $\times$ 1′ slit area for observation of point sources. Reproduced from Lorente et al. [2007], Figure 2.0.2.

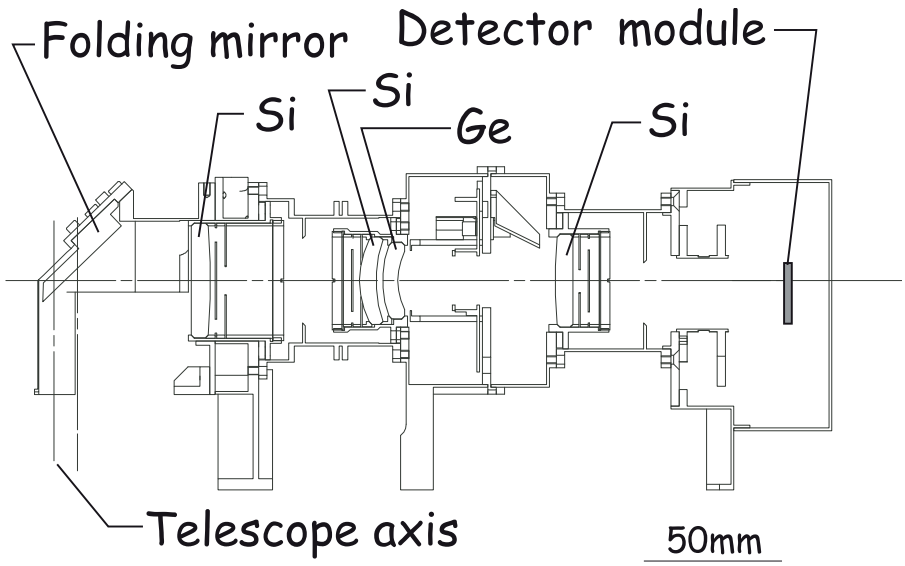

Figure 2.6. A schematic of the NIR channel. Reproduced from Lorente et al. [2007], Figure 2.1.3.

2.4 Observations

2.4.1 Mission phases

The AKARI mission was divided into four phases. Phase 0 was the performance verification stage. During Phase 1, the all-sky survey and other large scale surveys were carried out. During Phase 2, Mission Programmes and Open Time proposals were observed, until liquid helium burn-off in August 2007. After a period of stabilisation, Phase 3 observations at higher temperature commenced, and were halted in May 2010. Phase 3 observations were limited to the NIR region due to the large increase in hot pixels on the detector. The satellite was shutdown on May 24^{th} 2011, with the close of the AKARI mission on the 20^{th} of June 2011.

2.4.2 Operational modes

AKARI had two operational modes: survey and pointing. In the survey mode, AKARI performed a continuous scan of the sky. It was by using this mode that the all-sky survey was completed [Ishihara et al., 2010]. In pointing mode, AKARI observed a specific sky position, allowing longer exposure times than in the survey mode. In each pointing, a series of operations were performed, lasting around 30 minutes: the telescope was moved to the target position; the telescope was stabilised; the target was observed; the telescope was returned to survey mode. This process, in which observation time was approximately 10 minutes per pointing, is summarised in Figure 2.3b.

A pointed observation consisted of a series of exposure cycles with operations, such as filter changes, inserted between them. One exposure cycle lasted around 72.5 seconds, with all three cameras operating simultaneously. Within each exposure cycle, the NIR carried out one short (2.3 s) and one long (51 s) exposure. The short exposure frames were designed to prevent saturation of the detector by bright objects, but have significantly lower photometric accuracy than the long exposure frames. *Fowler 4* sampling, which reduces the readout noise by approximately half, was taken for all long exposure frames. A burst of four readouts were taken at the beginning of an integration and again at the

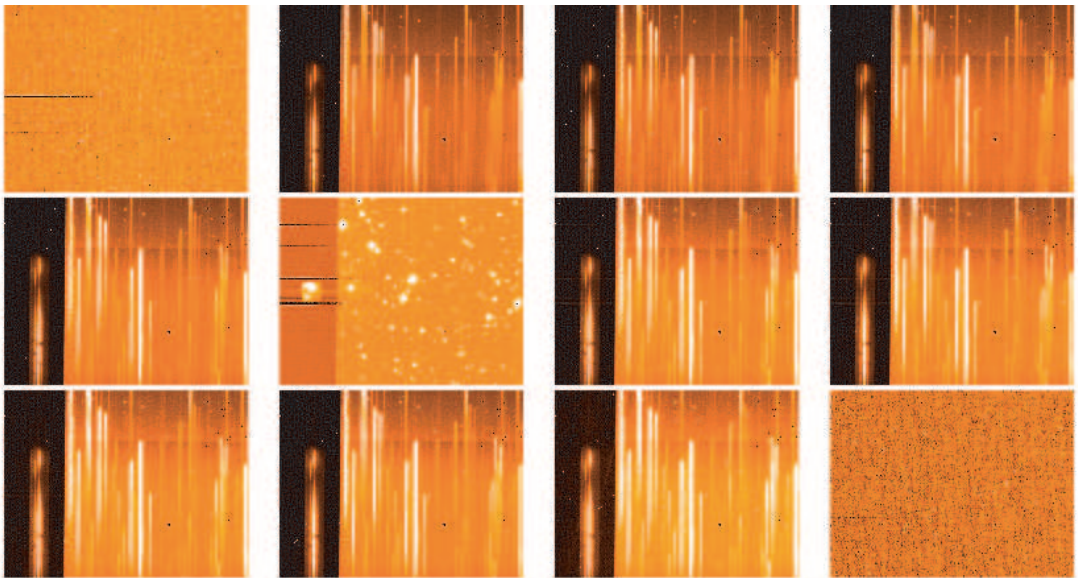

Figure 2.7. Near infrared spectral and image frames (long exposure) captured during one pointing in the IRC04 grism spectroscopic mode. The measured flux intensity increases from dark to light orange. Shown left to right from top left; one pre-dark frame, four spectral frames, one imaging frame, a further five spectral frames, and a post-dark frame were taken for each pointing in this mode. During data analysis, detailed in Chapter 3, the final spectral frame was discounted, as it was sometimes taken during maneuver of the satellite.

end of an integration to suppress read noise.

2.4.3 Spectroscopy

The IRC04 spectroscopic mode was a series of exposure cycles using a dispersion element, with one exposure cycle using an imaging filter included. In Phase 2 (where all data presented in this thesis was observed) the target position was defined as the centre of the 9.5′ × 10.0′ imaging FoV for prism mode observations, and the centre of the 1′ × 1′ square in grism mode. The roll angle of the satellite was undefined for all pointings. In the NIR, the combination of filters was either NP/ N3 (prism) or NG/ N3 (grism), where N3 is the imaging filter (see Table 2.1). MIR-S observations were made concurrently with the NIR observations, but these data are not addressed in the main body of this thesis, so the observations are not described here. Some discussion of the MIR-S data is made in Chapter 8.

Each observation dataset consists of a pre-dark frame; four spectroscopy frames; an imaging frame; a further four or five spectroscopy frames; and, possibly, a post-dark frame. This is depicted in Figure 2.7. In the cases where five spectroscopy frames were observed in the second series of spectroscopy exposures, the fifth was discounted, as it was likely taken during satellite maneuver.

The light from all objects observed in the imaging frame was dispersed in the spectroscopy frames, as the spectroscopy was performed in a slitless fashion. Thus, in a single observation, the spectra of multiple objects in the $1' \times 1'$ and $9.5' \times 10.0'$ imaging fields of view were obtained.

2.5 Concluding remarks

The AKARI satellite was well specified for observing the icy mantles on dust grains. It covered the 2.5 – 5 μm region, severely limited from the ground, for the first time since ISO, thus encompassing the stretching absorption bands of H_2O, CO_2 and CO. In the spectroscopic observation mode, slitless spectroscopy allowed the concurrent observation of all objects in a $1' \times 1'$ or $9.5' \times 10.0'$ FoV in a single pointing. AKARI observations are presented and analysed in Chapters 3 & 4.

References

AKARI User Support Team 2009, AKARI Observer's Manual for the Post-Helium (Phase 3) Mission. Version 1.2, Sagamihara, Japan, http://www.sciops.esa.int/SA/ASTROF/docs/akobsman12.pdf

ASTRO-F User Support Team 2005, ASTRO-F Observer's Manual. Version 3.0, Sagamihara, Japan, http://www.ir.isas.jaxa.jp/ASTRO-F/Observation/ObsMan/afobsman30.pdf

Pasadena: Jet Propulsion Laboratory (IPAC) 1994, IRAS Sky Survey Atlas (ISSA)

Ishihara, D., et al. 2010, VizieR Online Data Catalog, 2297, 0

Kaneda, H., Onaka, T., Kawada, M., & Murakami, H. 2003, Appl. Opt., 42, 708

Lorente, R., Onaka, T., Ita, Y., Ohyama, Y., Tanabe, T., & Pearson, C. 2007, AKARI IRC Data User Manual. Version 1.3., Sagamihara, Japan, http://www.ir.isas.jaxa.jp/ASTRO-F/Observation/IDUM/IRC_IDUM_1.3.pdf

Ohyama, Y., et al. 2007, PASJ, 59, 411

Onaka, T., et al. 2007, PASJ, 59, 401

Pearson, C. P., et al. 2004, MNRAS, 347, 1113

CHAPTER 3

OBSERVATIONAL DATA REDUCTION PIPELINE†

3.1 Synopsis

This chapter details observations of molecular clouds made using the AKARI satellite, and the data reduction pipeline written to analyse those observations. The observational strategy is introduced, and discussion is made of the advantages and limitations of AKARI for this study. The slitless nature of the spectroscopy on AKARI produces raw observational data which is complex to analyse, with overlapping spectra a particular problem. This posed the question: is it possible to extract the spectra of multiple objects in a crowded FoV, and if so, can the same analysis method be applied across multiple fields of view? A data reduction pipeline was written to deconvolve the spectra of different objects, producing flux and wavelength corrected spectra for multiple objects in a FoV. The long term aim of the observations is the development of a method for mapping large fields of view by slitless spectroscopy, and the data reduction pipeline presented here represents an important advance towards that goal. The 2.5 – 5 μm spectra of 30 objects – 22 field stars behind quiescent molecular clouds and eight low mass YSOs in cores – were successfully extracted using the pipeline.

†Chapters 3 & 4 are based upon results presented in a paper that will shortly be submitted to the Astrophysical Journal. Early results were published in Noble et al. [2009]; Aikawa et al. [2009]; Noble et al. [2010].

3.2 Introduction

In the NIR, the grism disperser of the IRC on AKARI produces spectra in the range 2.5 – 5 μm at a resolving power of 120 at 3.6 μm (where resolving power, R = $\frac{\lambda}{\delta\lambda}$, and $\delta\lambda$ is the smallest resolving element size, corresponding to the full width half maximum (FWHM) of the point spread function (PSF) in N3). This is the first time since ISO (1995 – 1998) that the full 2.5 – 5 μm range has been available in a single observation, as telluric absorptions prevent the observation of this range from the ground. Two big advantages of this include simultaneous observation of the stretching mode absorption bands of the three most abundant solid phase molecular species – H_2O, CO_2 and CO – and observation of the blue wing of the H_2O band, allowing for a more accurate calculation of the column density (the number density per unit area, measured along a column) of H_2O ice due to better fitting of reference spectra. A third advantage, unique to AKARI, is that the spectroscopy is slitless, with spectra being simultaneously captured for all objects in the FoV, allowing mapping of ices in a molecular cloud with a single pointing. However, as all spectra are captured on the imaging CCD detector, the reduction of the raw data can be complicated due to overlapping spectra whose light must be deconvolved. AKARI has a high sensitivity, allowing the observation of objects with much lower fluxes than those observed with ISO. Thus, while ISO was restricted mainly to observing high mass YSOs, AKARI can sample large numbers of low flux background stars and YSOs.

Ices in various environments have been studied with AKARI, although only three papers have been published to date. Two NIR studies of ices around extragalactic YSOs have been performed using the two dispersers on AKARI, the prism [Shimonishi et al., 2008] and the grism [Shimonishi et al., 2010]. These studies suggest that the abundance of CO_2 around YSOs in the Large Magellanic Cloud (LMC) is higher than that seen in our own galaxy. Ices on Titan were studied in the NIR, resulting in the tentative discovery of solid HCN [Burgdorf et al., 2010]. Ices in circumstellar disks were studied in the ISICE observing programme (a subset of which is analysed here), where H_2O, CO_2, CO, and OCN^- were clearly detected, as well as weak features of CH_3OH and, potentially, HDO [Aikawa et al., *submitted*]. Other topics studied with AKARI

include externally heated pre-stellar cores [Nutter et al., 2009], Neptune's atmosphere [Fletcher et al., 2010] and an all-sky survey [Ishihara et al., 2010]. Very few spectroscopic studies have been published.

3.3 Observational methodology

The data analysed and presented in this chapter and Chapter 4 derive primarily from the AKARI European Users Open Time Observing Programme IMAPE (P.I.: H. J. Fraser). This programme was devised as a study of ice abundances across a large number of quiescent molecular clouds and star forming cores – a subset of the c2d *Spitzer* Legacy program [Evans et al., 2003] – using the slitless spectroscopy of field stars behind the clouds as a method of ice mapping.

The aims of the IMAPE programme included: the observation of ices towards multiple lines of sight in multiple molecular clouds; the simultaneous observation of the stretching mode absorptions of the three most abundant solid phase molecular species, H_2O, CO_2, and CO; the simultaneous observation of the stretching mode and the bending mode absorptions of CO_2 using the NG or NP dispersion elements in the NIR channel and the LG1 dispersion element in the MIR-S channel; and the creation of convolved $9.5' \times 10'$ 2D ice maps of H_2O, CO_2, and CO by calculation of their relative abundances towards the lines of sight in the main imaging FoV.

In the IMAPE programme, clouds were selected by identifying those containing dense prestellar cores with $A_V > 2$, a statistically large number of identifiable field stars behind the cloud, and with the proviso that no previously identified YSO candidates were in the line of sight. This approach was intended to allow the simultaneous observation of 2.5 – 5.0 μm spectra of multiple background stars (and any embedded YSOs) in a single FoV, allowing the observation of a large number of H_2O, CO and CO_2 absorption features concurrently, and subsequently the mapping of the spatial distribution of these ices across the clouds. In addition, it was hoped to observe a large sample of objects with A_V in the range 2 – 10, to test the critical A_V of H_2O, CO_2 and CO in many molecular clouds.

The observation of multiple molecular clouds would provide a large number of new spectra towards quiescent lines of sight and the calculation of relative molecular abundances across a range of molecular clouds. Until the publication of a recent article by Boogert et al. [2011], the vast majority of the background stars observed spectroscopically were behind only two molecular clouds (Taurus and Serpens), and most studies focussed on a single cloud, rather than making observations towards multiple clouds. The intention of this AKARI study was to observe multiple objects behind multiple molecular clouds, and analyse the spectra using a standard method, to search for similarities and differences in the chemistry of different clouds. AKARI was ideally suited to this approach, as the slitless spectroscopy mode allowed the simultaneous observation of spectra towards all objects in the $9.5' \times 10'$ and the $1' \times 1'$ fields of view. In the $9.5' \times 10'$ fields of view, the number of objects observed towards the molecular clouds in the IMAPE programme was on the order of 100 – 200, and in the $1' \times 1'$ fields of view it was approximately 5 – 10.

This profusion of spectra did, however, pose certain problems, namely with the analysis of spectral data. Unlike traditional slitless spectrometers, AKARI did not produce a 3D data cube with different wavelengths observed in different frames. The dispersion of spectra by the dispersion elements was done in a 2D fashion (as seen in Figure 2.7) along the scan direction of the telescope. This feature of the AKARI design resulted in regions of highly confused spectra, where overlapping dispersions made the extraction of individual spectra very complex. It was initially assumed that the data reduction pipeline written by the AKARI User Support Team [Ohyama et al., 2007] could be used to analyse the observations in the IMAPE programme. However, it was discovered that, as the official pipeline was designed for use with single line of sight pointings and analysed spectra using an aperture method, it was inapplicable to the IMAPE observations. Thus, an inhouse data reduction pipeline was written, and this chapter details the technical aspects of that pipeline. That very little AKARI spectroscopic data has been published to date illustrates how complex the data analysis is. All previously published spectra [Shimonishi et al., 2008, 2010; Burgdorf et al., 2010] are towards single lines of sight extracted using the toolkit provided by the AKARI team, designed for the extraction of isolated objects.

In the NIR, observations were carried out using both the NP and NG dispersion elements, as it was not clear at the proposal stage which disperser would be best suited to ice mapping. The NG had a higher resolution, but the dispersion of the spectra on the detector was subsequently longer than for the NP, with the potential to cause a higher degree of confusion in regions of spectral overlap. It was envisaged that the CO and CO_2 absorption features might not be fully resolved at the NP resolution, but that when using the NG dispersion element, they would be resolved, and the H_2O band might be less saturated. As it was anticipated that the spectra towards crowded regions of the sky could become confused, two observations of each molecular cloud were scheduled, in the hope that in each case the roll angle of the satellite would be different, and the spectra of the objects would be dispersed in a different orientation, allowing the deconvolution of all objects by combination of all data (see clouds marked † in Table 3.1). It was not possible for the observer to define the roll angle of AKARI. Unfortunately, in most cases, both observations of a given molecular cloud were performed on concurrent orbits of the satellite, and thus the roll angle was almost identical for both observations. In the two cases where scheduling was temporally separated, the two roll angles were almost exactly 180° out of phase, again negating the approach. Fortunately, the two pointings approach did afford an improvement in the spectral signal-to-noise, and allowed for better removal of hot pixel and cosmic ray effects from the data.

Additional constraints on the observer included the specification of the observational coordinates. In Phase 2, the observer could specify the centre of the 9.5′×10′ FoV for NP observations, but only the centre of the 1′×1′ FoV for NG observations. Thus, molecular clouds were well observed in the larger 9.5′×10′ FoV in NP pointings, but due to the constraints on coordinate and roll angle specification, none of the molecular clouds targeted in the NG pointings were observed in the 9.5′×10′ FoV. The observational data in the NIR is therefore divided into two distinct categories: NP pointings in the 9.5′×10′ FoV and NG pointings in the smaller 1′×1′ FoV. This thesis focusses on the analysis of the latter category, although some discussion of early attempts at analysing the 9.5′×10′ NP observations is made in Chapter 8.

AKARI observed both the NIR and MIR-S simultaneously due to the beam

splitter in the MIR-S channel (§ 2.3). This potentially offered the ability to observe both the CO_2 stretching mode absorption at 4.27 μm and the bending mode absorption at 15.2 μm simultaneously. It was hoped that this would offer the opportunity to investigate the chemical and physical links apparent between the two bands and better constrain molecular abundance data by improving the fit of each band with reference to the other. However, during the performance verification, it was determined that the LG1 filter was not functioning, and thus no spectroscopy of the range 12.9 – 17.5 μm was possible.

No control over calibration data was available to observers as no calibration pointings could be proposed in Phase 2. This, for example, resulted in no flat field data being available for the 1′×1′ FoV, as this calibration was not made by the AKARI team. AKARI offered an absolute pointing accuracy of 30 arcseconds and a pointing stability of < 1 arcsec min^{-1} (or approximately 400 AU for an object at 400 parsec).

The main aim of the IMAPE programme was to determine the relative abundances of H_2O, CO_2 and CO across a cloud in order to produce convolved ice maps based on 100 – 200 objects observed in the 9.5′×10′ FoV. Due to the higher resolution of the NG dispersion element, and the efficiency of the inhouse data reduction pipeline described in this chapter, absorption features of objects observed in the 1′×1′ FoV were, in fact, resolved enough for the application of a component analysis fitting approach, and the calculation of absolute molecular abundances. Thus, although the ice maps presented in Chapter 4 are bubble plots, rather than maps convolved across the whole FoV, key insights into the chemistry of the molecular clouds mapped are provided. The data reduction pipeline presented in this chapter was developed with a view to analysing all of the data obtained in the IMAPE programme. Therefore, although this thesis only details the analysis of the NIR NG observations in the 1′×1′ FoV, the pipeline design also allows for the analysis of NIR NP observations in the 9.5′×10′ FoV, as well as the MIR-S and MIR-L observations. Further comments on the future development of the pipeline are made in Chapter 8. The NG 1′×1′ pointings have a small FoV, a linear dispersion element, minimal distortion and observe the centre of the cloud where large ice features are seen. All of these features make it ideal for the initial design and development of the data reduction pipeline.

3.4 Observations

Observations were carried out between December 2006 and August 2007 using the IRC04 spectroscopic mode of the Infrared Camera on AKARI [Onaka et al., 2007; Ohyama et al., 2007] of fields of view towards 19 dense molecular clouds. Of these, 11 were part of the IMAPE programme detailed in § 3.3; a total of 46 pointings were observed in this programme, 84% of those assigned. A further eight fields of view are included here from the Japan/Korea Users Open Time Observing Programme ISICE (P.I.: Y. Aikawa). Details of the 19 clouds are given in Table 3.1. All observations were carried out in IRC04 spectroscopic mode during Phase 2 (see Ohyama et al. [2007]; ASTRO-F User Support Team [2005] for detailed descriptions of all AKARI Astronomical Observation Templates (AOTs)). Details of the cloud selections in the ISICE programme, for which only single pointings were made of each cloud, are given in [Aikawa et al., *submitted*]; a selection of well known cloud cores was picked.

The observations presented here focus specifically on data obtained with the IRC04 AKARI AOT using the near infrared (NIR) grism disperser (NG). The AOT produces eight spectral frames, an imaging frame and a pre- and post-dark frame per FoV per pointing, as described in Chapter 2. The spectra were extracted from the Np aperture, a $1' \times 1'$ FoV with a spectral range 2.5 – 5.0 μm (R = 120 at 3.6μm). Imaging frames for 16 of the clouds are shown in Figure 3.1. The images were taken with the N3 filter (2.7 – 3.8 μm) at a reference wavelength of 3.2 μm. As is clear from Figure 3.1, some fields of view contain multiple objects. The complexity of extracting spectra from AKARI pointings is that each spectral frame is two dimensional, i.e. the wavelength dispersion is superimposed upon the y axis, unlike traditional slitless spectroscopy where a data cube is produced. Nevertheless, 30 individual objects were identified across these fields of view (highlighted in Figure 3.1) for which spectra were successfully extracted using the data reduction pipeline described in this chapter. The selection and classification of these individual objects are discussed later in § 3.5.4.1. As far as can be ascertained from the literature, ice spectra have not previously been published for any of the objects in the lines of sight observed here. Three clouds listed in Table 3.1 will not be discussed any further in this thesis. The FoV in DC 300.2-03.5 was too confused to enable

Table 3.1. Molecular clouds observed

Molecular Cloud	Coordinates (J2000)[a] R. A. /degree	Dec. /degree	AKARI[b] Observation ID	Date DD/MM/YYYY
L 1551	67.8708	+18.1356	3010019_001	28/02/2007
B 35A	86.1262	+ 9.1461	4120022_001†	16/03/2007
DC 269.4+03.0	140.5938	-45.7896	4120043_001	09/12/2006
			4121043_001	08/06/2007
DC 274.2-00.4	142.2042	-51.6153	4120007_001†	17/12/2006
DC 275.9+01.9	146.6904	-51.1000	4120009_001†	20/12/2006
DC 291.0-03.5	164.9663	-63.7227	4120023_001†	21/01/2007
BHR 59	166.7875	-62.0994	4120002_001†	19/01/2007
DC 300.2-03.5	186.0904	-66.2024	4121045_001†	07/08/2007
Mu 8	187.7146	-71.0227	4120018_001†	12/02/2007
DC 300.7-01.0	187.8771	-63.7233	4120024_001	02/02/2007
			4121024_001	05/08/2007
BHR 78	189.0583	-63.1920	4121041_001†	05/08/2007
B 228	235.6744	-34.1621	3011017_001	24/08/2007
BHR 144	249.3750	-35.2333	3010017_001	03/03/2007
L 1782-2	250.6333	-19.7272	3010010_001	03/03/2007
LM 226	254.3333	-16.1461	3010012_001	06/03/2007
L 1082A	313.3792	+60.2464	3010028_001	22/12/2006
L 1228	314.3956	+77.6282	3011006_001	22/08/2007
L 1165	331.6683	+59.0999	4121035_001†	07/07/2007
L 1221	337.1083	+69.0417	3010003_001	26/01/2007

[a]Right Ascension and Declination at the centre of the Np aperture.

[b]Observations where a second pointing with ID XXXXXXX_002 was made immediately after the first are represented by †. All other observations are explicitly tabulated.

the extraction of any spectra, even though ice features may have been present; data from L 1082A and DC 269.4+03.0 were below the lower flux limit at which the pipeline functioned effectively, as discussed in detail in § 3.5.4.1.

3.5 Data reduction

3.5.1 AKARI Reduction Facility (ARF)

Data reduction was performed using a purpose written data reduction pipeline – the AKARI Reduction Facility, hereafter referred to as ARF – developed to analyse AKARI NIR spectroscopic data. The pipeline was written in the Interactive Data Language (IDL), incorporating procedures taken from the IDL As-

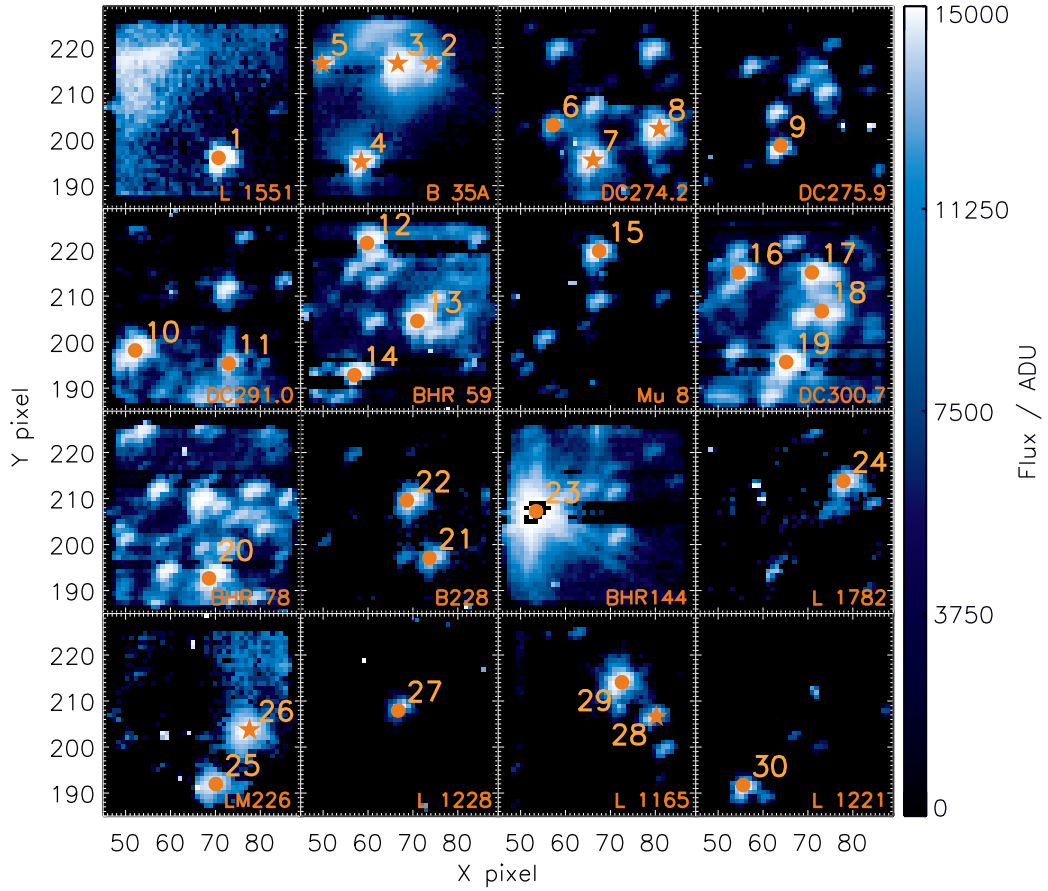

Figure 3.1. Imaging frames (at 3.2 μm) for the 1′ × 1′ grism field of view for all 16 cores observed. X pixel is aligned with right ascension, Y pixel to declination, and the colour bar indicates the flux in each pixel. The 30 objects for which ice spectra were extracted are numbered in order of ascending right ascension; this sample includes 22 background stars (•) and eight YSOs (⋆); of the 22 background stars, 12 were extracted completely and 10 are considered to provide upper limit values, whilst for the YSOs, six were fully extracted and two give upper limits. Details of each source object, including J, H, K photometric values and object coordinates are given in Table 4.1.

tronomy User's Library [Landsman, 1993] and the Markwardt Library [Markwardt, 2009].

The AKARI 1′ × 1′ aperture was designed for point source spectroscopy of single sources and the data reduction toolkit written by the IRC team (Ohyama et al. [2007], hereafter referred to as 'the toolkit') was intended to analyse such sources (as mentioned in § 3.3). In the majority of the observations in this thesis, there was more than one object in the 1′ × 1′ aperture, whose dispersed spectra overlapped and produced confused spectra when reduced using the

toolkit. The pipeline, ARF, was therefore developed specifically to address this issue.

The basic function of ARF is illustrated in Figure 3.2: the eight raw spectral data frames (Figure 3.2a) are dark-subtracted and corrected for bad and hot pixels before being shifted and stacked. Background sky subtraction is then performed (Figure 3.2b). Objects in the FoV are identified, then shifted to account for distortion. The spectrum of each object is then extracted by fitting the grism PSF to the dispersed flux (Figure 3.2c). Extracted data are divided by the spectral response function (SRF) of the NIR detector to produce spectra on a flux-wavelength scale (Figure 3.2d). Each of these reduction procedures is fully described in § 3.5.2 – 3.5.5. In general, this is a standard reduction technique, the main exception being the extraction method, described in detail in § 3.5.4.

3.5.2 Correction of raw data frames

The raw data frames are corrected for hot pixels and bad pixels. The result of this is evident by comparing Figure 3.2a & b; the white hot pixels in Figure 3.2a (e.g. at (X=59,Y=124)) are absent from Figure 3.2b.

A super-dark was provided in the toolkit to correct for, amongst other things, hot pixels in the CCD detector. Hot pixels which develop over time can not, however, be corrected for with this super-dark. Thus, in ARF the pre-dark frame from the pointing is subtracted from each raw spectral frame. While this pre-dark frame has a lower signal-to-noise than the super dark provided in the toolkit, it gives a measure of the dark current at the time of observation and therefore corrects for hot pixels which develop over time.

A hot pixel mask is calculated for each frame to remove cosmic ray hits or hot pixels which develop during the pointing. Three frames are used to create each mask: the frame to be corrected, and two other randomly selected frames, each shifted one pixel perpendicular to the dispersion in opposite directions ($X \pm 1$). The median flux of these three frames is calculated, subtracted from the frame to be corrected, and then the mask defined as any residual flux above a threshold value of 500 Automated Data Units (ADU, the units of flux of the

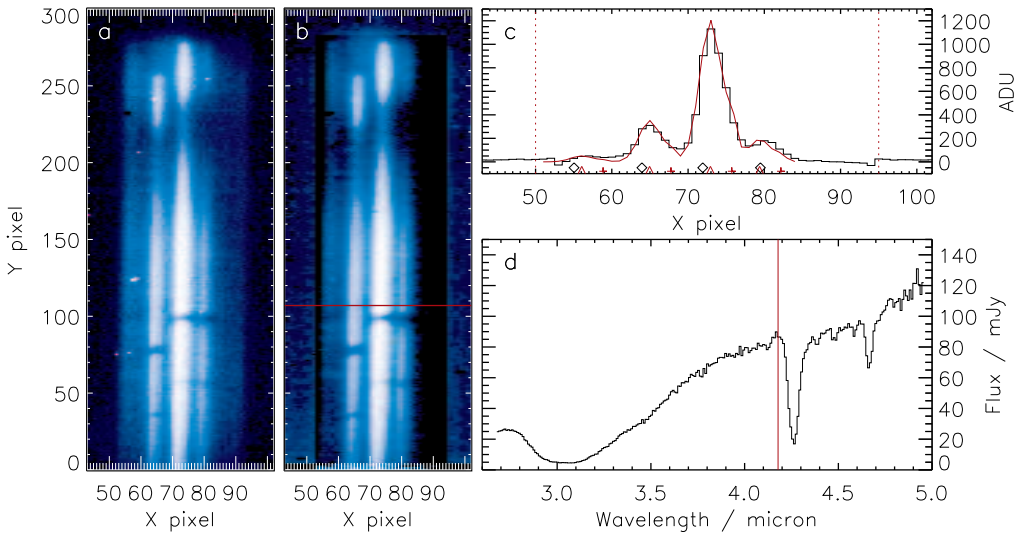

Figure 3.2. An illustration of the 'AKARI Reduction Facility' pipeline, using observations of molecular cloud B 35A. a) Single raw AKARI spectral data frame from the 1′ × 1′ region of the NIR detector. The light from the region of sky in the 1′ × 1′ field of view (B 35A imaging frame in Figure 3.1) is dispersed by the grism disperser along the Y axis. The X axis remains a spatial dimension, while the Y axis is both a spatial and dispersion direction. In the Z direction (represented here by colour intensity, as per the colourbar in Figure 3.1) is the flux information, in Automated Data Units (ADU). Dispersed spectra of at least three objects can be identified by eye in the frame (the positions of the four objects in this field of view are marked in Figure 3.1), and ice absorption features are visible as dark bands in the dispersed data. b) Fully corrected data frame. Eight spectral frames have been dark-subtracted, corrected for hot and bad pixels, shifted and stacked to produce a final, corrected spectral frame. Compared with (a), in this sharper image the dispersed spectra and the ice absorptions are more distinct. Extraction of spectral data proceeds row by row along the dispersion direction; the red line represents the row Y=108. c) The black line shows the resulting flux 'slice' (in ADU) versus X pixel along row Y=108 (red line in (b)). The data is fitted with a series of Gaussian functions, as described in § 3.5.4. In this case, there are four objects (whose X positions are represented by black diamonds on the X axis). The central positions of the Gaussian functions in the fit are plotted as red triangles (on the X axis); the overall fit is superimposed as a red line. This fit well describes the data and deconvolves the overlapping flux of the four distinct objects. This process is repeated for every row in the Y direction. d) Overall final spectrum of the brightest object in this field of view. The spectrum is reconstructed from the series of flux datapoints extracted by the row fitting illustrated in (c); the datapoint produced from the fit in (c) is represented by the red line. The final spectrum on a flux-wavelength scale is produced by division by the spectral response function.

detector), chosen after manual inspection of the data. This mask is subtracted from the frame and the process repeated for all eight spectral frames.

After dark and hot pixel correction, a bad pixel mask provided in the toolkit is applied to remove defective pixels from the frame.

Flat-fielding is not applied to spectral frames. Flat images provided in the toolkit are not applicable to spectroscopy in the $1' \times 1'$ aperture.

3.5.3 Stacking

Due to satellite jitter, there can be a shift of up to a few pixels between observed frames. The shift between frames is calculated by cross-correlation, for the direction perpendicular to dispersion only (X). Frames are shifted by real numbers, with linear interpolation of flux to maintain absolute flux values upon stacking.

Cross-correlation is used to align each of the eight frames [Press et al., 1994; Bracewell, 2000]. Convolution is a measure of the degree to which two or more quantities are linearly associated. Convolution of two functions, $f(t)$ & $g(t)$, and the convolution theorem are defined in Equations (3.1) – (3.2).

$$f * g \equiv \int_{-\infty}^{\infty} f(\tau) g(t - \tau) d\tau, \tag{3.1}$$

where τ is a dummy variable.

$$\widehat{(f * g)}(t) \equiv \hat{f}(t)\hat{g}(t). \tag{3.2}$$

Cross-correlation is a type of convolution typically used to mathematically reduce the noise in a set of data:

$$f \star g \equiv \bar{f}(-t) * g(t), \tag{3.3}$$

where $\bar{f}$ is the complex conjugate of f. Thus, cross-correlation and the cross-correlation theorem can be defined as in Equations (3.4) – (3.5):

$$f \star g \equiv \int_{-\infty}^{\infty} f(\tau + t) g(\tau) d\tau, \tag{3.4}$$

$$\widehat{(f \star g)}(t) \equiv \hat{f}(t)\hat{g}(-t). \tag{3.5}$$

The cross-correlation theorem is applied to each frame to align them before stacking.

Whilst the error caused by shifting in the X direction can be minimised during extraction, shifting in the dispersion (Y) direction would have introduced compound errors in the spectral position of absorption features, or their depth, or both. Although it is potentially feasible to allow shifting in the dispersion direction, this would have required the iterative modelling of the spectral profile using the imaging frame, based on a spectral energy distribution (SED) model of each individual object. Given the presence of the absorption bands which alter the profile with respect to a model SED, and the fact that at this stage data is not flux calibrated, preventing the use of photometric data in determining the model SED, this is an overly complex approach.

For each pixel, the mean flux is calculated across all eight frames, to produce a stacked spectroscopy frame per pointing. Background correction is then performed on this stacked frame, using a region of dark sky picked manually from the spectral aperture. The dark region extends the full length of the aperture in the dispersion direction, its width and position depending on the position of objects in the FoV. The median value of this dark region is calculated in the non dispersion direction, and subtracted from the whole aperture, column by column, producing a dark-corrected, stacked frame (e.g. Figure 3.2b).

3.5.4 Extraction of spectra

3.5.4.1 Target object specification

Target objects for extraction are introduced to the pipeline from target tables, prepared in different manners for the pointings from different observational programs. Pointings which were part of the IMAPE program were a subset of

the c2d *Spitzer* Legacy program and as such had target tables available from that program. Pointings in the ISICE program were not covered by the c2d survey, so target tables were prepared by hand from the Two Micron All Sky Survey (2MASS) project database for these pointings. The 2MASS K_S band flux (centred at 2.2 μm) was common to all objects and was used to determine inclusion in the analysis.

In ARF, the target lists are edited, firstly to exclude objects outside the $1' \times 1'$ aperture, and secondly to exclude those below a threshold K_S band magnitude. The threshold was defined as 1.19 mJy in the K_S band, the magnitude of the brightest isolated object (in DC 269.4+03.0) which could not be fitted with the PSF using the pipeline due to confusion in the fitting routine (discussed in § 3.5.4.3). Thus, the targets remaining are those in the $1' \times 1'$ aperture with a magnitude above the confusion limit of the extractor.

3.5.4.2 Dispersion modelling

In order to extract the dispersed spectrum of each target object, the position of the dispersed light upon the detector must be calculated. The position of the dispersion of each object is modelled based on the target object direct light position – the position of the light on the detector through the N3 imaging filter – and the disperser properties. In the model, the dispersion direction of the detector is defined as Y, with the perpendicular direction X. The start of the dispersion is calculated from the coordinates of the object position from the catalogue (X_{cat}, Y_{cat}), manually shifted to correct for distortion in the telescope optics $(\delta X, \delta Y)$ and the displacement of the first order dispersion relative to the direct light position by approximately 60 pixels in the dispersion direction, δY_{1st}.

The starting position of the dispersion is thus defined as:

$$(X_0, Y_0) = (X_{cat} + \delta X, Y_{cat} + \delta Y - \delta Y_{1st}). \tag{3.6}$$

As can be seen by inspection of Figure 3.2a, the peak position of the flux deviates from the vertical by a small amount along the length of the dispersion, so the model X position is corrected by applying:

$$X_r = X_0 - 0.00746929 \cdot (Y_0 - r), \tag{3.7}$$

where r is the row in the detector being corrected; $(Y_0 - r) = [0, 257]$ is the distance along the spectral dispersion in pixels.

The end of the dispersion is calculated from the start position by considering the wavelength range (2.5 – 5.0 μm) and the dispersion (0.0097 μm pixel^{-1}, a linear function). The end of the dispersion is defined as:

$$(X_f, Y_f) = (X_0 - \Delta X, Y_0 - \Delta Y), \tag{3.8}$$

where $\Delta X = 1.92$ pixels (from Equation (3.7)) and $\Delta Y = \frac{5.0-2.5}{0.0097} = 258$ pixels.

3.5.4.3 Point spread function

The PSF of the AKARI NG disperser was calculated by fitting various combinations of Gaussian functions or Lorentzian functions to a bright point source observed in AOT04 mode (Observation ID: 5020030_001, standard star KF09T1). The best fitting combination was a double Gaussian function:

$$f(X) = \left[A_1 \cdot exp\left\{ -\left(\frac{X - P_1}{\sigma_1} \right)^2 \right\} + 0.8A_1 \cdot exp\left\{ -\left(\frac{X - (P_1 + 2.7)}{\sigma_2} \right)^2 \right\} \right], \tag{3.9}$$

where X is X pixel; A_1 the peak height and P_1 the peak position of the first Gaussian function; and σ_n the FWHM of Gaussian functions n = 1,2.

Fitting the flux with a calculated PSF, rather than applying an aperture method, minimises the flux error introduced by shifting in the X direction. All of the flux in each row will still be considered in the fit, despite any shift. The PSF fitting method is also crucial to the success of ARF in deconvolving the flux of multiple objects in a FoV, which would not be possible using an aperture method.

3.5.4.4 Running the extractor

For each row, $r = [0, 284]$, the extractor runs in the same manner, illustrated in Figure 3.2c. For any given target, if any flux from the dispersion of this object is present in the row – as determined by Equations (3.6) & (3.8) – X_r is calculated using Equation (3.7). This value is substituted into Equation (3.9) with a guess height, A_1, proportional to both the K_S band magnitude of the target and the dispersion, $(Y_0 - r)$. The best fit parameters of Equation (3.9) are calculated with fixed σ_n; $P_1 = P_1 \pm 1$ pixel; weighted by the error on each pixel.

For rows containing more than one target, a linear sum of PSFs is fitted when any targets are within five pixels of each other (in X). This is the key strength of the reduction method presented here, as this approach allows the deconvolution of spectra which are overlapping in X, which would otherwise be discarded due to confusion. The limitations of this approach are discussed in § 3.7.

Bad pixels are masked during stacking, as discussed in § 3.5.3. In any row where two or more consecutive pixels, lying within five pixels of P_1, are masked, that target is removed from the fit in that row. This prevents all targets being misfitted due to confusion in the region of one target. This is particularly seen in the vicinity of a group of bad pixels measuring approximately 3×3 pixels (centred at approximately (X=56,Y=232) and visible as a dark spot in Figure 3.2a,b), which has to be treated specially. For all pointings, targets whose spectra impinge upon this area are removed from the fit for three rows to prevent misfitting of these data rows. Due to the position of this group of bad pixels, this results in a gap in the water band of extracted spectra in this region.

3.5.5 Flux and wavelength calibration

The SRF was generated from an observation of standard star KF09T1 in the $1' \times 1'$ aperture, with the pixel-to-wavelength relation determined by an observation of NGC 6543 in the Ns slit [Itsuki Sakon, *private communication*]. The spectrum extracted from this object was corrected for flux and wavelength by comparison with its calibrated model template spectrum [Cohen et al., 1999].

All extracted spectra are divided by the SRF to produce flux- and wavelength-corrected spectra, $F(\lambda)$ in units of millijansky (mJy), as illustrated in Figure 3.2d. There is no interpolation of wavelength values when dividing by the SRF, which may introduce an error in the wavelength. However, interpolation could increase the intrinsic error in the wavelength based on the pixel size and because shifting can not be performed in the dispersion direction.

The final spectrum of those objects which appear in more than one pointing is generated by combining both spectra after division by the SRF; the two spectra are summed, and the flux divided by two. Objects presented in this thesis which were produced from only a single spectrum are denoted by $*$ in Table 3.2.

3.5.6 Error propagation

The flux error in each pixel is ± 4 ADU [Youichi Ohyama, *Private communication*]. Thus the minimum error in each stacked pixel, ϵ, is calculated by:

$$\epsilon_{min} = \sqrt{n\sqrt{2 \cdot 4^2}}, \tag{3.10}$$

where n is the number of frames stacked, and the factor of two accounts for a contribution from subtracting the dark from each frame prior to stacking. During stacking, the standard deviation in the flux, ϵ_{sd}, is calculated. These errors are combined to calculate ϵ_{ADU}, the overall error in flux, used to weight the fit of the PSF during extraction. The error in the extracted flux, ϵ_{ext}, is the combination of the data error ϵ_{ADU} with the standard deviation of the fit. During division by the SRF, the final error on each datapoint is calculated by combination of the extracted flux error with the error on the SRF, to give $\epsilon_{F(\lambda)}$.

3.6 Observational results

In total, across the 19 clouds there were 94 target objects with 2MASS K_S band magnitude greater than 0 mJy; this was used to determine inclusion in the analysis. 27 of these objects fell below the signal-to-noise threshold of the

Table 3.2. Source list.[a]

Object[b]	2MASS Name	R. A. (J2000)	Dec. (J2000)	Core	J (mJy)	H (mJy)	K_S (mJy)
1†	04312835+1807427	67.868103	18.128599	L 1551	0.143	1.170	2.676
2	J054429.3+090857[c]	86.122498	9.1490002	B35A	...	...	...
3	05443000+0908573	86.124964	9.1492458	B35A	0.067	0.442	7.310
4	05443085+0908260	86.128544	9.1406136	B35A	0.0701	0.537	5.420
5†	05443164+0908578	86.131846	9.1494267	B35A	0.393	1.320	2.370
6†	09284840-5136379	142.20166	-51.610514	DC274.2-00.4	0.086	0.373	1.880
7	09285020-5136373	142.20929	-51.610411	DC274.2-00.4	2.380	8.000	13.600
8	09285128-5136588	142.21379	-51.616373	DC274.2-00.4	3.280	9.080	13.900
9	09464633-5105424	146.69306	-51.095141	DC275.9+01.9	5.530	6.260	4.580
10	10595211-6343000	164.96722	-63.716741	DC291.0-03.5	10.300	15.700	15.600
11	10595548-6343210	164.98119	-63.722508	DC291.0-03.5	1.150	2.320	2.370
12	11070622-6206057	166.77597	-62.101584	BHR59	0.705	4.190	7.760
13	11071041-6206013	166.79341	-62.100358	BHR59	0.804	5.380	11.900
14	11071034-6205345	166.79304	-62.092943	BHR59	0.0997	1.140	6.150
15	12305017-7101331	187.70904	-71.025906	Mu8	4.370	9.270	9.890
16	12312792-6343221	187.86635	-63.722816	DC300.7-01.0	1.370	5.090	7.230
17†	12313060-6343376	187.87753	-63.727139	DC300.7-01.0	3.960	16.400	24.700
18†	12313217-6343306	187.88413	-63.725144	DC300.7-01.0	0.718	4.370	7.250
19	12313247-6343105	187.88539	-63.719644	DC300.7-01.0	4.230	24.800	44.200
20	12361240-6311509	189.05177	-63.197538	BHR78	0.488	3.030	8.500
21†	15424095-3409598	235.67059	-34.166599	B228	0.225	1.376	1.916
22†	15424185-3409435	235.67439	-34.162102	B228	0.905	3.406	4.974
23†	16372876-3513588	249.36990	-35.233002	BHR144	13.125	121.759	331.688
24†	16423341-1943501	250.63921	-19.730600	L 1782-2	0.772	1.895	2.488
25†	16572088-1608241	254.33701	-16.139999	LM 226	0.400	2.004	3.594
26†	16572151-1608423	254.33960	-16.145100	LM 226	0.625	3.447	7.833
27†	20573495+7737415	314.39560	77.628197	L 1228	1.014	4.737	7.783
28	22064175+5906156	331.67388	59.104326	L1165	0.137	0.452	1.490
29	22064185+5906000	331.67432	59.100005	L1165	0.216	3.470	12.300
30†	22283131+6902272	337.13049	69.040901	L 1221	0.785	3.483	5.057

[a]This table contains properties and extraction details of all objects with a spectrum or an upper limit. As seen in Figure 3.1, objects are numbered in order of ascending RA. Here, the positional and photometric properties of these objects are detailed.

[b]The final spectra of all objects marked with † were created from only one extracted spectrum. Generally, these are the objects from the ISICE programme. For all other objects, two spectra were combined to produce the final extracted spectrum.

[c]This object does not have a 2MASS ID and is thus labelled with its *Spitzer* c2d ID. Neither does it have J, H, K_S band flux values.

pipeline, defined as K_S = 1.19 mJy, the magnitude of the brightest isolated object for which PSF fitting failed to converge, which includes all objects in DC 269.4+03.0 and L 1082A. The confusion limit for galactic cirrus and point sources is < 1 μJy in N3, the 3 μm imaging filter [ASTRO-F User Support Team, 2005]. Four objects were only partially observed due to their position at the edge of the FoV, and were thus discounted. 33 objects were too confused to extract any spectral data because of their low flux and overlap with nearby objects, including all those in DC 300.2-03.5. The objects which were successfully extracted using ARF are detailed in Table 3.2.

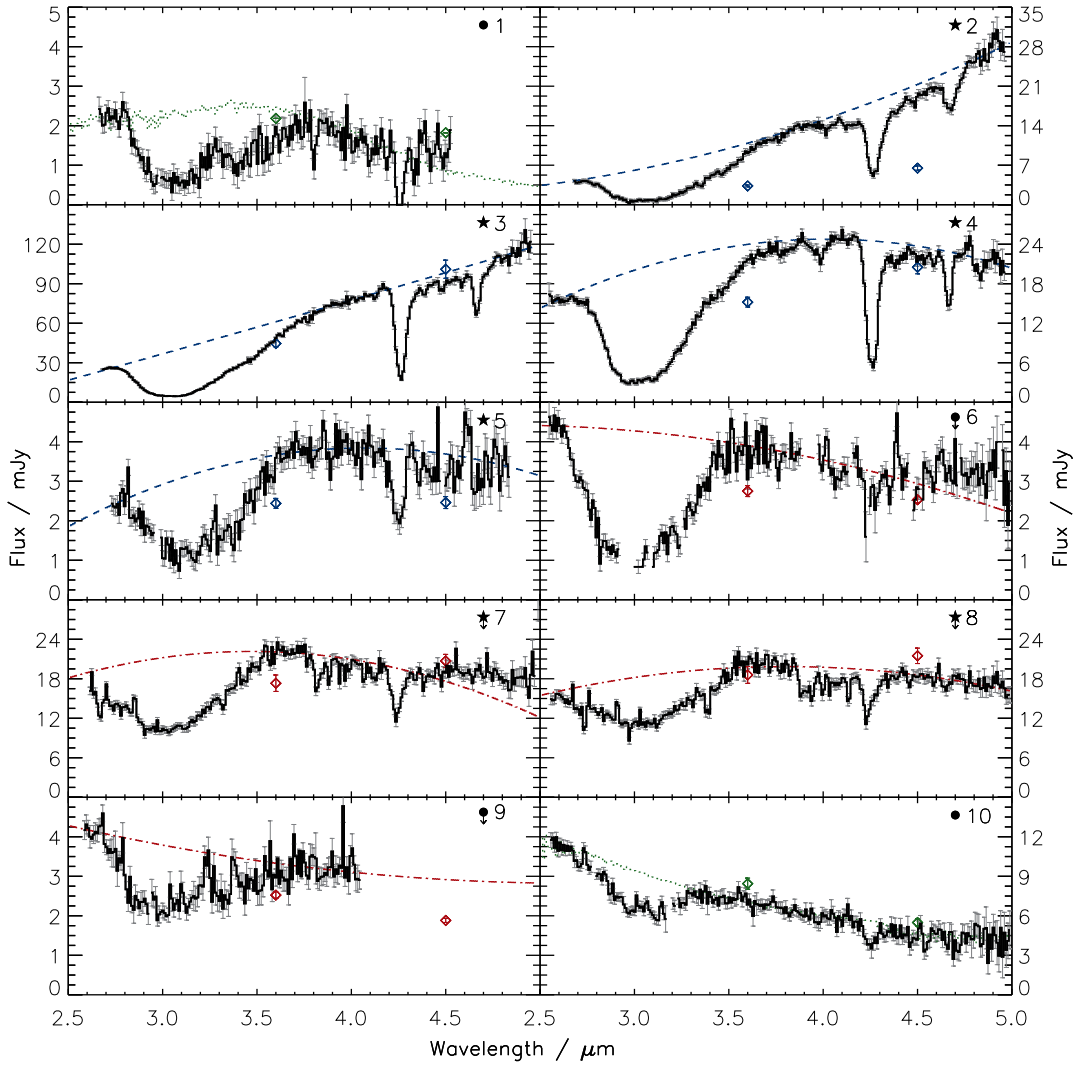

Figure 3.3a. Spectra of all extracted objects on a flux scale, numbered as in Table 3.2. YSOs are denoted by ⋆, while background stars are labelled •. Where spectra provide only upper limits on molecular abundances, they are labelled with an arrow. IRAC photometric data is overplotted as diamonds. In most cases, the photometry matches well with the extracted spectra. Baselines were fitted to all of the spectra (see § 3.6.2 for full details) and these are overplotted with the following styles: (blue) dashed for YSOs, (green) dotted for background stars, and (red) dot-dashed for upper limits.

All the spectra of the 30 remaining objects, extracted using ARF, are presented in Figures 3.3a – 3.3c, plotted as flux (in mJy) as a function of wavelength (in μm). Objects are numbered in order of ascending right ascension (as per Table 3.2). The final spectra are shown in black, with the error on each point overplotted in grey.

Spectra were extracted across the full 2.5 – 5 μm region, except in cases where the dispersion reached the edge of the CCD detector or overlap led to confusion in ARF, i.e. where the flux from two neighbouring objects could not be resolved in each row of the extractor. For example, due to detector limitations, in Object 9, the region of the spectrum beyond 4 μm was not extracted, while for a further four objects (Objects 1, 21, 24 & 27), the higher wavelength region of the spectrum, beyond 4.5 μm, was not extracted. Where unresolved overlap occurred between objects, it was possible to extract a partial spectrum, or a spectrum with some extra flux contribution, from which upper limits could be obtained on the molecular species present in the line of sight (Objects 6, 7, 8, 9, 11, 15, 16, 17, 18, 19 & 20). These upper limit objects are further addressed in Chapter 4.

The H_2O band (3.0 μm) was fully extracted for all objects, including the blue wing, which is not observed from the ground. In many spectra, such as Objects 2 & 4, it is clear that the H_2O band is saturated. In at least 12 objects the water band is still clearly visible even though the flux is < 5 mJy (see Figures 3.3a – 3.3c, Objects 1, 5, 6, 9, 21, 22, 24, 25, 26, 27, 28, 30). The absorption bands of CO_2 (4.25 μm) and CO (4.67 μm) are also clearly visible for the majority of objects.

On each spectrum in Figures 3.3a – 3.3c, the IRAC photometric data points are plotted as $\diamond$ at 3.6 and 4.5 μm. For most objects the photometric data matches the extracted flux very well. For some of the upper limits mentioned above, notably Objects 9, 11 & 16, the IRAC photometry does not exactly match the flux of the object, suggesting that there was excess light on the detector in the vicinity of the spectrum, vindicating the decision to only quote upper limits to the molecular abundances in these objects. In all cases where there is a slight photometry mismatch, the flux of the object has been over-, rather than underestimated, supporting the conjecture that there is excess light in these fields of view. The only two examples of completely isolated objects in the dataset are Objects 27 & 30. The photometric data points for these two objects match the extracted flux exactly, suggesting that the method of fitting the flux data with the PSF in ARF is a viable method for extracting accurate spectra.

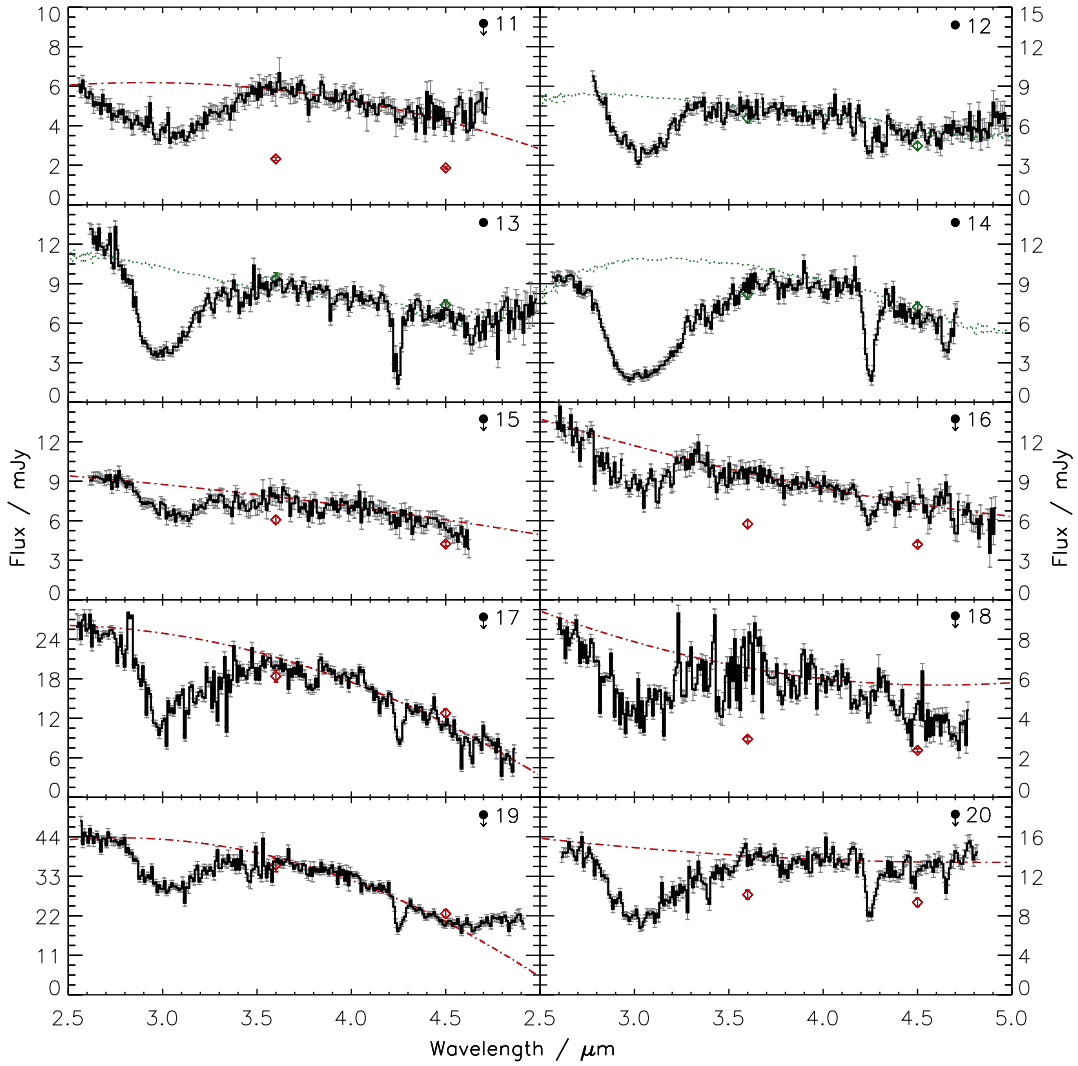

Figure 3.3b. Figure 3.3a continued.

3.6.1 Object classification

For further spectral analysis, it was necessary to classify each object according to whether it was a field star behind the molecular cloud ('star') or a YSO embedded in the cloud ('YSO'). All of objects in the IMAPE programme had a classification of this type preassigned by the c2d team, based on the full *Spitzer* photometric data as well as 2MASS photometry. The classification of objects in the ISICE programme, was performed during baseline fitting, based on 2MASS photometric data. If objects satisfied:

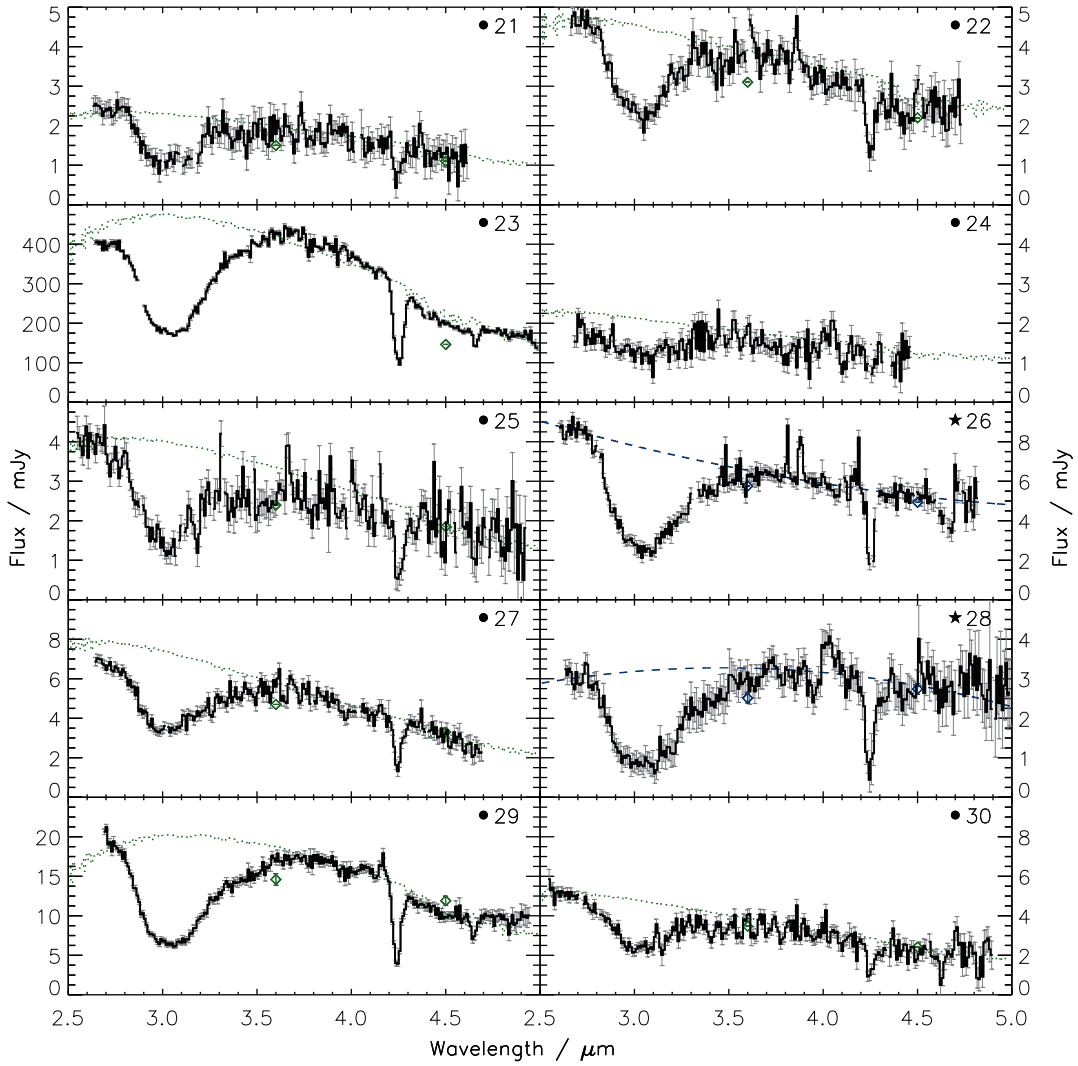

Figure 3.3c. Figure 3.3a continued.

$$1.75(H - K_S) - 0.04 \leq J - H, \tag{3.11}$$

they were classed as background stars; if not, they were classed as YSOs [Itoh et al., 1996; Shenoy et al., 2008]. This is illustrated by Figure 3.4, which shows a colour-colour plot of all the objects studied in this thesis, based upon their JHK photometry. Those objects in the ISICE programme are represented by solid black symbols; those in the IMAPE programme (preassigned by c2d) by open symbols. All but one of the ISICE objects fall within the region of reddened

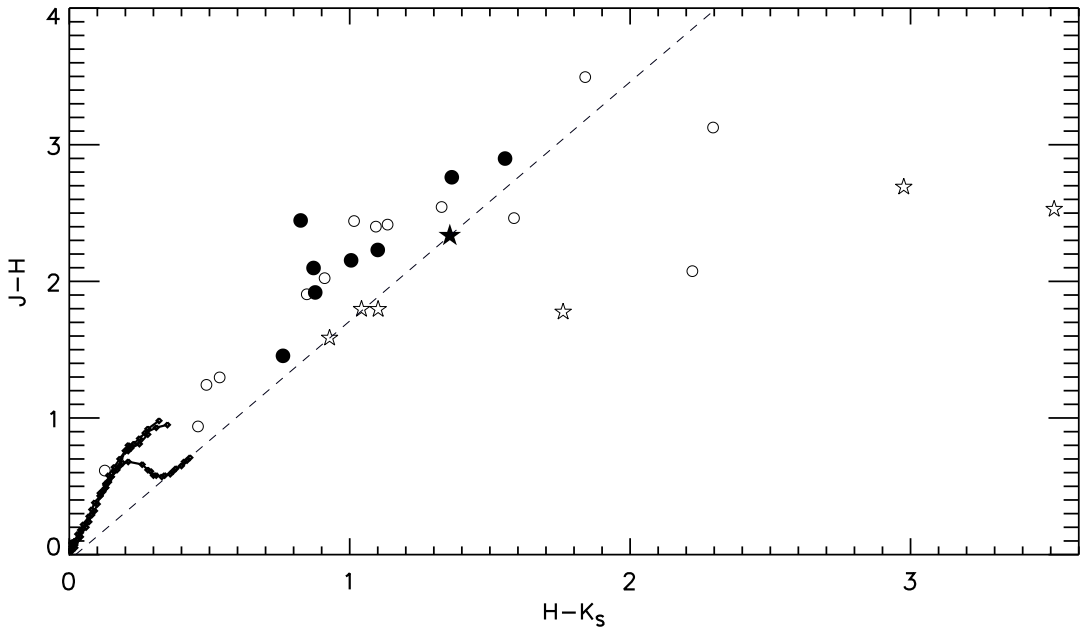

Figure 3.4. A colour-colour plot illustrating the classification of objects from the ISICE programme into YSOs and background stars based upon their JHK photometry. ISICE data is plotted as filled symbols and the preassigned IMAPE data as open symbols. The dashed line is the reddening law of Shenoy et al. [2008]. To the left of this line is the region of reddened main sequence stars, while to its right is the YSO region. The solid lines near the origin represent the intrinsic colours of normal stars in the main sequence, giant and supergiant branches. All but one of the ISICE objects fall within the region of reddened main sequence stars and were consequently labelled as background stars (•). One object was classified as a YSO (⋆), although its JHK photometry is borderline.

main sequence stars and were consequently labelled as background stars (•). One object was classified as a YSO (⋆), although its JHK photometry is borderline. The c2d object classifications also fit well with this picture, with the exception of Objects 6, 14 & 20 which were previously assigned as background stars but appear by this method to be YSOs. Objects 6 & 20 are upper limits, and so their classification is less important. Object 14 is a full spectrum, and is well fitted by a Nextgen model (see § 3.6.2). The shape of the baseline in Figure 3.3b indicates that it is in fact a background star. The c2d assignment for Object 14 has been retained, as the method employed by that team is more rigorous than the process used here.

Henceforth, in Chapters 3 & 4, irrespective of the observational programme from which they are derived, the objects are designated by a star symbol (⋆)

for YSOs, or a circle (•) for background stars; in the text they are referred to as 'YSO' and 'star' respectively.

3.6.2 Baseline fitting

To convert the observational data to spectra on an optical depth scale (most relevant for molecular abundance analysis), two different methods of baseline fitting were employed. This was either a second order polynomial (in the case of YSO objects) or a NextGen model [Hauschildt et al., 1999] (in the case of background stars), with the proviso that second order polynomial baselines were also fitted to 'upper limit' spectra, i.e. where the data were not fully extractable. These baselines are shown overplotted on each individual spectrum in Figures 3.3a – 3.3c, as either a green dotted line (NextGen models, background stars), a blue dashed line (second order polynomials, YSOs) or a red dash-dotted line (second order polynomials, 'upper limit' spectra).

The NextGen models were fitted to the background stars based on photometric data from 2MASS, IRAC and MIPS observations. Using the extinction law of Weingartner & Draine [2001], objects were dereddened along a reddening vector of 2.078 on a (J-H) vs (H-K_S) colour-colour diagram to determine their spectral type and A_V (see Figure 3.4). Potential spectral types were defined based on where the dereddened object crossed the main sequence, giant or dwarf branches. The object extinction was accounted for by convolving the NextGen model with a polynomial to reproduce the slope of the AKARI spectrum. The corrected NextGen model was then convolved to AKARI resolution before converting the spectrum to an optical depth scale. As is evident from Figures 3.3a – 3.3c, it appears that the modelled baseline spectra well match the extracted spectra, suggesting that this method of extinction correction is valid for these pointings.

The advantage of fitting baselines with NextGen models is that the models account for the star's photosphere. However, these models can not be used to fit YSOs, as such objects have a rising SED in the NIR region, and NextGen models only include evolved stars. The continuua of 'YSO's, and the upper limits of stars and YSOs, labelled 'star*' and 'YSO*', respectively, were therefore fitted by second order polynomials, as commonly done in the literature

[e.g. Gibb et al., 2004; Shimonishi et al., 2010]. Fitting regions varied slightly between the spectra, based on the position of bad pixels, but were generally < 2.65 μm, 3.85 – 4.18 μm and > 4.75 μm. The fits were weighted in favour of the blue end of the spectrum, as this had a higher signal-to-noise ratio than the red. Fitting the continuua with a polynomial baseline does not correct for stellar emission and absorption features in the AKARI spectrum, unlike the NextGen models.

3.7 Data reduction limitations

The data reduction pipeline has several limitations which are discussed below. In each case, the limitation was fully considered before a decision was made about whether and how to minimise its effect on the data produced by the pipeline.

3.7.1 Correction

Backgrounding was performed by subtracting the median of a region of dark sky from each frame. This approach did not fully account for the presence of excess emission in the region which was dispersed in the same manner as the light from point sources. The zodiacal light contribution in the NIR is generally minimal compared with the MIR and should be corrected for using the dark sky subtraction method. All of the pointings were at least nine degrees from the galactic equator, therefore zodiacal light contributions are expected to be small. Excess emission from gas and dust is seen in some of the pointings, particularly towards B 35A (see Figure 3.1). This emission is seen in the imaging frame and is dispersed in the spectral frames, as is evident in Figure 3.2a. To completely remove the contribution of this excess emission would require modelling of the emission pixel by pixel from the imaging frame, utilising the optical properties of the spectrometer and dispersion element to calculate the extent of the dispersed emission. This approach has not been attempted here due to its complexity and the likelihood of introducing errors in regions of the spectrum containing absorption features outweighs the potential benefits.

In the 1′ × 1′ aperture, flat fields are not available and thus flat-fielding was not performed. It is possible for detectors to have a pixel to pixel flatfield variation of up to 10 %. Thus, not flat-fielding both limits the signal-to-noise of the spectra and could potentially introduce spurious features. However, this is not an issue that could be addressed in ARF, as flat fields were not provided by the AKARI team. It is also important to note that there is no obvious evidence of spurious features, such as unexpected absorption or emission features, in the spectra presented in Figures 3.3a – 3.3c.

3.7.2 Stacking

Shifting in the non dispersion direction is carried out using real numbers of pixels, with the interpolation of flux to a new grid. This introduces error in the flux per pixel, due to interpolation. However, the total flux is maintained in each row as shifting is only performed in the non dispersion direction. Thus, this error can be minimised during PSF fitting as the total flux is fitted with a PSF, so the best fit function accounts for slight deviations from the standard PSF and these errors are included in the error per pixel. Shifting by an integer number of pixels would likely cause larger errors due to the low resolution (and thus the small number of pixels in the PSF) of AKARI. The difference between a shift of one pixel or two pixels in a PSF of length 11 pixels is significant.

Shifting of frames is performed in the non dispersion direction only, thus there is no correction for satellite jitter in the dispersion direction. In the non dispersion direction the change in flux per pixel is high and thus cross-correlation between frames is possible, with shifts of up to two pixels. In the dispersion direction, the change in flux per pixel is low and cross-correlation would produce higher shifts due to the shallower flux profile in this direction. The CO absorption feature at 4.67 μm has a width of approximately 10 pixels and thus shifting frames in the dispersion direction by 1 – 2 pixels could significantly affect the line profile of this absorption feature. The line profiles achieved using the pipeline without cross-correlation in the dispersion direction are also susceptible to this effect due to satellite jitter. Whether or not shifting in the dispersion direction is carried out, there is likely to be some smearing of the line profiles of absorption features, which can introduce uncertainty when fitting

the absorption bands and determining molecular abundances. It was judged that the potential errors outweighed the benefits of shifting in the dispersion direction. As will be shown in Chapter 4, the line profiles of CO, CO_2 and H_2O absorption features can be well fitted with a simple fitting strategy, therefore the question of shifting in the dispersion direction appears to have little effect.

3.7.3 Extraction

During extraction, the presence of isolated hot pixels caused misfitting of the model PSF for some rows. The hot pixel masks were designed to remove the contribution of cosmic ray hits and individual hot pixels that developed over the time of the pointing (around 70 seconds, see § 2.4.2 for details). The hot pixels caused by cosmic rays had a flux of several thousand ADU, so were distinguished easily as erroneous data. Some other hot pixels seem to have been the result of fluctuations in the detector response and typically fell in the region of several hundreds of ADU. The pipeline does not correct for these, as such small fluctuations could be found naturally in the data.

A single PSF function was fitted to data at all points along the dispersion from the NG dispersion element. It is potentially possible that the PSF is wavelength dependent and changes between 2.5 and 5.0 μm. It was assumed that a single PSF was sufficient to extract the spectra since the resolution of AKARI limits the number of pixels in the PSF to 11. Within such a small range, a variation in the PSF can not be easily calculated. Importantly, the chosen PSF gave the best fit at several points along the dispersion of the standard star used for its calculation (see § 3.5.4.3). Any variation from this standard PSF is reflected in the error bar on the data point. No significant wavelength dependent increase in error is seen, and thus it is assumed that the single PSF method is appropriate. In the NP dispersion, however, the PSF was found to be wavelength dependent, and this will be addressed in Chapter 8.

The pipeline was designed to resolve the flux from two objects whose flux overlaps during dispersion. The threshold distance between objects for such a resolution of flux was estimated, based on this work, to be approximately 3 pixels, which corresponds to ~ 0.07 arcminutes (or ~ 1800 AU for a cloud at 400 parsecs e.g. B 35A [Lee & Myers, 1999]). The closest objects which were

resolved were 2.5 pixels apart (Objects 17 & 18). The molecular cloud DC 300.7-01.0 is at a distance of 175 parsecs [Lee & Myers, 1999], thus the resolution achieved between Objects 17 & 18 is on the order of 650 AU. This threshold is subject to various caveats, such as the presence of other objects of low flux in the vicinity of the overlapping spectra, the presence of excess emission in the aperture and the position of the objects within the aperture, but allows the extraction of objects very close together in the FoV.

Even objects which satisfy the confusion threshold discussed above can be confused at higher wavelength due to the lower fluxes and higher signal-to-noise towards the high wavelength region of the detector, and the lack of flat fielding correction. As seen in Figures 3.3a – 3.3c, the higher wavelength regions of some spectra have been omitted due to confusion in the extractor in this region.

The flux extraction threshold on a single object is approximately < 50 ADU. Below this level, the extractor does not distinguish between the flux of an object and the noise in the observation. This threshold is based on the observation of an isolated object in DC 269.4+03.0 with a K_S band magnitude of 1.19 mJy. Thus the pipeline can not resolve spectra for objects with a flux of approximately 1 – 2 mJy, and objects with a K_S band magnitude of 1.19 mJy or below are excluded from the analysis. This threshold could vary from pointing to pointing depending on properties such as the background subtraction or the number of low flux objects in the aperture, but is assumed to be constant across all pointings.

3.7.4 Flux and wavelength calibration

The calculated SRF has an intrinsic error of ± 1 pixel, or ± 0.0097 μm in wavelength. This introduces an error in the peak position of the H_2O, CO_2 and CO bands. This is corrected for by allowing the position of the peak of these features to vary by a few wavenumbers during the fitting of laboratory spectra (see Chapter 4).

3.8 Concluding remarks

The data reduction pipeline, ARF, successfully extracts multiple spectra from AKARI fields of view, despite the complications arising from the slitless nature of the spectroscopy. It can also be applied across multiple fields of view and, despite some of the technical considerations discussed in this chapter (which can often be attributed to the limitations of AKARI), it is clear from a visual inspection of Figures 3.3a – 3.3c that in all cases ARF produces spectra with accurate fluxes and wavelengths, which match their J, H, K photometry to within observational uncertainties. Ultimately, the spectra of 30 objects – 22 field stars behind quiescent molecular clouds and eight low mass YSOs in cores – were extracted from lines of sight towards 16 molecular clouds, and baselines successfully fitted to all 30. The chemical analysis of these spectra is detailed in Chapter 4.

References

Aikawa, Y., et al. 2009, AKARI, a Light to Illuminate the Misty Universe, 418, 47

ASTRO-F User Support Team 2005, ASTRO-F Observer's Manual. Version 3.0, Sagamihara, Japan, http://www.ir.isas.jaxa.jp/ASTRO-F/Observation/ObsMan/afobsman30.pdf

Boogert, A. C. A., et al. 2011, ApJ, 729, 92

Bracewell, R. N. 2000, "The Fourier Transform and its Applications. Third Ed.", McGraw-Hill Higher Education

Burgdorf, M., Cruikshank, D. P., Dalle Ore, C. M., Sekiguchi, T., Nakamura, R., Orton, G., Quirico, E., & Schmitt, B. 2010, ApJL, 718, L53

Cohen, M., Walker, R. G., Carter, B., Hammersley, P., Kidger, M., & Noguchi, K. 1999, AJ, 117, 1864

Evans, N. J., II, et al. 2003, PASP, 115, 965

Fletcher, L. N., Drossart, P., Burgdorf, M., Orton, G. S., & Encrenaz, T. 2010, A&A, 514, A17

Gibb, E. L., et al. 2004, ApJS, 151, 35

Hauschildt, P. H., Allard, F., & Baron, E. 1999, ApJ, 512, 377

Ishihara, D., et al. 2010, A&A, 514, A1

Itoh, Y., Tamura, M., & Gatley, I. 1996, ApJL, 465, L129

Landsman, W. B. 1993, Astronomical Data Analysis Software and Systems II, 52, 246

Lee, C. W., & Myers, P. C. 1999, ApJS, 123, 233

Markwardt, C. B. 2009, Astronomical Society of the Pacific Conference Series, 411, 251

Noble, J. A., Aikawa, Y., Fraser, H. J., Pontoppidan, K. M., & Sakon, I. 2009, AKARI, a Light to Illuminate the Misty Universe, 418, 411

Noble, J. A., Fraser, H. J., Pontoppidan, K. M., Aikawa, Y., & Sakon, I. 2010, Highlights of Astronomy, 15, 730

Nutter, D., Stamatellos, D., & Ward-Thompson, D. 2009, MNRAS, 396, 1851

Ohyama, Y., et al. 2007, PASJ, 59, 411

Onaka, T., et al. 2007, PASJ, 59, 401

Press, W. H., Teukolsky, S. A., Vetterling, W. T., & Flannery, B. P. 1994, "Numerical Recipes in C. The Art of Scientific Computing. Second Ed.", Cambridge University Press

Shenoy, S. S., Whittet, D. C. B., Ives, J. A., & Watson, D. M. 2008, ApJS, 176, 457

Shimonishi, T., Onaka, T., Kato, D., Sakon, I., Ita, Y., Kawamura, A., & Kaneda, H. 2008, ApJL, 686, L99

Shimonishi, T., Onaka, T., Kato, D., Sakon, I., Ita, Y., Kawamura, A., & Kaneda, H. 2010, A&A, 514, A12

Weingartner, J. C., & Draine, B. T. 2001, ApJ, 548, 296

CHAPTER 4

ICE MAPPING IN MOLECULAR CLOUDS[†]

4.1 Synopsis

In Chapter 3, the spectra of 30 objects were reduced from AKARI observations. In this chapter, those spectra are analysed to calculate the abundances of key solid phase molecular species, including H_2O, CO_2, CO, CH_3OH, OCN^-, and $^{13}CO_2$. The methods of analysis are fully explained and justified. The correlations between the column densities of these species are discussed with respect to literature values and, for four of the molecular clouds observed, 2D maps are produced of A_V, and the abundances of H_2O, CO_2 and CO in the clouds. The length of this chapter reflects the complexities of analysing solid state observational spectra, with ice mapping the final stage of the process.

Currently, the key question relating to ice mapping is: can solid phase molecules be used as tracers and probes of chemistry and physics in interstellar environments? Observations towards large numbers of background stars provide a benchmark of the physical and chemical conditions in molecular clouds at the start of the star formation cycle, but can these observations be used to trace the abundance of other molecules in the solid or gas phase? In order to truly

[†]Chapters 3 & 4 are based upon results presented in a paper that will shortly be submitted to the Astrophysical Journal. Early results were published in Noble et al. [2009]; Aikawa et al. [2009]; Noble et al. [2010].

benchmark molecular abundances in these regions, it is necessary to develop a standard spectral analysis method, avoiding the mix and match approach to fitting spectral absorption features that largely prevailed in the past. Thus, the combination of laboratory studies with observations is fundamental to developing standard methodologies. Observers are reliant upon accurate, astrophysically relevant laboratory data to fit observational spectra, but they must themselves have good chemical knowledge in order to choose realistic laboratory spectra for fitting their data.

4.2 Introduction

The three most abundant solid phase molecular species in the InterStellar Medium (ISM) are H_2O, CO_2 and CO. Absorption bands of all three species are seen in the 2.5 – 5 μm region of the spectrum, and these features are analysed in this chapter. The correlations between abundances of these key molecular species reveal much evidence of the formation mechanisms of their components, and potentially those of other species. The objects observed are a mixture of background stars and young stellar objects (YSOs). AKARI NIR spectra, such as the spectra extracted in Chapter 3, are the first since ISO to contain the stretching mode vibrations of all three molecules observed concurrently.

As has been discussed previously, H_2O is seemingly ubiquitous in the ISM, and in particular is present at high abundances in interstellar dark clouds [Leger et al., 1979; Whittet et al., 1983; Boogert et al., 2011]. In these clouds, H_2O forms on the surface of silicate dust grains [Tielens & Hagen, 1982; Boogert & Ehrenfreund, 2004; Miyauchi et al., 2008; Ioppolo et al., 2008; Dulieu et al., 2010]. CO_2 has been observed towards numerous environments, including low mass YSOs [Nummelin et al., 2001; Pontoppidan et al., 2008] and background stars [Knez et al., 2005], as well as massive protostars [Gerakines et al. , 1999; Gibb et al. , 2004], galactic centre sources [de Graauw et al. , 1996], and in other galaxies [Shimonishi et al., 2010; Oliveira et al. , 2011]. CO is also present at high abundances throughout the ISM [Whittet & Duley, 1991; Chiar et al., 1995]. It is highly abundant in molecular clouds in the gas phase, with accretion of CO onto icy grain surfaces occurring above a critical freeze-out density [e.g.

Aikawa et al., 2001], resulting in a CO-rich layer in the ice. CO is commonly used as a gas phase tracer due to its high abundance, and can be used as a basis for radiative transfer modelling of clouds due to its numerous isotopologues [Craigon et al., *in preparation*, van Kempen et al. [2009]].

CO_2 is believed to form in the solid phase, due to low gas phase abundances [van Dishoeck et al. , 1996]. It can be produced from CO via several mechanisms, for example irradiation of mixed CO:H_2O ices with photons [Gerakines et al. , 1996], charged particles [Palumbo et al. , 1998] and electrons [Jamieson et al. , 2006]. The irradiation of hydrogenated carbon grains has also produced small quantities of CO and CO_2 [Mennella et al., 2004, 2006]. Solid phase CO_2 is abundant in quiescent, as well as star-forming regions [Pontoppidan, 2006; Nummelin et al., 2001]. While the role of energetic pathways can not be discounted entirely in these regions [Whittet et al., 1998], the study of non-energetic formation routes is fundamental to fully understanding the observed abundances of CO_2. Recent studies have shown that while CO + O does not proceed under typical interstellar conditions [Roser et al. , 2001], CO + OH is a possible source of CO_2 [Goumans et al. , 2008; Oba et al. , 2010; Ioppolo et al., 2011; Noble et al., 2011]. This reaction, fully addressed in Chapter 7, occurs in competition to H_2O formation via H + OH, and thus the chemistry of CO, CO_2 and H_2O in molecular clouds is intrinsically linked.

To date, background stars have not been widely studied spectroscopically. Due to telluric observations, much of the NIR is not visible from the ground. Successful ground-based studies have been carried out to observe the 4.67 μm CO stretch towards 12 background stars [Whittet et al., 1985, 1989; Eiroa & Hodapp, 1989] and the observable part of the 3 μm water band towards 73 background stars [Whittet et al., 1988; Eiroa & Hodapp, 1989; Murakawa et al., 2000]. Prior to AKARI, two space telescopes operated spectroscopically in the near to mid infrared region: ISO and *Spitzer*. Two background stars were observed by ISO: Elias 13 and Elias 16. Elias 13 was observed in the range 4.20 - 4.34 μm to investigate its CO_2 stretching mode at 4.25 μm [Nummelin et al., 2001], whilst Elias 16 was observed in the range 2.4 – 5 μm [Whittet et al., 1998; Gibb et al. , 2004], with detailed studies of the CO_2 stretching mode [Whittet et al., 1998; Gerakines et al. , 1999; Nummelin et al., 2001], and potentially the N_2 stretching mode [Sandford et al., 2001]. ISO was capable of observing in the

range 2.38 – 45.2 μm, but due to its low flux of $\sim$ 5 Jy in the K band, Elias 16 was not observed above 5 μm. A combination of ground based and ISO data provide a full 2.5 – 5 μm spectrum for this object, offering a direct comparison to AKARI spectral observations of background stars. With *Spitzer*, the spectra of two background stars were observed in the 5 – 20 μm range (Elias 13 and CK2), with the spectrum of Elias 16 observed from 5 – 14 μm [Knez et al., 2005]. A further 12 objects were investigated in the CO_2 bending mode region around 15.2 μm [Bergin et al., 2005; Whittet et al., 2007, 2009]. CO_2 was found to exist in a H_2O-poor environment in quiescent regions for the first time, with 15 % of the CO_2 towards Elias 16 found in an H_2O-poor ice [Bergin et al., 2005].

Most previous background star observations have been performed towards Taurus and Serpens molecular clouds, with the exception of two studies of the Cocoon Nebula (IC 5146) [Whittet et al., 2009; Chiar et al., 2011], one of ρ Ophiuchi [Tanaka et al., 1990], and a recent combined ground and *Spitzer* survey, which observed 31 background stars towards 18 molecular clouds [Boogert et al., 2011]. The survey quantified H_2O and CH_3OH towards these 31 lines of sight and confirmed that the threshold extinction for H_2O is in line with that of Taurus, and that CH_3OH has abundances in the range of 5 – 12 % H_2O. A recent study of ten stars behind the IC 5146 cloud provided H_2O abundance data for this cloud, as well as determining CH_3OH and NH_3 abundances of $\sim$ 2 % and $\sim$ 5 %, respectively, towards three of the lines of sight [Chiar et al., 2011]. All of these observations were made along single lines of sight. In order to determine a reliable model of conditions in molecular clouds, and to study ice evolution in star forming regions, it is necessary to observe a large number of background stars towards a large number of quiescent clouds, to determine both accurate initial conditions and the variation of these values across observed clouds on a spatial scale.

Thus, the only previously published spectrum towards a background star directly comparable to the AKARI spectra in this thesis is that towards Elias 16 [Whittet et al., 1998; Gibb et al. , 2004].

Low mass YSOs have been rather more extensively studied than background stars, with limited ISO observations, and large surveys performed using the *Spitzer* satellite [e.g. Gibb et al. , 2004; Boogert et al., 2008; Pontoppidan et al., 2008; Zasowski et al., 2009]. ISO revealed, amongst other things, the ubiquity

of CO_2 in the ISM [Guertler et al., 1996; de Graauw et al. , 1996; Gerakines et al. , 1999; Alexander et al., 2003] and the presence of $^{13}CO_2$ towards massive and low mass protostars, and the background star Elias 16 [Boogert et al., 2000]. *Spitzer*, more sensitive than ISO, observed many more low mass YSOs. The c2d spectroscopic study analysed the abundances of CO_2 [Pontoppidan et al., 2008], H_2O [Boogert et al., 2008], CH_4 [Öberg et al., 2008], and NH_3 [Bottinelli et al., 2010] ices towards a sample of 41 sources from low mass star forming regions, providing a large dataset of abundance values for these key interstellar molecules. A survey of the ice species present in circumstellar disks around YSOs has recently been completed [Aikawa et al., *submitted*].

The concept of ice mapping, introduced in Chapter 1, has yet to be widely applied in observational astrochemistry. The time consuming nature of observing multiple sources behind a single cloud using slit spectroscopy makes this technique very expensive in terms of telescope time. However, in the cases where it has been attempted, ice mapping has yielded important results.

A water ice map of the Taurus molecular cloud showed that H_2O correlates closely with $C^{18}O$ emission in the gas phase [Murakawa et al., 2000]; this gas phase molecule traces the most dense regions of CO gas. H_2O was also found to correlate well with A_V. This map had a spatial resolution of ~ 1 line of sight per 100 arcmin^2. Higher resolution mapping (1 line of sight per 0.02 arcmin^2) was introduced for H_2O ices in the Serpens cloud [Pontoppidan et al., 2004], providing a resolution comparable to that of gas phase mapping. Most relevant to the molecules studied in this thesis, the mapping of CO, CO_2 and H_2O abundance as a function of distance to the centre of the Ophiuchus-F core illuminated the inherently different abundances of CO_2 in H_2O-rich and CO-rich environments [Pontoppidan, 2006].

In this Chapter, the analysis of 2.5 – 5 μm AKARI spectra are presented. The abundances of H_2O, CO_2, CO and some other low abundance species are calculated for 22 background stars and eight YSOs. As the only prior spectrum of a background star in this region is that of Elias 16 taken by ISO, this represents the largest increase in data on background stars in the NIR region. In particular, many of the objects are at a low flux level, previously unobtainable using space based telescopes. For the first time since ISO, the CO_2 stretching mode at 4.25 μm is available for analysis (only three background stars have previously

been studied in this region), as is the blue wing of the H_2O band, allowing for much more accurate fitting of this band. In addition to H_2O, CO_2 and CO, it was possible in certain cases to calculate the abundances of CH_3OH, OCN^-, and CO gas-grain [Fraser et al., 2005]. This large increase in data offers much evidence about the initial conditions in quiescent molecular clouds before star formation begins. In particular, it offers clues to where ices form, and how the chemistry of different molecular species is linked in prestellar regions.

4.3 Spectral analysis

Spectra (extracted in Chapter 3) were converted to an optical depth scale by:

$$\tau = -ln(F/F_{con}), \tag{4.1}$$

where τ is optical depth, F is the spectral flux in mJy, and F_{con} the flux of the continuum in mJy (fitted in § 3.6.2). The optical depth scale spectral features are shown in Figures 4.1a – 4.1b for the 3 μm H_2O band, Figures 4.6a – 4.6b for the 4.25 μm CO_2 band, and Figures 4.4a – 4.4b for the 4.67 μm CO band.

The column densities of molecular species can be determined by integrating the area under their absorption bands on an optical depth scale and correcting by the optical constant for each species, using:

$$N = \int \frac{\tau d\nu}{A}, \tag{4.2}$$

where N is column density in molecules cm^{-2}, ν is wavenumber in cm^{-1}, and A is the band strength in cm $molecule^{-1}$ [Gerakines et al., 1995]. The specific analysis methods for H_2O, CO_2 and CO are described in detail below; in each case, small changes were made to the local baseline before fitting. All calculated column density values are presented in Table 4.1. Spectra which were considered to be upper limits (see Chapter 3 for details of the designation) are indicated by the symbol $*$ in Table 4.1. In all figures, they are denoted as upper limits by the use of $\downarrow$.

Table 4.1. Calculated ice column densities of the H_2O, CO_2, and CO bands.

Object	Type[a]	N(H_2O)[b,c] x10^{18} cm^{-2}	N(CO_2) x10^{17} cm^{-2} in CO	N(CO_2) x10^{17} cm^{-2} in H_2O	N(CO) x10^{17} cm^{-2} CO_{rc}	N(CO) x10^{17} cm^{-2} CO_{mc}	N(Minor component) x10^{17} cm^{-2} OCN^-	N(Minor component) x10^{17} cm^{-2} CO_{gg}
1	star (M5)	2.273 ± 0.284	0.111 ± 2.730	0.698 ± 1.454	...	...	...	...
2	YSO	3.897 ± 0.322	1.060 ± 0.665	0.738 ± 0.346	5.981 ± 2.668	0.684 ± 0.976	0.	2.355 ± 0.642
3	YSO	3.257 ± 0.080	0.	1.493 ± 0.019	3.329 ± 2.529	2.046 ± 2.896	0.	1.889 ± 0.437
4	YSO	3.094 ± 0.070	1.989 ± 0.417	0.599 ± 0.223	0.	3.126 ± 0.914	0.086 ± 0.477	1.134 ± 0.978
5	YSO	1.610 ± 0.293	0.661 ± 1.034	0.266 ± 0.544	0.	$1.494 \pm 4.250^*$	0.	0.
6	star*	4.460 ± 0.230	0.957 ± 0.287	0.	0.	0.649 ± 2.561	0.	0.710 ± 2.032
7	YSO*	1.424 ± 0.041	0.180 ± 0.393	0.341 ± 0.205	0.	0.	0.199 ± 0.290	0.
8	YSO*	0.789 ± 0.040	1.084 ± 0.073	0.	2.277 ± 2.563	0.	0.078 ± 0.380	0.
9	star*	1.690 ± 0.119	...	...	...	...	...	...
10	star (K0g)	0.673 ± 0.044	0.058 ± 0.751	0.391 ± 0.396	0.408 ± 6.910	1.206 ± 2.435	0.	0.
11	star*	1.061 ± 0.057	0.	0.176 ± 0.057	...	...	...	...
12	star (K0)	0.910 ± 0.034	0.	0.393 ± 0.386	0.	0.	$0.183 \pm 0.563^*$	0.
13	star (K0)	1.421 ± 0.047	0.546 ± 0.524	0.611 ± 0.281	2.937 ± 6.942	2.271 ± 7.130	0.	$1.034 \pm 0.925^*$
14	star (K0g)	2.636 ± 0.044	0.	1.494 ± 0.054	5.353 ± 10.500	1.770 ± 20.167	0.	0.
15	star*	0.571 ± 0.123	0.	0.126 ± 0.053	...	...	...	...
16	star*	0.537 ± 0.040	0.635 ± 0.083	0.	0.	1.855 ± 19.225	0.	0.
17	star*	1.005 ± 0.042	0.	0.495 ± 0.043	0.	2.607 ± 39.123	1.093 ± 0.793	0.
18	star*	1.092 ± 0.053	0.625 ± 0.119	0.	8.876 ± 9.146	0.	0.	0.791 ± 2.571
19	star*	0.570 ± 0.026	0.	0.339 ± 0.029	0.838 ± 3.845	0.826 ± 1.411	0.	3.488 ± 0.922
20	star*	0.994 ± 0.041	0.	0.537 ± 0.034	0.	1.772 ± 0.372	0.	1.817 ± 0.802
21	star (K0)	1.189 ± 0.127	0.	0.592 ± 0.138	...	...	...	...

Continued on Next Page...

Table 4.1. Continued

Object	Type[a]	N(H_2O)[b,c] x10^{18} cm^{-2}	N(CO_2) x10^{17} cm^{-2} in CO	N(CO_2) x10^{17} cm^{-2} in H_2O	N(CO) x10^{17} cm^{-2} CO_{rc}	N(CO) x10^{17} cm^{-2} CO_{mc}	N(Minor component) x10^{17} cm^{-2} OCN^-	N(Minor component) x10^{17} cm^{-2} CO_{gg}
22	star (K0g)	0.992 ± 0.065	0.	0.616 ± 0.080	0.	$1.915 \pm 10.075^*$	0.	0.
23	star (K0g)	1.454 ± 0.015	0.	1.032 ± 0.006	1.622 ± 2.414	1.731 ± 0.533	0.	$0.605 \pm 0.181^*$
24	star (K0)	0.825 ± 0.079	0.	0.580 ± 0.153	...	...	...	...
25	star (K0)	1.379 ± 0.152	0.	1.201 ± 0.154	3.853 ± 20.521	3.872 ± 9.174	0.	$0.054 \pm 1.014^*$
26	YSO	1.544 ± 0.057	0.	0.838 ± 0.107	0.	1.717 ± 2.016	$0.871 \pm 0.820^*$	0.
27	star (K0)	0.997 ± 0.047	0.	0.824 ± 0.055	...	...	...	...
28	YSO	2.079 ± 0.212	0.192 ± 1.724	1.307 ± 0.920	0.	0.	$0.087 \pm 0.087^*$	0.
29	star (K0g)	1.754 ± 0.040	0.	1.090 ± 0.027	2.708 ± 4.329	2.174 ± 0.559	0.	0.436 ± 0.737
30	star (G4g)	0.965 ± 0.065	0.655 ± 0.934	0.439 ± 0.496	0.	4.381 ± 46.429	0.	0.

[a]Objects from c2d target tables were categorised by the c2d team. For the objects taken from the 2MASS catalogue, the type was determined based on their J, H, K_S photometry as described in § 3.6.1. In addition, for 'stars', the spectral type, calculated during baseline fitting in § 3.6.2, is shown in parentheses. Despite being categorised as 'stars' or 'YSOs', all object marked with $*$ were considered to be upper limits only, due to confusion in the region of the object, and were thus fitted like YSOs, as detailed in § 3.6.2.

[b]Column densities marked ... indicate that no fit was performed on the spectrum in the wavelength range surrounding that spectral feature. In general, this is because the spectrum was not extracted for this region - either the flux was below the extraction threshold of the pipeline, or the region was too confused (due to overlapping spectra) for the pipeline to fit that object. A value of 0 indicates that a fit was performed, and a value of 0 was returned. Only in the second case can it be concluded that this spectral feature is not present towards this object.

[c]In addition to the objects to be considered in their entirety as upper limits, some individual peaks are also defined as upper limits, rather than fixed values. These are marked individually by *.

4.3.1 Correction of laboratory spectra used for fitting ice bands

The absorption bands of interstellar ice species are altered, with respect to those measured in the laboratory, by interaction with charged dust grains. Molecules in the ice experience electric fields due to the polarisation of the grain upon interaction with light from a background or embedded star. The resulting changes in absorption band peak position and shape can be modelled in reference laboratory spectra using a grain shape model. In this work, a continuous distribution of ellipsoids (CDE) model was applied to certain laboratory spectra in order to use them in the column density calculation.

In the 2.5 – 5 μm region of the NIR, the H_2O absorption band is particularly affected by grain interactions. In addition to a shift in the peak position, the red wing of the band includes contributions from scattered light and absorption due to O-H and C-H stretches, assigned to various molecules, including CH_3OH [Hagen et al., 1980; Dartois et al., 2003], polyaromatic hydrocarbons [Onaka et al., 2011], and larger organic molecules [Brooke et al., 1999]. This red wing is described in more detail in § 4.3.5 below.

In order to correct for the effect of interstellar grains on absorption features of laboratory spectra, accurate optical constants are required. Optical constants (the real and imaginary refractive indices n & k) are derived from a laboratory spectrum by application of a Kramers-Kronig analysis [Bohren & Huffman , 1983; Ehrenfreund et al., 1997], including the real part of the ice's refractive index at high frequency from literature [Hudgins et al., 1993].

The real part of the refractive index at all frequencies, $n(\nu)$, is derived from the Kramers-Kronig dispersion relation:

$$n(\nu) = 1 + \frac{1}{2\pi^2} \int_0^\infty \frac{\alpha(\nu')}{(\nu'^2 - \nu^2)} d\nu', \tag{4.3}$$

where $\alpha(\nu)$, the absorption coefficient, is given by:

$$\alpha(\nu) = \frac{4\pi k(\nu)}{\lambda} = \frac{1}{h} \left[\tau(\nu) + ln \left| \frac{\mathbf{t}_{01}\mathbf{t}_{01}/\mathbf{t}_{02}}{1 + \mathbf{r}_{01}\mathbf{r}_{12} exp(4i\pi h\mathbf{m}/\lambda)} \right|^2 \right], \tag{4.4}$$

and h is the ice thickness, $\tau(\nu)$ the measured optical depth of the ice, $\mathbf{m} = n + ik$ is the total refractive index, and $\mathbf{t}_{ij}$ & $\mathbf{r}_{ij}$ are the complex transmission and reflection coefficients at the boundaries of i & j between the substrate (0), the ice (1), and the vacuum (2).

The integration in Equation (4.3) must theoretically be done across all frequencies, but in reality is only carried out across the IR part of the spectrum. Other absorption bands in the ultraviolet and visible regions of the spectrum are well separated from those of interest in the infrared, and their contribution is approximated by a constant term, n_0, the ice's refractive index at high frequency [Hudgins et al., 1993]. Thus, Equation (4.3) becomes:

$$n(\nu) \approx n_0 + \frac{1}{2\pi^2} \int_{IR} \frac{\alpha(\nu')}{(\nu'^2 - \nu^2)} d\nu'. \tag{4.5}$$

The final values of $n(\nu)$ and $k(\nu)$ must be obtained by iteration, as they are not independent of one another. To obtain an absorption spectrum, a CDE grain shape correction is applied to the calculated optical constants [Klaus Pontoppidan, *private communication*].

A grain shape correction is applied to the laboratory spectrum to simulate the interaction of the stellar spectrum with dust grains in the line of sight. The interaction of this light with an interstellar grain polarises the grain, and thus molecules in the grain encounter electric field components, which alter the peak position and the profile of strong absorption features. In the NIR, the wavelength of the light is larger than the grain dimensions, and electrostatic theory applies. Scattering extinctions are neglected in this limit, and so a simple expression for the absorption cross section of ellipsoidal particles can be derived [Bohren & Huffman , 1983; Ehrenfreund et al., 1997]:

$$\frac{C_{abs}}{V} = \frac{2\pi}{3\lambda} \sum_{i=1}^{3} \frac{2nk/L_i^2}{(1/L_i - 1 + n^2 - k^2)^2 + (2nk)^2}, \tag{4.6}$$

where C_{abs} is the absorption cross section, V the ellipsoid volume, and L_i is the geometry of the ellipsoid along each of three axes, with $0 \leq L_i \leq 1$. In the CDE model, L_i is modelled as a distribution of ellipsoidal particles with all shapes equally probable, and the average absorption cross section becomes:

$$\frac{C_{abs}}{V} = \frac{4\pi}{\lambda} Im\left(\frac{\mathbf{m}^2}{\mathbf{m}^2 - 1} ln\mathbf{m}^2\right). \quad (4.7)$$

CDE is not a physically accurate model, as extreme grain shapes (such as very long and thin) are unlikely to be present in the ISM, but it has been successfully applied to many astronomical spectra [Tielens et al., 1991; Ehrenfreund et al., 1997; Pontoppidan et al., 2003a] and generally models the grain scattering in the NIR well.

Finally, before fitting the laboratory spectrum to the observed spectrum, it is converted to an optical depth scale, and corrections are applied for the instrumental line profile and the AKARI resolution. The instrumental line profile was determined by analysis of an observation of standard star KF09T1 (see § 3.5.4.3). The profile was obtained by summation of the imaging frame profile across four pixels in the X direction. The profile of the standard star observation was assumed to be a 'standard' profile, and was applied to all laboratory spectra.

4.3.2 H_2O

Spectral features on an optical depth scale are shown in Figures 4.1a – 4.1b. Column densities were calculated by fitting a lab spectrum of pure non-porous H_2O at 15 K to the absorption feature at 3 μm (3333 cm^{-1}) [Fraser & van Dishoeck, 2004], then using Equation (4.3) with A = 2 $\times$ 10^{-16} cm molecule^{-1} [Gerakines et al., 1995].

In order to fit the H_2O absorption feature, a CDE-corrected spectrum of H_2O was generated from a laboratory spectrum of pure H_2O at 15 K, as explained in § 4.3.1, then corrected for the instrumental line profile and resolution of AKARI. This spectrum was fitted to the observed H_2O peaks, considering uniquely the flux in the blue wing, from approximately 3600 – 3400 cm^{-1}, as this region of the peak is unaffected by scattered light. Also, in the AKARI spectra, the H_2O peak is almost always saturated due to loss of signal, so the blue wing is vital in making a good fit. As can be seen in Figures 4.1a & 4.1b, the converted pure H_2O spectrum fitted the H_2O bands well in all cases. Column densities of H_2O were calculated from the fitted laboratory spectrum us-

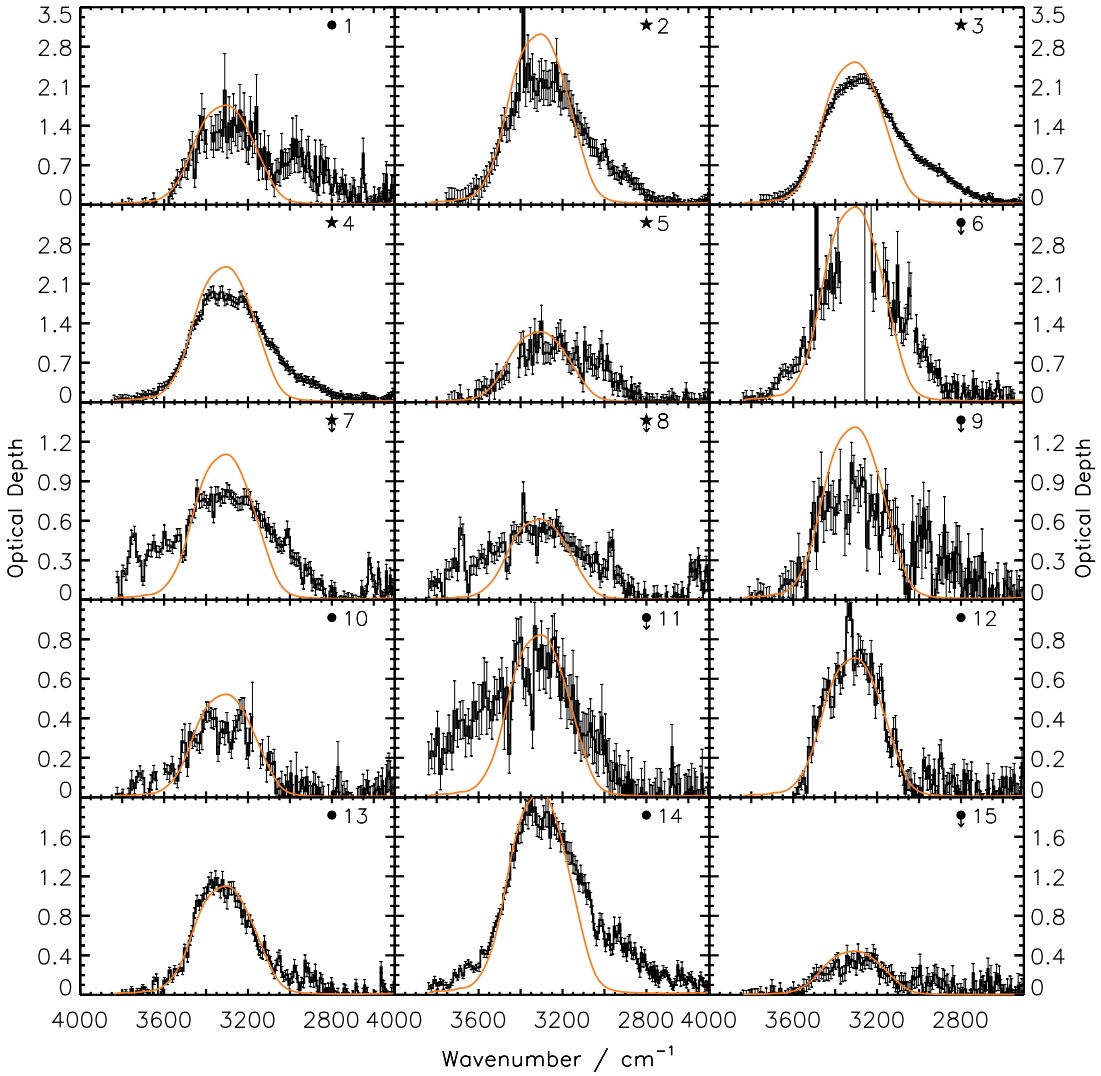

Figure 4.1a. The fits of a pure non-porous H_2O laboratory spectrum at 15 K, corrected with a CDE model and the instrumental line profile, to all H_2O absorption bands at 3 μm (3333 cm^{-1}). Observational data, on an optical depth scale, is plotted in black, with the fits overplotted in orange.

ing Equation 4.3, and are presented in Table 4.1. A single 15 K lab spectrum was used to fit every H_2O absorption feature in the 30 AKARI spectra, with no resort to a mix and match approach.

In these spectra, two distinct H_2O profiles were identified: one in which the red wing is weak compared to the absorption peak at 3 μm, and a second in which the long wavelength feature is relatively strong, and exhibits a separate shoulder profile. This is analogous to the results of Thi et al. [2006], who found

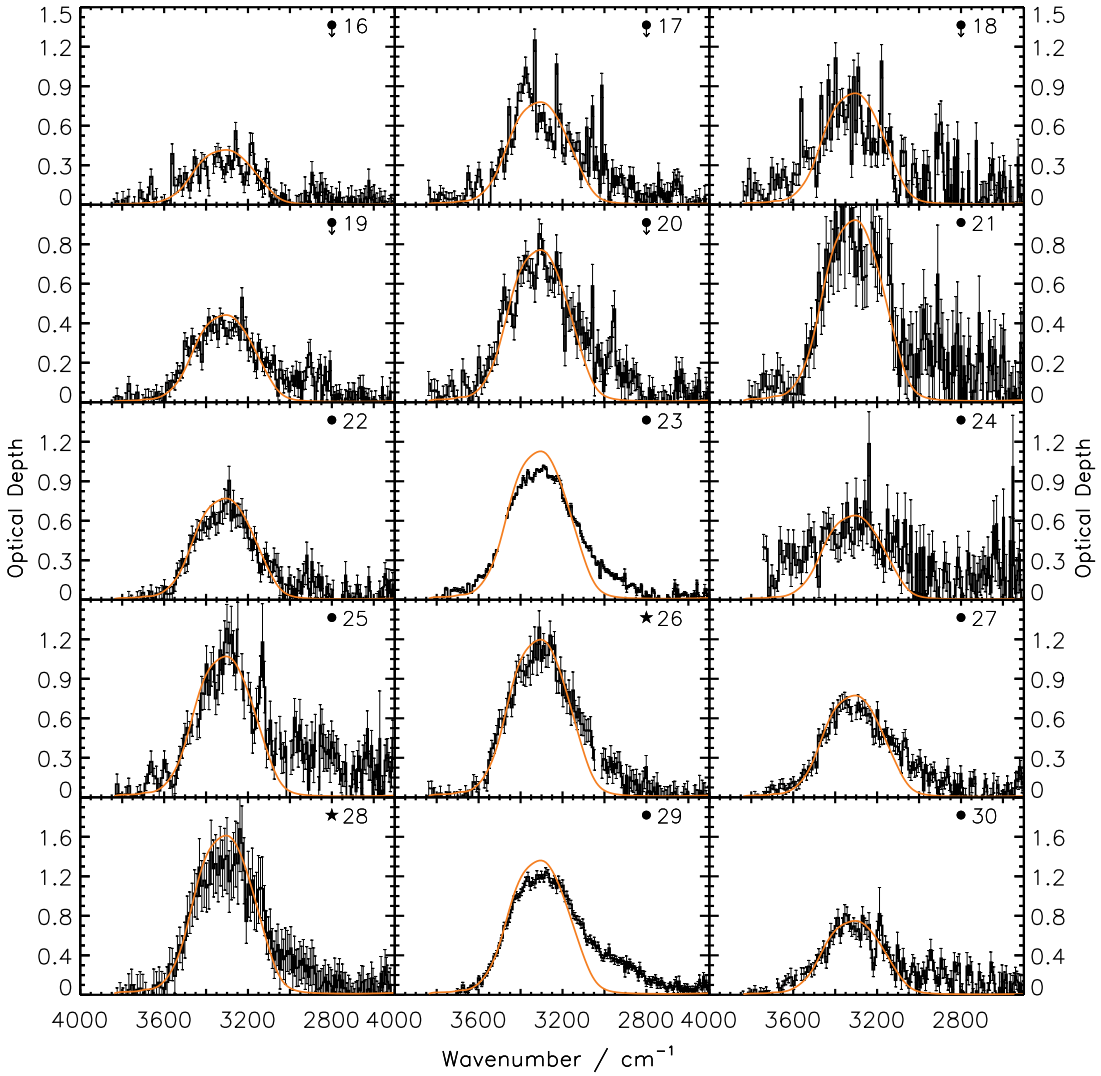

Figure 4.1b. Figure 4.1a continued.

two H_2O profiles in the spectra of intermediate mass YSOs in Vela. These two absorption band profiles are illustrated in Figure 4.2.

The first profile – present in the spectra of Objects 2, 3, 4, 5, 14, 23, 24, 26, 27, 28 & 29 – resembles the 'standard' water band observed towards many lines of sight. The long wavelength wing is generally attributed to the scattering of light from dust grains, as discussed above. The second profile – present in the spectra of Objects 1, 13, 21, 22, 25 & 30 – appears to contain a distinct red shoulder or secondary feature, as opposed to the usual red wing. It is unclear whether this second profile is in fact present towards these lines of sight, or

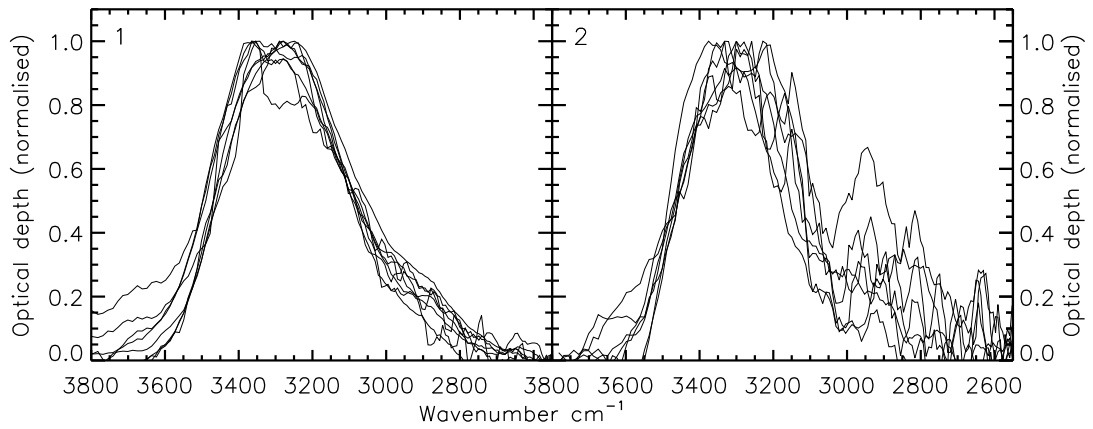

Figure 4.2. H_2O absorption band profiles, types 1 (left) and 2 (right). These data have been smoothed and normalised. Two distinct H_2O profile types are evident. It is particularly evident in this figure, from the flattened peak of the band profile, that the H_2O band is almost always saturated due to loss of signal using AKARI.

whether the atypical appearance of this band is an artefact of the data reduction. However, it could be a signature of the dust size distribution towards these regions. If there is little aggregation of dust in the clouds, it would remain as small grains which would not cause a high degree of scattering in the NIR. No red contribution at all is seen in the spectra of Objects 10 & 12, where a CDE-corrected pure H_2O spectrum appears to fully fit the observed data. In both spectra, there is possibly a small contribution towards longer wavelengths which could be considered a red shoulder, and the H_2O band is well fitted without a red wing, so they likely belong to the second group. Given the uncertainty on the data, and the low flux of both spectra ($<$ 12 mJy at all wavelengths observed) it is not possible to resolve this issue.

For all objects, a test fit was made to examine the possibility of a crystalline H_2O component towards each line of sight. Crystalline H_2O has a characteristic peak shape and position, and is typically observed in the circumstellar disks around YSOs, where material is subject to intense irradiation from the newly formed star [Creech-Eakman et al., 2002; Schegerer & Wolf, 2010]. As is evident from Figure 4.3, the peak of crystalline H_2O is shifted and narrow, compared to non-porous, amorphous H_2O. This shape does not resemble any of the observed spectra by eye, but to test for the presence of crystalline H_2O mathematically, a combination of two lab spectra (the amorphous H_2O spectrum described above, plus a crystalline H_2O spectrum [Fraser & van Dishoeck, 2004],

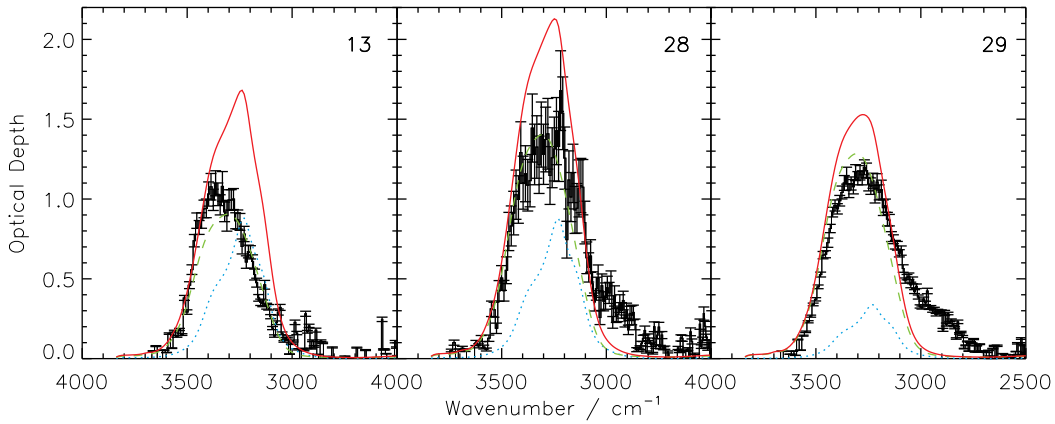

Figure 4.3. A combination of two laboratory spectra (amorphous H_2O and crystalline H_2O) was fit to all objects. For the majority of the objects, the crystalline water was not incorporated into the fit by the fitting routine. There were only three objects for which crystalline H_2O was included in the automatic fit, Objects 13, 28 and 29, plotted here in black. The amorphous H_2O is plotted in green (dashed), the crystalline H_2O in blue (dotted) and the overall fit in red (solid). The fits with crystalline water are not better than those with amorphous water only. It was decided to fit all water bands with only amorphous water, discarding the crystalline water fits.

corrected with a CDE model and the instrumental line profile) was fitted to all observed H_2O bands, using only the blue wing of the H_2O band, as above. For the majority of objects (27 of 30) the crystalline component was not included in the final fit. The fits of Objects 13, 28 & 29 are shown in Figure 4.3. For these three objects, a fit of the two ice species was possible. However, in all cases, but particularly for Objects 13 & 29, this combined fit approach significantly overestimates the abundance of H_2O in the observed H_2O band, even allowing for saturation of the feature. For Object 28, it is possible that a crystalline ice component is present in this band, but by reference to the amorphous H_2O fit in Figure 4.1b, it is clear that a single component fits this spectrum equally as well, if not better than, a two component fit. Thus, all objects in this study are considered to contain amorphous H_2O only, at abundances as presented in Table 4.1. This result is as expected for background stars probing quiescent regions, and lines of sight towards low mass YSOs.

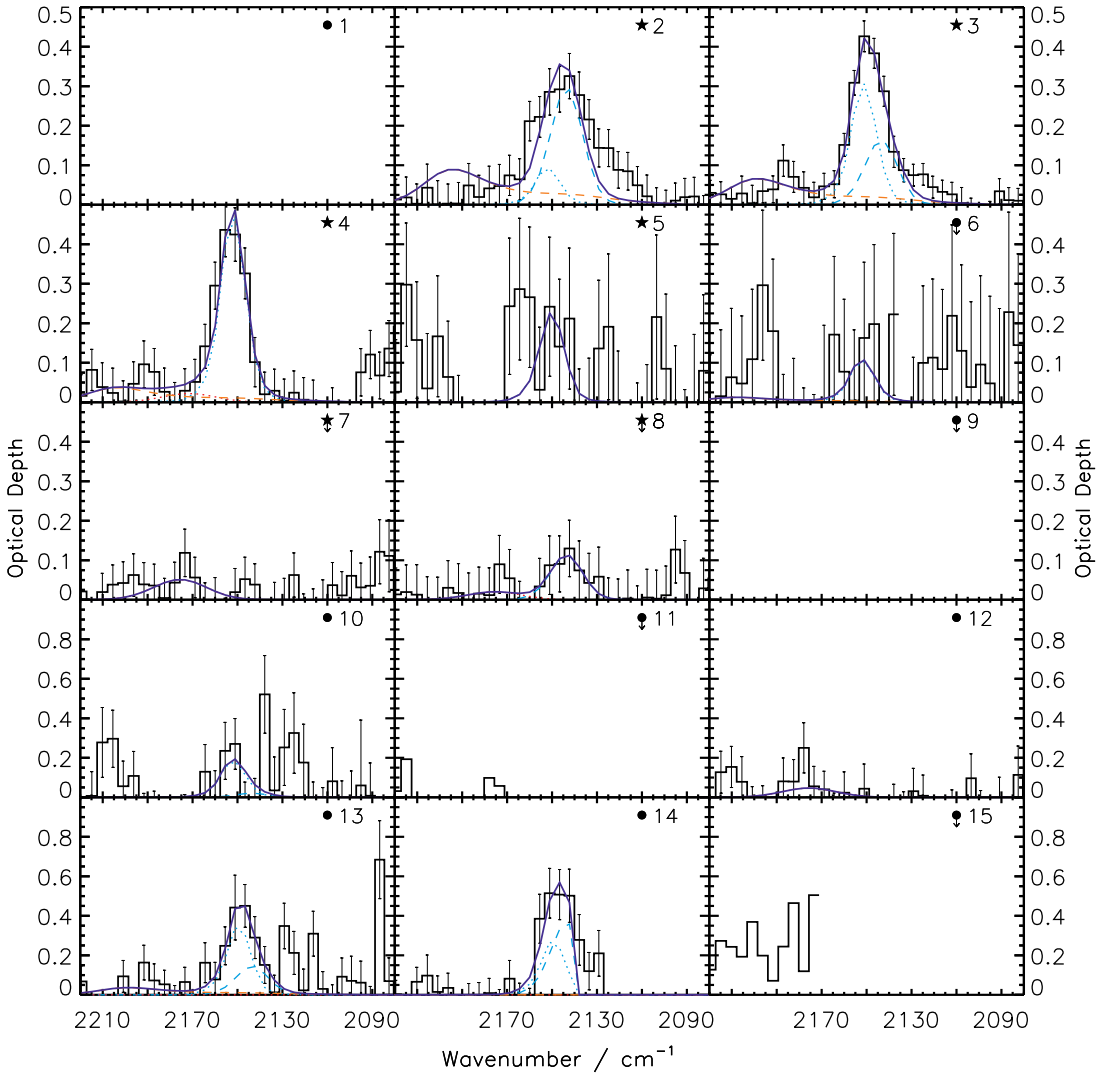

Figure 4.4a. Fits to all CO absorption bands using a component analysis method. Observational data, on an optical depth scale, is plotted in black, with the fits overplotted as follows: CO_{rc} light blue dashed, CO_{mc} light blue dotted, OCN^{-1} red dotted, CO_{gg} orange dashed, and the overall fit in dark blue (solid). All components are corrected for the AKARI instrumental line profile, and CO_{mc} is CDE corrected to account for grain shape effects. Where there is no data in a plot, it is because no data was extracted in this region of the spectrum e.g. Object 1. Where there is only a partial data extraction, the plot is shown, but no fit was made to the data e.g. Object 11.

4.3.3 CO

Spectral features on an optical depth scale are shown in Figures 4.4a – 4.4b, and column densities were calculated by a component analysis method.

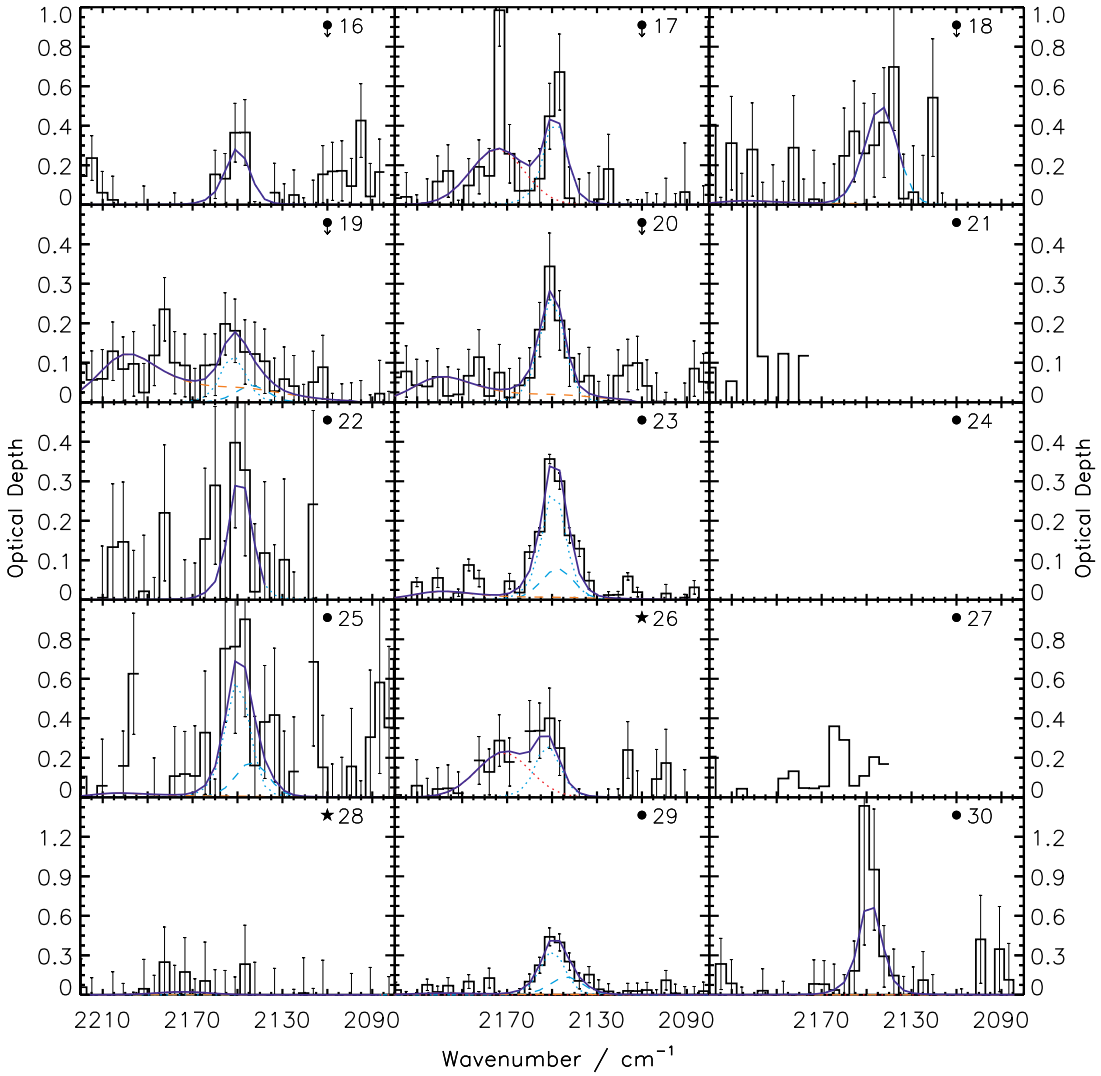

Figure 4.4b. Figure 4.4a continued.

The CO band was fitted based on the four component analysis of Pontoppidan et al. [2003a]. In the original analysis, the pure CO is fitted with a CDE-corrected Lorentzian at 2139cm^{-1} (middle component) and the water-rich CO is fitted with a second Lorentzian at 2136 cm^{-1} (red component). A third CO component – a Gaussian at 2143cm^{-1} representing a narrow feature first identified in interstellar spectra by [Tielens et al., 1991] – and the fourth component – a Gaussian at 2165cm^{-1} representing the CN stretch attributed to OCN^{-} – complete the model.

In this analysis, the red component, CO$_{rc}$, is replaced by a Gaussian calcu-

lated from laboratory data [Cottin et al., 2003], but the middle component, CO_{mc}, is retained as in Pontoppidan et al. [2003a]. The third CO component from Pontoppidan et al. [2003a] is not included, as it was not necessary to fit these data, and the fourth component is replaced with the Gaussian derived more recently by van Broekhuizen et al. [2005]. In addition, a laboratory spectrum of CO adsorbed directly on a surface (CO gas-grain, CO_{gg} [Fraser et al., 2005]) was added to the model, to fit the outlying absorption feature centred at 2175 cm^{-1}. All components are corrected for the AKARI instrumental line profile, and CO_{mc} is CDE corrected to account for grain shape effects. A CDE model is not applied to the other components as they are generally minor components in the fit. The fits of CO are presented in Figures 4.4a – 4.4b.

The column density of CO for the pure component, CO_{mc}, is calculated by:

$$N(CO_{mc}) = 6.03\ cm^{-1} \times \tau_{max,mc} \times A_{bulk}^{-1}, \tag{4.8}$$

where A_{bulk} = 1.1 $\times$ 10^{-17} cm $molec^{-1}$ is the band strength of the bulk material, and $\tau_{max,mc}$ is the optical depth at maximum absorption (Equation 3, Pontoppidan et al. [2003a]).

$N(CO_{rc})$ and $N(OCN^-)$ are calculated using Equation (4.3), with band strengths $A_{rc} = 1.1 \times 10^{-17}$ cm $molec^{-1}$ [Gerakines et al., 1995] and $A_{OCN^-} = 1.3 \times 10^{-16}$ cm $molec^{-1}$ [van Broekhuizen et al., 2004]. The column density of the CO gas-grain population is calculated by:

$$N(CO_{gg}) = 1.07\ cm^{-1} \times \tau_{max,gg} \times A_{bulk}^{-1}, \tag{4.9}$$

where $A_{bulk} = 4.0 \times 10^{-19}$ cm $molec^{-1}$ is the band strength of the bulk material [Fraser et al., 2005], and $\tau_{max,gg}$ is the optical depth at maximum absorption. All column densities calculated for CO_{rc}, CO_{mc}, OCN^-, and CO_{gg} are presented in Table 4.1. It should be noted that A_{bulk} is measured in the laboratory for a particular ice. If astrophysical ices differ in mixture or concentration, the relationship between optical depth and molecular abundance will change, and thus the relative concentration of one component to another will differ with respect to the values calculated here.

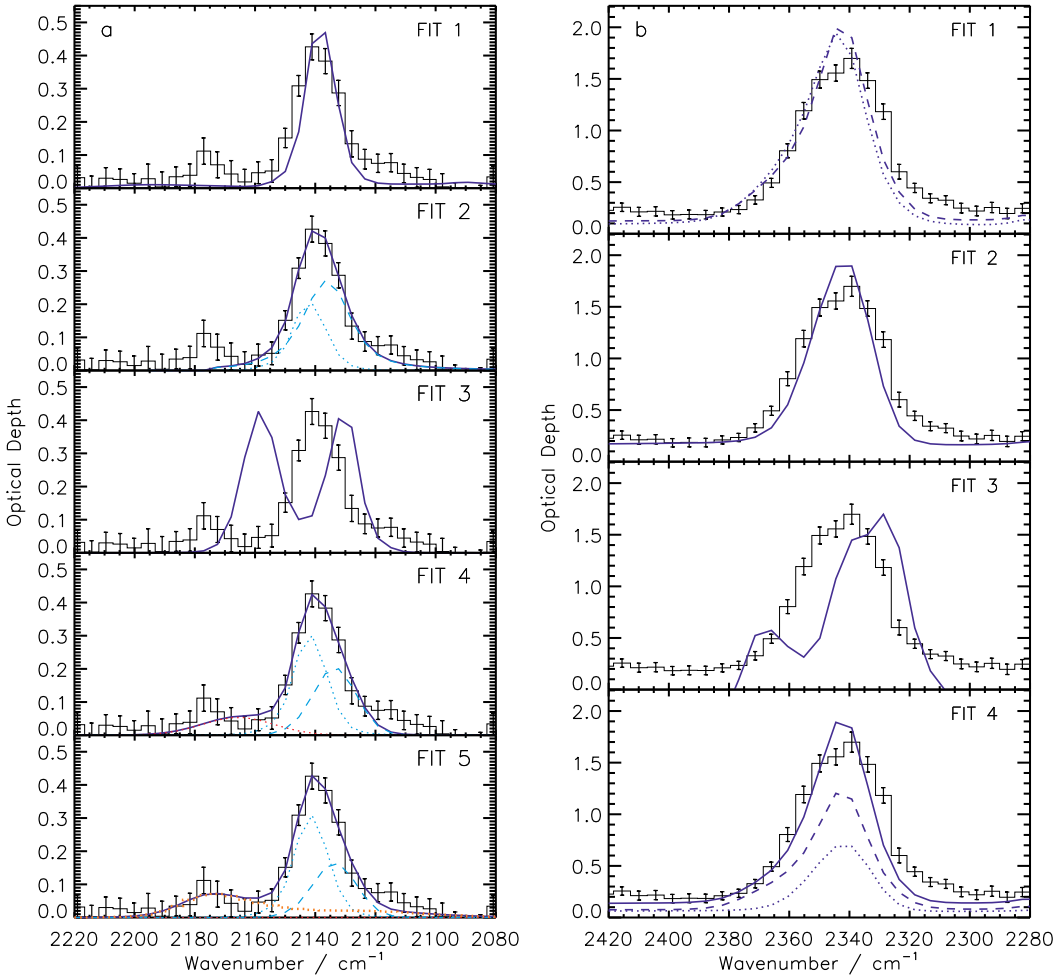

Figure 4.5. The fitting methodology for CO and CO_2 absorption features. Various methods were attempted before picking the final, best-fitting approach. a) CO fitting methodology. Fit 1 is a pure CO laboratory spectrum [Ehrenfreund et al., 1996], Fit 2 is a combination of CO_{rc} and CO_{mc} [Pontoppidan et al., 2003a], Fit 3 is a model CO gas phase absorption, Fit 4 is a combination of CO_{rc}, CO_{mc} and OCN^- [Pontoppidan et al., 2003a; van Broekhuizen et al., 2005], Fit 5 is the final fitting approach, with a combination of CO_{rc}, CO_{mc}, OCN^-, and CO_{gg} [Pontoppidan et al., 2003a; van Broekhuizen et al., 2005; Fraser et al., 2005] b) CO_2 fitting methodology. Fit 1 is two different fits of a pure CO_2 laboratory spectrum [Ehrenfreund et al., 1996] and [Helen Fraser, *private communication*], Fit 2 is a CO_2:H_2O mixture laboratory spectrum [Gerakines et al., 1995], Fit 3 is a model CO_2 gas phase absorption, and Fit 4 is the final fitting approach, a combination of mixed CO_2:CO [Fraser & van Dishoeck, 2004] and CO_2:H_2O [Gerakines et al., 1995] laboratory spectra.

The fitting methodology for CO was developed by consideration of various possible methods, the most crucial of which are illustrated in Figure 4.5a. A single component fit of pure CO using a lab spectrum (Figure 4.5a, Fit 1) was discounted as it did not fit the CO bands of AKARI. A two component fit of a pure CO and CO in a water environment (middle component and red component, Pontoppidan et al. [2003a]) better described the CO feature, especially the wings (Figure 4.5a, Fit 2). A similar, two-component analysis of CO was first made by Tielens et al. [1991]. However, it did not account for the 2175 cm^{-1} feature. Gas phase CO rovibrational lines can introduce error into the fit of the solid phase CO feature. At AKARI resolution, gas phase lines are not resolved, but the possibility of gas phase CO features in absorption was considered, and rejected, based upon the fit in Figure 4.5a, Fit 3.

OCN^- was believed to be formed around YSOs, based upon upper limits established by studies of background stars [Whittet et al., 2001] which suggested that OCN^- is not found in quiescent clouds. However, more recent studies have revealed higher upper limits on OCN^- towards background stars probing quiescent regions [Knez et al., 2005]. A feature representing OCN^- was introduced to the fit to account for the potential presence of OCN^- in the data (Figure 4.5a, Fit 4). As is evident with reference to Table 4.1, an OCN^- component was fitted towards very few lines of sight (five YSOs and two background stars, all but one of which were upper limits). The addition of a CO_{gg} component, as introduced by Fraser et al. [2005], produced a fit that well described both the CO band and the 2175 cm^{-1} feature (Figure 4.5a, Fit 5).

The original aim of the ice mapping observations with AKARI was only to determine the relative abundances of H_2O, CO_2 and CO ices in molecular clouds. It was not anticipated that the spectral absorption features would be fully resolved, and thus a component fitting method was not envisioned. That only two components are required to fit the main CO feature (CO_{mc} and CO_{rc}) supports the assertions made in Chapter 3 that the pipeline, and in particular the stacking method, was appropriate for analysis of these data.

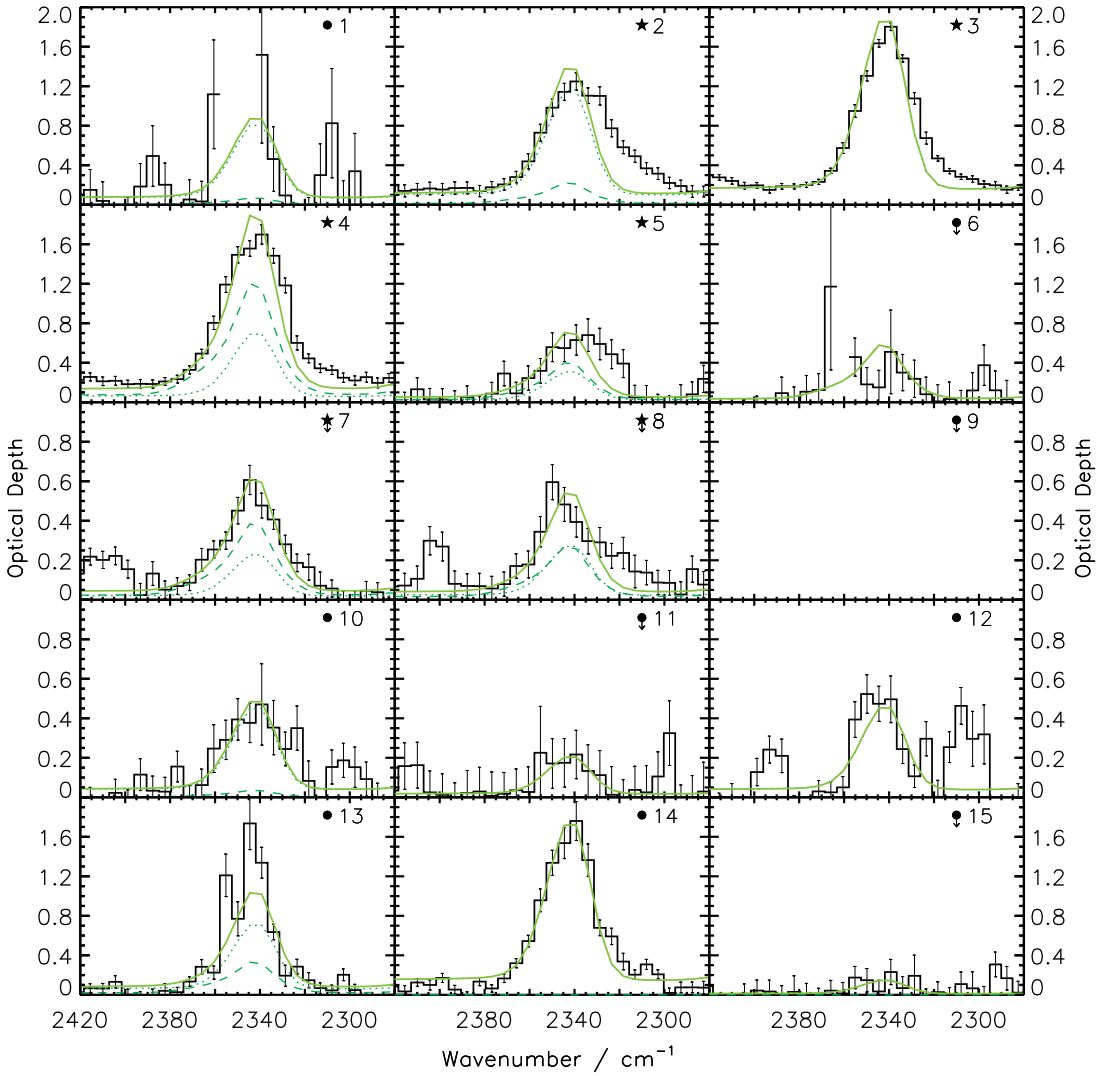

Figure 4.6a. Fits to all CO_2 absorption bands using a combination of H_2O-rich and CO-rich CO_2 laboratory ices. Observational data, on an optical depth scale, is plotted in black, with the fits overplotted as follows: CO_2 in a CO-rich ice is dark green dashed, CO_2 in a H_2O-rich ice is dark green dotted, and the overall fit in light green (solid). Both components are corrected for the AKARI instrumental line profile and CDE corrected to account for grain shape effects.

4.3.4 CO_2

Spectral features on an optical depth scale are shown in Figures 4.6a – 4.6b. Column densities were calculated by fitting a combination of lab spectra to the absorption band at 4.25 μm ($\sim$ 2350 cm^{-1}), then using Equation (4.3) with A = 7.6 $\times$ 10^{-17} cm molecule^{-1} [Gerakines et al., 1995].

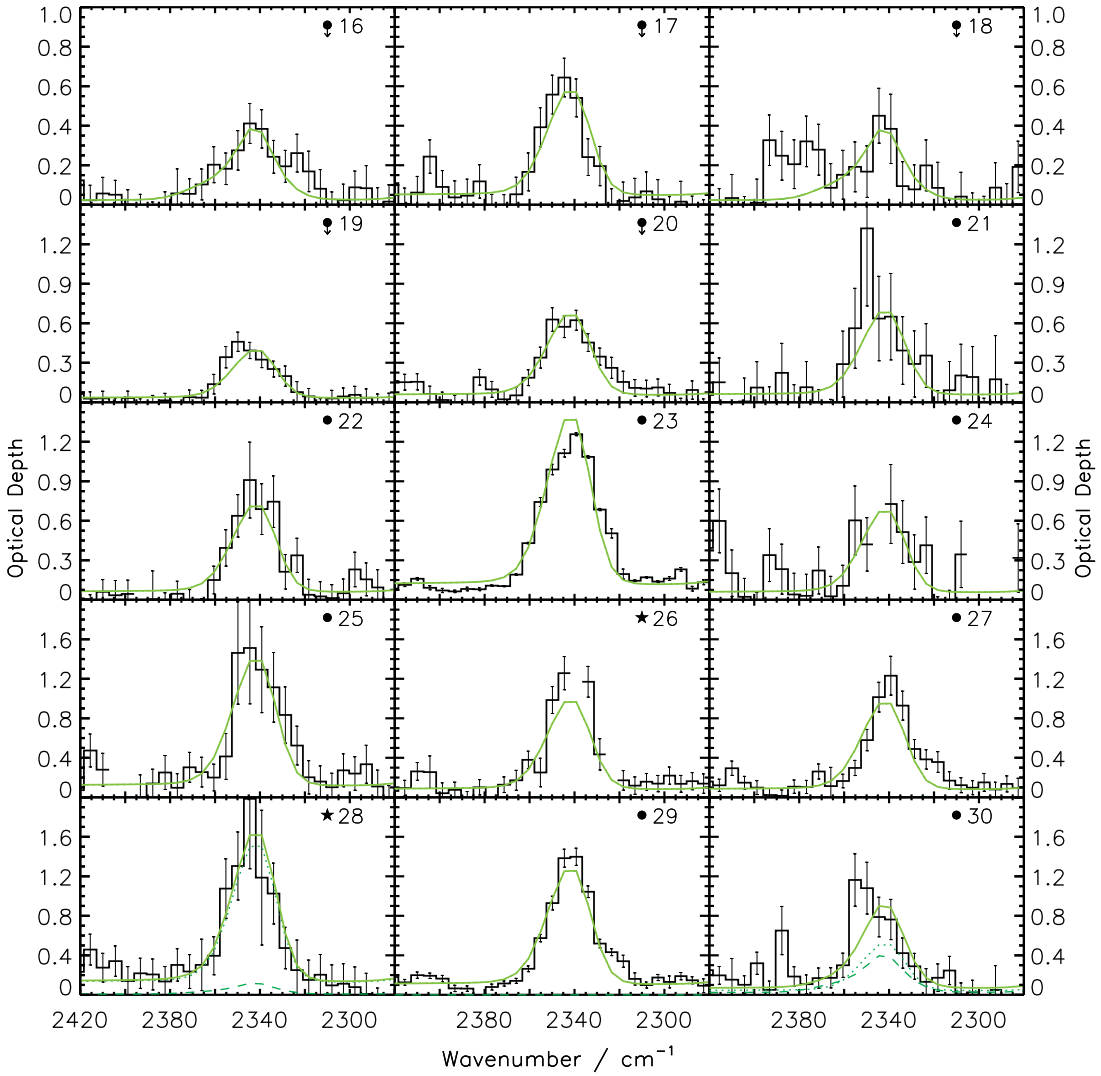

Figure 4.6b. Figure 4.6a continued.

Column densities were calculated by fitting laboratory spectra of CO_2 corrected with a CDE grain shape model and convolved by the AKARI instrumental line profile, and are presented in Table 4.1. Various spectra were tested, including CO_2:H_2O and CO_2:CO mixtures, gas phase models, and combinations of each of these spectra, as illustrated in Figure 4.5b. The addition of extra components did not hugely improve the fit (measured by a Pearson χ^2 test) but, as previously discussed, it is believed that CO_2 exists in two environments in molecular clouds (a water-rich ice and a carbon monoxide-rich ice, sometimes referred to as 'polar' and 'apolar', or 'non-polar', environments) so it was decided to fit the feature with two laboratory spectra: a CO_2:H_2O 14:100

ice at 10 K [Gerakines et al., 1995] and a CO_2:CO 1:1 ice at 15 K [Fraser & van Dishoeck, 2004]. A Kramers-Kronig analysis, followed by a CDE grain shape model and the AKARI instrumental line profile were applied to both laboratory spectra before fitting. This two component fitting model successfully fits the CO_2 bands for all objects, as illustrated in Figures 4.6a, 4.6b.

As seen for the H_2O band, the CO_2 stretching mode can become saturated, and in this case it is suspected that the CO_2 peaks are saturated, as they would be expected to be very deep absorption features. The abundances of CO_2 calculated here seem low compared with previous observations, which is likely due to underfitting of the CO_2 peak. Due to the low resolution in these data, it is difficult to fit the CO_2 bands with the wings only, as in the case of H_2O. From Figures 4.6a & 4.6b, it is clear that the strategy fits the observed data well, including the peak. If there is saturation of the CO_2 band, then the CO_2 abundance will be underestimated using this methodology.

4.3.5 Additional ice features

CH_3OH, ^{13}CO, $^{13}CO_2$ and (tentatively) HDO features were potentially present towards some lines of sight, as they all absorb in the 2.5 – 5 μm region of the IR. However, because the observational data was not flatfielded (see Chapter 3) it is likely that the absorption features of minor species such as these are all within the noise of the spectra. In particular, the absorption band of OCS at 4.9 μm was searched for, but due to the low signal-to-noise in this region of the spectrum, it was not positively identified in these data. The analyses were performed for completeness, but all values can only be considered as upper limits, based on these data. No CDE correction was made for these components, as they are minor ice species and thus their profiles are not susceptible to grain shape effects to the same extent as the major components.

4.3.5.1 H_2O red wing

The red wing of the H_2O band contains absorption features which have not yet been fully characterised. In some spectra, it was possible to isolate an absorption band at 3.54 μm, attributed to the CH stretch of methanol, CH_3OH. The

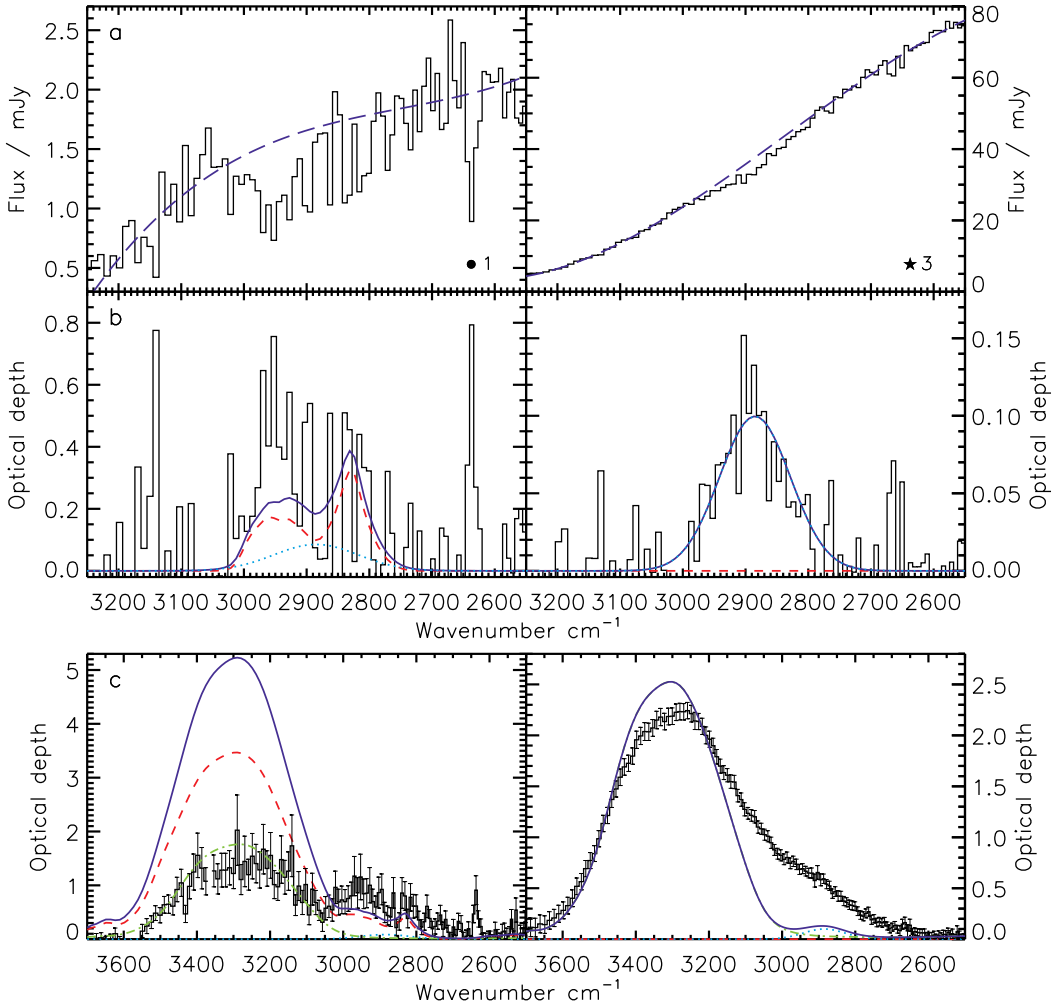

Figure 4.7. Best-fitting CH_3OH band to a the spectra towards a background star and a YSO, fitted using the method of Brooke et al. [1999]; Pontoppidan et al. [2003b]. a) Fit 3^{rd} order polynomial baseline (dark blue dashed) to spectrum over a fitting range of 3.1 – 3.25 μm and 3.65 – 4 μm. b) Fit a combination of a 3.47 μm feature (light blue dotted, Gaussian function from Brooke et al. [1999]) and 3.53 μm CH_3OH feature (red dashed, instrumental line profile-corrected laboratory spectrum H_2O:CH_3OH:CO_2 1:1:1 at 10 K [Gerakines et al., 1995]) to the baselined spectrum. The full fit is overplotted (dark blue solid). c) Compare H_2O fit (green dot-dash), CH_3OH (red dash), 3.47 μm (light blue dotted) and sum of the three (dark blue solid). Evidently, the sum of both spectra overfits the OH 3 μm stretching absorption band for Object 1.

Table 4.2. Calculated upper limits on CH_3OH, $\tau_{3.47\mu m}$, and $^{13}CO_2$.

Object	N(CH_3OH) 10^{18} molecules cm^{-2}	% H_2O	$\tau_{3.47\mu m}$	N($^{13}CO_2$) 10^{16} molecules cm^{-2}	$^{12}C/^{13}C$
1	1.784	78	0.085	...	...
2	...	...	...	2.89	16
3	...	...	...	3.92	15
4	...	...	...	4.82	12
20	0.290	29	0.057	...	...
21	0.313	26	0.090	...	...
25	1.014	74	0.057	...	...
30	0.527	55	0.064	...	...

CH_3OH molecule has been observed towards multiple lines of sight including both low mass YSOs and background stars [Brooke et al., 1999; Pontoppidan et al., 2003b; Boogert et al., 2008].

CH_3OH was fitted using the method outlined in Pontoppidan et al. [2003b], and the best fitting results are presented in Figure 4.7. A third order polynomial was fitted to the original spectral region around the CH_3OH feature (typically between 3.1 – 3.3 μm and 3.65 – 4.0 μm) to estimate the 'continuum'. The spectra were converted to an optical depth scale, before being fitted simultaneously with a Gaussian feature peaking at 3.47 μm (2881 cm^{-1}) and a lab spectrum containing CH_3OH. The 3.47 μm feature has been attributed to diamonds or an ammonia hydrate [Allamandola et al., 1992; Pontoppidan et al., 2003b]. The characteristics of the Gaussian used here, taken from Brooke et al. [1999], are peak position of 2881 cm^{-1}, with FWHM 87 cm^{-1}. The lab spectrum, taken from the Leiden database [Gerakines et al., 1995], was a H_2O:CH_3OH:CO_2 1:1:1 mixture at 10 K, convolved with the AKARI instrumental line profile. CH stretching absorption features are expected in this region. In objects without the 'standard' H_2O profile, as discussed in § 4.3.2, the 3.47 μm feature is potentially explained by the presence of small, highly hydrogenated dust grains. This would account both for the lack of scattering, and the sometimes large 3.47 μm secondary feature.

It is clear, when this additional CH_3OH component is added to the previously

calculated H_2O fit (see Figure 4.7c), obtained using a standard fit of laboratory data to the blue wing of the H_2O peak, that the sum of the two components drastically overfits the OH stretching absorption feature at 3 μm (3333 cm^{-1}). This is a fundamental problem for the analysis of infrared spectra of interstellar ices. Fitting methodologies generally concentrate on one band at a time, particularly the bands of high abundance species. This is for practical reasons, both observational (it is rare to obtain enough observing time on enough different telescopes to observe the entire infrared region of a single line of sight, and thus have the entire vibrational spectrum for analysis, let alone the time to observe multiple lines of sight) and experimental (in order to analyse interstellar ices they must be compared to laboratory ices, but the exact mixture composition can not be known, so single or double component laboratory ices are generally used for comparison). Thus, in this case, analysis of the OH stretch at $\sim$ 3 μm and the CH stretch at 3.53 μm were performed independently, but upon combination, the sum of the contributing spectra was found to overfit the observed spectrum. As space based telescopes become more sensitive, and provide vibrational spectra of higher resolution, it will be necessary to refine the techniques used to analyse infrared spectra, in order to more accurately determine the relative abundances of molecular species present in the icy grain mantle mixtures. Also, comparison between the features of components at different wavelengths [e.g. Boogert et al., 2011] could help to develop a more holistic approach.

Of the 30 objects in this study, six had no excess in the H_2O wing, and for a further 19 objects, the excess in the H_2O band was completely accounted for by the 3.47 μm feature, and thus no CH_3OH was present towards those lines of sight. The 3.54 μm peak, characteristic of CH_3OH, was only seen for five objects. For these five objects, the CH_3OH abundance was calculated using Equation (4.3), with A = 5.4 $\times$ 10^{-18} cm $molec^{-1}$ [Kerkhof et al., 1999]. The calculated CH_3OH abundances are presented in Table 4.2. As illustrated by Figure 4.7, CH_3OH abundances calculated by this method are believed to be overestimated.

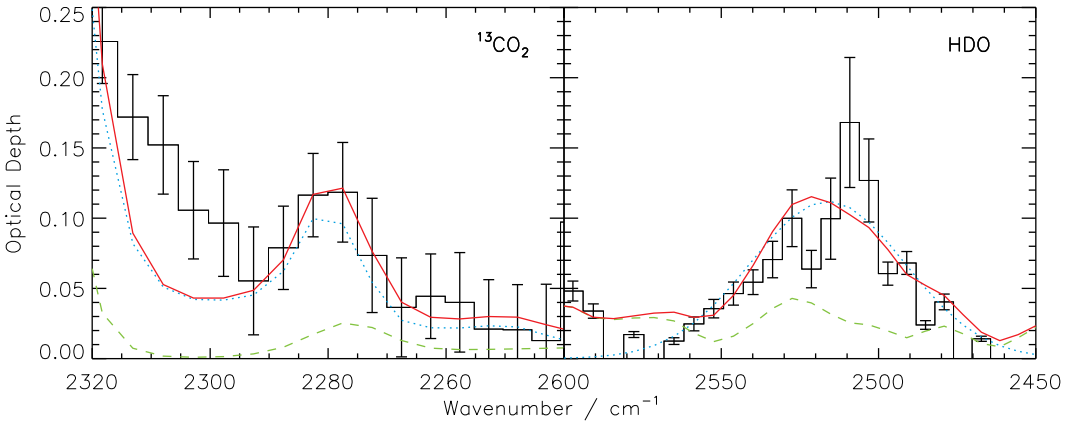

Figure 4.8. Upper limits were extracted for $^{13}CO_2$ and HDO towards some lines of sight. Quantification was complicated by low signal-to-noise of the features. Left: $^{13}CO_2$ in Object 3 was fitted as for $^{12}CO_2$ with a combination of two laboratory spectra. CO_2 in a CO-rich ice is blue dotted, CO_2 in a H_2O-rich ice is green dashed, and the overall fit in solid red. Right: The HDO feature at 2518 cm^{-1} overlaps with combination bands of CH_3OH at 2530 cm^{-1} [Dartois et al., 2003]. This is the spectrum of Object 4, fitted with a combination of pure CH_3OH (green, dashed) and a Gaussian representing HDO (blue, dotted). The overall fit is plotted in solid red.

4.3.5.2 HDO

An absorption signature is seen at $\sim$ 2510 cm^{-1} ($\sim$ 4 μm) towards Object 4. The origin of this feature is likely to be complicated, as discussed extensively in Dartois et al. [2003]. Shown in Figure 4.8 is a simple fit to the 4 μm band as a blue dotted line (a Gaussian representing HDO, peaking at 2518 cm^{-1} (3.97 μm) with FWHM 51 cm^{-1}). Upon integration according to Equation (4.3), the single HDO Gaussian fit gives N(HDO) $\leq$ 1.54 $\times$ 10^{17} molecules cm^{-2}, or N(HDO)/N(H_2O) $\leq$ 4.98 %, which is very high compared with previous results of $\leq$ 3 % [Dartois et al., 2003; Parise et al., 2003, 2005]. It is known, however, that CH_3OH combination bands are also seen in this region of the spectrum [Dartois et al., 2003].

A simple fit of CH_3OH laboratory data is plotted on Figure 4.8 as a green dashed line. By combining the CH_3OH and HDO contributions in a single fit (red, continuous line) the observed feature can be better fitted. The HDO Gaussian peaks at 2515cm^{-1} (3.98μm), with FWHM 41 cm^{-1}. This combined approach gives N(HDO)/N(H_2O) $\leq$ 3.34 %, which, although high, is approximately in line with previous results. Due to the low resolution of AKARI, this

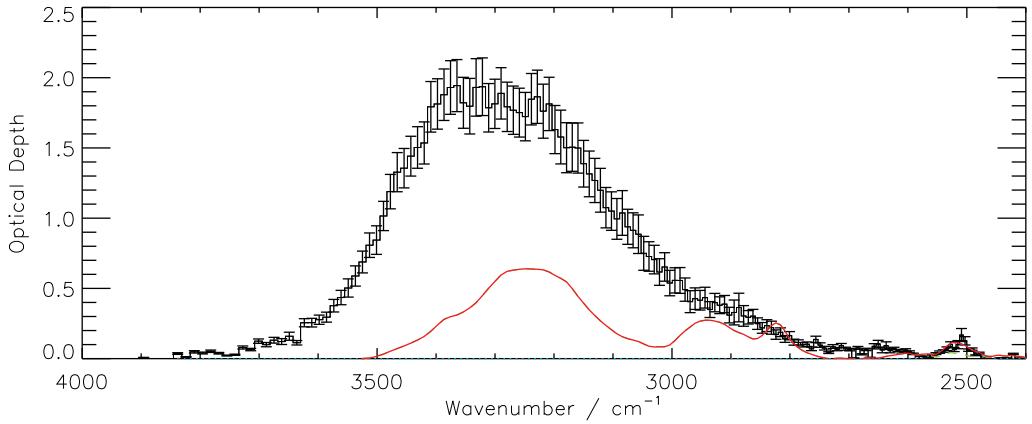

Figure 4.9. The HDO fit for Object 4 in Figure 4.8, extended to include the H_2O absorption band at 3 μm (3333 cm^{-1}). No CH_3OH was extracted for this line of sight (see § 4.3.5.1) but the CH_3OH fitted to the HDO feature does appear to fit some of the red wing well.

result is considered to be a tentative upper limit only. The only other spectrum that potentially contains an HDO contribution is that of Object 2. A similar analysis gives N(HDO) $\leq$ 8.61 $\times$ 10^{16} molecules cm^{-2}, or N(HDO)/N(H_2O) $\leq$ 2.2 %, with a Gaussian peaking at 4.01 μm and FWHM 48 cm^{-1}.

Interestingly, whilst no CH_3OH at 3.53 μm (2830 cm^{-1}) was extracted for Object 4 (see § 4.3.5.1), the fit of HDO including CH_3OH reveals that CH_3OH may be present towards this object, as evident from Figure 4.9. In Figure 4.9, the combined HDO and CH_3OH fit of Figure 4.8 has been plotted on the observed spectrum from 4000 – 2400 cm^{-1}. In the red wing of the H_2O band, it is clear that the CH_3OH from Figure 4.8 could account for at least some of the unexplained absorption, in the region of 3000 – 2800 cm^{-1}. This is another example of the necessity of a combined methodology when analysing observational spectra.

If the absorption features of HDO are validated, both in this study and that of Aikawa et al. [*submitted*], these AKARI observations represent the first observations of solid phase HDO in the ISM since the unconfirmed study of Teixeira et al. [1999]. In these data, HDO is observed only towards two objects, 2 & 4, which are both highly extincted, embedded YSOs. They are both observed towards the same core, B 35A, and, as deuteration is typically seen towards deeply embedded objects, it is reasonable that these two lines of sight would

be most likely to probe deuterated species.

4.3.5.3 ^{13}CO and $^{13}CO_2$

The vibrational stretch of ^{13}CO produces a weak absorption feature at 2092 cm^{-1} [Boogert et al., 2002]. In the spectra presented here, no ^{13}CO is seen. This is likely due to the low signal-to-noise in the region redward of $\sim$ 2100cm^{-1}. However, the $^{13}CO_2$ stretch at 4.35 μm ($\sim$ 2300 cm^{-}) is tentatively observed towards three lines of sight, Objects 2, 3 & 4, in molecular cloud B 35A. In Figure 4.8, the $^{13}CO_2$ feature in the spectrum of Object 3 is plotted. To fit this feature, a combined fit of CO_2 in H_2O ice and CO_2 in CO ice was applied, as for the $^{12}CO_2$ band. See § 4.3.4 for details. Abundances of $^{13}CO_2$ and the calculated $^{12}C/^{13}C$ ratios are presented in Table 4.2. The $^{12}C/^{13}C$ ratios are low compared with previous observations of $\sim$ 71 – 80 [Boogert et al., 2000, 2002], offering further evidence that the AKARI observations of $^{12}CO_2$ are saturated, and the analysis underestimated abundances.

4.4 Correlation plots

In order to determine the relationships between different solid phase species in molecular clouds, it is necessary to consider the relationships between their abundances. The aim of this correlation plotting is to ascertain the links between H_2O, CO_2 and CO ice abundances, to test the chemistry present in the regions observed and, ultimately, to compare 1D correlations with 2D ice maps to test the relationships between the two methods.

Figure 4.10a shows the calculated abundances of the three most abundant solid phase molecular species, H_2O, CO_2 and CO, plotted against visual extinction, A_V. The lowest A_V of any object in these AKARI data is 5.68. In all figures in this section, background stars are plotted as $\bullet$ and low mass YSOs as $\star$, with upper limits designated by $\downarrow$. Also plotted, as empty symbols, are literature values for comparison. Intermediate and high mass YSOs from the literature have been included for completeness, and these are plotted as Δ.

In Figure 4.10a, the results of the AKARI observations follow the pattern of

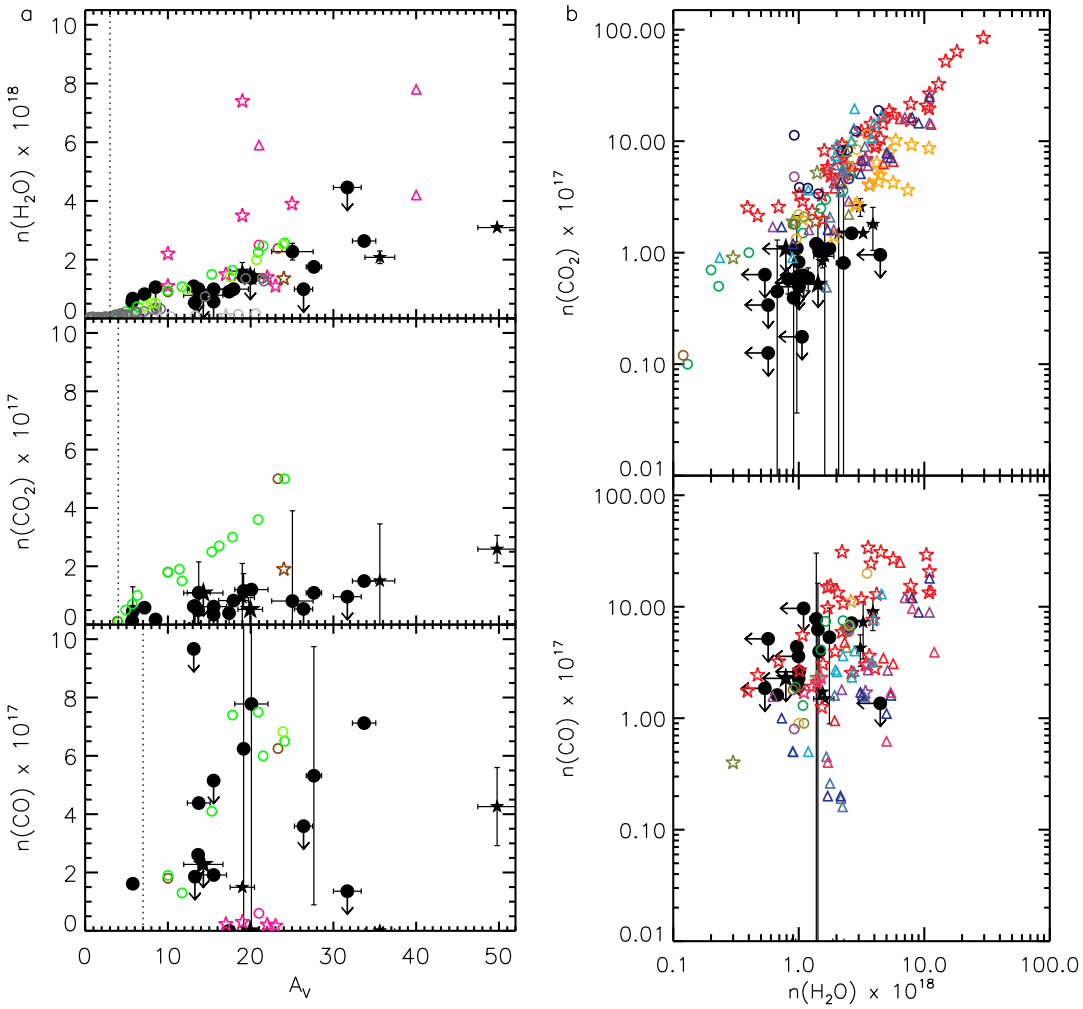

Figure 4.10. Correlation plots of calculated H_2O, CO_2 and CO abundances with extinction. Data calculated in this thesis are plotted as solid black symbols, with literature values as open symbols. In this figure, different studies are plotted in different colours. In this, and all subsequent, correlation plots, background stars are plotted as •, low mass YSOs as ⋆ and high mass YSOs as Δ. a) Column densities of H_2O, CO_2, and CO plotted against A_V. In each plot, the dotted line represents the critical A_V value calculated by previous studies. H_2O and CO_2 clearly increase in abundance towards more dense regions of the molecular clouds observed, while the pattern is less obvious for CO. b) Column densities of CO_2 and CO plotted against H_2O. There is a clear correlation between CO_2 and H_2O, indicating a linked chemistry, but between CO and H_2O there is no correlation. [Whittet et al., 1988; Gerakines et al. , 1999; Murakawa et al., 2000; Nummelin et al., 2001; Gibb et al. , 2004; van Broekhuizen et al., 2004; Knez et al., 2005; Bergin et al., 2005; Whittet et al., 2007; Pontoppidan et al., 2008; Zasowski et al., 2009; Shimonishi et al., 2010; Boogert et al., 2011; Chiar et al., 2011; Oliveira et al. , 2011]

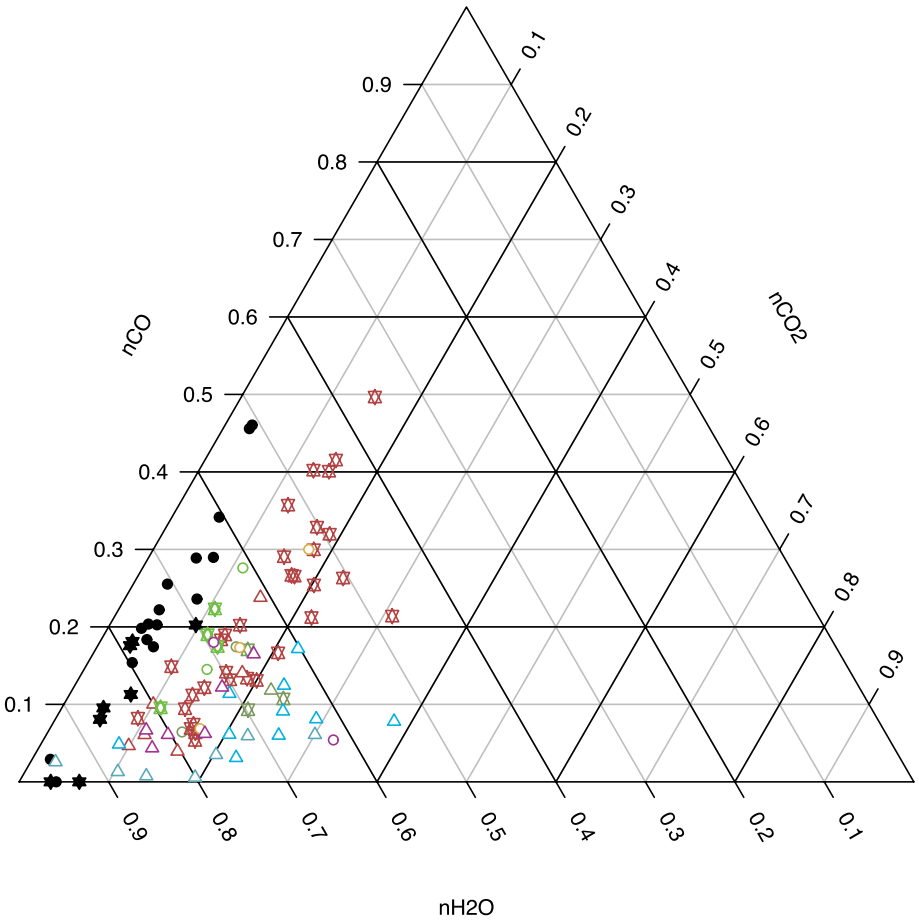

Figure 4.11. Ternary plot of the relative calculated abundances of H_2O, CO_2 and CO. For each line of sight, the sum of all three axes is 1. [Nummelin et al., 2001; Gibb et al. , 2004; Knez et al., 2005; Whittet et al., 2007; Pontoppidan et al., 2008; Shimonishi et al., 2010; Oliveira et al. , 2011]

previous observations. Both H_2O and CO_2 clearly increase with A_V, with critical A_V of ~ 3 and ~ 4, respectively; both molecules form on grain surfaces and are thus expected to be more abundant at higher extinctions. As anticipated in § 4.3.4, the calculated abundances of CO_2 are low when compared with previous results. This is likely due to underfitting the CO_2 absorption feature in the AKARI data due to its saturation at the relatively low resolution of the grism disperser. When only the background stars are considered, the AKARI CO_2 gradient seems very different to that of the literature data. The majority of the literature values for background stars (shown in green in Figure 4.10a) are taken from Whittet et al. [2007], a survey of background stars in Taurus performed using *Spitzer*. Thus, the data are derived from bending

mode observations. This difference highlights the complexities of calculating molecular abundances from only a single band; it is possible that the *Spitzer* data slightly overestimate the CO_2 abundances towards higher A_V, while the AKARI data slightly underestimate it, explaining the difference in their gradients. It is likely that neither band, when analysed in isolation, is an excellent diagnostic of the CO_2 abundance, although in this case, as the 15 μm bending mode data from *Spitzer* was not saturated, the bending mode probably provides a better test of CO_2 abundance with respect to A_V. In the AKARI study presented in this thesis, the critical A_V could be tested for neither H_2O nor CO_2, as the lowest A_V object extracted had A_V = 5.68.

In Figure 4.10a, there is no clear relationship between CO and A_V. There is a much greater spread in CO values compared to those seen for H_2O and CO_2 in the same figure. CO is known to form in the gas phase and freeze-out onto the grain surface above a critical A_V of ~ 7. Towards one line of sight, CO is observed in the solid phase at a lower extinction than the critical value, but this could be due to CO sticking to grains then migrating into the H_2O ice via pores, in outer regions of the cloud [Collings et al., 2003]. It should also be noted that this value is an upper limit. This figure indicates that, although A_V traces the dust in a cloud, it doesn't necessarily trace the physical factors crucial to CO freeze-out, such as gas density. An important aim of AKARI ice mapping was to test the critical A_V of ice onset towards background stars, and this will be further discussed in Chapter 8.

Figure 4.10b shows the abundances of CO_2 and CO plotted against the abundance of H_2O. Overall, the data calculated in this study agree well with literature values; the relationships between H_2O, CO_2 and CO in molecular clouds and around YSOs are well established and it is important that new data continue to reinforce previous results. There is no relation between H_2O and CO, as expected, but a clear correlation between H_2O and CO_2 is evident by considering all the data, indicating a potential link in the formation chemistry of these two species. Abundance values for low and high mass YSOs tend to be higher than those for background stars, suggesting that UV processing or longer timescales promote CO_2 formation, or the initiation of further CO_2 formation mechanisms.

Again, from these data it is clear that CO_2 abundance has been underestimated

in the analysis method. It is apparent that the CO_2 abundance, as derived from the AKARI 1′ × 1′ NG FoV, has been consistently underestimated by a factor of around 3 – 4. This is a limitation of observing ice absorption bands at low resolution. It should be noted that, although the CO_2 abundances calculated in this thesis were derived from a standard method, the fits were made to saturated bands, and thus the optical depth may vary from object to object, possibly proportional to CO_2 abundance. The absolute values of CO_2 towards each line of sight can not be determined from this data, or by application of a simple correction factor. Thus, comparisons of CO_2 abundance values with other abundances, and within the dataset, must be made with caution. This means that the absolute values of CO_2 abundance can not be mapped in this study, but this does not restrict the mapping of the calculated abundances to test the technique of ice mapping. It is clear from previous AKARI studies that CO_2 abundance quantification using AKARI spectra is difficult. Shimonishi et al. [2008] calculated the CO_2 abundance towards massive YSOs in the Large Magellanic Cloud as $\sim$ 36 % H_2O using the NG dispersion element, and a previous study with the NP dispersion element produced even higher values of $\sim$ 45 % H_2O [Shimonishi et al., 2008].

Figure 4.11 is a ternary plot showing the abundances of all three species on a single plot. By plotting the relative abundances of H_2O, CO_2 and CO on one plot, it is clear that these data include a wide range of CO and H_2O abundances, similar to literature data. However, CO_2 values are again illustrated to be significantly lower than those calculated in previous studies.

The minor ice constituents, OCN^- and CH_3OH, are considered in Figure 4.12. The abundance of OCN^-, a species observed towards five YSOs and two background stars, is plotted against A_V, N(H_2O) and N(CO) in Figure 4.12a. The species does not correlate with any of these variables, suggesting that it has a very complex formation mechanism, unrelated to cloud density or the formation and abundance of key interstellar species. Potential formation routes to OCN^- include the reaction of HNCO with NH_3, CO with N. From these data, it seems that CO is not a likely precursor of OCN^-, but as NH_3 was not observed it is not possible to comment on the reaction scheme HNCO + NH_3.

CH_3OH abundances, calculated towards only five lines of sight (all of which are background stars), are plotted against the abundances of H_2O, CO_2 and

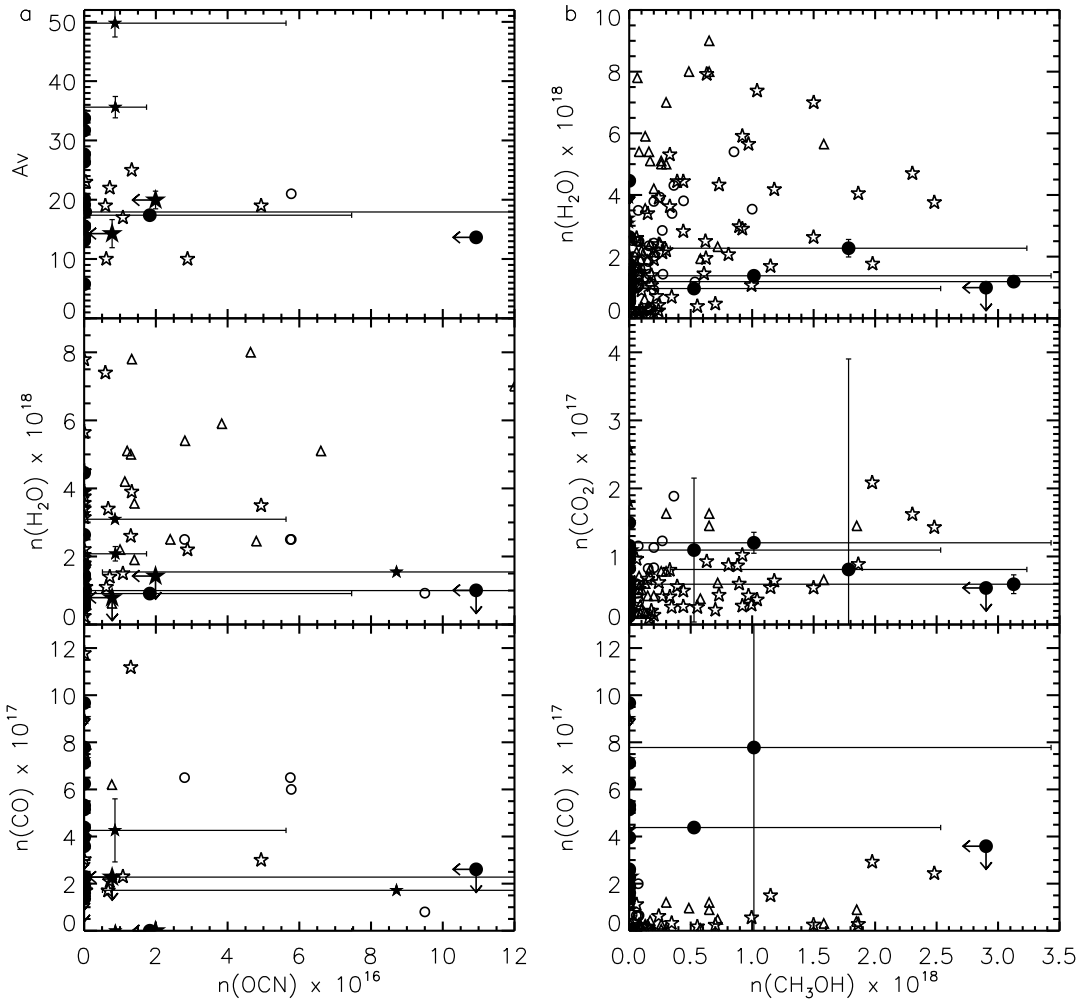

Figure 4.12. Correlation plots for the minor species OCN^- and CH_3OH. a) Column densities of H_2O and CO, and A_V plotted against the column density of OCN^-. b) Column densities of H_2O, CO_2, and CO plotted against CH_3OH. [Gerakines et al. , 1999; Nummelin et al., 2001; Pontoppidan et al., 2003b; Gibb et al. , 2004; van Broekhuizen et al., 2004; Knez et al., 2005; Pontoppidan et al., 2008; Zasowski et al., 2009; Boogert et al., 2011; Chiar et al., 2011]

CO in Figure 4.12b. It has already been noted that the method used to calculate CH_3OH likely overestimates its abundance. There is no correlation of $N(CH_3OH)$ with $N(H_2O)$, but there are possible correlations with $N(CO_2)$ and N(CO). CH_3OH is believed to form by the repeated hydrogenation of CO [Watanabe et al., 2004; Fuchs et al., 2009; Cuppen et al., 2009] and can form both in quiescent regions and around YSOs. In both experimental studies, CO_2 was formed as a byproduct, which could suggest that the formation of CO_2 and

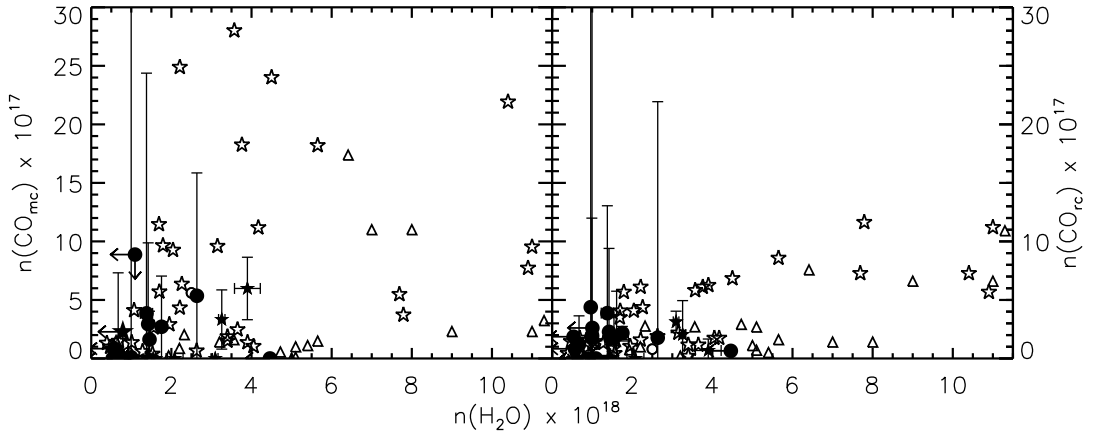

Figure 4.13. Correlation plots of CO components with H_2O. [Gerakines et al. , 1999; Gibb et al. , 2004; Pontoppidan et al., 2008]

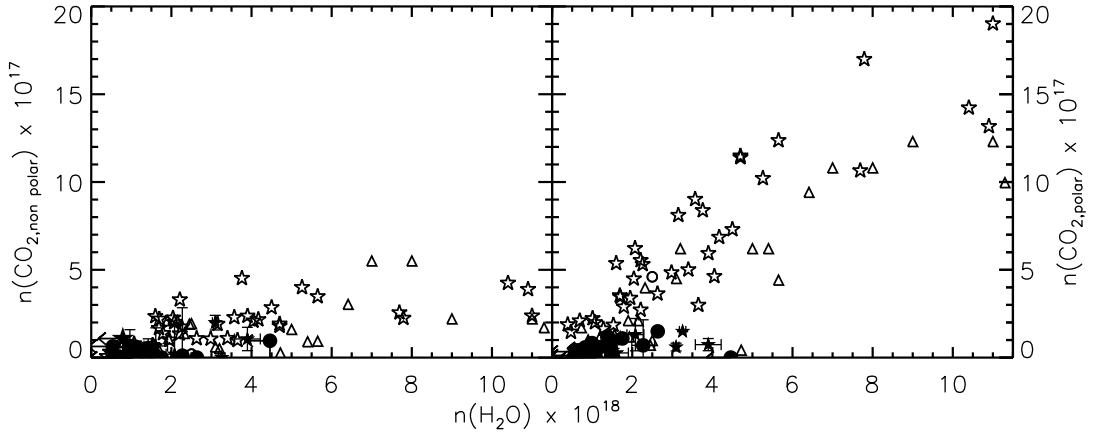

Figure 4.14. Correlation plots of CO_2 components with H_2O. [Gerakines et al. , 1999; Gibb et al. , 2004; Pontoppidan et al., 2008]

CH_3OH occurs in competition in some regions, and merits further investigation.

Looking more closely at the three major ice components, more can be learnt by considering the individual components of each of the observed species. It is possible to consider the relationship between H_2O abundance and the abundances of pure CO (CO_{mc}) and CO in a H_2O-rich ice environment (CO_{rc}), as in Figure 4.13. It is clear that there is no correlation of H_2O with pure CO, which condenses out of the gas phase as a layer on top of the H_2O. However, for the H_2O-rich phase of the CO, as expected, there is a strong correlation with $N(H_2O)$. Collings et al. [2003] offer evidence for the porosity of H_2O in

the ISM, as their experiments suggest that the population of CO in a H_2O-rich environment develops upon heating of a layered system. A higher abundance of H_2O ice suggests a larger number of pores for the CO to migrate into with time or temperature to produce a mixed phase [Pontoppidan et al., 2003a]. As Figure 4.13 shows, towards YSOs, there is clearly a higher abundance of CO in a H_2O-rich environment. The ice has been present in these regions for longer, so it is therefore more likely that the CO has had the time (or the temperature change) necessary to migrate into a mixed H_2O layer. Otherwise, background stars would be expected to probe lines of sight with equally high abundances of CO_{rc}. It is important to note that CO_{rc} is a derived feature, as it can not be measured in isolation in the laboratory.

Figure 4.14 illustrates the relationship between the H_2O abundance and that of the two components of CO_2 – CO_2 in a CO-rich ice ($CO_{2,nonpolar}$) and CO_2 in a H_2O-rich ice ($CO_{2,polar}$). It is evident by considering the difference in the gradients of the correlations that the formation mechanisms for these two populations of CO_2 are independent of one another. It is also clear that towards background stars, there is generally a lower abundance of CO_2 in a H_2O-rich environment than towards low or high mass YSOs, suggesting that in these regions there is a second production mechanism dominating the CO_2 abundance. It is assumed that the CO_2 component observed in a CO-rich environment is produced in situ, from pure CO. The H_2O-rich CO_2 component, however, forms from CO in a H_2O-rich environment, and so it is important to test the correlation of the CO components with CO_2.

Figure 4.15a plots the total abundance of CO against that of CO_2; there is only a tentative link between these variables. This illustrates that there is not a direct link between CO freeze-out and all CO_2 formation. In Figure 4.15b, the plot of the pure component of CO against the CO-rich component of CO_2 shows no correlation, suggesting that the formation route to CO_2 formed in the CO layer is not a simple one, and probably not driven only by CO reacting with O, H or OH from the gas phase.

Figure 4.16 shows plots of $N(CO_2)$ versus the abundance of the CO components CO_{mc} and CO_{rc}. It is very clear from these plots that there is a strong link between the abundance of CO_2 and that of CO in a H_2O-rich environment (CO_{rc}). Thus, some CO_2 must form from CO in a H_2O environment. Mirroring

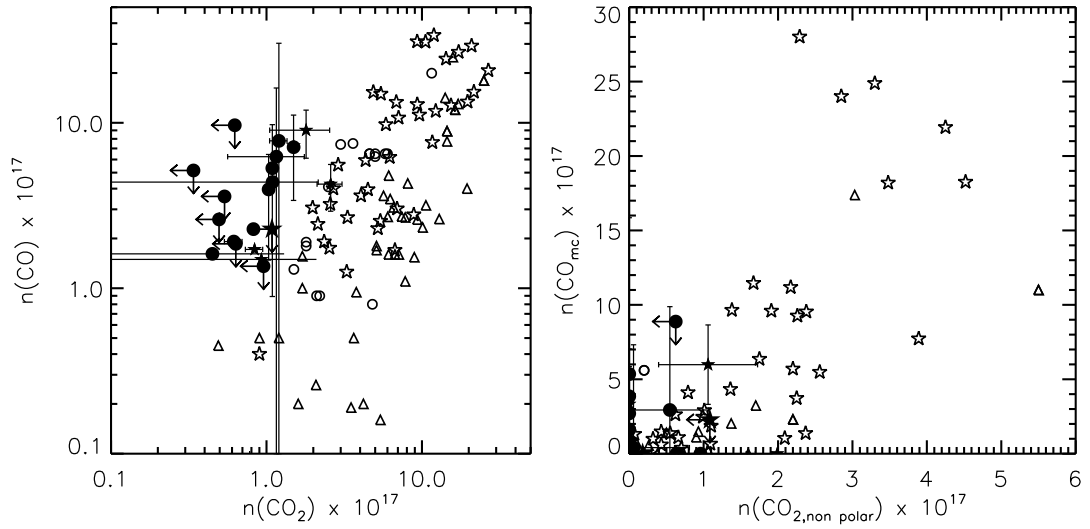

Figure 4.15. Correlation plots of CO with CO_2. Left: Total calculated CO abundance plotted against total calculated CO_2 abundance. Right: CO_{mc} abundance plotted against CO_2 in a CO-rich ice environment. [Gerakines et al. , 1999; Nummelin et al., 2001; Gibb et al. , 2004; Knez et al., 2005; Bergin et al., 2005; Whittet et al., 2007; Pontoppidan et al., 2008; Shimonishi et al., 2010; Oliveira et al. , 2011]

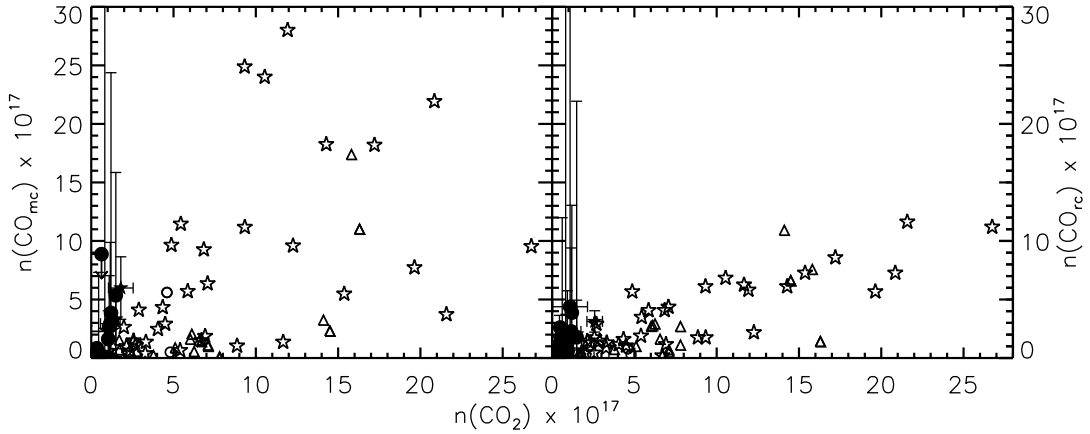

Figure 4.16. Correlation plots of CO components with CO_2. [Gerakines et al. , 1999; Gibb et al. , 2004; Pontoppidan et al., 2008]

the relationship established between H_2O and CO_2 in a H_2O-rich environment (Figure 4.14), background stars probing quiescent lines of sight have the lowest abundances of CO in a H_2O-rich environment, while in the more evolved YSOs, there is a higher abundance, suggesting that CO_2 forms from CO which has migrated into the H_2O upon formation of a star in the core. This correlation is even stronger when only the CO_2 in a H_2O-rich environment is considered,

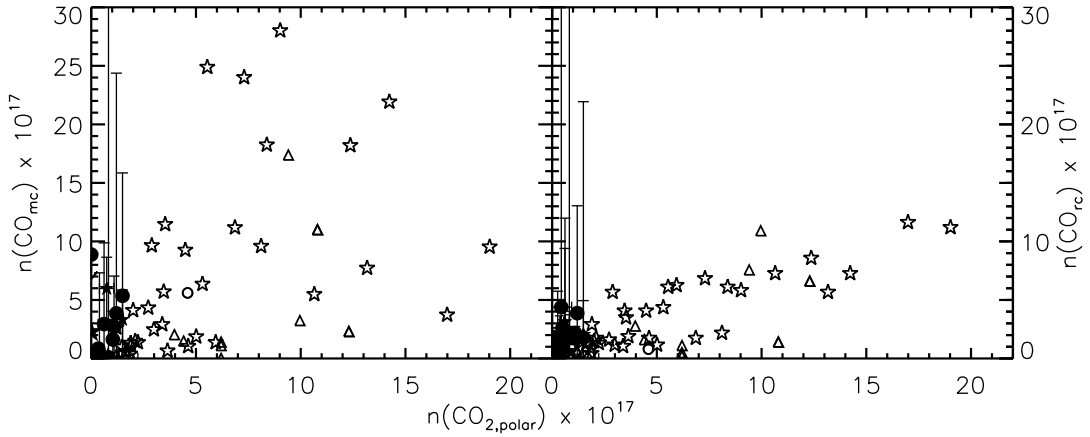

Figure 4.17. Correlation plots of CO components with CO_2 in a H_2O-rich ice environment. [Gerakines et al. , 1999; Gibb et al. , 2004; Pontoppidan et al., 2008]

as in Figure 4.17. It is clear that there is no link between CO_{mc} with either total CO_2 abundance or the abundance of CO_2 in a H_2O-rich environment, but for CO_{rc} there is a definite relationship. This is key evidence supporting the conclusions of the ice mapping in Pontoppidan [2006].

These data illustrate the links between all of the components present in the CO and CO_2 absorption features, and the sequence of CO_2 formation in molecular clouds and star-forming cores. The proposed sequence is outlined here: initially, CO_2 forms concurrently with H_2O, producing an abundance of CO_2 in H_2O. This mechanism is tested experimentally in Chapter 7. Upon critical freeze-out of CO, further CO_2 is formed by reactions of CO with O, H and OH, producing a CO_2 component in a CO-rich ice. With time, and potentially processing, some CO migrates into the H_2O ice, where it can react to form large abundances of CO_2 in a H_2O-rich ice, likely by an energetic route enhanced by UV radiation from a newly formed YSO.

The correlation plots provide important evidence about the formation mechanisms of solid phase species in molecular clouds, particularly the formation of CO_2. It is also possible to investigate these relationships in terms of the spatial distribution of molecular abundances across the clouds, by ice mapping.

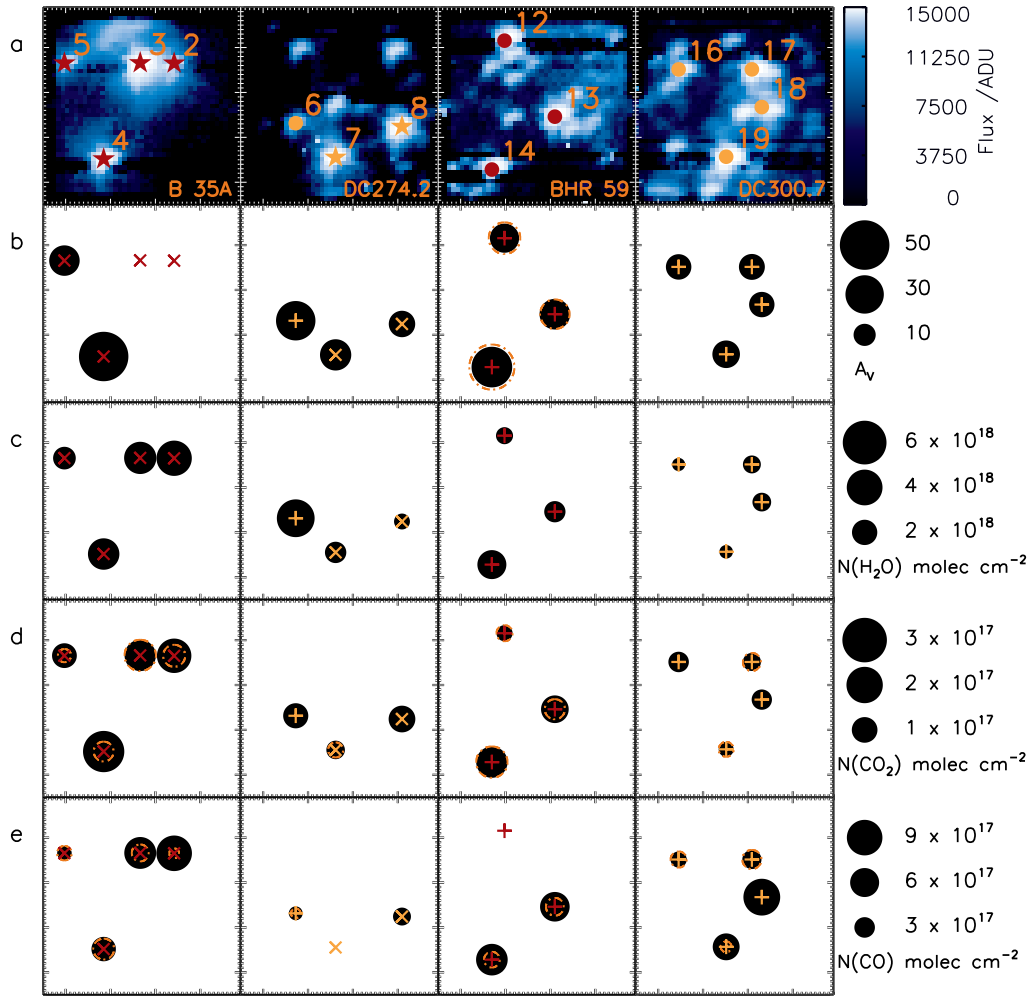

Figure 4.18. Ice maps of AKARI FoVs. The four FoVs mapped are B 35A, DC 274.2-00.4, BHR 59, DC 300.7-01.0. Objects are marked in red or yellow, according to whether they are full or 'upper limit' spectra. In a) the objects are marked with $\star$ for YSOs, or $\bullet$ for background stars, while in b – e these symbols are replaced by $\times$ and $+$, respectively, for clarity. For all maps, the area of the black circle corresponds to the quantity being mapped, according to the scale on the right hand side. All abundances are presented in Table 4.1. The maps presented are as follows: a) Imaging frame from AKARI, as in Figure 3.1. b) A_V. Black circles are A_V calculated by the c2d team [Evans et al., 2009], as discussed in Chapter 3, while for objects whose A_V was calculated from JHK photometry, those values are overplotted as an orange circle. Objects 2 & 3 have no calculated A_V values. c) Abundance of H_2O, calculated in § 4.3.2. d) Abundance of CO_2, calculated in § 4.3.4. CO_2 present in a H_2O environment is overplotted as orange circles. e) Abundance of CO, calculated in § 4.3.3. CO present in a H_2O environment (CO_{rc}) is overplotted as orange circles. Objects 7 & 12 have no CO ice.

4.5 Ice mapping

Of the 16 FoVs that yielded ice spectra (see Figure 3.1), only four contained three or more objects. For these FoVs, maps of the calculated ice column densities were constructed, and are presented in Figure 4.18. The maps of BHR 59 and DC 300.7-01.0 contain only background star observations, and so are likely to trace only quiescent regions, while the maps of B 35A and DC 274.2-00.4 include data from embedded objects. The two closest objects which could be resolved by ARF are Objects 17 & 18, as mentioned in Chapter 3. As DC 300.7-01.0 lies at a distance of 175 parsecs [Lee & Myers, 1999], the resolution between these objects represents $\sim$ 650 AU, and thus the map probes chemistry over very small spatial distributions.

The original AKARI FoVs are shown in Figure 4.18a. Figure 4.18b shows A_V plotted as bubble plots. In black are the A_V values from the c2d catalogues (see Chapter 3), while overplotted in orange for background stars are A_V values calculated from JHK photometry, as discussed in Chapter 3. For the objects with both A_V values plotted, there is very good agreement between the c2d and JHK values, providing further evidence for the validity of the Nextgen baseline fitting and dereddening method employed in ARF. Objects 2 & 3 have no calculated A_V values in the c2d catalogues, but based on gas phase observations of this cloud, it is estimated that the values will be roughly equivalent to the other two objects in the FoV [Craigon et al., *in preparation*].

Ice maps are shown in Figure 4.18c,d & e. H_2O ice maps (Figure 4.18c) show H_2O abundances closely related to A_V, as in Figure 4.10. The ice maps are, however, testing the spread in the 1D correlation plot of Figure 4.10. This agrees well with previous studies [Whittet et al., 1988] that A_V and N(H_2O) are closely correlated. Although the relationship is consistent within the clouds, it is not possible to predict the abundance of H_2O, given the A_V, nor vice-versa. For example, in DC 300.7-01.0, the A_V is relatively constant towards all lines of sight, but the H_2O abundance varies over a small scale. Thus, there must be other physical and astronomical influences to consider in the formation and distribution of ice in clouds, and ice mapping provides a powerful tool for investigating them. The information in an ice map illustrates the link between chemical reagents and products on a spatial scale, and CO_2 and CO are a good

test of this.

In Figure 4.18d, the CO_2 ice maps show a general agreement with the H_2O ice maps. This is unsurprising, as Figures 4.10 and 4.14 have already established the existence of a correlation between the abundances of H_2O and CO_2 in interstellar ices. A notable exception to this pattern is Object 8, where the CO_2 abundance appears to be high in relation to that of H_2O. However, as this spectrum is an upper limit, it is not possible to conclude anything from this abberation. It is possible that the H_2O band for this object has been slightly underfitted due to its non-standard profile (as seen in Figure 4.1a). Anomalies such as this will become less important on a larger scale ice map, as discussed in Chapter 8.

CO ice maps are shown in Figure 4.18e and are in general agreement with both the A_V and H_2O maps. All of the lines of sight are above the critical extinction threshold for CO freeze-out, and so CO abundances are expected to be approximately 20 – 30 % H_2O [Chiar et al., 1995; Boogert & Ehrenfreund, 2004]. Towards Objects 7 and 12 there is no CO ice, but this is a reasonable result when the spectra in Figures 3.3a – 3.3b are considered. There is little or no CO peak visible in these spectra, suggesting that, within the detector limits, there is no CO ice towards these lines of sight. A potential explanation for this is that heating in these isolated regions has caused CO to desorb into the gas phase. To more fully probe these regions, combined mapping of the solid and gas phase would be useful. This is one of the long term aims of ice mapping, and is discussed in Chapter 8.

When considering the component analysis of CO_2 and CO, it is interesting to note that in the mapped components of each, there is no obvious pattern in any of the fields of view. For example, towards B 35A, the CO_2 towards Object 3 is entirely in a H_2O-rich ice (the H_2O-rich component being denoted by the orange dotted line overplotted on the maps), the CO_2 towards Objects 2 and 5 is roughly equally divided between H_2O-rich and CO-rich environments, while towards Object 4, the majority is in a CO-rich ice. For CO, Objects 4 and 5 have predominantly CO in a H_2O-rich ice, Object 2 has a large proportion of pure CO, and Object 3 has an even division between the two environments. This suggests that even within a single cloud, the chemistry can be different towards different lines of sight and that making generalisations might not be a

reasonable approach to take. The relationships established by the component analysis comparisons in 1D correlation plots become more complex still when spatial distribution is considered. However, it is important to reiterate that, given the limitation in data quality achieved with AKARI, local variations in abundances are not necessarily indicative of localised chemistry in the clouds observed.

If it is assumed, as was proposed in § 4.4, that some CO_2 formation occurs at early times, concurrent with H_2O, it would be reasonable to assume that some CO_2 in a H_2O-rich component would be visible towards all lines of sight. The component analysis in Figure 4.18d shows that no CO_2 in H_2O is observed towards Objects 6, 16 & 18. This is probably a limitation of the detection method, with very small abundances of CO_2 present in these lines of sight, but requires observations at higher sensitivity and resolution for clarification. As was discussed earlier, most of the CO_2 in a H_2O-rich environment is likely formed at later times, so correlation should be seen between CO_{rc} and CO_2 in H_2O. This is generally the case in B 35A and BHR 59, but there are anomalies. For example, Objects 7 & 12, which have no CO ice have almost all of their CO_2 ice in a H_2O-rich phase. This could suggest that all of the CO has desorbed or has reacted to form CO_2 in the H_2O-rich ice, as seen in the ice models of Pontoppidan et al. [2003a, 2008]. This could be evidence of heating and UV processing, or older objects.

Considering minor components which are not mapped here, Objects 4, 7, 8 & 12 were all found to have OCN^-, which is a tracer of UV or temperature processing. This corresponds well to the assertions made about the non-detection of CO towards Objects 7 & 12. Object 4 has the highest (calculated) A_V of any of the mapped objects, and thus is the most highly embedded. It may be that the observations are more sensitive to OCN^- at higher extinctions. Objects 7 & 8 have low CO and OCN^- detections, which could suggest that this region of DC 274.2-00.4 is heated. None of the objects mapped have CH_3OH identified in their spectra.

There is some evidence of the presence of CO_{gg} towards all clouds, but not towards all lines of sight. As CO_{gg} is believed to be a component that corresponds to CO interacting directly with dust grain surfaces, it could trace a CO component that can form CO_2 at very early times in a cloud, before there is ac-

cumulation of an icy mantle on grains. In B 35A, Objects 2, 3 & 4 all have CO_{gg} components, and it is also present towards Objects 6, 13, 18 & 19. As this is a mixture of background stars and YSOs, with varying extinctions, a correlating factor is not immediately evident. Further observations could provide more insight into this issue.

HDO was potentially identified along the lines of sight towards Objects 2 & 4. As the B 35A FoV has relatively high A_V, and deuteration is linked to density [Millar, 2005], this could support the identification of this feature. There is some evidence from gas phase observations that in the region of Objects 2 & 3 there is high turbulence, and potentially shocks, from a stellar jet [Craigon et al., *in preparation*], which again could indicate a region where deuteration was more likely. Potentially, HDO is forming in the gas phase and has frozen out into the solid phase along the lines of sight towards Objects 2 & 4. This region of B 35A is a good candidate for further gas phase studies using Herschel or ALMA, due to the potentially interesting solid and gas phase chemistry identified there.

All of the ice mapping presented here illustrates the potential complexity of ice chemistry when considering spatial distribution. It has been suggested that chemistry in interstellar regions could be very local, changing even from object to object within one cloud. Further observations utilising higher resolution spectrometry will be required to validate and measure these local variations.

One of the original aims of this ice mapping was to compare it to gas phase mapping of the same clouds, and investigate the relationships between the solid phase and gas density, temperature, chemistry, and astrophysics. At present, very tentative attempts have been made, as further discussed in Chapter 8, but Figure 4.19 presents plots of *Spitzer* c2d data for comparison with the AKARI data. In Figure 4.19b,c,d & e, the object positions are those of the original c2d catalogue, before shifting was performed. See § 3.5.3 for details of the shifts. The astrometry of AKARI does not precisely match that of *Spitzer*, and the discrepancies in the object positions highlight the distortion in AKARI.

Figure 4.19b is A_V plotted as bubble plots, as in Figure 4.18b, but with contour maps of A_V provided by c2d [Klaus Pontoppidan, *private communication*]. The objects in BHR 59 and DC300.7-01.0 are seen to be located towards the most

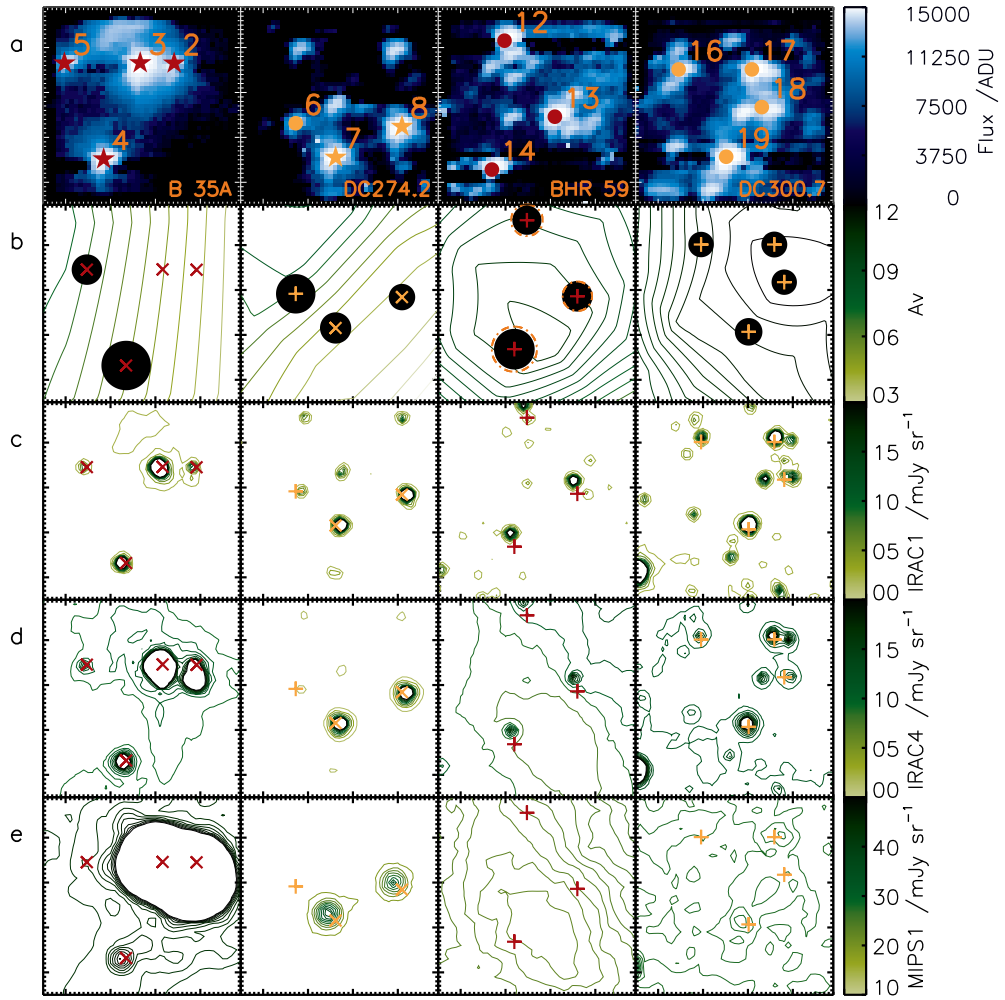

Figure 4.19. Contour maps of *Spitzer* c2d data. In b – e, the object positions reflect the original c2d catalogue positions, before shifting in ARF (see § 3.5.4 for details). The maps presented are as follows: a) Imaging frame from AKARI, as in Figure 4.18a. b) Black circles as in Figure 4.18b. Contours are A_V maps produced by the c2d team [Klaus Pontoppidan, *private communication*]. c) Map of the FoVs in the IRAC 1 photometric band at 3.6 μm. d) Map of the FoVs in the IRAC 4 photometric band at 8.0 μm. e) Map of the FoVs in the MIPS 1 photometric band at 24 μm [Evans et al., 2009].

extincted regions of their molecular clouds, whilst for B 35A and DC274.2-00.4, they are not. Visual extinction is correlated to the dust abundance in the cloud, suggesting that objects in BHR 59 and DC 300.7-01.0 are located in the most dense regions of the clouds.

Figure 4.19c,d & e shows contoured data from three *Spitzer* photometric bands:

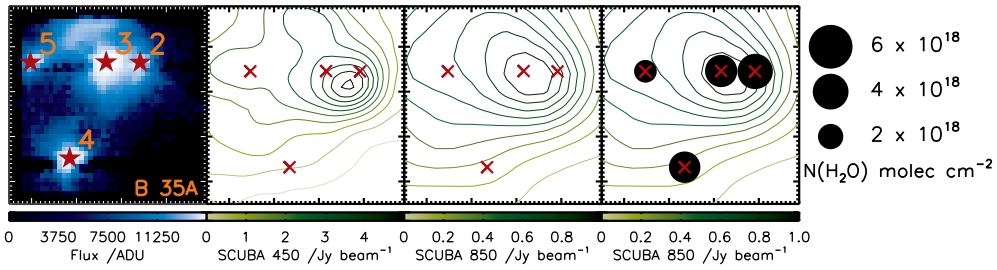

Figure 4.20. SCUBA maps of B 35A at 450 and 850 μm. In the final plot, the calculated H_2O abundances are overplotted as circles, as in Figure 4.18c. [Di Francesco et al., 2008].

IRAC 1 (3.6 μm), IRAC 4 (8.0 μm) and MIPS 1 (24 μm). In Figure 4.19c & d, the individual objects are clearly visible in the contour plots. In Figure 4.19e, however, objects in BHR 59 and DC 300.7-01.0 are no longer individually defined. In B 35A, the emission from Objects 2 and 3 coalesces and is very intense, supporting gas phase observations that suggest stellar activity in this region [Craigon et al., *in preparation*]. In the BHR 59 and DC300.7-01.0 clouds, there are no strong features in the 24 μm map, indicating that there are no YSOs forming in these regions, and reinforcing the designation of all objects in these fields of view as background stars. This is also the case for the only other background star, Object 6.

The Submillimetre Common-User Bolometer Array (SCUBA) continuum detector on the James Clerk Maxwell Telescope (JCMT) measures in the submillimetre region of the electromagnetic spectrum, where it is sensitive to thermal emission from interstellar dust. Thus, observations with SCUBA map the dusty component of a molecular cloud. SCUBA maps of B 35A at 450 and 850 μm are shown in Figure 4.20, but were not available for the other ice mapped clouds. It is clear from these maps that the dust in the core of B 35A is centred around Objects 2 and 3, explaining the high abundances of H_2O, CO_2 and CO ice present towards these objects, as seen in Figure 4.18c,d & e. There is, however, a discrepancy in the CO_2 abundance towards Object 4, which is very high, disproportionately so compared to the dust abundance in this part of the cloud. However, in Figure 4.18b, it is clear that the calculated A_V is high towards Object 4, another indication of a high dust abundance. Overall, the SCUBA maps reinforce that the presence of more dust in a line of sight does not always indicate that there is more ice, and that both dust density and gas

density must be considered to ascertain ice growth mechanisms. Importantly, the abundance of ices can not be calculated by a simple relationship between dust and ice.

4.6 Conclusions

In this chapter, the 2.5 – 5 μm spectra of 22 background stars and eight YSOs have been analysed to determine the abundances of key solid phase molecular species towards those lines of sight, with the aim of determining whether or not solid phase molecular species can be used as tracers of chemistry in molecular clouds. Prior to this study, only one spectrum of a background star had been obtained in this wavelength region, a region containing absorption bands for the three most abundant molecules present in interstellar ice. Thus, the addition of 22 spectra towards background stars to the literature provides valuable data to the community, which could help to benchmark the initial conditions in star-forming regions.

Both CO_2 and H_2O were found to be ubiquitous where ice was observed. CO_2 abundances were found to be low compared to literature values. This is likely due to the saturation of the CO_2 absorption band at the relatively low resolution of the AKARI grism disperser, which was not accounted for during fitting due to the small number of datapoints for the fit. CO abundances were calculated towards 23 lines of sight, the CO absorption band not being extracted towards the other seven lines of sight. CO abundances were found to be in good agreement with previous studies.

The analysis of this large sample of data by a rigorous, single-fit approach reinforces the argument that this type of approach is possible for large datasets (as previously shown by the analysis of *Spitzer* data by the c2d team [e.g. Pontoppidan et al., 2008; Boogert et al., 2008; Öberg et al., 2008]). It is not necessary to employ a mix and match approach using multiple laboratory spectra in order to well define the ice characteristics of a wide range of objects.

One line of sight observed with AKARI potentially probes CO frozen on the dust grain surface below the critical A_V for CO freeze-out. If verified, this could suggest CO ice formation occurring closer to that of H_2O and CO_2 than

is generally believed. In this study, only one object was observed to have CO ice below A_V critical, therefore future observations are required to test the limitations of detection of ice species. However, if CO can be frozen on grain surfaces at low A_V, this could indicate an early formation route for CO_2 formation, as discussed in Chapter 7. Where ice is seen on the grain surface, H_2O and CO_2 abundances increase linearly with A_V, but CO freeze-out depends on more complex physical factors that require 2D mapping and the combination of gas phase and solid phase observations to resolve.

The chemical information extracted by a component analysis method can provide interesting 1D correlations. By considering the abundances of CO and CO_2 in different ice components, it is possible to postulate a CO_2 formation scenario involving two or three distinct stages. The proposed timeline is: early formation concurrent with H_2O; late formation by energetic routes when CO has frozen out and migrated into an H_2O environment; and the formation of CO_2 in the CO layer at an uncertain time, and by uncertain mechanisms. Future CO_2 formation experiments are required to address this, and some discussion of this is made in Chapter 8. The early formation route to CO_2 is studied experimentally in Chapter 7, and also provided a motivation for studying the sub-monolayer characteristics of molecules on surfaces, as presented in Chapter 6.

Observed towards some lines of sight were the minor species CH_3OH, $^{13}CO_2$, OCN^-, CO_{gg} and, tentatively, HDO. That these species were observed, even as upper limits, illustrates the fact that the NG disperser provided more detailed spectra than expected based upon its resolving power. The initial aim of the study was only to map the relative abundances of H_2O, CO_2, and CO.

Ice mapping probes the spread of 1D correlation plots, investigating the relationships between molecular species on a spatial scale. The ice mapping presented in this chapter, probing resolutions as low as 650 AU, has suggested that, even for the most abundant molecular species in a small FoV, the trends between species are not necessarily constant, nor predictable. The local environment could have a large effect on ice abundance, composition and growth. Even the individual components of a species potentially vary across a cloud. In order to use solid phase molecular species as probes of ice and gas chemistry, it will be necessary to make many more observations of both solid phase

species, and also gas phase molecules, as well as deriving temperature and pressure data from gas phase observations. Ice mapping is a powerful tool, but it is not as trivial, observationally, as gas phase mapping; ideally, linking both mapping techniques will yield more answers, and this is discussed in Chapter 8.

Having discussed the use of laboratory spectra in the analysis of observational data, and the importance of combining observations with detailed laboratory studies under controlled conditions, the second part of this thesis details experiments performed on simple interstellar relevant molecules.

References

Aikawa, Y., Ohashi, N., Inutsuka, S.-i., Herbst, E., & Takakuwa, S. 2001, ApJ, 552, 639

Aikawa, Y., et al. 2009, AKARI, a Light to Illuminate the Misty Universe, 418, 47

Alexander, R. D., Casali, M. M., André, P., Persi, P., & Eiroa, C. 2003, A&A, 401, 613

Allamandola, L. J., Sandford, S. A., Tielens, A. G. G. M., & Herbst, T. M. 1992, ApJ, 399, 134

Bergin, E. A., Melnick, G. J., Gerakines, P. A., Neufeld, D. A., & Whittet, D. C. B. 2005, ApJL, 627, L33

Bohren, C. F., Huffman D. R., 1983, Absorption and Scattering of Light by Small Particles. John Wiley & Sons, New York, Ch. 5

Boogert, A. C. A., et al. 2000, A&A, 353, 349

Boogert, A. C. A., Blake, G. A., & Tielens, A. G. G. M. 2002, ApJ, 577, 271

Boogert, A. C. A., & Ehrenfreund, P. 2004, Astrophysics of Dust, 309, 547

Boogert, A. C. A., et al. 2008, ApJ, 678, 985

Boogert, A. C. A., et al. 2011, ApJ, 729, 92

Bottinelli, S., et al. 2010, ApJ, 718, 1100

Brooke, T. Y., Sellgren, K., & Geballe, T. R. 1999, ApJ, 517, 883

Chiar, J. E., Adamson, A. J., Kerr, T. H., & Whittet, D. C. B. 1995, ApJ, 455, 234

Chiar, J. E., et al. 2011, ApJ, 731, 9

Collings, M. P., Dever, J. W., Fraser, H. J., McCoustra, M. R. S., & Williams, D. A. 2003, ApJ, 583, 1058

Cottin, H., Moore, M. H., & Bénilan, Y. 2003, ApJ, 590, 874

Creech-Eakman, M. J., Chiang, E. I., Joung, R. M. K., Blake, G. A., & van Dishoeck, E. F. 2002, A&A, 385, 546

Cruikshank, D. P., Burgdorf, M. J., Nakamura, R., Sekiguchi, T., & Orton, G. S. 2009, Bulletin of the American Astronomical Society, 41, 562

Cuppen, H. M., van Dishoeck, E. F., Herbst, E., & Tielens, A. G. G. M. 2009, A&A, 508, 275

Dartois, E., Thi, W.-F., Geballe, T. R., Deboffle, D., d'Hendecourt, L., & van Dishoeck, E. 2003, A&A, 399, 1009

de Graauw, T., et al. 1996, A&A, 315, L345

Di Francesco, J., Johnstone, D., Kirk, H., MacKenzie, T., & Ledwosinska, E. 2008, ApJS, 175, 277

Dulieu, F., Amiaud, L., Congiu, E., Fillion, J.-H., Matar, E., Momeni, A., Pirronello, V., & Lemaire, J. L. 2010, A&A, 512, A30

Ehrenfreund, P., Boogert, A. C. A., Gerakines, P. A., Jansen, D. J., Schutte, W. A., Tielens, A. G. G. M., & van Dishoeck, E. F. 1996, A&A, 315, L341

Ehrenfreund, P., Boogert, A. C. A., Gerakines, P. A., Tielens, A. G. G. M., & van Dishoeck, E. F. 1997, A&A, 328, 649

Eiroa, C., & Hodapp, K.-W. 1989, A&A, 210, 345

Evans, N. J., II, et al. 2003, PASP, 115, 965

Evans, N. J., et al. 2009, VizieR Online Data Catalog, 218, 10321

Fraser, H. J., & van Dishoeck, E. F. 2004, Advances in Space Research, 33, 14

Fraser, H. J., Bisschop, S. E., Pontoppidan, K. M., Tielens, A. G. G. M., & van Dishoeck, E. F. 2005, MNRAS, 356, 1283

Fuchs, G. W., Cuppen, H. M., Ioppolo, S., Romanzin, C., Bisschop, S. E., Andersson, S., van Dishoeck, E. F., & Linnartz, H. 2009, A&A, 505, 629

Gerakines, P. A., Schutte, W. A., Greenberg, J. M., & van Dishoeck, E. F. 1995, A&A, 296, 810

Gerakines, P. A., Schutte, W. A., & Ehrenfreund, P. 1996, A&A, 312, 289

Gerakines, P. A., et al. 1999, ApJ, 522, 357

Gibb, E. L., Whittet, D. C. B., Boogert, A. C. A. & Tielens, A. G. G. M. 2004, ApJS, 151, 35

Goumans, T. P. M., Uppal, M. A., & Brown, W. A. 2008, MNRAS, 384, 1158

Guertler, J., Henning, T., Koempe, C., Pfau, W., Kraetschmer, W., & Lemke, D. 1996, A&A, 315, L189

Hagen, W., Allamandola, L. J., & Greenberg, J. M. 1980, A&A, 86, L3

Hudgins, D. M., Sandford, S. A., Allamandola, L. J., & Tielens, A. G. G. M. 1993, ApJS, 86, 713

Ioppolo, S., Cuppen, H. M., Romanzin, C., van Dishoeck, E. F., & Linnartz, H. 2008, ApJ, 686, 1474

Ioppolo, S., van Boheemen, Y., Cuppen, H. M., van Dishoeck, E. F., & Linnartz, H. 2011, MNRAS, 413, 2281

Itoh, Y., Tamura, M., & Gatley, I. 1996, ApJL, 465, L129

Jamieson, C. S., Mebel, A. M., & Kaiser, R. I. 2006, ApJS, 163, 184

Kerkhof, O., Schutte, W. A., & Ehrenfreund, P. 1999, A&A, 346, 990

Knez, C., et al. 2005, ApJL, 635, L145

Landsman, W. B. 1993, Astronomical Data Analysis Software and Systems II, 52, 246

Lee, C. W., & Myers, P. C. 1999, ApJS, 123, 233

Leger, A., Klein, J., de Cheveigne, S., Guinet, C., Defourneau, D., & Belin, M. 1979, A&A, 79, 256

Markwardt, C. B. 2009, Astronomical Society of the Pacific Conference Series, 411, 251

Mennella, V., Palumbo, M. E., & Baratta, G. A. 2004, ApJ, 615, 1073

Mennella, V., Baratta, G. A., Palumbo, M. E., & Bergin, E. A. 2006, ApJ, 643, 923

Millar, T. J. 2005, Astronomy and Geophysics, 46, 020000

Miyauchi, N., Hidaka, H., Chigai, T., Nagaoka, A., Watanabe, N., & Kouchi, A. 2008, Chemical Physics Letters, 456, 27

Murakawa, K., Tamura, M., & Nagata, T. 2000, ApJS, 128, 603

Noble, J. A., Aikawa, Y., Fraser, H. J., Pontoppidan, K. M., & Sakon, I. 2009, AKARI, a Light to Illuminate the Misty Universe, 418, 411

Noble, J. A., Fraser, H. J., Pontoppidan, K. M., Aikawa, Y., & Sakon, I. 2010, Highlights of Astronomy, 15, 730

Noble, J. A., Dulieu, F., Congiu, E., & Fraser, H. J. 2011, ApJ, 735, 121

Nummelin, A., Whittet, D. C. B., Gibb, E. L., Gerakines, P. A., & Chiar, J. E. 2001, ApJ, 558, 185

Oba, Y., Watanabe, N., Kouchi, A., Hama, T., & Pirronello, V. 2010, ApJL, 712, L174

Öberg, K. I., Boogert, A. C. A., Pontoppidan, K. M., Blake, G. A., Evans, N. J., Lahuis, F., & van Dishoeck, E. F. 2008, ApJ, 678, 1032

Ohyama, Y., et al. 2007, PASJ, 59, 411

Oliveira, J. M., et al. 2011, MNRAS, 411, L36

Onaka, T., et al. 2007, PASJ, 59, 401

Onaka, T., Sakon, I., Ohsawa, R., Shimonishi, T., Okada, Y., Tanaka, M., & Kaneda, H. 2011, EAS Publications Series, 46, 55

Palumbo, M. E., Baratta, G. A., Brucato, J. R., Castorina, A. C., Satorre, M. A., & Strazzulla, G. 1998, A&A, 334, 247

Parise, B., Simon, T., Caux, E., Dartois, E., Ceccarelli, C., Rayner, J., & Tielens, A. G. G. M. 2003, A&A, 410, 897

Parise, B., et al. 2005, A&A, 431, 547

Pontoppidan, K. M. 2006, A&A, 453, L47

Pontoppidan, K. M., et al. 2003, A&A, 408, 981

Pontoppidan, K. M., Dartois, E., van Dishoeck, E. F., Thi, W.-F., & d'Hendecourt, L. 2003, A&A, 404, L17

Pontoppidan, K. M., van Dishoeck, E. F., & Dartois, E. 2004, A&A, 426, 925

Pontoppidan, K. M. 2006, A&A, 453, L47

Pontoppidan, K. M., et al. 2008, ApJ, 678, 1005

Roser, J. E., Vidali, G., Manicò, G., & Pirronello, V. 2001, ApJL, 555, L61

Sandford, S. A., Bernstein, M. P., Allamandola, L. J., Goorvitch, D., & Teixeira, T. C. V. S. 2001, ApJ, 548, 836

Schegerer, A. A., & Wolf, S. 2010, A&A, 517, A87

Shenoy, S. S., Whittet, D. C. B., Ives, J. A., & Watson, D. M. 2008, ApJS, 176, 457

Shimonishi, T., Onaka, T., Kato, D., Sakon, I., Ita, Y., Kawamura, A., & Kaneda, H. 2008, ApJL, 686, L99

Shimonishi, T., Onaka, T., Kato, D., Sakon, I., Ita, Y., Kawamura, A., & Kaneda, H. 2010, A&A, 514, A12

Tanaka, M., Sato, S., Nagata, T., & Yamamoto, T. 1990, ApJ, 352, 724

Teixeira, T. C., Devlin, J. P., Buch, V., & Emerson, J. P. 1999, A&A, 347, L19

Thi, W.-F., van Dishoeck, E. F., Dartois, E., Pontoppidan, K. M., Schutte, W. A., Ehrenfreund, P., D'Hendecourt, L., & Fraser, H. J. 2006, A&A, 449, 251

Tielens, A. G. G. M., & Hagen, W. 1982, A&A, 114, 245

Tielens, A. G. G. M., Tokunaga, A. T., Geballe, T. R., & Baas, F. 1991, ApJ, 381, 181

Watanabe, N., Nagaoka, A., Shiraki, T., & Kouchi, A. 2004, ApJ, 616, 638

Weingartner, J. C., & Draine, B. T. 2001, ApJ, 548, 296

Whittet, D. C. B., Bode, M. F., Baines, D. W. T., Longmore, A. J., & Evans, A. 1983, Nature, 303, 218

Whittet, D. C. B., McFadzean, A. D., & Longmore, A. J. 1985, MNRAS, 216, 45P

Whittet, D. C. B., Bode, M. F., Longmore, A. J., Adamson, A. J., McFadzean, A. D., Aitken, D. K., & Roche, P. F. 1988, MNRAS, 233, 321

Whittet, D. C. B., Adamson, A. J., Duley, W. W., Geballe, T. R., & McFadzean, A. D. 1989, MNRAS, 241, 707

Whittet, D. C. B., & Duley, W. W. 1991, A&A Rev., 2, 167

Whittet, D. C. B., et al. 1998, ApJL, 498, L159

Whittet, D. C. B., Pendleton, Y. J., Gibb, E. L., Boogert, A. C. A., Chiar, J. E., & Nummelin, A. 2001, ApJ, 550, 793

Whittet, D. C. B., Shenoy, S. S., Bergin, E. A., Chiar, J. E., Gerakines, P. A., Gibb, E. L., Melnick, G. J., & Neufeld, D. A. 2007, ApJ, 655, 332

Whittet, D. C. B., Cook, A. M., Chiar, J. E., Pendleton, Y. J., Shenoy, S. S., & Gerakines, P. A. 2009, ApJ, 695, 94

van Broekhuizen, F. A., Keane, J. V., & Schutte, W. A. 2004, A&A, 415, 425

van Broekhuizen, F. A., Pontoppidan, K. M., Fraser, H. J., & van Dishoeck, E. F. 2005, A&A, 441, 249

van Dishoeck, E. F., et al. 1996, A&A, 315, L349

van Kempen, T. A., et al. 2009, A&A, 501, 633

Zasowski, G., Kemper, F., Watson, D. M., Furlan, E., Bohac, C. J., Hull, C., & Green, J. D. 2009, ApJ, 694, 459

CHAPTER 5

THE FORMOLISM EXPERIMENT

5.1 Synopsis

In this chapter, the FORMOLISM laboratory experiment will be introduced. This setup is composed of a main chamber held under ultra-high vacuum, within which is a cryogenically cooled silicate surface upon which reactions are performed. Reactions are monitored by the use of temperature programmed desorption spectroscopy. This chapter describes the technical aspects of FORMOLISM, including its constituent parts and its utilisation. The experiment is designed to emulate, as far as possible, the physical and chemical conditions in the ISM, and to allow the investigation of key reactions and reagent processes in a controlled, reproducible manner.

5.2 FORMOLISM

The FORMOLISM (FORMation of MOLecules in the InterStellar Medium) experiment was designed to study the interaction and reactions of atomic and molecular species under simulated interstellar conditions of temperature and pressure. The instrument (see Figure 5.1) is composed of a stainless steel chamber held under ultra-high vacuum (UHV, $< 10^{-10}$ mbar), in the centre of which is mounted a copper sample, covered with an amorphous silicate film. The sample temperature can be controlled in the range 5.5 – 350 K by the cold fin-

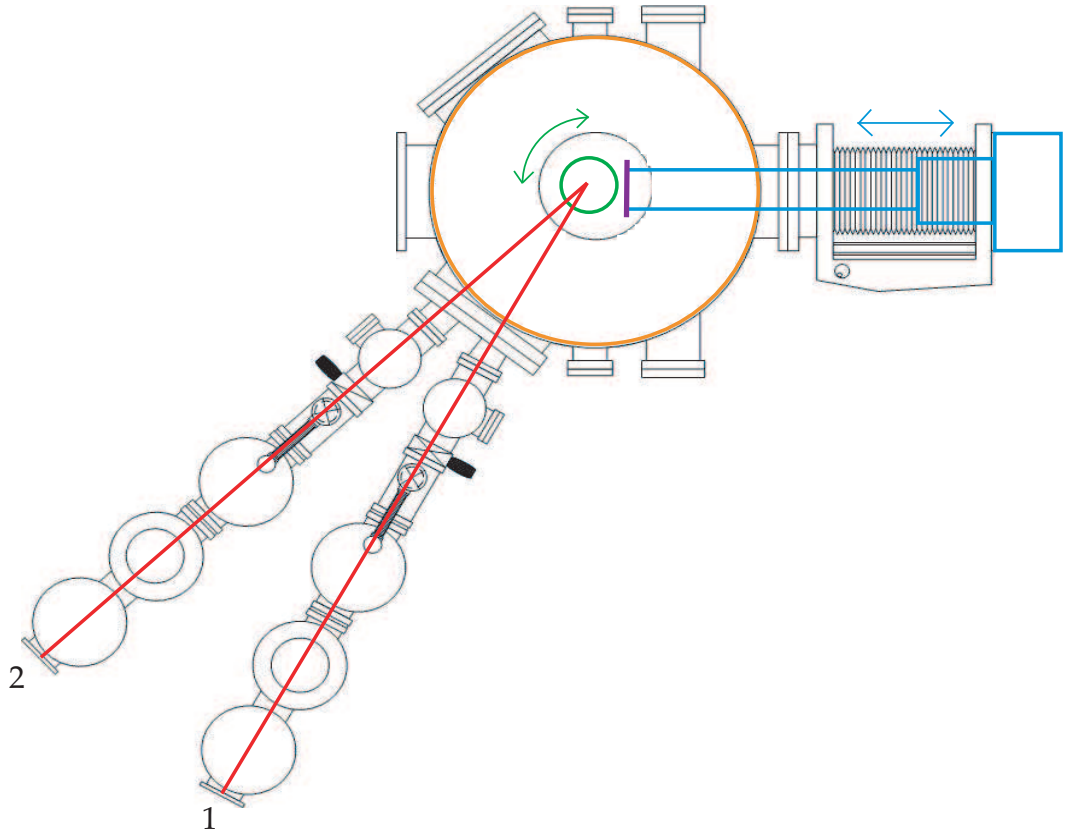

Figure 5.1. A 2D schematic of the FORMOLISM experiment, as viewed from above. The main chamber is highlighted in orange, the cryostat in blue, the surface in purple, the main axes of molecular beams 1 & 2 in red, and the position of the QMS (which is installed in the top of the chamber, along the axis normal to the page) marked in green. The surface can be moved along the axis of the cold finger (in the direction left/right on this schematic, marked in blue) so that it is positioned in line with the molecular beam lines during deposition or in front of the QMS during desorption experiments. The QMS is raised upwards during movement of the surface to prevent collision. The QMS can rotate 360 ° around the axis normal to the page (shown in green) so that it faces the beams or the surface.

ger of a closed-cycle He cryostat and heater mechanism. Atomic and molecular gases are introduced into the chamber via two beam lines directed towards the silicate surface. Species are detected in the gas phase via a quadrupole mass spectrometer (QMS).

5.2.1 The main chamber

The main chamber, illustrated in Figure 5.1, is a non-magnetic stainless steel cylinder, 120 cm tall, with a diameter of 30 cm, built by MECA2000. A molecular turbo pump with pumping speed 1000 l s^{-1}, a titanium sublimation pump, and an ionic pump maintain UHV in the chamber, at a base pressure of $< 10^{-10}$ mbar.

A pressure of $\sim 10^{-10}$ mbar represents a density of $\sim 10^6$ cm^{-3}; at 300 K this corresponds mainly to H_2, as the pollutants CO_2 and H_2O are efficiently pumped out of the chamber. This density remains significantly higher than those typical of the ISM, where estimates suggest values of $\sim 10^4$ cm^{-3} in dense molecular cores [Williams & Herbst, 2002]. The reason for working under conditions of UHV is thus not strictly to model interstellar conditions, but rather to minimise the presence of pollutant species in the chamber and thus prevent contamination of the surface by the adsorption of residual molecules from the gas phase. At a pressure of 10^{-10} mbar, it takes just over two and a half hours for a dynamic monolayer of H_2 to form on the surface (assuming a surface density of sites $\sim 10^{15}$ cm^{-2}, a collision rate of $\sim 10^{11}$ molec cm^{-2} s^{-1} [Woodruff & Delchar, 1994], and unity sticking). This allows time to perform experiments on a surface which is clean and well characterised, with only a few per cent of a monolayer contamination per hour.

The vacuum quality is limited by the constant desorption of species previously adsorbed to, in particular, the chamber walls and the cold finger. This degassing rate is of the order 5×10^{-10} mbar l s^{-1} cm^{-2} [Baouche, 2004], limited by the pumping rate. In order to maintain UHV following periods of prolonged experimentation, or reattain UHV after the chamber is opened for maintenance (when the minimum pressure obtainable using the molecular turbo pump is of the order 10^{-9} mbar), baking of the chamber is performed. Baking consists of heating the chamber in order to increase temporarily the degassing rate and eliminate the majority of the adsorbed pollutants (i.e. H_2O), thus lowering the base pressure. Heating wires are attached to the chamber, which is then covered in aluminium foil. The chamber is heated gradually over two days, under the control of a Labview program, up to a maximum temperature of ~ 350 K, with lower maxima specified for fragile sections such

as windows. After three days at this temperature, heating is stopped and the chamber temperature equilibrates with that of the laboratory over a further two days, the base pressure returning to 10^{-10} mbar.

5.2.2 The surface

5.2.2.1 The cryogenic system

The temperature of the experimental surface is controlled by a cryocooler, as illustrated in Figure 5.2. The sample is an OFHC (Oxygen-Free High Conductivity) polished copper cylinder, mounted on an 800 K cryostat interface containing a ruby crystal which acts as a thermal switch, allowing the sample to be heated to up to 800 K (although in practise, it is not heated above 350 K due to the risk of damage to the amorphous silicate film, the silicon diode serving as temperature sensor, or mechanical elements of the cryostat). A thin layer of indium foil between the sample and the interface ensures good thermal conductivity. The interface is mounted on the second stage of the cryostat, and this whole region is thermally isolated from the environment by a thermal shield. The protective cover consists of a nickel-coated copper cylinder (by Arscryo) with a homemade ring of copper (internal) and stainless steel (external surface) surrounding the copper sample; the whole assemblage is attached to the first stage of the cryostat.

The cryostat is an Arscryo DE204 with a base temperature of 4.2 K, working on the principal of gaseous helium circulation and attached to an APD HC-4 compressor. Transfer of thermal energy is induced by the mechanical action of a piston (the compression-relaxation cycle follows the Gifford-McMahon principal [Gifford & McMahon, 1959]), with a typical cooling power of 0.4 W at 10 K. Two stages of the cryostat, mentioned above, are under UHV, and the whole cryocooler is mounted on a translation stage, allowing translation of the surface in and out of the main chamber, respectively in the same plane as, and perpendicular to, the molecular beams and the QMS.

Three different sensors are used to measure the temperatures in different parts of the cryocooler: a KP-type thermocouple (Au 0.07 %-Fe/Chromel) attached to the sample, along with a silicon diode (DT 470); a K-type thermocouple

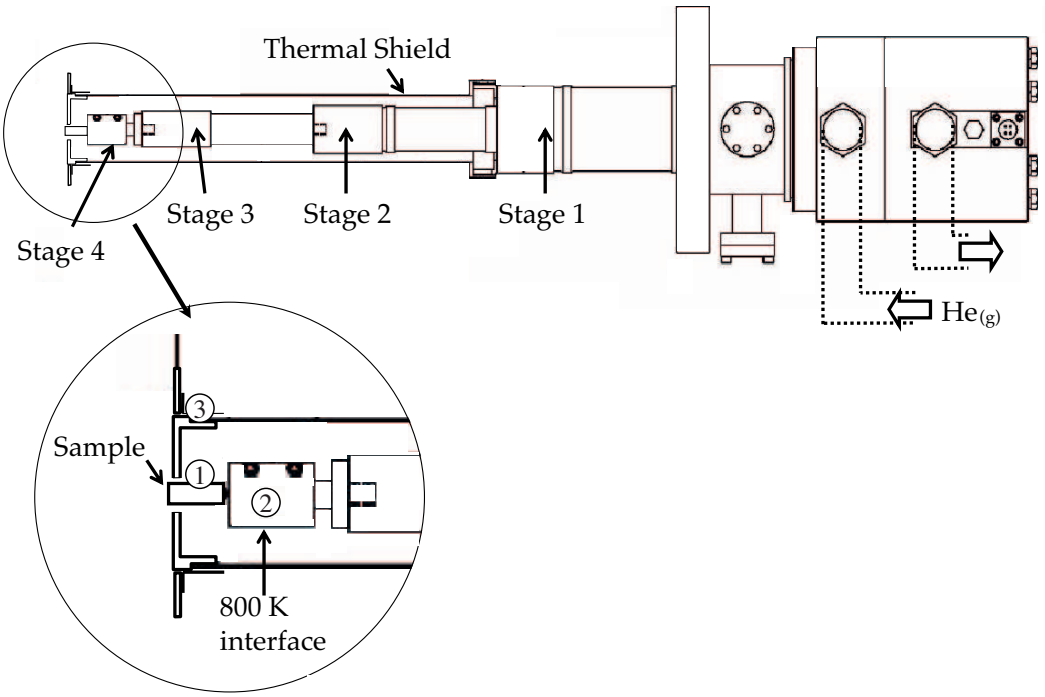

Figure 5.2. A detailed schematic of the cryocooler and surface. Sensor positions are marked as 1) a KP-type thermocouple and a silicon diode, 2) a K-type thermocouple and a heating resistor, and 3) a Pt diode sensor.

(Nickel-Chromium/Nickel-Aluminium) on the 800 K interface; and a platinum sensor attached to the thermal shield (see Figure 5.2). In addition, a heating resistor is attached to the 800 K interface. All four are connected to a Lakeshore 340 temperature controller, with which the temperature of the sample is regulated. A compensating system ensures the correct measurement of the voltage across the thermocouples, while the controller establishes the correspondence between voltage and temperature. Calibration of the sensors is done by measuring the sublimation temperatures of argon and nitrogen [Schlichting & Menzel, 1993]. The Proportional-Integral-Derivative (PID) control mechanism of the Lakeshore temperature controller allows precision tuning of the sample temperature by altering the power of the heating resistor on the 800 K interface, and works by minimising the difference between the current and the desired sample temperature.

The Lakeshore 340 is controlled remotely by a specially designed Labview program which allows the following operations: setting the PID parameters de-

pending upon the temperature range of the sample; regulating heating ramps during cooling or heating of the sample; monitoring and recording the temperatures captured by the sensors during an experiment; regulating the heating power in real time to ensure a linear increase in sample temperature over large temperature ranges.

Although the temperature of the second stage of the cryostat can reach 4.2 K, as discussed above, due to successive losses to the 800 K interface, the thermal shield, and the chamber (because of the open geometry of the cryocooler system), the minimum temperature of the surface is $\sim$ 8 K. This is sufficient to model interstellar chemistry, as molecular clouds are estimated to have temperatures in the region of $\sim$ 10 K [Williams & Herbst, 2002].

5.2.2.2 The silicate surface

The copper sample is gold plated with a final amorphous olivine-type silicate film layer [Lemaire et al., 2010] deposited by thermal evaporation of an olivine sample with bulk composition $Mg_{1.8}Fe_{0.2}SiO_4$. The amorphous nature of the silicate film was confirmed by infrared spectroscopy of a silicate film deposited on a KBr substrate at the same time as the copper sample was coated. The relevance of silicate as a dust grain mimic was addressed previously, in Chapter 1.

5.2.2.3 Growth of water ice substrates

Ice substrates are obtained by the condensation of water vapour onto the silicate surface. The properties of the ice depend upon the incident angle of the water molecules, the temperature of the surface both during deposition, and any changes in temperature experienced after deposition. It is possible to grow water substrates by a slow deposition or 'background' method, resulting in a porous, amorphous ice [Dulieu et al., 2010]. However, in this thesis, only the case of water substrates grown by fast deposition methods – resulting in compact amorphous solid water (ASW) – is considered, as described below.

As discussed in Chapter 1, non-porous ASW (*np*-H_2O) is believed to be a useful mimic of the icy mantle found on interstellar grain surfaces. *np*-H_2O is grown by spraying water vapour from a microchannel array doser directly onto the

surface. The water is demineralised, and is purified by three freeze-thaw cycles before introduction to the experiment from a test tube (water vapour pressure $\sim$ 20 mbar at room temperature) via a Varian low rate leak valve (allowing leak rates down to 10^{-10} mbar). The water diffuses into the chamber via an array of microcapillaries at the end of a stainless steel tube (30 cm long, 4 mm diameter) positioned directly in front of the sample, at a distance of 20 mm. The surface of the microcapillary array is 1 cm in diameter, and is composed of hundreds of water vapour sources delivering the gaseous water to the sample at an angle of 45 $^\circ$ relative to the sample. The diffuser is mounted on a translation stage so, when it is not in use, the diffuser is placed in a high position in order that it does not perturb the electric field of the QMS, collide with it, or impede molecules in the beams from reaching the sample.

Between the doser and the sample, the local pressure is estimated at 10^{-6} mbar, although the pressure in the main chamber is measured at $\sim 10^{-9}$ mbar. The contribution of water molecules to the main chamber pressure is limited because the majority of molecules stick to either the surface or the thermal shield. The sticking probability of H_2O at low temperatures is close to unity [Tielens, 2005], but can vary with angle [Batista et al., 2005]. A deposition of four minutes with a background pressure in the chamber of 2×10^{-9} mbar at the sample held at 120 K results in the deposition of $\sim$ 50 monolayers (ML) of *np*-H_2O. The sample temperature is held at 120 K until the pressure in the main chamber has returned to its base value, before the sample is cooled for experiments to commence. This process is illustrated in Figure 5.3.

A crystalline water ice surface was grown for certain experiments (see Chapter 6 for further details); it is not necessarily used as an ISM mimic, but rather for control experiments. Crystalline H_2O is grown in the same manner as *np*-H_2O, but after deposition the temperature of the sample is raised to crystallise the water. After deposition at 120 K, the sample temperature is flash heated to 140 K at a rate of 50 K min^{-1}, then raised more slowly to 142.5 K at a rate of 10 K min^{-1}. Figure 5.3 illustrates the deposition method for both water ice substrates.

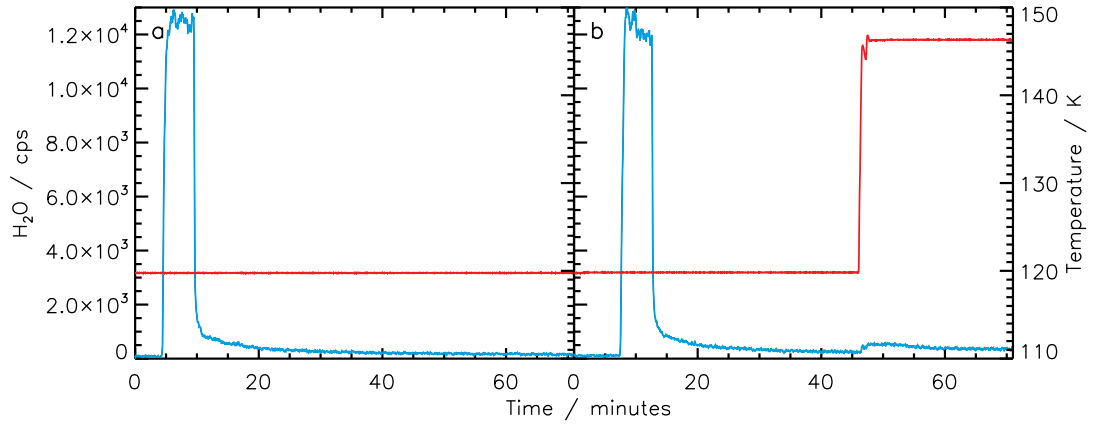

Figure 5.3. Deposition of a) *np*-H_2O and b) crystalline H_2O substrates. The H_2O signal is plotted in blue, while the surface temperature is plotted in red. For *np*-H_2O, H_2O is deposited at 120 K and the temperature is held constant until the background pressure of H_2O returns to the pre-deposition level. For crystalline H_2O, after deposition the surface temperature is increased, as described in the text, to instigate crystallisation.For both substrates, upon stabilisation of the background pressure in the main chamber, the surface temperature is lowered to begin experiments.

5.2.3 The quadrupole mass spectrometer (QMS)

The QMS (Hiden 51/3F) measures the quantity of gas present in the main chamber as a function of atomic or molecular mass (in the range 1 – 50 amu). It is employed in one of two measurement modes, either mass-specific or scanning across a given mass range.

5.2.3.1 Operational principle

The QMS consists of an ion source; ion optics to accelerate and focus the ions; pre-, quadrupole and post filters; and an ion detector with detection electronics. An illustration of the principle of operation of a QMS is shown in Figure 5.4. Molecules and atoms enter the ionisation head of the QMS where they are ionised by electrons emitted by a filament (typically 20 eV, with an adjustable range 10 eV – 200 eV). The ionised species are focussed and accelerated into an initial radio frequency (RF) filter where they are further focussed into the quadrupole mass analyser, a group of four cylindrical electrodes with each opposing pair connected electronically. A combination of dc and ac RF voltages is applied across the system; the applied voltages affect the trajectory

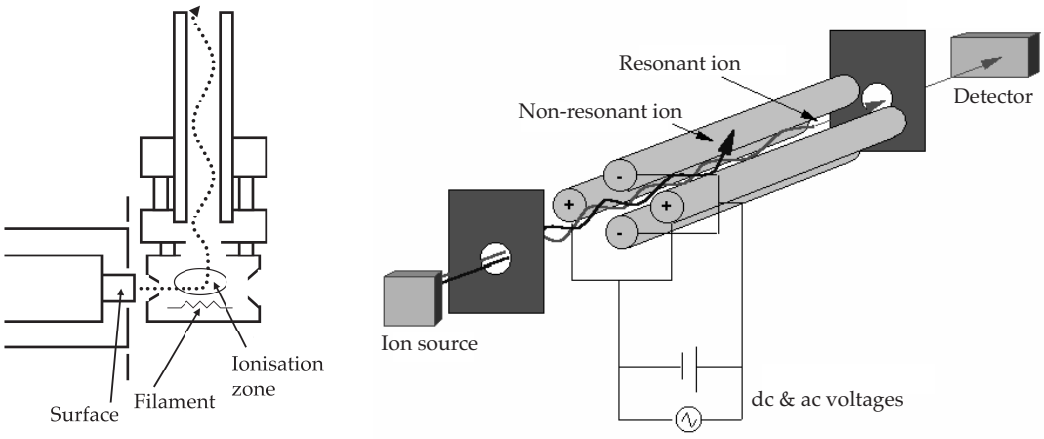

Figure 5.4. On the left, is a diagram of the ionising head of the QMS installed in FORMOLISM, where the dotted line represents a molecule's trajectory from the surface, through the ionisation zone, and towards the detector. On the right, is a schematic of the operational principle of a QMS. Ions produced in the source pass through the quadrupole, where non-resonant ions are ejected. Ions with the selected m/z ratio pass to the detector, where they are quantified. Image adapted from the Chemistry Hypermedia Project at http://www.files.chem.vt.edu/chem-ed/ms/quadrupo.html

of the ions travelling down the centre of the electrodes. For given dc and ac voltages, only ions of a certain mass-to-charge (m/z) ratio pass through the quadrupole filter, while other ions have unstable trajectories and collide with the electrodes. A third RF filter further focusses the selected ions into an ion detector. A mass spectrum is obtained by varying the voltages on the electrodes and monitoring the ions passing through the quadrupole at different m/z with the ion detector. The Channeltron detector, operating at a voltage of 3000 V, creates secondary electronic avalanches following ion impact and allows the detection of partial pressures as low as 10^{-14} Torr. The output current of the Channeltron is converted into a digital signal expressed as the number of counts per second (cps). The detector functions only at pressures lower than 10^{-6} Torr, with a dynamic range of 10^{7} cps, measurement frequency of ~ 4 Hz.

5.2.3.2 Utilisation

The QMS is located in the main chamber and thus is held under UHV, with no differential pumping. It can be rotated through 360 $^{\circ}$ and translated verti-

cally. The QMS is used for three main purposes: in its high position, to analyse residual gas in the main chamber; in its low position, facing either molecular beam, to characterise the chemical nature of the beam, or to aid in its alignment; and in its low position, facing the surface, to measure the desorption of species from the surface during a temperature programmed desorption (TPD).

The head of the QMS is a partially open volume, accessible only via an inflow and an outflow aperture. The dimensions of these apertures are as follows: external hole diameter, 9.7 mm; internal hole diameter, 6.0 mm; aperture angle $\pm$ 12 °. This allows the QMS to sample the entire beam when facing a molecular beam, or to collect all molecules desorbing from the surface during deposition.

The ionising filament in the head degasses when first heated, so the QMS is switched on before experimentation begins and remains on for the duration of the experiment. A degassing procedure which strongly heats the filament can be performed to limit this source of pollution. Other potential sources of pollution include gases released upon translation or rotation of the QMS, translation of the cryocooler or the opening of valves. These signals have a very short lifetime, on the order of hundreds of milliseconds, due to the efficient pumping of the main chamber. During experiments, the signal of the masses under investigation must be corrected for by measuring the background signal of that mass before a TPD is started. During analysis, this value is subtracted from the experimental signal. This is particularly important when recording the masses of typical pollutants such as H_2O, CO or H_2.

The QMS is controlled via a software program provided by Hiden. Technical settings, such as the energy of the ionising electrons and the dwell time for each mass, can be controlled via this interface. It also records both the masses being measured and the temperature of the surface, input from the Lakeshore 340 (§ 5.2.2.1) as an external signal on the auxiliary entry. The software is used to scan continuously a given mass range, analysing the residual gas in the chamber, or to record sequentially several different masses during a TPD.

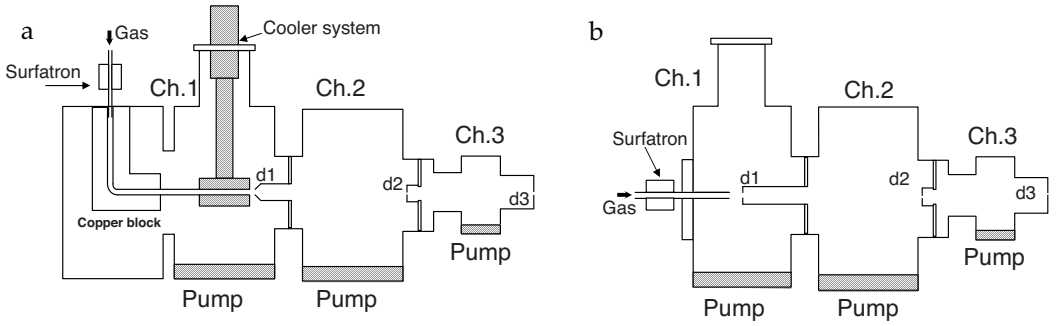

Figure 5.5. A schematic of molecular beams a) 1 and b) 2. The three chambers are marked Ch.1, Ch.2 and Ch.3, with corresponding apertures marked d. The main difference between the beams is the orientation of the Surfatron for producing plasma, as explained in § 5.2.4.3. For both beams, gas enters via the quartz tube of the Surfatron, passes through chambers 1, 2 & 3 via apertures 1, 2 & 3, before entering the main chamber. Correct alignment of the apertures ensures that gas entering the chamber is incident upon the silicate surface.

5.2.4 The molecular beam lines

FORMOLISM has two molecular beam lines, based upon the model of Walraven & Silvera [1982], used to deposit molecular and atomic species on the surface in the main chamber. Each beam line is composed of three stages of differentially pumped chambers separated by apertures, as illustrated in Figure 5.5. A microwave discharge cavity for producing atomic beams is located in the first chamber of each beam line. The beams can be molecular or, if the discharge is activated, a mixture of atomic and molecular (but never purely atomic due to recombination of atomic species on surfaces of the beam lines). Species are delivered from the beam line to the main chamber at ambient temperature of $\sim$ 300 K, even if produced in a discharge, due to the transfer of kinetic energy by collisions in the beam line.

5.2.4.1 Operational principle

The molecular beams are designed to deliver atomic and molecular species into the main chamber at a rate low enough to maintain a pressure $< 10^{-9}$ mbar in the main chamber at all times. In addition, they ensure that the beams are incident upon the surface by selecting those molecules or atoms within

Table 5.1. Properties of the molecular beams. Where appropriate, the beams are distinguished by their indices 1,2.

Chamber	Background pressure mbar	Mean free path[a] m	Distance travelled cm	Aperture diameter mm	Pump speed $1\,s^{-1}$
Tube	1	10^{-5}	45^1 / 10^2	4	...
1	10^{-4}	10^{-1}	2	2.5	500
2	10^{-6}	1	33^1 / 40^2	2.5	100
3	10^{-8}	10^2	48	2.5	100
Main	10^{-10}	10^4	25	$3.3^b \times 5.4^1$ / 4.0^2	1000

[a]Mean free path for a collision cross section of 1 $\mathring{A}^2$ at 300 K.

[b]Vertical (y) and horizontal (x) axes of the elliptic intersection of the beam with the surface.

a given trajectory range (very small solid angle $\sim 8 \times 10^{-6}$ steradian). Gas is introduced into the first chamber via a quartz tube located in the microwave discharge cavity. The gas passes through three chambers and into the main chamber via three aligned apertures.

The pressure of the gas in the quartz tube is $\sim$ 1 mbar, diminishing gradually at each stage of the molecular beam due to pumping at particular capacities by molecular turbo pumps in each chamber. The properties of each stage of the beam lines are presented in Table 5.1. The molecular beams are effusive, rather than nozzle, sources, as gas effuses from the tube into the first chamber. Free molecular flow along the beam is guaranteed as the Knudsen number ($K_n = \frac{\lambda}{D}$, where λ is the gas mean free path $\sim$ few cm, and D the diameter of the tube aperture $\sim$ 4 mm) is greater than unity [Woodruff & Delchar, 1994]. In an effusive source, the molecules in the beam have temperatures close to that of the tube.

A valve in the third chamber can be closed to prevent the penetration of the beam into the main chamber, and a rotatable flag in the main chamber can be employed to prevent direct irradiation of the surface, while still allowing the beam gas to contribute to the background pressure of the main chamber.

5.2.4.2 Alignment and flux calibration

Due to the fixed geometry of the experiment, the molecular beams are roughly aligned at all times, both with the surface and the QMS. Fine alignment of the molecular beams with the surface and each other is done by adjusting the three apertures between the three chambers of the beam and the main chamber. These are adjustable in x (horizontal) and y (vertical) directions by tightening and loosening a series of bolts. Alignment commences with Beam 1. With the QMS facing the beam, the apertures are adjusted until the maximum QMS signal is obtained. The QMS is turned to face Beam 2, and the process repeated. The aim of alignment is 100 % overlap of the beams upon the surface, as this would allow maximum physical interaction between two different species deposited via the two beams. However, this is unobtainable for a number of reasons: the beams are incident upon the surface at different angles (Beam 1, 28 °; Beam 2, 47 °) so their deposition cross sections are different; also, the method of alignment is not perfect. It is possible to align Beam 2 by shining a laser along the beam path or illuminating the microwave discharge (discussed in § 5.2.4.3); the light from these sources is incident upon the surface, allowing fine adjustment. However, this is not possible with Beam 1 due to the non-linear geometry of the quartz tube in the microwave discharge cavity.

The fluxes of the molecular beams are estimated to be 10^{12} cm^{-2} s^{-1} for Beam 1 and 10^{13} cm^{-2} s^{-1} for Beam 2, within an error of $\pm$ 30 %. The flux for each beam is measured using three complementary methods, while the error represents the disparity between the methods. Flux calibration is illustrated in Figure 5.6.

Method 1: The QMS can be positioned directly facing either beam, as mentioned in § 5.2.3.2. A comparison is made between the signal of the beam with the flag off and on. This compares the signal of the beam to the background signal in the chamber, respectively, and allows calculation of the flux.

Method 2: The surface is cooled to 10 K and a timed deposition of molecules is made, with the beam incident upon the surface. As the surface is cool, the molecules adsorb with a sticking coefficient of ~ 1. The surface is heated and the molecules measured with the QMS as they desorb from the surface. The experiment is repeated with the flag on (preventing the beam directly hitting

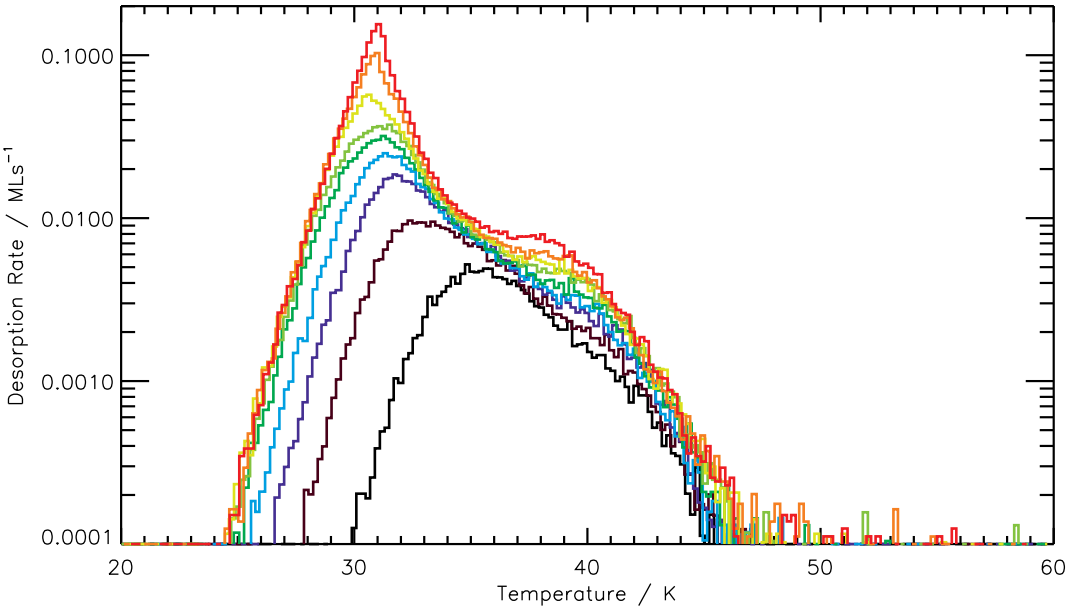

Figure 5.6. Flux calibration of the molecular beams by Method 3 using O_2 on non-porous, amorphous H_2O (see text for details). The time of deposition increases from black to red depositions, with coverages ranging from sub-monolayer to the multi-layer.

the surface), and the comparison between direct and background depositions allows calculation of the beam pressure on the surface, and thus the flux. This method has the advantage of measuring the effective flux on the surface, rather than simply the flux of the beam, and is good if the surface is well characterised.

Method 3: As in Method 2, the surface is cooled to 10 K and a timed deposition of molecules is made, with the beam incident upon the surface. The surface is heated and the molecules measured with the QMS as they desorb from the surface. This process is repeated multiple times, with varying deposition times, until a series of TPD spectra are obtained (see Figure 5.6). The deposition representing one monolayer of molecules is identified (the dark green plot in Figure 5.6), and since the time to deposit one monolayer of molecules is known, the effective flux on the surface can be calculated (assuming that one monolayer of molecules occupies 10^{15} adsorption sites.

5.2.4.3 Microwave plasma discharge

To obtain an atomic flux incident on the surface, molecular gases are dissociated in a plasma discharge. The quartz tube (inner diameter 4 mm) in the microwave cavity is cooled with compressed air and water in an outer jacket, and molecular gas is passed through at a pressure of 0.3 – 3 mbar. Microwave power (300 W at 2.45 GHz) is supplied by a magnetron and transmitted to the gas via a Surfatron 2450 MHz (Sairem) in the form of electromagnetic surface waves, generating a plasma upon spark ignition. Impedance matching of the microwave cavity is performed using the coupler on the magnetron and an adjustment screw on the Surfatron to ensure the maximum transmission of power through the Surfatron.

Microwaves in the cavity cause the electrons in the gas to oscillate; these electrons then collide with other atoms to create and maintain a plasma. Dissociative excitation of the molecules in the gas forms atoms, but at the pressures used, collisions with the walls of the tube favour molecular recombination, although this is minimised by cooling the tube.

The only difference between the two beams is that Beam 1 has a bent geometry, in order to prevent the light of the plasma impinging upon the surface, whereas Beam 2 is linear. The gas in Beam 1 is directed into a Teflon tube through an aluminium nozzle before entering the first chamber (as seen in Figure 5.5). As the tube in Beam 2 is shorter, it allows a slightly larger flux of molecules or atoms.

The dissociation rates obtained for H_2 are typically 30 – 70 %. The value is calculated before every experiment involving H, and tends to improve if the plasma is switched on for some time before the experiments begin. The rate is calculated using the QMS by comparing the molecular flux when the discharge is switched on and off. It is assumed that the volume of gas passing through the beam does not change with the discharge switched on. The fact that, before and after the discharge the pressure ratio determining gas outflow is conserved, and that the gas exiting the discharge is cooled by collisions before its expansion into the first chamber, support this assumption.

5.3 Temperature Programmed Desorption (TPD)

5.3.1 Introduction

Experiments performed using FORMOLISM are analysed by the indirect technique of TPD. The method consists of increasing the surface temperature with a linear heating ramp. Molecules adsorbed to the surface desorb at specific temperatures dependent upon the binding energy of that species. By monitoring the desorption using the QMS, the molecular species can be identified by their masses and characteristic desorption temperatures.

The following information can be obtained by analysis of TPD spectra: the surface coverage (θ) of each species is obtained by calculating the area under its desorption peak; the peak profile and the coverage dependence of the desorption give information on the bonding state of the molecular species to the surface; the desorption temperature and the peak of the desorption relate to the binding strength, and thus the activation energy for desorption (and adsorption, E_{ads}, if these are equal) of the molecules to the surface.

Surface material and morphology play a large role in the desorption characteristics of a molecular species, and a change in surface can change the shape of the TPD spectrum, or shift the peak desorption temperature (T_p) for a given species. This is expanded in Chapter 6.

5.3.2 Desorption kinetics

Thermal desorption is an activated process that can be described in terms of an Arrhenius law, expressed by the Polanyi-Wigner equation [King, 1975], where the rate of desorption, r, is described by:

$$r = -\frac{dN}{dt} = AN^n e^{-E_{ads}/kT}, \tag{5.1}$$

where A is the pre-exponential factor, N is the number of adsorbed molecules on the surface (cm^{-2}), n is the order of the reaction, E_{ads} is the energy of adsorption of a molecule to the surface (eV), k is the Boltzmann constant (eV

molec^{-1}K^{-1}), and T is the temperature of the surface (K). The units of A depend on n: molecules^{1-n}cm^{-2+2n}s^{-1}.

During a TPD, desorption is driven by the linear increase in the surface temperature. Time (t /s) and temperature (T /K) are related by:

$$T = T_0 + \beta t, \tag{5.2}$$

where $\beta = \frac{dT}{dt}$ = 10 Kmin^{-1} is the heating rate. By making the substitution:

$$\frac{dN}{dt} = \frac{dN}{dT} \cdot \frac{dT}{dt} = \frac{dN}{dT}\beta. \tag{5.3}$$

Equation (5.1) can be rewritten as:

$$r = -\frac{dN}{dT} = \frac{A}{\beta}N^n e^{-E_{ads}/kT}. \tag{5.4}$$

In practise, all desorbing species are detected by the QMS, with a signal intensity proportional to r because the pumping regime is efficient ($\frac{dN}{dt} << v_{pump}$). This is not the case in some experiments, resulting in long tails on TPD spectra [e.g. Fraser & van Dishoeck, 2004] due to inefficient pumping.

The desorption order, n, corresponds, in general, to stoichiometric coefficients in the desorption equations and can be determined by considering the profiles and peak temperatures of TPD spectra. Chemisorbed monolayers generally exhibit first or second order desorption kinetics, but multilayer systems tend to be zeroth order. The first monolayer of a multilayer system is often strongly chemisorbed to the surface and displays coverage-dependent kinetics. However, the second and subsequent layers are bonded to pure adsorbate and the surface influence diminishes quickly. Multilayer desorption peaks are thus observed at lower temperatures than the monolayer desorptions of the same molecular species, assuming that the molecules are bonded by chemisorption. This is not necessarily the case, however, when physisorption is involved.

Zeroth order desorption implies that the rate of desorption is not dependent upon the surface coverage and that it increases exponentially with temperature, according to:

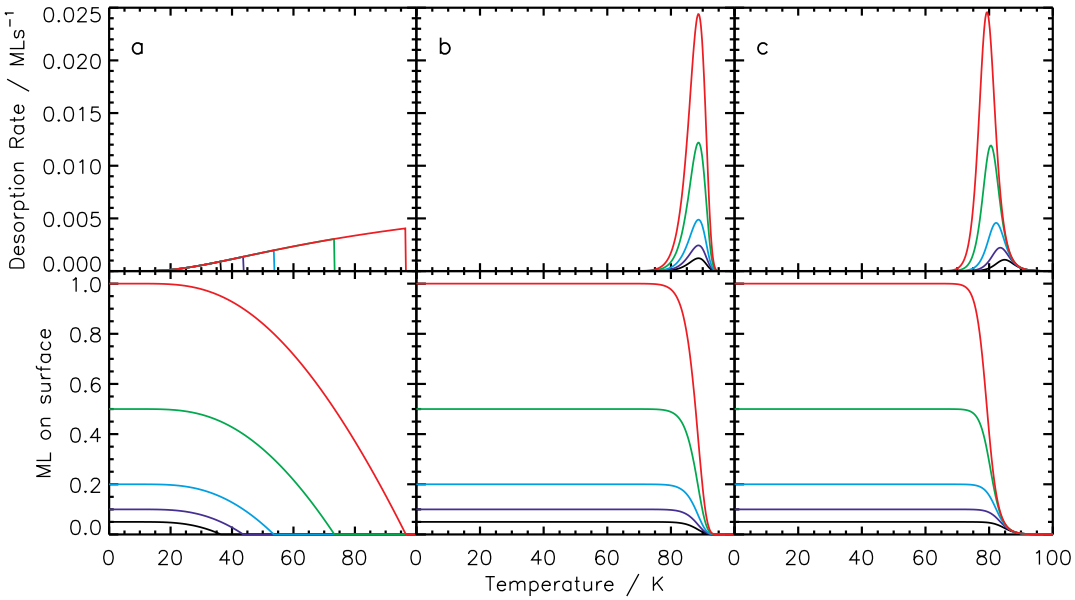

Figure 5.7. Simulated desorption profiles of TPD spectra with a) 0^{th}, b) 1^{st} and c) 2^{nd} order desorption kinetics. Coverages are 0.05 ML (black), 0.1 ML (violet), 0.2 ML (blue), 0.5 ML (green), 1.0 ML (red). For each desorption order, the upper plot shows desorption rate (MLs^{-1}) while the lower plot shows the number of ML remaining on the surface. Values for the simulations are a) E_{ads} = 0.0075 eV, $A = 10^{13}$ molecules cm^{-2}s^{-1}, b) E_{ads} = 0.25 eV, $A = 10^{13}$ s^{-1}, c) E_{ads} = 0.3 eV, $A = 10^{3}$ cm^{2}molecule^{-1}s^{-1}

$$-\frac{dN}{dT} = \frac{A}{\beta} e^{-E_{ads}/kT}. \tag{5.5}$$

As seen in Figure 5.7a, all coverages have a common leading edge, T_p increases with coverage, and there is a rapid drop in signal above the peak temperature as all molecules have desorbed. Zeroth order kinetics are observed in multilayer desorption, where the number of surface molecules ready to desorb is high and approximately constant for a long period of time, for example in non-wetting systems [Smith et al., 1996]. Exponential growth dominates the kinetics, allowing desorption rates up to several MLs^{-1} until the final layer desorbs. Pseudo zeroth order desorption is observed if there are strong attractive interactions between molecules on the surface.

In first order desorption, the desorption rate is proportional to the coverage on the surface and the desorption peak is at a constant temperature, independent of the coverage (Figure 5.7b). First order kinetics typically correspond to the

desorption of an adsorbate with a coverage lower than one monolayer. T_p increases with E_{ads}. Desorption proceeds with a characteristic asymmetric peak profile, due to the balance between the pre-exponential and exponential terms of the rate equation:

$$-\frac{dN}{dT} = \frac{A}{\beta} N e^{-E_{ads}/kT}. \tag{5.6}$$

Second order desorption has a rate proportional to the coverage squared:

$$-\frac{dN}{dT} = \frac{A}{\beta} N^2 e^{-E_{ads}/kT}. \tag{5.7}$$

As seen in Figure 5.7c there is a characteristic, almost symmetrical, peak shape with a common trailing edge. T_p decreases with increasing coverage. Pseudo second order desorption is observed when two adsorbed species exhibit strongly repulsive interactions. The repulsive interactions increase with coverage, lowering the average desorption temperature. As the coverage decreases with increasing temperature, the repulsions decrease, explaining the long trailing edge of the peaks.

At T_p, $d^2N/dt^2 = 0$, therefore the adsorption energy can be obtained by differentiation of Equation (5.4):

$$E_{ads} = kT_p^2 \frac{A}{\beta} n N^{n-1} e^{-E_{ads}/kT_p}. \tag{5.8}$$

For a given activation energy, therefore, second order kinetics implies a decrease in T_p with increasing coverage.

Very often, fractional order desorption is observed, with $0 < n < 1$. This indicates island formation on the surface and desorption of molecules from the edges or tops of these islands. However, assuming that the fractional order is close to 0 or 1, the kinetics are generally approximated by zeroth or first order kinetics.

If the pre-exponential factor A is known, it is possible to calculate E_{ads} from Equation (5.8). As the term E_{ads} appears in both terms of the equation, how-

ever, it is necessary to estimate this term and find a convergent result by an iterative method [Attard & Barnes, 1998]. It is often assumed for $n = 1$ that A is 10^{13} s^{-1}, the same order of magnitude as the molecular vibrational frequency. In general, this method is too simplistic and a more complex analysis is required. This will be further addressed in Chapter 6.

5.4 Concluding remarks

This chapter has introduced the FORMOLISM experiment, a powerful tool for analysing the properties and reactions of molecules on a surface under astrophysically relevant conditions of temperature and pressure. The main diagnostic tool of FORMOLISM is the TPD, described in detail in this chapter. Molecules and atoms are deposited on the cold surface using the two molecular beam lines, then the surface is heated with a linear ramp, and the desorbing molecular species are quantified using a QMS. In this experiment, the surface type can be altered by the growth of an ice upon the silicate surface, to mimic the icy mantles found on dust grains in molecular clouds and other astrophysical environments. FORMOLISM is utilised in Chapter 6 to investigate surface properties, and in Chapter 7 for a study into the formation of CO_2.

References

Attard, G., & Barnes, C. 1998, "Surfaces", Oxford University Press

Baouche, S. 2004, "Formation d'hydrogène moléculaire sur des surfaces d'intérêt astrophysique : premiers résultats sur des glaces d'eau à très basse température et sur le graphite à haute température", Ph.D. Thesis, Univ. Paris VI & Observatoire de Paris

Batista, E. R., Ayotte, P., Bilic, A., Kay, B. D., & Jonsson, H. 2005 , Phys. Rev. Lett., 95, 223201

Davoisne, C., et al. 2008, A&A, 482, 541

Dulieu, F., Amiaud, L., Congiu, E., Fillion, J.-H., Matar, E., Momeni, A., Pirronello, V., & Lemaire, J. L. 2010, A&A, 512, A30

Fraser, H. J., & van Dishoeck, E. F. 2004, Advances in Space Research, 33, 14

Gifford, W.E., & Mc Mahon, H.O. 1959, "A low temperature heat pump", Proceedings 10th International Congress of Refrigeration, Vol. 1

King, D. A. 1975, Surf. Sci., 47, 384

Lemaire, J. L., Vidali, G., Baouche, S., Chehrouri, M., Chaabouni, H., & Mokrane, H. 2010, ApJL, 725, L156

Schlichting, H., & Menzel, D. 1993, Rev. Sci. Instrum., 64, 2013

Smith, R. S., Huang, C., Wong, E. K. L., & Kay, B. D. 1996, Surf. Sci., 367, L13

Tielens, A. G. G. M. 2005, "The Physics and Chemistry of the Interstellar Medium", Cambridge University Press

Walraven, J. T. M., & Silvera, I. F. 1982, Rev. Sci. Instrum., 53, 1167

Williams, D., & Herbst, E. 2002, Surf. Sci., 500, 823

Woodruff, D. P., & Delchar, T. A. 1994, "Modern Techniques of Surface Science - Second Edition", Cambridge University Press

CHAPTER 6

THERMAL DESORPTION CHARACTERISTICS OF CO, O_2 AND CO_2 ON NON-POROUS WATER, CRYSTALLINE WATER AND SILICATE SURFACES†

6.1 Synopsis

The desorption characteristics of molecules on interstellar dust grains are important for modelling the behaviour of molecules in icy mantles and, critically, in describing the solid-gas interface. Results in Chapter 4 suggested that low concentrations of molecules, particularly CO, could be present on dust grains at early stages in molecular clouds. Thus, a greater understanding of the physical behaviour characteristics of molecules at sub-monolayer surface coverages is important to interpreting these observational data. In this chapter, a series of laboratory experiments exploring the desorption of three small molecules from three astrophysically relevant surfaces are presented. The desorption of CO, O_2 and CO_2 at both sub-monolayer and multilayer coverages was inves-

†This chapter is based upon results presented in a paper submitted to the journal Monthly Notices of the Royal Astronomical Society.

tigated from non-porous water, crystalline water and silicate surfaces, using the FORMOLISM experiment introduced in Chapter 5. Experimental data was modelled using the Polanyi-Wigner equation to produce a mathematical description of the desorption of each molecular species from each type of surface, uniquely describing both the monolayer and multilayer desorption in a single combined model. The implications of desorption behaviour over astrophysically relevant timescales is discussed.

6.2 Introduction

The interaction of molecular species with surfaces is of critical importance in astrophysical environments. Much interstellar chemistry occurs on or in the icy layers which cover dust grains in molecular clouds, the birthplace of stars and planets [Fraser et al., 2002]. These dust grains are believed to be composed of silicates and carbonaceous material [Draine, 2003]. The silicate is at least $\sim$ 95 % amorphous, as determined from the breadth of the 9.7 μm band [Li & Draine, 2002], and although its composition has not been determined precisely, is well approximated by amorphous olivine ($MgFeSiO_4$) [Sofia & Meyer, 2001; Draine, 2003]. The silicates are believed to be 'fluffy' in nature, with a large surface area upon which reactions can occur [Mathis, 1998].

At the low temperatures in molecular clouds (T $<$ 20 K) atoms and molecules freeze-out onto these silicate surfaces, forming the icy mantles. Amorphous solid water (ASW) is by far the largest component of this ice, with abundances of $\sim$ 1 x 10^4 with respect to the total H column density [Williams & Herbst, 2002], equivalent to coverages of up to 100 monolayers (ML). Given that the extinction threshold for H_2O mantles is $A_V \sim 3.3$ mag [Whittet et al., 1988], it is reasonable to assume that between the dense pre-stellar cores (where dust grains are completely coated by this icy mantle) and the cloud edges (where competition between ice formation and photodesorption of H_2O yields a population of bare silicate grains [Smith et al., 1993]), there must be a region where icy surfaces and bare silicates co-exist.

As interstellar regions evolve, the icy grains are further processed, either by gentle heating or cyclic desorption-deposition events [Visser et al., 2009], pro-

ducing crystalline H_2O. This has been detected in various stellar and pre-planetary environments, including, for example, M giant stars [Omont et al., 1990], Quaoar in the Kuiper Belt [Jewitt & Luu, 2004], Trans Neptune Objects [Merlin et al., 2007], comets [Lisse et al., 2006], and in the outer disks around T Tauri stars [Schegerer & Wolf, 2010].

As gas-grain modelling of interstellar environments becomes more sophisticated [Wakelam et al., 2010; Acharyya et al., 2011; Cuppen & Garrod, 2011], key questions impeding the full implementation of surface chemistry include: what effect does the underlying grain surface have on the desorption characteristics of key molecules, and to what extent is this desorption affected during the transition from the multilayer to sub-monolayer coverage regime? A third issue is how to realise the transition between the multilayer and monolayer regimes in a gas-grain model without overloading the model with many more layers of complexity.

CO, O_2 and CO_2 are all interstellar molecules that potentially could populate bare interstellar grains at sub-monolayer coverages. On ice, only one previous study focussed on sub-monolayer coverages of CO, highlighting the spectroscopic rather than desorption characteristics of the porous ASW:CO system [Collings et al., 2005]. To date, no desorption studies of CO, O_2 or CO_2 have been made on a silicate surface, at either multilayer or sub-monolayer coverages.

CO is the second most abundant interstellar molecule [Tielens, 2005], and is known to form in the gas phase, then freeze-out on to H_2O covered grains to form overlayers of pure CO ice, the layer thickness critically depending on gas density rather than grain temperature [Pontoppidan et al., 2003]. Consequently, extensive temperature programmed desorption studies have been made of multilayer CO coverages on various surfaces, including Au [Collings et al., 2004; Fuchs et al., 2006; Bisschop et al., 2006; Acharyya et al., 2007], H_2O [Collings et al., 2003a,b], a meteorite sample [Mautner et al., 2006] and highly oriented pyrolytic graphite (HOPG) [Ulbricht et al., 2006]. CO is also used extensively in general surface science studies, and thus its desorption characteristics over a wide range of coverages have been well studied, both experimentally and theoretically [Ertl et al., 1977; Raval et al., 1990; Frenklach et al., 1993; Wang et al., 2009; Lakhlifi & Killingbeck, 2010; Dohnalek et al., 2006].

It is widely accepted that both CO_2 and H_2O form on dust grains in molecular clouds, and recent experimental and theoretical studies (including the one detailed in Chapter 7) suggest that at least some of the CO_2 and H_2O is formed concurrently [Goumans et al. , 2008; Noble et al., 2011; Ioppolo et al., 2011]. Since CO is the key precursor to CO_2 formation, such mechanisms would require CO freeze-out onto bare grain surfaces long before CO ice, or even large quantities of H_2O ice, are detected. Although tenuous, spectroscopic observational and experimental evidence exists for such a freeze-out process [Fraser et al., 2005], as well as the evidence presented in Chapter 4, but an investigation of the desorption behaviour of CO at sub-monolayer coverages on ice and silicate surfaces is vital in order to be certain that it can reside at an interstellar grain surface long enough to form more complex species.

Similarly, O_2 is a potential precursor in H_2O formation [Ioppolo et al., 2008; Oba et al., 2009], and is a species that could form in the gas phase then freeze-out onto grain surfaces, rather than forming on the grain itself. However, as a homonuclear diatomic O_2 is infrared inactive, so its detection in interstellar ice, though occasionally claimed via a forbidden transition [Elsila et al., 1997] remains elusive. It is not clear whether this is related to the weak transition probability, lack of a significant O_2 population in the ice, or that the O_2 has rapidly reacted (upon adsorption) to exclusively form H_2O. Nevertheless, the multilayer desorption behaviour of O_2 has been studied previously alongside CO and N_2 [Acharyya et al., 2007; Fuchs et al., 2006], as well as on Au, porous ASW [Collings et al., 2004] and TiO_2 [Dohnalek et al., 2006]. These studies show that the multilayer desorption characteristics of O_2 are very similar to CO, so it is interesting from both a chemical and astrophysical viewpoint to also investigate the desorption behaviour of O_2 at sub-monolayer coverages on ice and silicate surfaces.

The desorption characteristics of CO_2 have not been extensively studied on any surface, despite it being one of the most abundant solid phase molecular species in the interstellar medium. The desorption characteristics of multilayer CO_2 have been previously studied on HOPG [Ulbricht et al., 2006], porous ASW and Au [Collings et al., 2004]. However, given that the observational [Pontoppidan, 2006] and experimental [Noble et al., 2011] evidence shows that a fraction of CO_2 ice must form concurrently with the water ice layer, some

CO_2 molecules must populate both the bare silicate grains and the ice layers at sub-monolayer coverages.

This chapter details an experimental study of the desorption of CO, O_2 and CO_2 from three different surfaces; non-porous ASW, crystalline ice, and amorphous olivine-type silicate. As these are, for the first time, all undertaken in the same experimental setup – FORMOLISM – it is possible to investigate both the individual effect of each surface on the desorption characteristics, as well as determining whether the molecular composition or morphology of the surface is most relevant in determining the desorption behaviour of molecules. For each of the nine combinations of CO, O_2 and CO_2 on each surface, this study has encompassed both the multilayer and sub-monolayer regimes. These data are modelled to determine a simple analytical expression which accurately calculates both the sub-monolayer and the multilayer desorption energies. By changing the model to incorporate interstellar, rather than experimental, heating rates, it is possible to address the key questions above, namely: what effect does the underlying surface have on the desorption characteristics of the molecules adsorbed there, and how is this desorption modified in the sub-monolayer coverage regime?

6.3 Experimental

The experiments were conducted using the FORMOLISM setup, described in detail in Chapter 5. A sample of either O_2, CO or CO_2 was deposited onto the surface at 18 K via the triply differentially pumped beam line 1; a linear temperature ramp was then applied to the surface, and the QMS used to measure the desorption of each species into the gas phase, as a function of temperature.

Three surfaces were investigated in this study: non-porous ASW ($H_2O_{(np)}$), crystalline ice ($H_2O_{(c)}$) and amorphous silicate (SiO_x). The SiO_x surface was recently installed in the FORMOLISM experiment [Lemaire et al., 2010], and mimics bare dust grains in molecular clouds. At the time these experiments were performed, the surface was capable of reaching base temperatures of 18 K, which is how the molecular deposition temperature on all the surfaces was predetermined. For the ice surfaces, 50 ML films were grown on top of

Table 6.1. Description of experimental exposures.

Molecule	Surface	Depositions[a] ML
O_2	$H_2O_{(np)}$	0.25, 0.50, 0.75, 1, 1.25[c], 1.38, 1.75, 2.25[c], 2.75
	$H_2O_{(c)}$	0.08, 0.17, 0.50, 0.67, 1, 1.33
	SiO_x	0.20, 0.60, 1, 1.20, 1.60, 1.67
CO	$H_2O_{(np)}$	0.25, 0.50, 0.75, 0.88, 1, 1.06[b], 1.13[b], 1.25[b], 1.75[b], 2.50
	$H_2O_{(c)}$	0.10, 0.20, 0.60, 0.80, 1, 1.20[b], 1.60
	SiO_x	0.50, 1, 1.25[b], 1.75, 2.25
CO_2	$H_2O_{(np)}$	0.1, 0.2[b], 0.4[b], 0.6[b], 1[b], 2
	$H_2O_{(c)}$	0.1, 0.2, 0.3, 0.5[c], 1, 2
	SiO_x	0.05, 0.1, 0.2, 0.3, 0.5, 1

[a]Defined as $\frac{exposure}{N_{mono}}$, where N_{mono} is defined in § 6.4.2.

[b]Omitted from model (shown in grey in Figure 6.1).

[c]Modelled, but omitted from Figure 6.3 for clarity.

the silicate surface by spraying water vapour from a microchannel array doser located 2 cm in front of the surface. The water vapour was obtained from deionised water which had been purified by several freeze-pump-thaw cycles, carried out under vacuum. $H_2O_{(np)}$ mimics the ASW which comprises the bulk of interstellar ice, and $H_2O_{(c)}$ mimics the crystalline ice seen in some star-forming regions. To produce $H_2O_{(np)}$, water was dosed while the surface was held at a constant temperature of 120 K. To form $H_2O_{(c)}$, the surface was held at 120 K during the deposition, then flash heated at 50 $Kmin^{-1}$ to 140 K, and finally at 10 $Kmin^{-1}$ to 142.5 K, as described in Chapter 5. For each type of ice surface, the temperature was then held constant until the background pressure in the chamber stabilised, before cooling it back down to 18 K, at which temperature adsorbates were dosed onto the respective surfaces.

For each of the nine combinations of molecule and surface, a series of depositions were made, varying the adsorbate surface coverage, from sub-monolayer to multilayer, as outlined in Table 6.1. After the first adsorbate exposure, the surface was then heated at a rate of 10 $Kmin^{-1}$ until the adsorbate was fully desorbed from the surface (below 100 K on the ice surfaces and 130 K on the sil-

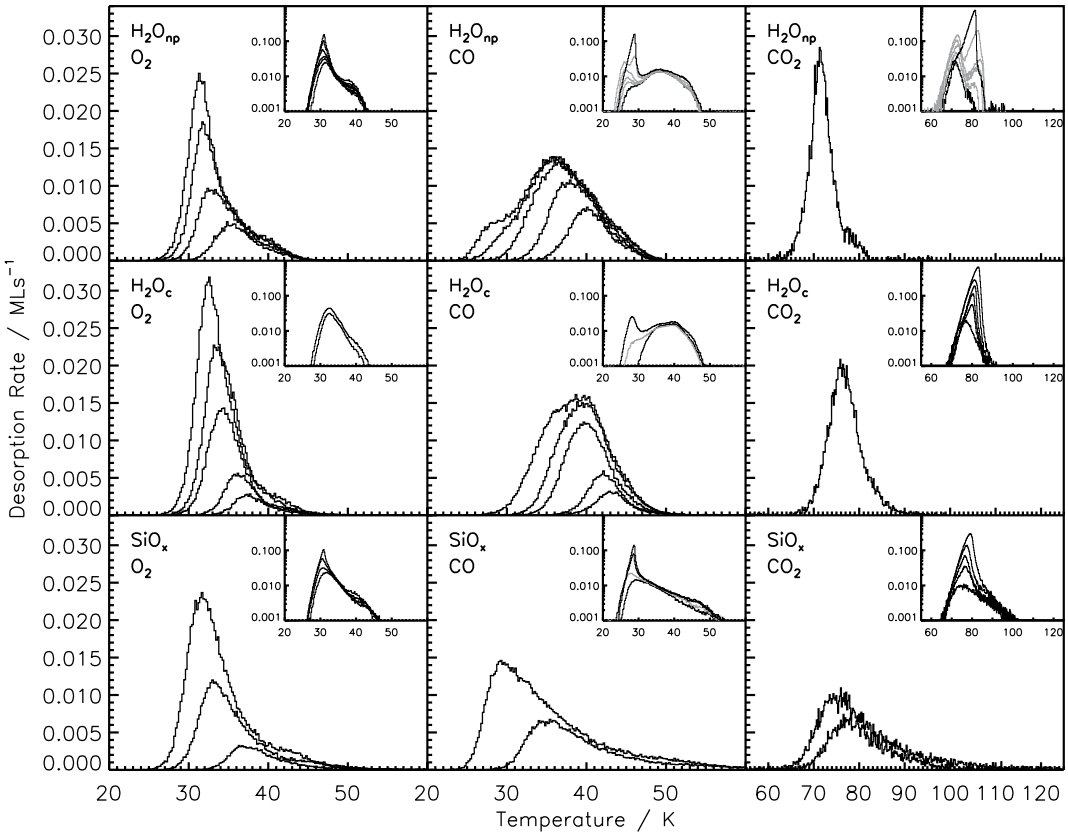

Figure 6.1. Temperature-programmed desorption spectra of O_2, CO and CO_2 from $H_2O_{(np)}$, $H_2O_{(c)}$ and SiO_x. For each molecule-surface combination, the main window shows a series of TPD spectra from the lowest sub-monolayer coverage up to 1 ML; inset are TPD spectra from 1 ML up to the highest multilayer coverage, as specified in Table 6.1. Spectra shown in black were included in the model, whilst those in grey were omitted. In all cases, the line profile of the TPD spectra in the multilayer regime differ from those in the sub-monolayer regime and, with the exception of CO, the form of the TPD profiles is very similar in the sub-monolayer regime, independent of surface. The desorption profiles of all three molecules from the SiO_2 surface in the sub-monolayer regime strongly resemble each other, unlike the ices.

icate surface). The original surface therefore remained intact and, by constraining the temperature of the ice to below 100 K, no further thermal annealing of the ice occurred during an experimental sequence. Subsequently, the surface was then recooled to 18 K, and a new coverage of the same adsorbate added. In this way it was ensured that the same surface was used for a single series of adsorbate exposures, allowing real comparison of the coverage effect for the first time. In the multilayer, the underlying surface is not important to the des-

orption, as adsorbate-adsorbate interactions between molecules determine the kinetics. In the sub-monolayer, the interaction between the adsorbate and the substrate is fundamental in determining the desorption characteristics. Thus, by including both regimes, the intention was to probe the differences between these two coverages for different molecules and different surfaces.

A porous ASW surface was not included in this study for several reasons. Firstly, the presence of pores in the ice surface can produce very complex desorption profiles, due to the competing kinetics which arise after entrapment of adsorbates in the pores [e.g. Collings et al., 2003a]. Additionally, pore collapse starts at only 10 – 15 K, so the experimental approach used here, of exposing a single ice surface to a variety of adsorbate coverages, is simply not possible with the porous ASW. A new ASW sample would have been required for each experiment; each time a porous ice is formed in the laboratory its structure is slightly different, resulting in a potentially massive change in surface area and non-reproducible adsorbate exposures being required to obtain monolayer coverages. Furthermore, one aim of this experiment was to compare surface characteristics using a simple model for the whole dataset, and such an approach would not have been possible when including both porous and non-porous ices, again because the monolayer surface area is almost impossible to define. Finally, it has recently been shown experimentally that it is very likely that all water ice in interstellar regions is non-porous ASW due to collapse of pores [Accolla et al., 2011], even though observations previously suggested that invoking a porous ASW was the only way to explain observed quantities of mixed H_2O and CO ices [Pontoppidan et al., 2003, and Chapter 4].

6.4 Results and discussion

6.4.1 Experimental data

All the TPD results are shown in Figure 6.1. The results are ordered from top to bottom by surface type – $H_2O_{(np)}$, $H_2O_{(c)}$ and SiO_x – and from left to right by adsorbate molecule – O_2, CO and CO_2. For each molecule-surface combination, the main plot shows the series of sub-monolayer exposure TPD spectra,

from the lowest molecular coverage up to a coverage of 1 ML (as per the values given in Table 6.1). The inset shows the equivalent data for coverages of 1 ML and above. In all cases, it is immediately apparent that the TPD line profile differs between the sub-monolayer and the multilayer regime, as expected. In some cases (shown in grey on Figure 6.1), an intermediate region is visible in those TPD spectra which trace coverages between one monolayer and the multilayer, for example in CO or CO_2 on $H_2O_{(np)}$. It is clear that structural reorganisations must occur at these intermediate coverages, as desorption spectra with double and triple peaked profiles are observed. Describing such processes is beyond the scope of this investigation and for this reason these particular data have been omitted from the later modelling, only being shown in Figure 6.1 for completeness.

For both O_2 and CO_2, it is also apparent from Figure 6.1 that the TPD line profiles are similar in the sub-monolayer regime, independent of the underlying surface. For CO this is clearly not the case, although the multilayer data are more consistent across all surfaces. Likewise, in both the sub-monolayer and multilayer regimes, the TPD spectra for different adsorbates on the SiO_x surface strongly resemble each other; the same can not be said for the ice surfaces. For all the adsorbates, it is evident that multilayer desorption from the crystalline ice surface starts at a slightly higher temperatures than from either the amorphous ice or amorphous SiO_x surface, suggesting a trend dependent on the morphology of the underlying surface. Specifically, for O_2, the peak temperature occurs between 30.9 and 32.6 K, but desorption starts around 24 – 25 K on amorphous surfaces ($H_2O_{(np)}$ and SiO_x), compared to 25 – 26 K on $H_2O_{(c)}$. For CO, the peak temperatures are in the range 28.1 – 28.9 K, while desorption starts at 22 – 23 K from the amorphous substrates and 23 – 24 K from $H_2O_{(c)}$. For CO_2, the peak desorption range is wider (79.3 – 83.0 K) and desorption begins at 63 – 65 K from SiO_x, 64 – 65 K from $H_2O_{(np)}$ and 66 – 67 K from $H_2O_{(c)}$.

To compare the sticking efficiency of each molecule on each surface, the area under the TPD peak, corrected for QMS sensitivity [Matar et al., 2010], was plotted against deposition time for each molecule on each surface, and is shown in Figure 6.2. Data can be divided into adsorbates – circle (CO), triangle (O_2), and square (CO_2) – and surfaces – $H_2O_{(np)}$ in red, $H_2O_{(c)}$ in green and SiO_x in

blue. Such a direct comparison is possible because the experimental method employs the same surface for a series of adsorbate exposures. Furthermore, the dosing rates of all three molecules, and the effective beam pressures employed, are always approximately equal. Straight lines of the form $y = mx + c$ were fitted to each molecule-surface combination and overplotted on the experimental data in Figure 6.2. Within experimental uncertainty (shown as error bars in Figure 6.2), these straight line fits all pass through zero, as expected, indicating that the sticking probability is constant (within $< 10\%$) across the dynamic range of each experiment. This means that no discernible change in sticking probability occurs for any of these molecules on any of these surfaces between the sub-monolayer and multilayer regimes. Adsorbate coverage is always linear as a function of exposure time. Crucially, for all three adsorbate molecules, the sticking efficiency on $H_2O_{(np)}$ (red lines in Figure 6.2) is slightly lower when compared with the other two surfaces. This is likely due to the fact that the average adsorption energy on $H_2O_{(np)}$ peaks at a lower energy than for the other substrates.

One final point, with reference to Figure 6.2, is the relationship between the time at which a surface will have been exposed to an equivalent dose of 1 ML (i.e. 10^{15} molecules), and the coverage (exposure time) at which the TPD data show a deviation from sub-monolayer to multilayer behaviour, defined in § 6.4.2 as N_{mono}. For CO and O_2 this occurs on all surfaces between around 250 – 300 s exposure; for CO_2 the switch occurs at much lower surface coverages (exposure times $\sim$ 10 % those for CO and O_2). It is postulated that this difference is related to the wetting behaviour of the molecules on different surfaces, and this issue is readdressed in § 6.4.3.

6.4.2 Modelling

To obtain a more quantitative understanding of the interactions between the molecules and the surfaces, the TPD spectra were reproduced from an empirical kinetic model. To do this, the results were divided into sets of TPD spectra associated with sub-monolayer and multilayer behaviour and the kinetic parameters in each regime determined independently, before being recombined to reproduce the experimental TPD data. A simple model was therefore de-

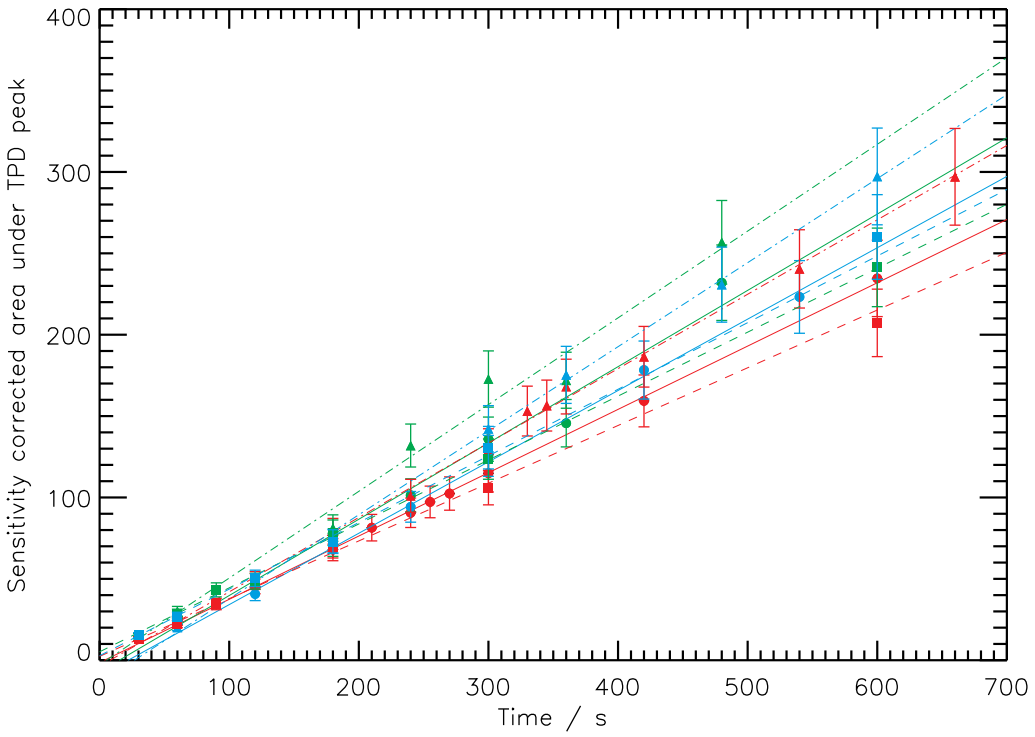

Figure 6.2. The area under the TPD peak, corrected for QMS sensitivity, plotted against deposition time. Experimental data is plotted as points, with $H_2O_{(np)}$ in red, $H_2O_{(c)}$ in green and SiO_x in blue; CO as circles, CO_2 as squares and O_2 as triangles. Overplotted are the straight line fits to the data, as described in the text. Colours are as above for the three surfaces, with CO solid, CO_2 dashed and O_2 dot-dashed lines. As expected, for each molecule-surface combination, the area increases with deposition time, and the straight line fit goes through zero, within experimental errors. For each molecular species, sticking occurs approximately equivalently on all three surfaces, with an error of < 10 %, although sticking is slightly lower on $H_2O_{(np)}$ for all molecules.

rived to fit all nine molecule-surface combinations from sub-monolayer to multilayer adsorbate coverages.

As already introduced in Chapter 5, on any surface, at any coverage, thermal desorption can be described in terms of an Arrhenius law, expressed by the Polanyi-Wigner equation (Equation (5.1)). Reformulating Equation (5.1), as in Equation (5.4), reflects the measured experimental TPD signal; in this case $dT/dt = 10$ Kmin^{-1}.

When the rate of desorption is independent of surface coverage, as is the case

in multilayer desorption, $n = 0$ and the TPD desorption profiles share a common leading edge, as is readily apparent from the insets in Figure 6.1.

For each molecule-surface combination, the leading edge of the highest multilayer exposure TPD spectra was used to determine E_{ads} (in K). Although some multilayer desorption TPD data show that the order of reaction can deviate slightly from zero (e.g. Brown & Bolina [2007]) it is a reasonable approximation, so henceforth it is assumed that $n = 0$. As applied previously by Acharyya et al. [2007], the pre-exponential factor in Equation (5.4) was assumed to be a function of E_{ads} approximated by:

$$A = N_{ML} \cdot \nu = N_{ML} \sqrt{\frac{2 N_{ML} E_{ads}}{\pi^2 M}}, \tag{6.1}$$

where M is the mass of the adsorbate molecule, and $N_{ML} \sim 10^{15}$ cm^{-2}. The key advantage of this method is that the multilayer fitting requires only one variable, E_{ads}, removing the interdependency of fitting both the pre-exponential factor and E_{ads} concurrently. The results of fitting E_{ads} are presented in Table 6.2.

In the sub-monolayer regime, the rate of desorption is dependent on surface coverage, $\theta = N/N_{mono}$, where N_{mono} is the maximum number of molecules on the surface prior to the onset of multilayer behaviour, and $N \leq N_{mono}$. Previous publications have shown that the reaction order can deviate slightly from 1 [e.g. Brown & Bolina, 2007], but for the purposes of this work it is assumed that $n = 1$. In general, in the case of first order desorption, the peaks of the TPD data appear at a single temperature value, provided that the desorption energy is independent of coverage [Fraser et al., 2001]. However, as is evident from the main plots in Figure 6.1, in this instance it is the trailing edge of the TPD curves that are common in each molecule-surface system. Such behaviour is known to arise when the adsorbate is occupying multiple sites on the surface, such that the adsorption energy is a continuous function of the number of molecules on the surface [e.g. Amiaud et al., 2006]. By inverting Equation (5.4), a TPD spectrum can be converted to a function, $E(N)$, given by:

$$E(N) = -kTln\frac{r\beta}{AN}. \tag{6.2}$$

Table 6.2. Multilayer desorption parameters calculated using Equation (5.4), compared to previous literature values *in italics*.

Molecule	Surface	Calculated values [a] ν /10^{26} molec cm^{-2}s^{-1}	E_{ads} /K
O_2	$H_2O_{(np)}$	6.9	898(3)
	$H_2O_{(c)}$	7.0	936(12)
	SiO_x	6.9	895(9)
	Au	*6.9*	*912(15)*[b]
		...	*925(25)*[c]
CO	$H_2O_{(np)}$	7.1	828(3)
	$H_2O_{(c)}$	7.1	849(30)
	SiO_x	7.1	831(15)
	Au	*7.2*	*858(15)*[b]
		...	*826(24)*[d]
		...	*855(25)*[e]
CO_2	$H_2O_{(np)}$	9.3	2267(3)
		...	*2490(24)*[f]
	$H_2O_{(c)}$	9.5	2356(12)
		...	*2393(24)*[f]
	SiO_x	9.3	2269(12)
	porous ASW	...	*2690(50)*[g]
	HOPG	...	*2982(-)*[h]

[a]For values calculated in this work, the values in parentheses are the 3 σ statistical errors on E_{ads} calculated during the fit of Equation (5.4). In all other cases the error is as quoted in the relevant literature.

[b]Acharyya et al. [2007], using an identical multilayer modelling method. [c]Fuchs et al. [2006], calculated assuming a fixed pre-exponential factor. [d]Collings et al. [2003b], calculated assuming a fixed pre-exponential factor. [e]Öberg et al. [2005]; Fuchs et al. [2006]; Bisschop et al. [2006], calculated assuming a fixed pre-exponential factor. [f]Gálvez et al. [2007], calculated using spectroscopic data, assuming a first order desorption profile. [g]Sandford & Allamandola [1990], calculated using spectroscopic data, assuming a first order desorption profile. [h]Burke & Brown [2010], calculated empirically with a non-integer reaction order.

To fit $E(N)$ for each molecule-surface system, the TPD spectrum corresponding to the surface exposure just prior to the appearance of multilayer peaks, or (in the case of CO_2) more complex desorption characteristics, is selected and defined as the monolayer coverage, i.e. $\theta = N/N_{mono} = 1$, ensuring that the maximum range of adsorption sites and energies at the surface are included. This is a very reasonable approach, given that it is well known that $E(N)$ is independent of reaction order at exactly $N = N_{mono}$ [Ulbricht et al., 2006]. This monolayer TPD is then fitted using an analytical expression of $E(N)$, redefined in terms of surface coverage, $E(\theta)$, given by:

$$E(\theta) = \alpha_0 + \alpha_1\,\theta + \alpha_2\,\theta^2 + \alpha_3\,e^{\alpha_4\,\theta} + \alpha_5\,e^{\alpha_6\,\theta} + \alpha_7\,e^{\alpha_8\,\theta} + \alpha_9\,e^{\alpha_{10}\,\theta}. \qquad (6.3)$$

The resulting coefficients α_0 – α_{10} are listed in Table 6.3 and can be used to calculate $E(\theta)$ from Equation (6.3), which can then be substituted into Equation (6.2), along with an appropriate value for A, to reproduce all sub-monolayer TPD data for a specific molecule-surface system.

As the choice of A has a large effect on the value of $E(\theta)$ calculated from the model, the first analytical method attempted was to reproduce the sub-monolayer coverages by concurrently optimising A and $E(N)$ [Stirniman et al., 1996]. During the calculation of $E(N)$, A is set at a fixed range of values from 10^5 – 10^{15} s^{-1}. The optimal value of A is that which minimises the difference between the functions $E(N)$ for each sub-monolayer coverage in terms of least-squares. This method was not successful for all molecule-surface combinations, as there was not always a minimum in the least-squares calculation. In those cases where a minimum was calculated, the corresponding A value was found to be significantly lower than the expected value (typically around 10^6 s^{-1}, whereas the actual A expected was 10^{12} –10^{13} s^{-1}). This optimisation method for A assumes that there is no difference in the occupation of the high energy binding sites (i.e. the tail of the TPD spectra) with increasing coverage. Thus, all $E(N)$ calculated for a given A value should coincide at low coverage; in these experiments, there were some minor differences in the tails of the TPD spectra, and consequently this method could not be successfully applied to the data, and was rejected. To reproduce the TPD spectra at sub-monolayer coverages, A was fixed at 10^{12} s^{-1}.

Table 6.3. Calculated coefficients to describe $E(\theta)$, as in Equation (6.3).

Molecule	Surface	Coefficients α_0	α_1	α_2	α_3	α_4	α_5
O_2	$H_2O_{(np)}$	0.094	0.	0.	0.036	-4.276	0.008
	$H_2O_{(c)}$	0.097	0.	0.	0.050	-324.639	0.023
	SiO_x	0.107	-0.023	0.006	0.010	-295.271	0.033
CO	$H_2O_{(np)}$	-0.100	0.	0.	0.227	-0.148	0.060
	$H_2O_{(c)}$	0.086	0.	0.	0.032	-342.830	0.011
	SiO_x	0.066	0.	0.	0.062	-1.380	0.035
CO_2	$H_2O_{(np)}$	0.214	-0.105	0.211	0.070	-141.810	-0.043
	$H_2O_{(c)}$	0.250	-0.010	0.	0.030	-86.765	-0.036
	SiO_x	0.265	0.	0.	0.048	-38.447	-0.020

Molecule	Surface	Coefficients α_6	α_7	α_8	α_9	α_{10}
O_2	$H_2O_{(np)}$	-78.201	-4.589×10^{-07}	9.005	0.053	-460.690
	$H_2O_{(c)}$	-2.733	-1.264×10^{-07}	9.713	0.016	-22.691
	SiO_x	-7.531	-5.150×10^{-08}	10.460	0.024	-96.024
CO	$H_2O_{(np)}$	-436.840	-1.145×10^{-06}	9.304	0.013	-11.647
	$H_2O_{(c)}$	-25.851	-1.534×10^{-08}	13.337	0.048	-0.820
	SiO_x	-10.856	-1.187×10^{-07}	9.379	0.	0.
CO_2	$H_2O_{(np)}$	2.046	1.750×10^{-06}	9.416	0.072	1.079
	$H_2O_{(c)}$	-1779.430	-8.078×10^{-09}	9.970	0.024	-6.452
	SiO_x	0.712	-4.007×10^{-07}	9.395	0.081	-4.515

To successfully reproduce all the TPD data, from sub-monolayer to multilayer regimes, the results from the two coverage models are then combined, such that (a) when $\theta \leq 1$, in Equation (5.4), E_{ads} is replaced by $E(N)$ (derived from Equation (6.3)), n = 1, and $N \leq N_{mono}$, or (b) when $\theta > 1$, the TPD is the sum of the monolayer trace generated in (a), plus Equation (5.4), where E_{ads} is taken from Table 6.2, A defined by Equation (6.1), n = 0, and N is redefined as $N - N_{mono}$.

6.4.3 Discussion

From Figure 6.3, it is clear that the combined model can very accurately reproduce the desorption profiles of all molecular species on all surfaces (O_2, CO and CO_2 on $H_2O_{(np)}$, $H_2O_{(c)}$ and SiO_x). In particular, the model faithfully re-

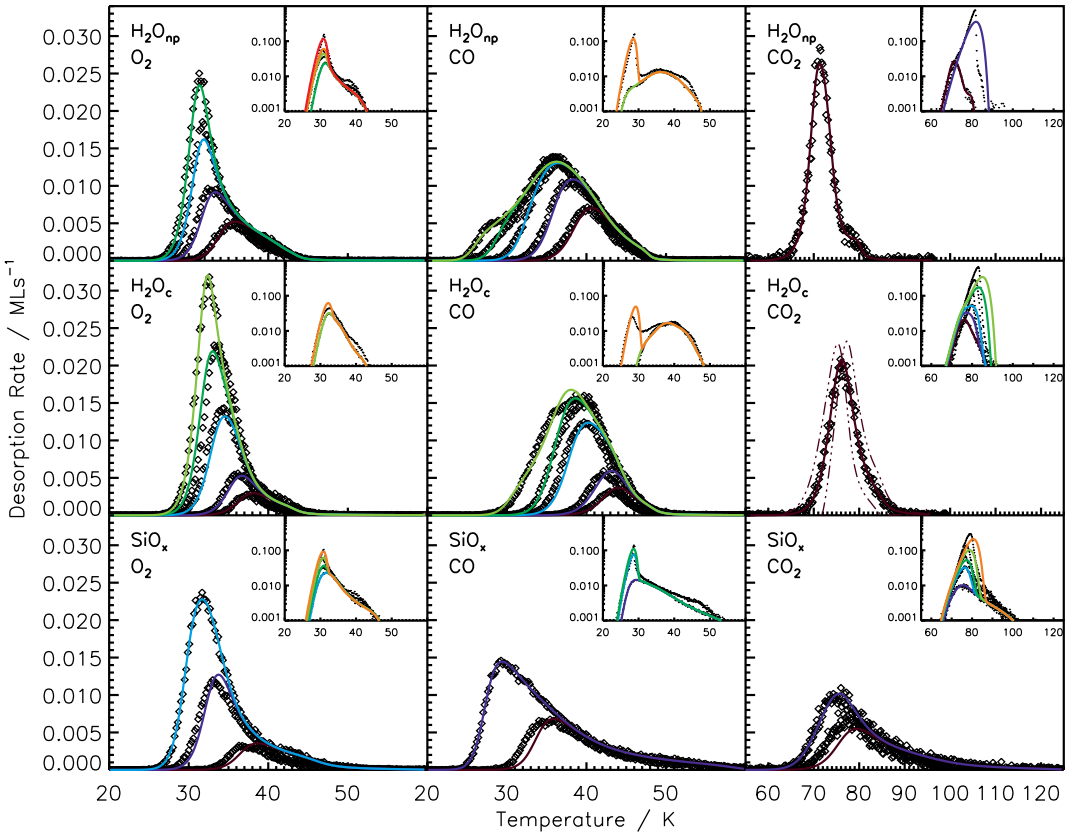

Figure 6.3. Modelled temperature-programmed desorption spectra. Experimental data, as in Figure 6.1 are plotted in black diamonds; coverages up to and including 1 ML are shown in the main window, with coverages of 1 ML and greater inset. Model data is overplotted as coloured lines. Typical 3σ errors on the model are overplotted as dot-dashed lines on the plot of CO_2 on $H_2O_{(c)}$ only, for clarity. Some of the original TPD data are omitted for clarity (see Table 6.1).

produces the sub-monolayer coverage TPD spectra. Although in a few cases the model data do not perfectly describe the empirical line profiles, the two clearly coincide within the 3 σ errors on the model, as illustrated by the over-plotted dot-dashed lines on the sub-monolayer coverage of CO_2 on $H_2O_{(c)}$. These errors are omitted from all the other plots for clarity. The errors result from the assumption that all the TPD spectra are concurrent in the highest energy binding sites, i.e. their tails overlap, which is a necessary assumption when applying this model.

The multilayer TPD spectra, and their associated fits, are shown in the insets in Figure 6.3. Most importantly, as noted previously from the experimental data,

Table 6.4. Calculated values of $E(\theta)$ at a range of sub-monolayer surface coverage values, calculated using Equation (6.3) and the coefficients from Table 6.3. All values are in K.

Molecule	Surface	$E(\theta = 0.1)$	$E(\theta = 0.2)$	$E(\theta = 0.5)$	$E(\theta = 0.9)$	$E(\theta = 1.0)$
O_2	$H_2O_{(np)}$	1161	1082	972	928	914
	$H_2O_{(c)}$	1149	1092	1017	975	969
	SiO_x	1255	1146	1019	945	930
CO	$H_2O_{(np)}$	1307	1247	1135	956	863
	$H_2O_{(c)}$	1330	1288	1199	1086	1009
	SiO_x	1418	1257	1045	896	867
CO_2	$H_2O_{(np)}$	2346	2258	2197	2197	2236
	$H_2O_{(c)}$	2514	2451	2364	2341	2361
	SiO_x	3008	2798	2487	2317	2271

the model data also show that multilayer desorption begins at the same temperature for each molecule-surface combination (the leading edges of the TPDs are identical), although the onset of this desorption occurs at a higher temperatures on the $H_2O_{(c)}$ surface when compared with the amorphous $H_2O_{(np)}$ and SiO_x surfaces. From Table 6.2 it is clear that E_{ads} is consistently marginally greater on the crystalline surface, as compared to the amorphous surfaces, resulting in slightly lower desorption rates from crystalline surfaces, and the later onset (in time or temperature) of the desorption process. This trend is even consistent with previously reported results (see Table 6.2). Given that species such as CO, CO_2 and O_2 could be present on interstellar ices or grains at multilayer coverages of up to a few ML, this result indicates that a similar effect from underlying surface crystallinity could be relevant in interstellar regions. This is addressed further in § 6.5.

Surprisingly, given its ubiquity in interstellar ices, the multilayer desorption energy of pure CO_2 ice is not widely reported in the literature. One value has been measured previously from multilayers of CO_2 on HOPG [Burke & Brown, 2010], where analysis proved that the reaction order is zero, and estimated the magnitude of the pre-exponential factor at around 10^{30}. However, consistent with the rather complex TPD spectra shown in grey in the insets on Figure 6.1, it was very difficult to undertake a detailed analysis of multilayer CO_2 desorption from the HOPG surface. Consequently, the value of E_{ads} quoted by Burke & Brown [2010] is not only somewhat higher than the value calculated here,

but also has a quoted error greater than the value of E_{ads} itself ($\pm$ 19484 K , which is omitted from Table 6.2 for clarity). Three other multilayer CO_2 desorption measurements are claimed in the literature, as indicated in Table 6.2; unfortunately all three were determined from transmission infrared data, assuming the desorption kinetics were first and not zeroth order. Consequently, although included for completeness, as the values are often quoted in models, the numbers are not comparable to the results quoted here.

For multilayer coverages of CO and O_2 , the E_{ads} calculated from this model can be compared directly to previous (multilayer) results in the literature (see Table 6.2). Within the errors, these results for CO and O_2 on $H_2O_{(c)}$ - a crystalline surface - are identical to those obtained previously by Acharyya et al. [2007] for O_2 and CO on a polycrystalline Au substrate, using the same fitting method. This last point is particularly relevant when comparing the results, as both here and in Acharyya et al. [2007] the parameterisation of the fit is reduced to one by expressing the pre-exponential factor in terms of E_{ads}. Consequently, the pre-exponential factor calculated here also correlates well with that reported by Acharyya et al. [2007] previously. Even though the calculated E_{ads} for the amorphous surfaces are slightly lower than the result from the $H_2O_{(c)}$ surface, they also are consistent, within the 3 σ error, with the values from Acharyya et al. [2007]. The other values of E_{ads} listed in Table 6.2 for CO and O_2 on polycrystalline Au [Collings et al., 2003b; Öberg et al., 2005; Fuchs et al., 2006; Bisschop et al., 2006], were calculated assuming a fixed pre-exponential factor (A) of magnitude around 10^{30}: as A and E_{ads} are not mutually exclusive, it is not possible to make a direct comparison between literature data and the results presented here. However, it is interesting to note that, despite a difference of over four orders of magnitude in the value of the pre-exponential factor, the reported values of E_{ads} are all remarkably consistent. The only uncertainty remaining is the extent to which these subtle differences in the value of E_{ads} affect the desorption of ice multilayers in interstellar space, and how to account for such subtleties in gas-grain models (see Section 6.5).

In modelling the sub-monolayer desorption of key interstellar molecules from different surfaces, the aim was to provide the chemical modelling community with a useful equation (Equation (6.3) and Table 6.3) for mathematically describing the desorption characteristics of the surfaces, as well as an indication

of the coverage at which a particular adsorbate's behaviour switches from the sub-monolayer to the multilayer regimes (a measure of N_{mono}). The excellent agreement between experimental data and the model is also validation of the method employed here, described in § 6.4.2. The only limitation of this method is the certainty with which the TPD curve which most closely matches – not the monolayer adsorbate exposure, but rather the monolayer coverage of each surface – was selected. Of all the data fitted here, only the CO ice systems show minute deviations at the highest sub-monolayer coverages. Such effects could be due to CO (the smallest molecule studied) being able to probe defects and cracks in the ice surface prior to forming a multilayer, as described previously in studies of CO on ASW [Collings et al., 2003a,b], an effect omitted from this model. This may also explain why, in these systems, it is difficult to reproduce a perfect match in the transition regime between the monolayer and multilayer coverages. Although the fits shown here to the CO_2 ice systems are excellent, a number of 'intermediate' TPD spectra, shown in grey in Figure 6.1, with double and triple TPD peaks, had to be omitted from the modelling process. These spectra are indicative of 2D island growth on a surface, as seen in the formation of N_2 ices [Öberg et al., 2005], and indicate that the growth mechanism of CO_2 on ice surfaces is different to that of CO or O_2. While each island is entirely independent of all others on the surface, and there is no diffusion between them or bridges linking them, it is assumed that the regime is a sub-monolayer coverage. Once the islands have fully merged and overlayers of CO_2 ice form, then the multilayer regime has been reached. Nevertheless, such effects should not detract from the broad applicability of the sub-monolayer model. Furthermore, as a general rule, the outcome of the monolayer TPD choice suggests that for CO and O_2 it is reasonable to assume $N_{mono} = 10^{15}$, whereas for CO_2 it is around $N_{mono} = 10^{14}$. This result is consistent with the exposures discussed previously in Figure 6.2 and reflects the CO_2 island growth.

As can be seen from the main plots in Figure 6.3, at very low coverages (< 0.5 ML) there is sometimes a small deviation in the leading edge of the modelled desorption compared to the experimental results, most evident on the SiO_x surface. Although this lies within the error range of the fitting, there are two potential explanations for why such discrepancies could arise, both of which are related to the assumption made in the model that all desorptions from a given surface share the same TPD trailing edge profile. As the sites in the

tail of the TPD are the most energetically favourable, it follows that any adsorbate able to diffuse across the surface will bind most readily to these sites, occupying them first on adsorption and last on desorption. Such an effect has clearly been seen previously with H_2 and D_2 on ice surfaces [Amiaud et al., 2006]. Even under ultra-high vacuum conditions, molecules such as H_2, CO and H_2O are still present in the experimental chamber, all be it at very low concentrations (partial pressures around 10^{-13} – 10^{-14}). Consequently, over the very long timescales required to complete the experiments described here (14 – 16 hours for each molecule-surface combination), it is potentially possible that some of the surface sites could be dynamically occupied for a short period by a 'pollutant' adsorbate, thus blocking the adsorbate molecule of interest from occupying a highest energy binding site. Such an effect would lead to increased occupation of the lower energy binding sites and discrepancies between the experimental and model data, the latter appearing at slightly higher temperatures. This effect would not have been evident in the work of Amiaud et al. [2006] because they were only cyclically heating their ice surfaces between 10 and 30 K, and consequently could complete the experiment on a much shorter timescale than was possible here. As H_2 and CO are reasonably volatile pollutants, the build up of H_2O would be most likely to have an effect on the nature of the surface, and such an effect would be most evident on the SiO_x surface. However as the experimental sequence was always run from low to high coverage, if this were the key reason for any discrepancy, it should be more pronounced as the monolayer coverage data is reached. Evidently this is not the case.

It is also important to consider mass effects; in comparison to the H_2 ice system studied previously [Amiaud et al., 2006], CO, O_2 and CO_2 are more massive molecules, and therefore likely to diffuse more slowly on the surfaces. Therefore, unlike the H_2, when deposited on the surface at relatively low concentrations, CO, O_2 and CO_2 may not sample all the binding sites before adsorbing, but rather ballistically deposit in a 'stick and stop' process. Subsequently, during application of the TPD heating ramp, all the molecules will diffuse, but the heavier molecules may not fully sample the surface before desorbing. Then, at very low coverages, not all the highest energy binding sites will be occupied, and the TPD tails may not be quite coincident. As a result, the model would slightly underestimate the leading edge of such TPD curves. From this expla-

nation it is also possible to rationalise why the discrepancy between the model and empirical data would be greatest for the SiO_x surface; the breadth of the sub-monolayer TPD peaks from the molecule-silicate systems in comparison to the molecule-ice systems clearly indicates a broader range of binding sites on the SiO_x surface. By contrast, the water surfaces have a narrow, and an energetically similar range of binding sites, which may also intimate that the ice surfaces do not have many dangling bonds or much proton disorder in them [Fraser et al., 2004]. This is contrary to what might be expected, as it is often assumed that amorphous water ice potentially has a very broad range of binding sites at its surface. However, without spectroscopic data it is not possible to comment further on this. Consequently, the probability of sampling the highest energy binding sites is even lower at low coverages on SiO_x than the ice surfaces, provided that the diffusion rates on all three surfaces are approximately equal. Nevertheless, these tiny differences should not detract from the overall quality of the fits, nor that the model can be executed whilst ignoring the pumping speed in the chamber; this is because in FORMOLISM the pumping is so effective that as soon as a molecule desorbs from the surface it is effectively removed from the chamber, much like conditions in the ISM. In experiments without such efficient pumping, the experiments described here would be impossible to undertake, as the TPD tails would never overlap.

To compare the $E(\theta)$ calculated here with previous adsorption energy values of CO, O_2 and CO_2 as reported in the literature, the values in Table 6.4 were calculated. This illustrates the specific values of $E(\theta)$ for each molecule on each surface at coverages ranging from $\theta = 0.1 - 1.0$. The errors on each energy value are determined by the error on the fit to the experimental data and are around $\pm$ 25 K in all cases. The comparison is complicated by the fact that no previous study has fitted coverage dependent adsorption energies for these particular molecules at sub-monolayer coverages on surfaces of astrophysical relevance. In general, the effective adsorption energy is higher at lower coverage – reflecting the fact that the highest energy binding sites are occupied first – and tends towards the calculated multilayer value for the same molecule-surface system as the coverage increases to that of one monolayer. Although, upon reaching the monolayer coverages, the binding energy on the crystalline surface is consistently higher than on the amorphous surfaces, the same is not true at lower coverages.

Previous studies using different methods have reported the monolayer energy of CO as: 1564 ± 120 K on HOPG [Ulbricht et al., 2006], 1624 ± 360 K on meteorite [Mautner et al., 2006], and 1179 ± 24 K on a highly porous ASW [Collings et al., 2003b]. The calculated values for CO on the ice surfaces cover a range of values including the result of Collings et al. [2003b], and at the lowest coverages, the calculated value on the SiO_x surface is closer to that reported for HOPG. It is pertinent to compare the lowest coverage value, since the HOPG data were measured in a molecular beam scattering experiment, indicating that only a low concentration, with a dynamic coverage, was resident on the HOPG surface for a relatively short time, and therefore must have been occupying the highest energy binding sites. The meteorite sample would doubtless encompass a much wider variety of binding sites than even the amorphous silicate used here, so it is not surprising that the desorption energy is even higher on this surface. This excellent agreement between these results and previous results is further justification that the model is viable and effectively reproduces the effects of sub-monolayer desorption from a variety of interstellar-relevant surfaces.

For O_2, previously calculated sub-monolayer energies are: 1082 ± 120 K on HOPG [Ulbricht et al., 2006], and 1203 K on graphite [Bojan & Steele, 1987]. Again, the values calculated at the lowest coverages on SiO_x compare favourably with previously reported values from carbonaceous surfaces. The desorption energy of the CO_2 monolayer has been calculated as: 2766 ± 241 K on HOPG [Ulbricht et al., 2006], 3079 ± 20 K on graphite [Terlain & Larher, 1983], and 2553 ± 232 K on $H_2O_{(c)}$ [Andersson et al., 2004]. The range of the calculated data compares favourably with these literature values; in particular, at the lowest coverages, the value of $E(\theta)$ for CO_2 on SiO_x is consistent with the molecular beam scattering result from HOPG, and the value of $E(\theta)$ for CO_2 on $H_2O_{(c)}$ is identical (within the quoted errors) to that measured by Andersson et al. [2004]. Both studies were based upon a molecular beam scattering experiment, and therefore probed the highest energy binding sites for CO_2 on the crystalline ice and HOPG surfaces. Such excellent overlap between the results verifies both that the choice of TPD spectrum to define as the monolayer coverage for CO_2 on the ice surfaces was the appropriate one, and also the calculation of N_{mono}.

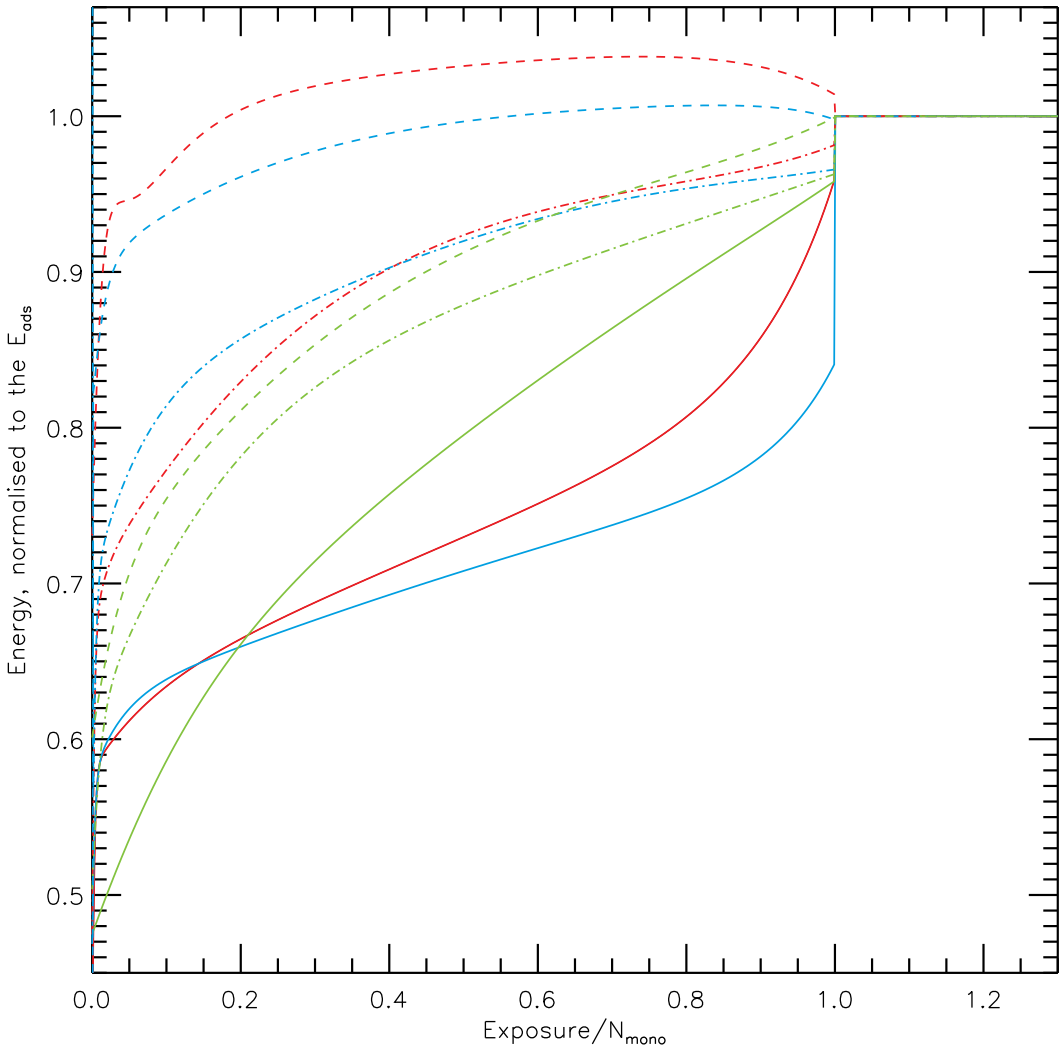

Figure 6.4. Total modelled energy as a function of exposure/N_{mono} for all molecule-surface combinations. Plots are as follows: O_2 dot-dashed, CO solid, CO_2 dashed; $H_2O_{(np)}$ red, $H_2O_{(c)}$ blue, SiO_x green.

The adsorption behaviour of the molecule-surface combinations can be divided into roughly three categories related to the difference between the multilayer energy (or adsorbate-adsorbate interactions) and the energy distribution of the surface adsorption sites. These behaviours can be explained with reference to Figure 6.4, a plot of the modelled energy as a function of coverage, $E(\theta)$. Where the energy of the multilayer is significantly higher than the energy distribution at coverages below 1 ML, as is the case for CO on $H_2O_{(c)}$, molecules will preferentially adsorb onto the substrate at low coverages, rather

Table 6.5. Adsorption behaviour of each molecule-surface combination, estimated from the modelled energies in Tables 6.2 & 6.3 and the desorption characteristics in Figure 6.1.[a]

Molecule	Surface	Adsorption behaviour
O_2	$H_2O_{(np)}$	Full wetting
	$H_2O_{(c)}$	Full wetting
	SiO_x	Full wetting / Intermediate
CO	$H_2O_{(np)}$	Full wetting
	$H_2O_{(c)}$	Full wetting
	SiO_x	Full wetting / Intermediate
CO_2	$H_2O_{(np)}$	Non-wetting
	$H_2O_{(c)}$	Non-wetting
	SiO_x	Non-wetting / Intermediate

[a] 'Full wetting' behaviour is seen for molecules which fill all the lowest energy sites on the surface before forming a multilayer. 'Intermediate' behaviour is when the molecules start to fill the surface, but form islands before it is full. 'Non-wetting' behaviour is when islands are almost immediately formed by molecules on the surface.

than starting to form a multilayer or island. In this 'full wetting' regime, the multilayer appears only after all of the sites on the surface are filled. Where the multilayer energy is lower than the monolayer energy, such as for CO_2 on $H_2O_{(np)}$, molecules preferentially form islands on the surface at very low coverages, well before 1 ML, and a multilayer is rapidly reached in this 'non-wetting' regime. These two regimes can be further contrasted by considering the TPD spectra of CO on $H_2O_{(c)}$ versus those of CO_2 on $H_2O_{(np)}$ in Figure 6.1. CO_2 rapidly forms a double peaked multilayer while CO shows a gradual filling of the surface sites before a multilayer forms. Intermediate between these two regimes, molecules first fill the lowest energy surface sites, before starting to form islands close to the multilayer energy. The boundaries between these three states are difficult to define, but the behaviour of each molecule-surface combination is estimated in Table 6.5.

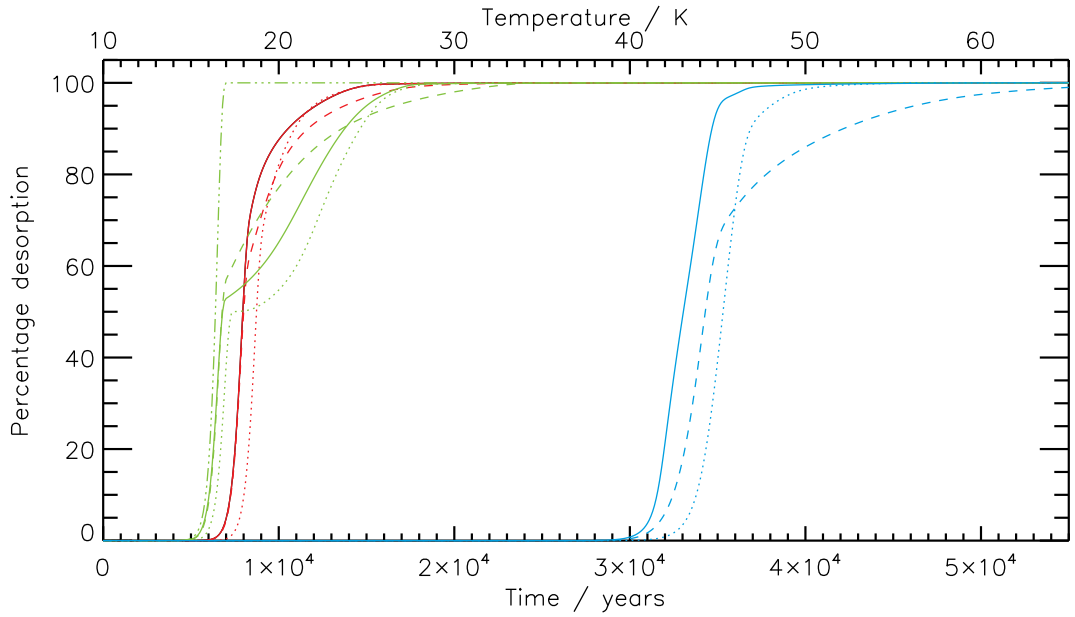

Figure 6.5. The simulated desorption of 2 ML of CO (green), O_2 (red) and CO_2 (blue) from $H_2O_{(np)}$ (solid), $H_2O_{(c)}$ (dotted) and SiO_x (dashed) at a heating rate of 1 Kcentury^{-1}. For comparison, the dot-dashed line shows the modelled desorption characteristics of CO on $H_2O_{(np)}$ if only multilayer desorption is included in the model.

6.5 Astrophysical Implications

Under astrophysical conditions, the heating rate is likely to be on the order of 1 Kcentury^{-1} (hot core heating rate [Viti & Williams, 1999]), many orders of magnitude slower than the laboratory value of 10 Kmin^{-1} employed here. By simulating the desorption profiles of the molecule-surface combinations here, it is possible to investigate whether surface type is likely to affect desorption characteristics on astrophysically relevant timescales. Figure 6.5 presents the results of such a simulation for all molecule-surface combinations. It is clear that, while the molecules desorb at different times (and temperatures), there is a clear pattern to the order of desorption from the various substrates. Desorption from $H_2O_{(np)}$ and SiO_x occur almost concurrently for all species, while desorption from $H_2O_{(c)}$ occurs later, at a higher temperature. The residence time of molecules on a $H_2O_{(c)}$ surface is significantly higher than on the amorphous surfaces. Starting from a 2 ML coverage, the time taken for 50 % of the

O_2 on SiO_x or $H_2O_{(np)}$ to desorb is 8000 years, while on $H_2O_{(c)}$ this value is 8700 years, an increase of 8.75 %. Similarly, the difference between desorption of 50 % of the molecules from $H_2O_{(np)}$ and from $H_2O_{(c)}$ is 8.82 % for CO and 6.97 % for CO_2.

In Figure 6.5, the dot-dashed line shows the modelled desorption characteristics of 2 ML of CO from $H_2O_{(np)}$ if only multilayer desorption is considered. It is evident that without including the sub-monolayer component of the model, the desorption time is vastly underestimated (by over 10,000 years for full desorption). Thus sub-monolayer desorption characteristics are fundamental to describing the overall desorption profile of species on astrophysical timescales.

Green et al. [2009] conclude that, while surface type is important, it is ultimately the heating rate and grain size that dominate desorption kinetics; the results presented here, however, suggest that the surface type is still very important under conditions where the heating rate and grain size are constants. Furthermore, the definition of surface type must include both the surface material and the degree of crystallinity, and not simply the material. From the data presented here, it is clear that the desorption characteristics of molecular species from $H_2O_{(np)}$ and SiO_x, two amorphous surfaces, are much more similar than those from $H_2O_{(np)}$ and $H_2O_{(c)}$, which are composed of the same underlying material.

6.6 Conclusions

Temperature programmed desorption was used to measure the desorption characteristics of O_2, CO and CO_2 from $H_2O_{(np)}$, $H_2O_{(c)}$ and SiO_x. The experimental data was modelled using the Polanyi-Wigner equation in both sub-monolayer and multilayer coverage regimes, proving that it is possible to model the complete desorption of a molecular species with a simple combined model. As it is rather trivial to model the energy distribution $E(\theta)$, it is believed that this approach could be easily integrated into current chemical models.

Results suggest that the morphology of the underlying surface is very important, even on an astrophysically relevant timescale, as the desorption characteristics of molecules from the amorphous substrates $H_2O_{(np)}$ and SiO_x were

found to be very similar, while molecules desorbed from the crystalline $H_2O_{(c)}$ at higher temperatures and on a longer timescale. The desorption can be categorised as 'full wetting', 'intermediate' or 'non-wetting', and the degree of wetting critically governs the interaction of molecules with the surface, and therefore their desorption characteristics.

These laboratory results suggest that is it possible to retain CO on the surface for a long time, especially if the surface is composed of SiO_x, posing the observational question: could CO_2 form from CO on grain surfaces at very low coverages. It is possible that CO is present on grain surfaces at early times, before the critical freeze-out of most of the CO, at abundances too low to observe. If that were the case, then the CO_{gg} component (introduced in Chapter 4) and its interaction with the grain surface would be important for the chemistry in these regions, and investigations of reactions at sub-monolayer coverages are vital to understanding potential chemical mechanisms active at low grain coverages.

References

Accolla, M., et al. 2011, Physical Chemistry Chemical Physics (Incorporating Faraday Transactions), 13, 8037

Acharyya, K., Fuchs, G. W., Fraser, H. J., van Dishoeck, E. F., & Linnartz, H. 2007, A&A, 466, 1005

Acharyya, K., Hassel, G. E., & Herbst, E. 2011, ApJ, 732, 73

Amiaud, L., Fillion, J. H., Baouche, S., Dulieu, F., Momeni, A., & Lemaire, J. L. 2006, J. Chem. Phys., 124, 094702

Andersson, P. U., Nagard, M. B., Witt, G., & Pettersson, J. B. C. 2004, J. Phys. Chem. A, 108, 4627

Bisschop, S. E., Fraser, H. J., Öberg, K. I., van Dishoeck, E. F., & Schlemmer, S. 2006, A&A, 449, 1297

Bojan, M. J., & Steele, W. A. 1987, Langmuir, 3, 1123

Brown, W. A., & Bolina, A. S. 2007, MNRAS, 374, 1006

Burke, D. J., & Brown, W. A. 2010, PCCP, 12, 5947

Collings, M. P., Dever, J. W., Fraser, H. J., McCoustra, M. R. S., & Williams, D. A. 2003a, ApJ, 583, 1058

Collings, M. P., Dever, J. W., Fraser, H. J., & McCoustra, M. R. S. 2003b, Ap&SS, 285, 633

Collings, M. P., Anderson, M. A., Chen, R., Dever, J. W., Viti, S., Williams, D. A., & McCoustra, M. R. S. 2004, MNRAS, 354, 1133

Collings, M. P., Dever, J. W., & McCoustra, M. R. S. 2005, Chem. Phys. Lett., 415, 40

Cuppen, H. M., & Garrod, R. T. 2011, A&A, 529, A151

Dohnalek, Z., Kim, J., Bondarchuk, O., White, J. M., & Kay, B. D. 2006, J. Phys. Chem. B, 110, 6229

Draine, B. T. 2003, ARA&A, 41, 241

Elsila, J., Allamandola, L. J., & Sandford, S. A. 1997, ApJ, 479, 818

Ertl, G., Neumann, M., & Streit, K. M. 1977, Surface Science, 64, 393

Fraser, H. J., Collings, M. P., McCoustra, M. R. S., & Williams, D. A. 2001, MNRAS, 327, 1165

Fraser, H. J., McCoustra, M. R. S., & Williams, D. A. 2002, Astronomy and Geophysics, 43, 020000

Fraser, H. J., Collings, M. P., Dever, J. W., & McCoustra, M. R. S. 2004, MNRAS, 353, 59

Fraser, H. J., Bisschop, S. E., Pontoppidan, K. M., Tielens, A. G. G. M., & van Dishoeck, E. F. 2005, MNRAS, 356, 1283

Frenklach, M., Huang, D., Thomas, R. E., Rudder, R. A., & Markunas, R. J. 1993, Appl. Phys. Lett., 63, 3090

Fuchs, G. W., et al. 2006, Faraday Discussions, 133, 331

Gálvez, O., Ortega, I. K., Maté, B., Moreno, M. A., Martín-Llorente, B.,Herrero, V. J., Escribano, R., & Gutiérrez, P. J. 2007, A&A, 472, 691

Goumans, T. P. M., Uppal, M. A., & Brown, W. A. 2008, MNRAS, 384, 1158

Green, S. D., Bolina, A. S., Chen, R., Collings, M. P., Brown, W. A., & McCoustra, M. R. S. 2009, MNRAS, 398, 357

Ioppolo, S., Cuppen, H. M.,Romanzin, C., van Dishoeck, E. F., & Linnartz, H. 2008, ApJ, 686, 1474

Ioppolo, S., van Boheemen, Y., Cuppen, H. M., van Dishoeck, E. F., & Linnartz, H. 2011, MNRAS, 413, 2281

Jewitt, D. C., & Luu, J. 2004, Nature, 432, 731

Lakhlifi, A., & Killingbeck, J. P. 2010, Surface Science, 604, 38

Lemaire, J. L., Vidali, G., Baouche, S., Chehrouri, M., Chaabouni, H., & Mokrane, H. 2010, ApJL, 725, L156

Li, A., & Draine, B. T. 2002, ApJ, 564, 803

Lisse, C. M., et al. 2006, Science, 313, 635

Matar, E., Bergeron, H., Dulieu, F., Chaabouni, H., Accolla, M., & Lemaire, J. L. 2010, J. Chem. Phys., 133, 104507

Mathis, J. S. 1998, ApJ, 497, 824

Mautner, M. N., Abdelsayed, V., El-Shall, M. S., Thrower, J. D., Green, S. D., Collings, M. P., & McCoustra, M. R. S. 2006, Faraday Discussions, 133, 103

Merlin, F., Guilbert, A., Dumas, C., Barucci, M. A., de Bergh, C., & Vernazza, P. 2007, A&A, 466, 1185

Noble, J. A., Dulieu, F., Congiu, E., & Fraser, H. J. 2011, ApJ, 735, 121

Oba, Y., Miyauchi, N., Hidaka, H., Chigai, T., Watanabe, N., & Kouchi, A. 2009, ApJ, 701, 464

Öberg, K. I., van Broekhuizen, F., Fraser, H. J., Bisschop, S. E., van Dishoeck, E. F., & Schlemmer, S. 2005, ApJL, 621, L33

Omont, A., Forveille, T., Moseley, S. H., Glaccum, W. J., Harvey, P. M., Likkel, L., Loewenstein, R. F., & Lisse, C. M. 1990, ApJL, 355, L27

Pontoppidan, K. M., et al. 2003, A&A, 408, 98

Pontoppidan, K. M. 2006, A&A, 453, L47

Raval, R., Haq, S., Harrison, M. A., Blyholder, G., & King, D. A. 1990, Chem. Phys. Lett., 167, 391

Sandford, S. A., & Allamandola, L. J. 1990, ApJ, 355, 357

Schegerer, A. A., & Wolf, S. 2010, A&A, 517, A87

Smith, R. G., Sellgren, K., & Brooke, T. Y. 1993, MNRAS, 263, 749

Sofia, U. J., & Meyer, D. M. 2001, ApJL, 554, L221

Stirniman, M. J., Huang, C., Smith, R. S., Joyce, S. A., & Kay, B. D. 1996, J. Chem. Phys., 105, 1295

Terlain, A., & Larher, Y. 1983, Surface Science, 125, 304

Tielens, A. G. G. M. 2005, The Physics and Chemistry of the Interstellar Medium, Cambridge University Press

Ulbricht, H., Zacharia, R., Cindir, N., & Hertel, T. 2006, Carbon, 44, 2931

Visser, R., van Dishoeck, E. F., Doty, S. D., & Dullemond, C. P. 2009, A&A, 495, 881

Viti, S., & Williams, D. A. 1999, MNRAS, 305, 755

Wakelam, V., et al. 2010, Space Sci. Rev., 156, 13

Wang, S.-X., Yang, Y., Sun, B., Li, R.-W., Liu, S.-J., & Zhang, P. 2009, Phys. Rev. B, 80, 115434

Whittet, D. C. B., Bode, M. F., Longmore, A. J., Adamson, A. J., McFadzean, A. D., Aitken, D. K., & Roche, P. F. 1988, MNRAS, 233, 321

Williams, D., & Herbst, E. 2002, Surface Science, 500, 823

CHAPTER 7

CO_2 FORMATION IN QUIESCENT CLOUDS; AN EXPERIMENTAL STUDY OF THE CO + OH PATHWAY†

7.1 Synopsis

The formation of CO_2 in quiescent regions of molecular clouds is not yet fully understood, despite CO_2 having an abundance of around 10 – 34 % H_2O. As suggested in the previous chapter, the formation of CO_2 from CO adsorbed on the dust grain surface at early stages in a molecular cloud could be an important formation scenario, as yet outwith observational limitations. The reaction of CO + OH could also be important to explaining the component of CO_2 observed in a CO-rich ice, as suggested in Chapter 4. This chapter presents a study of the formation of CO_2 via the non-energetic route CO + OH on non-porous H_2O and amorphous silicate surfaces. Results are in the form of temperature programmed desorption spectra of CO_2 produced via two experimental routes: O_2 + CO + H and O_3 + CO + H. The maximum yield of CO_2 is around 8 % with respect to the starting quantity of CO, suggesting a barrier to CO + OH. The rate of reaction, based on modelling results, is 24 times slower than O_2 + H. The model suggests that competition between CO_2

†This chapter is based upon results published in Noble, J. A., Dulieu, F., Congiu, E., & Fraser, H. J., 2011, Astrophysical Journal, 735, 121 [Noble et al., 2011].

formation via CO + OH and other surface reactions of OH is a key factor in the low yields of CO_2 obtained experimentally, with relative reaction rates $k_{CO+H} \ll k_{CO+OH} < k_{H_2O_2+H} < k_{OH+H}, k_{O_2+H}$. Astrophysically, the presence of CO_2 in low A_V regions of molecular clouds could be explained by the reaction CO + OH occurring concurrently with the formation of H_2O via the route OH + H.

7.2 Introduction

As is evident from the results in Chapters 4 & 6, CO_2 is highly abundant in molecular clouds and has interesting desorption characteristics. The first observations of solid CO_2 were made by the InfraRed Astronomical Satellite (IRAS, D'Hendecourt & Jourdain de Muizon [1989]). The molecule has since been observed in numerous environments, including towards galactic centre sources [de Graauw et al. , 1996], massive protostars [Gerakines et al. , 1999; Gibb et al. , 2004], low mass young stellar objects (YSOs) [Nummelin et al. , 2001; Pontoppidan et al. , 2008], background stars [Knez et al. , 2005], and in other galaxies [Shimonishi et al. , 2010; Oliveira et al. , 2011]. Based on these observations, CO_2 is seen to be seemingly ubiquitous, and one of the most abundant solid phase molecular species, approximately 10 – 34 % H_2O. It is believed to form in the solid phase, due to low gas phase abundances [van Dishoeck et al. , 1996], with evidence suggesting that much CO_2 production occurs in quiescent regions [Pontoppidan , 2006; Nummelin et al. , 2001], yet the key question remains: how does CO_2 form?

Many experimental studies have been performed to study the energetic formation routes to CO_2. Irradiation of pure CO ices with photons [Gerakines et al. , 1996], charged particles [Palumbo et al. , 1998], and electrons [Jamieson et al. , 2006] have yielded CO_2. Similar experiments with mixtures of CO and H_2O were also successful [Ehrenfreund et al. , 1997; Palumbo et al. , 1998; Ioppolo et al. , 2009; Laffon et al. , 2010]. The irradiation of hydrogenated carbon grains with ions and electrons produced small quantities of CO and CO_2 [Mennella et al., 2004, 2006].

CO_2 is abundant in quiescent, as well as star-forming regions. While the role

of energetic pathways can not be discounted entirely in these regions [Whittet et al., 1998], the study of non-energetic formation routes is fundamental to fully understanding the observed abundances of CO_2. Potential non-energetic formation routes [Ruffle & Herbst, 2001] are:

$$CO + O \rightarrow CO_2 \tag{7.1}$$

$$CO + OH \rightarrow CO_2 + H \tag{7.2}$$

$$HCO + O \rightarrow CO_2 + H \tag{7.3}$$

$$HCO + OH \rightarrow CO_2 + H_2 \tag{7.4}$$

Theoretical studies of route (7.1) suggest that the formation of CO_2 proceeds with a high barrier of around 2500 – 3000 K, lowered on surfaces via the hot O atom or Eley-Rideal mechanisms described in Chapter 1 [Talbi et al. , 2006; Goumans et al. , 2008]. A solid phase study determined that this pathway was feasible only via reaction in water pores, under a water ice cap, and upon heating [Roser et al. , 2001], suggesting that it would not occur under the conditions present in quiescent molecular clouds. Reactions (7.3) and (7.4) have never been studied expressly in the solid phase.

Route (7.2) has been extensively studied in the gas phase, both experimentally [Frost, Sharkey & Smith , 1993; Fulle et al. , 1996; Baulch et al. , 2005] and theoretically [Yu, Muckerman & Sears , 2001; Chen & Marcus , 2005; Sun & Law , 2008], due to its importance in atmospheric and combustion chemistry. Recently, reaction (7.2) was experimentally studied in the solid phase by Reflection Absorption InfraRed Spectroscopy (RAIRS) for the first time, with positive results [Oba et al. , 2010]. Due to the limitations of the adopted method, it was not possible to produce a pure beam of OH, and therefore the chemistry is difficult to constrain with a simple series of reactions; in particular, it was experimentally complex to distinguish between (7.2) – (7.4). OH was produced in the gas phase via a plasma discharge of H_2O, a process which yields a mixture of products including OH, H, H_2, O and O_2. Although it is claimed that all OH radicals are in the rovibrational ground state due to collisions with the beam walls, well defined spectroscopic studies of plasma discharges suggest that interaction with the walls is likely to lead to OH recombination, rather than

yield ground state OH, and that the major components of a plasma of H_2O are H_2 and H_2O, with lower abundances of OH [Médard et al., 2002; Fujii et al. , 2002]. Furthermore, experiments in the absence of CO produced H_2O_2 and O_3, whose yields varied with surface temperature, suggesting that surface temperature itself, mobility of the discharge products on the surface, and, potentially, the desorption rate of CO from the surface, rather than the rovibrational state of the OH, is responsible for the changing yields of CO_2 observed at different temperatures. Finally, reaction (7.2) was found to proceed with little or no barrier, suggesting the presence of rovibrationally excited OH. Under these conditions, the CO_2 yield can not be assumed to be independent of the excitation state of OH and thus further study of reaction (7.2) is imperative. A subsequent RAIRS study produced OH in the solid phase from a mixture of O_2:CO in a multilayer regime [Ioppolo et al., 2011a]. Due to the multilayer regimes investigated, both previous studies also involved more complex chemistry than simply CO_2 formation, such as the formation of H_2CO_3 and CH_3OH, which further complicate the quantitative analysis of reaction (7.2).

This chapter presents the first temperature programmed desorption spectra of CO_2 formed via (7.2) in the solid phase, under interstellar conditions of temperature and pressure. In this study, OH was produced on the surface by reaction of O_2 and O_3 with H in order to constrain better the reaction pathways in the system. The reaction was studied on both an amorphous silicate and a non-porous water surface, in a low coverage regime, with the aim of limiting chemistry to only CO_2 production. In contrast to previous studies, a simple kinetic model was developed to determine relative reaction efficiencies and calculate the activation energy of reaction (7.2).

7.3 Experimental

Experiments were performed using the FORMOLISM apparatus [Amiaud et al. , 2006], fully detailed in Chapter 5. The experiments were performed on either bare silicate, or a non-porous, amorphous water film of $\sim$100 monolayers grown on the silicate by spraying water vapour from a microchannel array doser (held at 120 K during water desorption, then cooled to 10 K before com-

mencing the experiments).

Two different surfaces were investigated in order, firstly, to mimic two interstellar environments and, secondly, to determine the surface dependency of route (7.2). Amorphous silicate is an appropriate mimic of interstellar dust grains, composed of siliceous and carbonaceous material [Greenberg , 2002]. In molecular clouds these grains are covered in an ice mantle, the largest component of which is H_2O, at abundances of up to 100 ML [Williams & Herbst, 2002]. $H_2O_{(np)}$ was used in this study to eliminate the complexity of chemistry occurring in pores.

Neither O_3 nor O_2 has been observed in an interstellar ice, so these experimental conditions are not likely to be directly astrophysically relevant, but were used to produce OH in a controlled, reproducible manner. It is experimentally complex to create, maintain, and deposit onto a surface, a pure, stable beam of the OH radical in the ground state. Thus, in this work, OH was produced on the surface via two routes: the hydrogenation of O_2 and of O_3. O_2 is easier to utilise experimentally, but a study involving both species constrains reaction mechanisms better than using a single species. Due to the limits of sensitivity of the QMS, quantities below 0.1 ML were not investigated.

OH was not measured directly on the surface, due to its short lifetime, but the production of O_2, H_2O_2 and H_2O, during control experiments on the hydrogenation of O_2 and O_3, confirms its presence, according to the reaction scheme:

$$O_3 + H \rightarrow O_2 + OH \tag{7.5}$$

$$O_2 \xrightarrow{H} HO_2 \xrightarrow{H} H_2O_2 \xrightarrow{H} H_2O + OH \tag{7.6}$$

Figure 7.1 describes the chemical network of OH relevant to these experiments. The OH radical, produced by reactions (7.5) and (7.6), could react with CO as in reaction (7.2) to produce CO_2, or with H to form H_2O, and thus, the relative rate of these reactions is an important factor determining the yield of CO_2 and the aim of this work was to elucidate the relative rates of these reactions.

All experiments are summarised in Table 7.1; approximately 1.5 ML of O_3 or 0.5 ML of O_2 were dosed onto the surface via one molecular beam, followed by $\sim$0.5 ML of isotopically labelled ^{13}CO via a second beam. Finally, H atoms

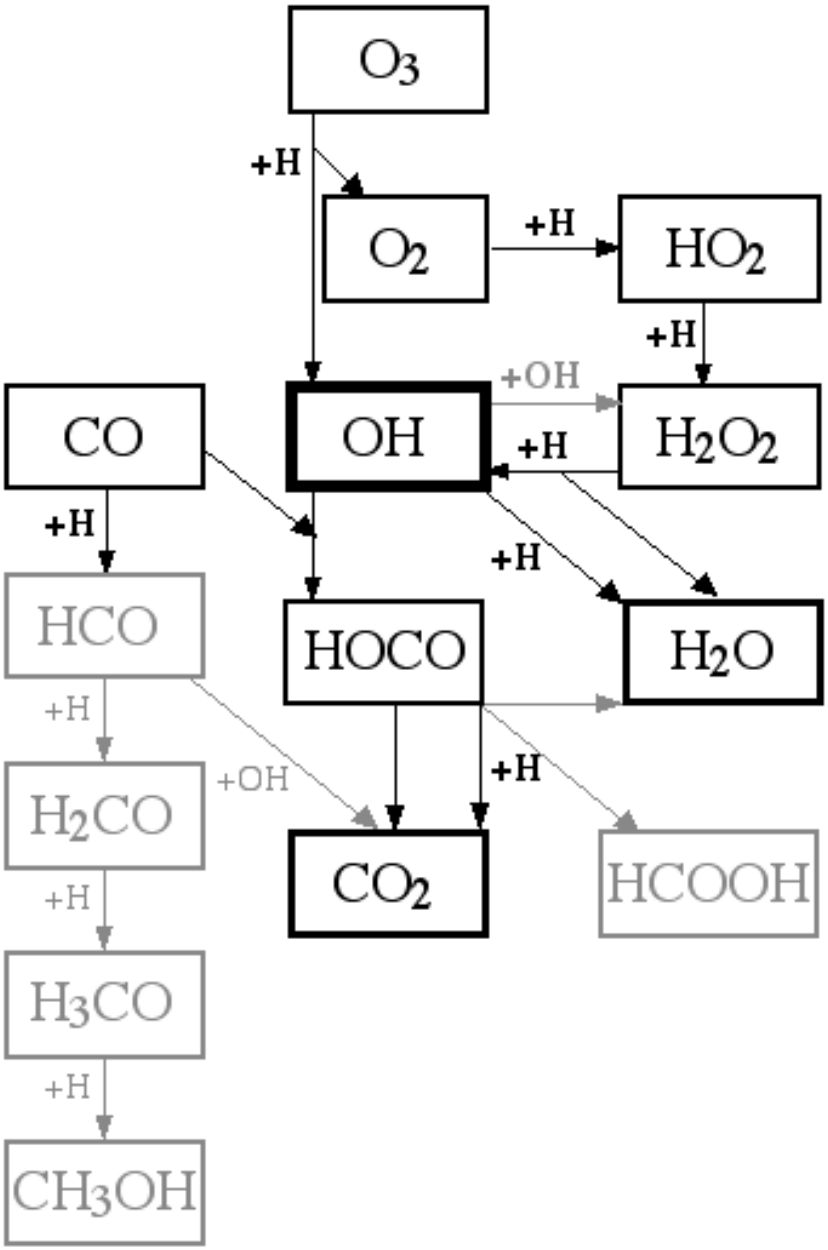

Figure 7.1. Chemical network of OH in these experiments as a schematic diagram. Reactions which occurred in the present study are depicted in black, whilst those that didn't are shaded grey. See text for details.

were deposited, via a plasma discharge of H_2 on beam 1, for a range of exposure times of between 0 and 20 minutes. The deposition rate of H on the surface was $\sim 5 \times 10^{12}$ atoms $cm^{-2}s^{-1}$, taking into account the dosing pressure and the dissociation rate of H_2 [Amiaud et al. , 2007]. During O_3 deposition,

Table 7.1. Experiments performed in this work.

Experiment (label)	Substrate	N(O_2) (ML)	N(O_3) (ML)	N(^{13}CO) (ML)	t(H) (minutes)
A	H_2O	0.5	···	$0.6^{\dagger}$	0
B	H_2O	0.5	···	$0.6^{\dagger}$	10
C	H_2O	0.5	···	$0.6^{\dagger}$	20
D	H_2O	···	1.6	0.5	0
E	H_2O	···	1.4	0.5	2
F	H_2O	···	1.6	0.5	10
G	H_2O	···	1.1	0.6	20
H	Silicate	0.45	···	0.45	0
I	Silicate	0.45	···	$0.45^{\dagger}$	20
J	Silicate	···	1.5	0.13	0
K	Silicate	···	1.3	0.45	20

Note. — Species were deposited on the surface in order from left to right, apart from those marked †, where ^{13}CO was deposited first. All species except ^{13}CO were deposited using the same beam (see §7.3 for details.)

the surface was held at 45 K to ensure that any traces of O_2 present in the O_3 beam desorbed from the surface (for detailed O_3 production method, see Mokrane et al. [2009]); it was then cooled to 10 K before continuing. For all other molecules, the surface was held at 10 K during dosing.

H atoms were hot when produced in the plasma discharge of H_2, but cooled to room temperature before exiting the molecular beam, due to collisions with the walls. Isotopically labelled ^{13}CO was used to avoid contamination of the results by $^{12}CO_2$ or ^{12}CO, pollutants present at very low gaseous concentrations in the chamber.

To measure the products of the reaction, the surface was heated from 10 to 100 K; desorbing molecular species were monitored with the QMS. Each TPD cycle lasted approximately three hours.

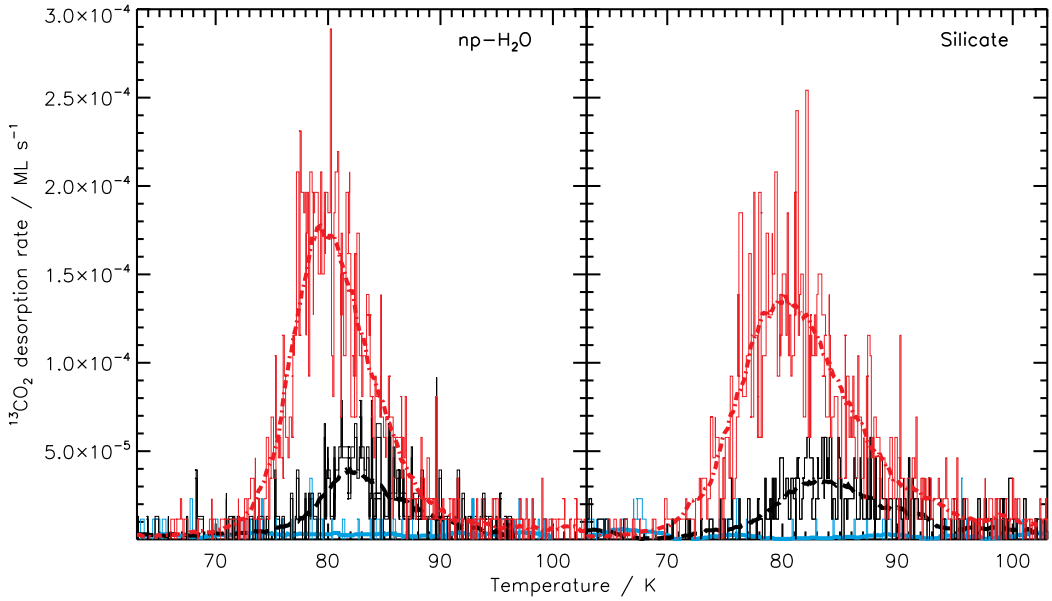

Figure 7.2. Temperature programmed desorption spectra of Mass 45 ($^{13}CO_2$). The left panel shows desorption from a water surface while the right panel, a bare silicate surface. Experimental data are plotted in their raw form, accompanied by a smoothed version to guide the eye. Curves are labelled as follows: solid blue line, experiments A and H (0.5 ML O_2, $\sim$ 0.5 ML ^{13}CO, no H irradiation); dashed black line, experiments C and I (0.5 ML O_2, $\sim$ 0.5 ML ^{13}CO, 20 minutes H irradiation); dot-dashed red line, experiments G and K ($\sim$ 1 ML O_3, $\sim$ 0.5 ML ^{13}CO, 20 minutes H irradiation). Production of $^{13}CO_2$ is seen for both starting molecules (O_2 and O_3) on both surfaces but O_3 yields significantly more $^{13}CO_2$ than O_2. There is no discernible surface dependence of the reaction under current experimental conditions.

7.4 Results and Discussion

Figure 7.2 shows TPD spectra of $^{13}CO_2$ produced by H irradiation of O_3 with ^{13}CO, and O_2 with ^{13}CO. $^{13}CO_2$ was produced during all experiments where H irradiation was performed. The $^{13}CO_2$ desorbs from each surface over a similar temperature range, but with a slightly different peak shape, indicative of the roughness of the underlying surfaces. It is clear that, since all data in Figure 7.2 are measured at the same H irradiation time, substantially more $^{13}CO_2$ is produced by the reaction of O_3 than O_2. This is evident from reactions (7.5) and (7.6): three hydrogenation steps are required to generate a single OH radical from O_2, whereas O_3 also generates an OH directly.

As the solid blue line in Figure 7.2 shows, if the experiment was conducted

without H irradiation, no $^{13}CO_2$ was produced. Nor was $^{13}CO_2$ production seen during control TPDs of ^{13}CO, O_2 or O_3. When ^{13}CO was not present, H_2O and H_2O_2 formed, rather than $^{13}CO_2$. It was assumed that all the $^{13}CO_2$ formed during H irradiation, in agreement with previous experiments [Oba et al. , 2010; Ioppolo et al., 2011a]. Within the limits of measurement, no gas phase $^{13}CO_2$ was observed during the irradiation, indicating that the $^{13}CO_2$ remained on the surface. No additional $^{13}CO_2$ was produced during the TPDs because control experiments, where O_3 was irradiated with H before deposition of ^{13}CO, yielded negligible $^{13}CO_2$, suggesting that when OH is produced, it reacts quickly on the surface.

When searched for, no evidence of the production of $H^{13}COOH$ was seen, validating the hypothesis that investigating a sub-monolayer coverage restricts the chemistry to CO_2 production, unlike previous studies [Oba et al. , 2010; Ioppolo et al., 2011a]. Neither were $H_2^{13}CO$ nor $^{13}CH_3OH$ seen in desorption. However, H_2, ^{12}CO, ^{13}CO, $^{12}CO_2$ were seen during all TPDs; $^{13}CO_2$ was seen upon H irradiation; H_2O_2, H_2O were seen upon H irradiation, during extended TPDs to higher temperature; O_3 was seen only when O_3 had been deposited; O_2 was seen in all experiments, except those with O_3 and no H irradiation.

Figure 7.3 illustrates $^{13}CO_2$ production as a function of H irradiation time (solid symbols). It is clear that $^{13}CO_2$ was produced at comparable rates on both surfaces (solid triangles versus solid squares), regardless of the starting material (O_2 or O_3), vindicating the earlier conclusion that the underlying surface does not play a significant role in this reaction. In every experiment, some ^{13}CO desorbed during the TPD, suggesting it was present in excess, never completely reacting with OH or H. In addition, as O_3, O_2 and H were dosed via one beam, while ^{13}CO was dosed via a second, even after alignment the maximum overlap attainable is less than 100 %, so not all reagents were dosed on the same region of the surface. Conversely, as Figure 7.3 shows, the reactions are very sensitive to the quantity of OH generated, which itself depends upon the starting quantity of O_2 or O_3 on the surface. Although surface coverages were controlled to within $\pm$ 0.2 ML between experiments, this difference was sufficient to account for the varying concentration of $^{13}CO_2$ observed in Figure 7.3.

By comparison of the TPD spectra in Figure 7.2 to those in Chapter 6, Figure 6.1, it is clear that the CO_2 produced in these experiments is in the sub-monolayer regime. The profiles of the desorption peaks in Figure 7.2 are all very similar, and show sub-monolayer desorption. The maximum yield of $^{13}CO_2$ was calculated as $\sim$ 8 % with respect to ^{13}CO (Table 7.1, experiments F,K); the presence of a complex barrier helps to explain this. Gas phase and theoretical studies predict a three-stage barrier ($\sim$ 500 K, e.g. Frost, Sharkey & Smith [1993]; Yu, Muckerman & Sears [2001]). The reaction proceeds via an energetic HOCO intermediate, which isomerises from *trans*-HOCO to *cis*-HOCO, before dissociating to form CO_2 [Smith & Zellner , 1973; Alagia et al. , 1993; Lester et al. , 2000]. Lester et al. [2001] suggest that a precursor OH-CO complex forms prior to the HOCO intermediate. On a surface, the reaction probability is even more reliant upon the relative orientation of CO and OH. A recent theoretical study on a coronene surface shows that OH physisorbs with the hydrogen atom pointing towards the surface [Goumans et al. , 2008]. Compared to the gas phase, the activation barrier to *trans*-HOCO formation is slightly lowered, and the intermediate stabilised. A barrierless reaction between this stabilised HOCO complex with a further H atom could produce CO_2 + H_2. However, experiments suggest this reaction could also yield HCOOH or H_2O + CO [Ioppolo et al., 2011b], while reaction with OH could yield H_2CO_3 [Oba et al. , 2010]. From the results presented here, it is not possible to determine whether $^{13}CO_2$ formed from *cis*-HOCO $\rightarrow$ CO_2 + H, or by hydrogenation of HOCO, although no H^{13}COOH was observed when TPDs were run to 200 K, thus it is assumed that, under these experimental conditions, reaction (7.2) produces only $^{13}CO_2$.

This complex barrier somewhat explains the low $^{13}CO_2$ yields, but there are further constraints to be considered. Due to the low coverages investigated here, the probability of ^{13}CO and OH meeting on the surface is small. OH recombination could produce H_2O_2, or the competitive reaction OH + H could remove OH from the surface [Ioppolo et al. , 2008]. Also, in these experiments, ^{13}CO was dosed after O_3 or O_2, so at high enough coverages it could block H from reaching these reagents, allowing CO hydrogenation to artificially dominate. Previous studies show that hydrogenation of O_3 [Mokrane et al. , 2009] and O_2 [Ioppolo et al. , 2008; Dulieu et al., 2010] occurs with no barrier, while hydrogenation of CO proceeds via:

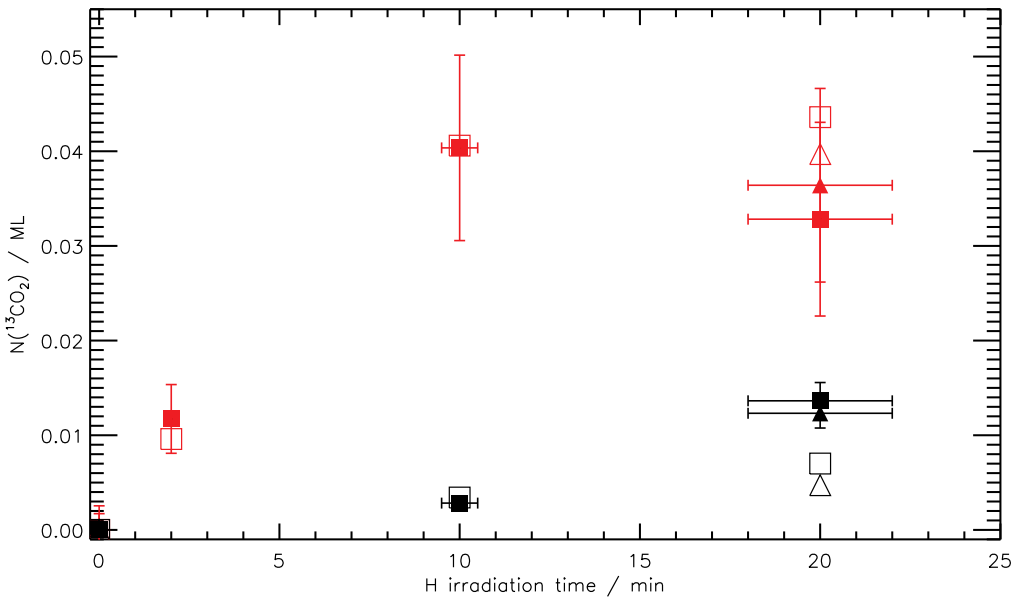

Figure 7.3. The evolution of $^{13}CO_2$ with H irradiation time, presented in monolayers of CO_2, for all experiments. The data is labelled as follows: red, closed squares O_3 + ^{13}CO on $H_2O_{(np)}$; red, closed triangles O_3 + ^{13}CO on silicate; black, closed squares O_2 + ^{13}CO on $H_2O_{(np)}$; black, closed triangles O_2 + ^{13}CO on silicate. Overplotted (as corresponding open shapes) are the results of the kinetic model developed to describe the formation of $^{13}CO_2$. See text for details.

$$CO \xrightarrow{H} HCO \xrightarrow{H} H_2CO \xrightarrow{H} H_3CO \xrightarrow{H} CH_3OH, \tag{7.7}$$

with a barrier of 390 K at 12 K to CO + H [Fuchs et al. , 2009; Watanabe & Kouchi, 2002]. Here, the ^{13}CO surface coverage was always below 1 ML, and neither $H_2^{13}CO$ nor $^{13}CH_3OH$ desorbed during extended TPDs, indicating that little ^{13}CO hydrogenation occurred. If $H^{13}CO$ was not produced in significant concentrations via (7.7), it follows that $^{13}CO_2$ was not produced at measurable quantities via (7.4), not least due to the low probability of any $H^{13}CO$ produced encountering OH on the surface. These conclusions indicate that in this experiment $^{13}CO_2$ formation occurred exclusively via reaction (7.2).

A simple kinetic model of the experimental system was developed to describe the production of $^{13}CO_2$ via (7.2), based on a set of coupled second order rate equations, of the type:

$$-\frac{dA}{dt} = k[A][B], \tag{7.8}$$

where A & B are reactants, [A] & [B] their concentrations, and k is the rate constant. As the concentration of H atoms was a constant, for most reactions the rate equations simplified to pseudo first order kinetics:

$$-\frac{dA}{dt} = k[A][B] = k'[A]. \tag{7.9}$$

Figure 7.1 shows the potential detailed reaction scheme for these experiments. However, as illustrated above, given the low surface coverages employed here, a number of reactions, for example OH recombination, can be eliminated and are thus shown in grey in the figure. Neither CO_2 nor HCOOH react further with H [Bisschop et al., 2007], so such reactions were also ignored in the model. As discussed above, $H^{13}CO$ was likely not produced at significant concentrations in these experiments. However, the rate of CO hydrogenation under present conditions was constrained by control experiments with only CO on the surface. It was assumed that the underlying surface had no effect on the reaction rate (as illustrated by Figure 7.3), so the model treats both surfaces simultaneously. The best fit to the experimental data was found by varying the rates of reaction, k_i, of CO + OH and H_2O_2 + H, while constraining all other k_i with empirical data (reactions shown in black in Figure 7.1). That only two free parameters (k_{CO+OH} and $k_{H_2O_2+H}$) were required to fit all of the data presented here, provides strong evidence for the validity of the model, and the previous deductions that all $^{13}CO_2$ in the experiments was produced via reaction (7.2).

The results of the model are plotted over the experimental data as open symbols in Figure 7.3, and are summarised in Table 7.2. At low H irradiation times, the model describes well the production of $^{13}CO_2$, but starts to deviate slightly at longer times. This could be attributed to route (7.4) becoming competitive, but in that case, the O_3 and O_2 experiments should deviate with the same trend, while in reality the production of $^{13}CO_2$ from O_3 is slightly overestimated while that from O_2 is underestimated. Reaction (7.5) is exothermic [McKinley et al., 1955], so the excess energy of this reaction could be transferred to the products, which may then desorb from the surface. The model

Table 7.2. Modelled relative rate constants.

Reaction	k_i/k_{O_2+H}
O_3 + H	1
O_2 + H	1
HO_2 + H	1
H_2O_2 + H	0.125†
CO + H	0.025
OH + H	1
CO + OH	0.042†

Note. — †Rate was a free parameter in the model. All other rates were fixed, based on published empirical values detailed in the text.

does not account for this possibility, and thus overestimates the $^{13}CO_2$ yield by the O_3 route.

The model, while a simplistic approach to explaining the surface chemistry, as it ignores the complexity of the barrier known to exist in the CO + OH pathway, suggests that the relatively low yield of $^{13}CO_2$ in these experiments results from competition between (7.2) and other reactions involving OH. The relation between key reaction rates is:

$$k_{CO+H} \ll k_{CO+OH} < k_{H_2O_2+H} < k_{OH+H}, k_{O_2+H}, \tag{7.10}$$

indicating that water formation should always dominate the formation of ice species at low surface coverages. The overall effective reaction rate of CO + OH was determined to be 24 times slower than hydrogenation of OH, O_3 or O_2, and 1.7 times faster than CO + H. The relative rate between the hydrogenation of O_2 and CO was 40, while between the hydrogenation of O_2 and H_2O_2, it was 8, consistent with literature values of 31 – 90 and 3.3, respectively [Miyauchi et al., 2008]. The factor of two difference between this and the previous value

of $k_{O_2+H}/k_{H_2O_2+H}$ can be explained by the fact that molecular species such as H_2O_2 were more accessible to H in the (approximately 1 ML) experiments and therefore reacted more quickly than in the multilayer regime of Miyauchi et al. [2008].

The activation barrier to a chemical reaction is the energy required in order for the reaction to occur. Activation barriers are fundamental in astrochemical modelling as they determine the relative probability of different reaction pathways occurring in a molecular cloud. As activation barriers are difficult to calculate based upon laboratory data, and many crucial reactions have yet to be performed experimentally, astrochemical modellers are often required to estimate barriers based upon all available evidence. The calculation of new barriers by experimentalists is key in ensuring that future models become ever more accurate and robust.

It is not possible to extract the activation barrier for HOCO formation or its subsequent reactions to form CO_2 in reaction (7.2) from the model. It is possible, however, to calculate an effective barrier to CO_2 production by comparison of the modelled relative rates to the activation barrier of 390 K at 12 K for CO + H [Fuchs et al. , 2009]. If first order kinetics and a constant pre-exponential factor are assumed in both reactions, the effective barrier to (7.2) is 384 ± 40 K, where the error is derived from the barrier to hydrogenation of CO. This is the first calculation of the effective barrier to (7.2) in the solid phase, and the result is contradictory to that of Oba et al. [2010] who conclude that, in their study, the reaction proceeds with little or no activation barrier, but do not calculate a value. As suggested above, the presence of some fraction of excited OH in the beam could produce CO_2 in a barrierless reaction with CO. Current grain models include grain surface activation barriers to (7.2) of e.g. 80 K [Yuri Aikawa, *private communication*] or 176 K [Cuppen et al., 2009], which would seem very low for an effective first order rate equation, potentially overproducing CO_2. All evidence suggests that CO + OH is a more efficient route to CO_2 formation than the non-energetic CO + O route, reaction (7.1), yet Roser et al. [2001] estimate the barrier to (7.1) is only 290 K, and suggest that the reaction proceeds under quiescent cloud conditions. If this were correct, then in comparison to the results of Fuchs et al. [2009] and those presented here, CO + O would be more likely to proceed than either CO + H or CO + OH.

It is relevant, therefore, to address briefly the value of the CO + O barrier as derived by Roser et al. [2001] which, if implemented in gas-grain models, would result in the incorrect pathway to CO_2 formation dominating the reaction scheme. Roser et al. [2001] derived the barrier from an experiment where a water ice cap was deposited on top of CO which had previously been exposed to O atoms, assuming that reaction (7.1) occurred in the water pores as the surface was heated, and explicitly relying upon the reagents being trapped at the surface by the water ice cap. Although other laboratory studies show that CO trapping can occur in water ice pores [Collings et al., 2003], observations and models confirm that CO freeze-out occurs after the formation of water ice layers in both molecular clouds [Pontoppidan et al., 2003] and protostellar disks [Visser et al., 2009], implying that a water ice cap is not a realistic mimic of any interstellar ice, including those found in quiescent regions. In fact, scenarios investigating reaction (7.1) by Roser et al. [2001] under conditions comparable to those present in quiescent molecular clouds yielded no CO_2, nor did subsequent experimental studies by Oba et al. [2010]. Together with the effective barrier to (7.2) of 384 $\pm$ 40 K presented here, this suggests the importance of readdressing the value of the CO + O barrier implemented in astrochemical models.

A recent study by Zins et al. [2011] investigated the reaction of CO with OH at 3.5 K. It is similar to that of Oba et al. [2010] in that CO and OH are introduced onto a surface simultaneously, and the composition of the ice mixture is monitored by infrared spectroscopy (reflection mode in Oba et al. [2010] and transmission mode in Zins et al. [2011]). Oba et al. [2010] produced OH in a microwave-induced plasma of H_2O and deposited species at 10 or 20 K, while Zins et al. [2011] used a series of H_2O:He mixtures to generate OH and deposited at 3.5 K. In both studies, the CO_2 signal increased during deposition, indicating that CO_2 was produced in the ice. The use of H_2O:He mixures to generate OH should produce cooler OH radicals.

Zins et al. [2011] do not quantify the barrier to the reaction CO + OH in their study (although Oba et al. [2010] suggested that there was no barrier to reaction). In this study, we have calculated an effective barrier of 384 $\pm$ 40 K for the conversion of CO to CO_2, but it was not possible to extract the barriers to the intermediate steps, such as HOCO formation. Oba et al. [2010] observe

the formation of both *trans*-HOCO and *cis*-HOCO during their experiments, but Zins et al. [2011] do not observe HOCO intermediates in their study. As no HOCO intermediate is observed, it is unlikely that Zins et al. [2011] are probing the same chemistry as Oba et al. [2010]. Quantification of the products of these reactions is critical in determining the chemistry occurring in the systems, and the relative rates of the reactive pathways.

As CO_2 is formed at 3.5 K in the study of Zins et al. [2011], this suggests that the barrier to CO_2 formation in their system is low. It is also noted that large quantities of H_2O were produced by OH recombinations if the experiments were conducted at 10 K. It is possible that, by constraining our experiments to submonolayer coverages, the limiting factor to CO_2 formation is the meeting of CO and OH on the surface, and that this contributes to the calculated energy barrier and the favourable production of H_2O in our study. If OH is mobile at 10 K, then despite the low concentration of OH in our experiments, two OH radicals could recombine on the surface to produce H_2O. Further experiments investigating CO_2 formation in both submonolayer and multilayer regimes could help to clarify this. However, as no quantification of the energy barriers and reaction rates has been attempted by Zins et al. [2011], a direct comparison with our calculated relative reaction rates is not possible.

7.5 Astrophysical Implications

The reaction of CO + OH is seen to be viable under astrophysical conditions of temperature and pressure, on silicate and $H_2O_{(np)}$ surfaces. Small quantities of CO_2 were produced, in competition with other reactions involving OH (for example hydrogenation of OH to form H_2O). Thus, the mechanism CO + OH could be key to explaining the formation of CO_2 at the edges of dark clouds (low A_V), where CO_2 is seen to form concurrently with H_2O on bare dust grains [Pontoppidan , 2006], before a large quantity of CO ice is present.

By modelling the reaction scheme, it was possible to determine the empirical relationship $k_{CO+H} \ll k_{CO+OH} < k_{H_2O_2+H} < k_{OH+H}, k_{O_2+H}$, where the overall effective rate of CO + OH is determined to be 24 times slower than OH + H, and 1.7 times faster than CO + H, indicating why H_2O ice is always the most

abundant species.

In dense molecular clouds, gas phase hydrogen is observed to be mainly in the molecular form, but atomic H is present at a constant, low abundance ($H/H_2 \sim 10^{-3}$, Li & Goldsmith [2003]) due to the balance of H_2 formation on grain surfaces and its destruction by cosmic rays. The abundance of OH increases with density, in line with that of O Harju et al. [e.g. 2000]; Quan et al. [e.g. 2008]. Thus, after the freeze-out of CO, the reaction CO + OH could proceed on the ice mantle due to higher abundances of CO on the grain surface. As the abundance of OH increases, so does the potential for formation of CO_2 via CO + OH. The formation of H_2O via the competitive reaction OH + H will also increase with density, and thus CO_2 and H_2O formation in central, more quiescent regions of molecular clouds is possible. This conclusion agrees well with the postulations of Goumans et al. [2008].

7.6 Conclusions

As first discussed in Chapter 1, the formation of CO_2 is a fundamental reaction in molecular clouds, producing one of the most abundant solid phase molecular species seen in the interstellar medium. To date, much experimental emphasis has been placed upon CO_2 formation routes requiring energetic inputs, such as electrons or charged particles, in order for the reaction to proceed. This chapter has presented the results of a study into the production of CO_2 via the non-energetic pathway CO + OH at low coverages. For the first time, TPD spectra of CO_2 produced via an astrophysically relevent, non-energetic pathway have been presented. This study has also used a simple kinetic model to derive rate constants for the reactions occurring during CO_2 production, and to calculate a tentative activation barrier to the reaction CO + OH $\rightarrow$ CO_2. It is suggested that competition with the H_2O formation route OH + H limits the production of CO_2 in this experiment. CO + OH is shown to be a viable non-energetic formation route to CO_2 at early stages in molecular clouds. Building on the results of concurrent studies of CO_2 formation by this route [Oba et al. , 2010; Ioppolo et al., 2011a], these experiments have investigated low coverage regimes, more applicable to chemistry in the ISM, and have allowed the calcu-

lation of relative rates of reaction, and a tentative activation barrier, which will hopefully prove useful to chemical modellers.

References

Alagia, M., Balucani, N., Casavecchia, P., Stranges, D. & Volpi, G. G. 1993, J. Chem. Phys., 98, 8341

Amiaud, L., Fillion, J. H., Baouche, S., Dulieu, F., Momeni, A. & Lemaire, J. L. 2006, J. Chem. Phys., 124, 094702

Amiaud, L., Dulieu, F., Fillion, J.-H., Momeni, A., & Lemaire, J. L. 2007, J. Chem. Phys., 127, 709

Baulch, D. L. et al. 2005, J Phys Chem Ref Data, 34, 757

Bisschop, S. E., Fuchs, G. W., van Dishoeck, E. F., & Linnartz, H. 2007, A&A, 474, 1061

Chen, W. C. & Marcus, R. A. 2005, J. Chem. Phys., 123, 094307

Collings, M. P., Dever, J. W., Fraser, H. J., McCoustra, M. R. S., & Williams, D. A. 2003, ApJ, 583, 1058

Cuppen, H. M., van Dishoeck, E. F., Herbst, E., & Tielens, A. G. G. M. 2009, A&A, 508, 275

van Dishoeck, E. F., et al. 1996, A&A, 315, L349

Dulieu, F., Amiaud, L., Congiu, E., Fillion, J.-H., Matar, E., Momeni, A., Pirronello, V., & Lemaire, J. L. 2010, A&A, 512, A30

Ehrenfreund, P., Boogert, A. C. A., Gerakines, P. A., Tielens, A. G. G. M., & van Dishoeck, E. F. 1997, A&A, 328, 649

Frost, M. J., Sharkey, P. & Smith, I. W. M. 1993, J. Chem. Phys., 97, 12254

Fuchs, G. W., Cuppen, H. M., Ioppolo, S., Romanzin, C., Bisschop, S. E., Andersson, S., van Dishoeck, E. F., & Linnartz, H. 2009, A&A, 505, 629

Fujii, T., Selvin, P. C., & Iwase, K. 2002, Chem. Phys. Lett., 360, 367

Fulle, D., Hamann, H. F., Hippler, H. & Troe, J. 1996, J. Chem. Phys., 105, 983

Gerakines, P. A., Schutte, W. A., & Ehrenfreund, P. 1996, A&A, 312, 289

Gerakines, P. A., et al. 1999, ApJ, 522, 357

Gibb, E. L., Whittet, D. C. B., Boogert, A. C. A. & Tielens, A. G. G. M. 2004, ApJS, 151, 35

Goumans, T. P. M., Uppal, M. A., & Brown, W. A. 2008, MNRAS, 384, 1158

de Graauw, T., et al. 1996, A&A, 315, L345

Greenberg, J. M. 2002, Surface Science, 500, 793

Harju, J., Winnberg, A., & Wouterloot, J. G. A. 2000, A&A, 353, 1065

D'Hendecourt, L. B., & Jourdain de Muizon, M. 1989, A&A, 223, L5

Ioppolo, S., Cuppen, H. M., Romanzin, C., van Dishoeck, E. F., & Linnartz, H. 2008, ApJ, 686, 1474

Ioppolo, S., Palumbo, M. E., Baratta, G. A., & Mennella, V. 2009, A&A, 493, 1017

Ioppolo, S., van Boheemen, Y., Cuppen, H. M., van Dishoeck, E. F., & Linnartz, H. 2011, MNRAS, 413, 2281

Ioppolo, S., Cuppen, H. M., van Dishoeck, E. F., & Linnartz, H. 2011, MNRAS, 410, 1089

Jamieson, C. S., Mebel, A. M., & Kaiser, R. I. 2006, ApJS, 163, 184

Knez, C., et al. 2005, ApJL, 635, L145

Laffon, C., Lasne, J., Bournel, F., Schulte, K., Lacombe, S., & Parent, Ph. 2010, PCCP, 12, 10865

Lemaire, J. L., Vidali, G., Baouche, S., Chehrouri, M., Chaabouni, H., & Mokrane, H. 2010, ApJL, 725, L156

Lester, M. I., Pond, B. V., Anderson, D. T., Harding, L. B. & Wagner, A. F., 2000, J. Chem. Phys., 113, 9889

Lester, M. I., Pond, B. V., Marshall, M. D., Anderson, D. T., Harding, L. B., & Wagner, A. F. 2001, Faraday Discuss., 118, 373

Li, D., & Goldsmith, P. F. 2003, ApJ, 585, 823

McKinley, J. D., Garvin, D., & Boudart, M. J. 1955, J. Chem. Phys., 23, 784

Médard, N., Soutif, J.-C., & Poncin-Epaillard, F. 2002, Langmuir, 18, 2246

Mennella, V., Palumbo, M. E., & Baratta, G. A. 2004, ApJ, 615, 1073

Mennella, V., Baratta, G. A., Palumbo, M. E., & Bergin, E. A. 2006, ApJ, 643, 923

Miyauchi, N., Hidaka, H., Chigai, T., Nagaoka, A., Watanabe, N., & Kouchi, A. 2008, Chemical Physics Letters, 456, 27

Mokrane, H., Chaabouni, H., Accolla, M., Congiu, E., Dulieu, F., Chehrouri, M., & Lemaire, J. L. 2009, ApJL, 705, L195

Noble, J. A., Dulieu, F., Congiu, E., & Fraser, H. J. 2011, ApJ, 735, 121

Nummelin, A., Whittet, D. C. B., Gibb, E. L., Gerakines, P. A., & Chiar, J. E. 2001, ApJ, 558, 185

Oba, Y., Watanabe, N., Kouchi, A., Hama, T., & Pirronello, V. 2010, ApJL, 712, L174

Oliveira, J. M., et al. 2011, MNRAS, 411, L36

Palumbo, M. E., Baratta, G. A., Brucato, J. R., Castorina, A. C., Satorre, M. A., & Strazzulla, G. 1998, A&A, 334, 247

Pontoppidan, K. M., et al. 2003, A&A, 408, 981

Pontoppidan, K. M. 2006, A&A, 453, L47

Pontoppidan, K. M., et al. 2008, ApJ, 678, 1005

Quan, D., Herbst, E., Millar, T. J., Hassel, G. E., Lin, S. Y., Guo, H., Honvault, P., & Xie, D. 2008, ApJ, 681, 1318

Roser, J. E., Vidali, G., Manicò, G., & Pirronello, V. 2001, ApJL, 555, L61

Ruffle, D. P., & Herbst, E. 2001, MNRAS, 324, 1054

Shimonishi, T., Onaka, T., Kato, D., Sakon, I., Ita, Y., Kawamura, A., & Kaneda, H. 2010, A&A, 514, A12

Smith, I. W. M. & Zellner, R. 1973, J. Chem. Soc, Faraday Trans. II, 69, 1617

Sun, H. & Law, C. K. 2008, J. Mol. Struct.: THEOCHEM, 862, 138

Talbi, D., Chandler, G. S., Rohl, A. L. 2006, Chem. Phys., 320, 214

Visser, R., van Dishoeck, E. F., Doty, S. D., & Dullemond, C. P. 2009, A&A, 495, 881

Watanabe, N., & Kouchi, A. 2002, ApJL, 571, L173

Whittet, D. C. B., et al. 1998, ApJL, 498, L159

Williams, D., & Herbst, E. 2002, Surface Science, 500, 823

Yu, H. G., Muckerman, J. T. & Sears, T. J. 2001, Chem. Phys. Lett., 349, 547

Zins, E.-L., Joshi, P. R., & Krim, L. 2011, ApJ, 738, 175

CHAPTER 8

CONCLUSIONS AND FURTHER WORK

8.1 Conclusions

All work presented in this thesis addresses its major aim of determining the physical and chemical behaviour characteristics of solid phase molecular species and their interactions with dust grain surfaces in astrophysical environments. This chapter summarises the major results of the observational and laboratory studies presented in this thesis, then discusses potential future work that could provide further insight into these areas of research.

8.1.1 Observational

The observational part of this thesis (Chapters 2, 3 & 4) detailed the analysis of observations of molecular clouds made with the AKARI satellite. The aim of the observations was to perform ice mapping of the molecular clouds by observing the ice absorption features present in the spectra towards stars located behind the clouds. The slitless spectroscopy mode of AKARI was uniquely suited to mapping ices in this manner, but did pose technical problems in the extraction of spectra from highly crowded fields of view.

The major results of these observations are:

- The data reduction pipeline ARF was written to analyse slitless spectroscopic observations obtained using the AKARI satellite. Slitless spectroscopy provides some analytical complexities, but this thesis has shown that the analysis of spectra observed by this method is possible.
- New background star observations in the 2.5–5 μm region offer the first study of this key spectral range for multiple background stars. The three most abundant ice species, H_2O, CO_2 and CO, all have absorption bands in this range. This study of 22 background stars represents a large addition of background star spectra to the literature.
- In this thesis are presented the first examples of solid phase mapping obtained by slitless spectroscopy in single pointings towards molecular clouds, probing resolutions down to 650 AU.

Other important results include the potential evidence of CO frozen on the dust grain surface below the critical A_V for CO freeze-out towards one object. This could suggest CO ice formation occurring at lower A_V, closer to that of H_2O and CO_2, testing the detection limitation of ice species. H_2O and CO_2 abundances increase linearly with A_V, but CO freeze-out depends on more complex physical factors that require 2D mapping and the combination of gas phase and solid phase observations to resolve. This, along with evidence from the component analysis method employed to analyse the abundances of CO and CO_2, could provide further clues to the formation of CO_2 at different times in the lifetime of a molecular cloud. These results provided the impetus to study CO_2 formation in the laboratory, as summarised in § 8.1.2.

The minor species CH_3OH, $^{13}CO_2$, OCN^-, CO_{gg} and, tentatively, HDO were observed towards some lines of sight probed by the AKARI observations. That these species were observed, even as upper limits, illustrates that the NG disperser provided more detailed spectra than expected based upon its resolving power. The initial aim of the study was only to map the relative abundances of H_2O, CO_2, and CO. Future analysis of other data from the AKARI IMAPE programme is discussed in § 8.2.1.

The ice mapping presented in this thesis has shown that, even for the most abundant molecular species in a small FoV, the trends between species are not necessarily constant, nor are they predictable. The local environment poten-

tially has a large effect on ice abundance, composition and growth. Even the individual components of a species could vary across a cloud. In order to use solid phase molecular species as probes of ice and gas chemistry, it will be necessary to make many more observations of both solid phase species, and also gas phase molecules, as well as deriving temperature and pressure data from gas phase observations.

8.1.2 Experimental

In the experimental section of this thesis (Chapters 5, 6 & 7), laboratory studies of astrophysically relevant molecules and surfaces were performed to address specific questions resulting from the observational results detailed above, and also to study topics of general interest to the astrochemical community. In Chapter 6, a study into the effect of surface type on molecular desorption characteristics was presented, while in Chapter 7, the results of a study of CO_2 formation by the non-energetic route CO + OH were detailed.

The major results of these experimental studies were:

- The desorption of a molecular species at a sub-monolayer coverage is important to the overall desorption behaviour of that species, and must be included in models. A change in surface type can critically alter the desorption characteristics of a molecular species, even considered over astrophysically relevant timescales.
- The first TPD study of CO_2 production by a quiescent formation route was presented. Modelling the experimental data provided key reaction rates and a provisional activation energy to the reaction CO + OH was calculated for incorporation into astrochemical models.

Laboratory astrochemistry is vital to understanding and testing the results of observational studies, but the combination of both branches of astrochemistry is critical to identifying solutions to current questions in the field, and new avenues of research.

8.2 Further work

Some potential areas of further work to complete and complement the results presented in this thesis are given in this section.

8.2.1 Observational

In Chapter 3, the observing strategy of the IMAPE programme was outlined. The discussion detailed some of the key advantages and limitations of AKARI for ice mapping, and the observations made as part of that programme. In particular, the main aim of the programme was the creation of convolved 9.5′×10′ 2D ice maps of H_2O, CO_2, and CO.

Observations were made using both the NG and NP dispersion elements of the IRC, and thus data was potentially available in the NIR for four fields of view: the 1′×1′ NG, the 9.5′×10′ NG, the 1′×1′ NP, and the 9.5′×10′ NP. In each observation, NP or NG, the 1′×1′ and 9.5′×10′ fields of view are observed simultaneously on the same CCD, as detailed in Chapter 2. As already mentioned, the 9.5′×10′ NG did not observe the molecular clouds targeted due to the roll angle of the telescope at the time of observation. For a similar reason, the 1′×1′ NP fields of view contain few or no lines of sight containing ice absorption spectra, as the targeted molecular cloud was observed in the 9.5′×10′ FoV in NP observations. As the 1′×1′ NG data was analysed in this thesis, that leaves the 9.5′×10′ NP data. Thus, in order to map molecular clouds on a 9.5′×10′ FoV, these data must be reduced.

Compared to the 1′×1′ NG fields of view, the analysis of the 9.5′×10′ NP pointings is, in some respects, easier and, in other respects, more complicated. The main advantage is that the dispersion of the NP spectra is only 66 pixels in length, compared with 258 for NG spectra. Thus, the degree of confusion between spectra is significantly reduced for NP spectra, and for objects positioned near the edge of the FoV, there is less chance of spectral information being lost due to dispersion off the edge of the CCD. In addition, in the 9.5′×10′ FoV, flat fields are available for application to the observed fields of view, and thus flat-fielding can be performed on all NP data.

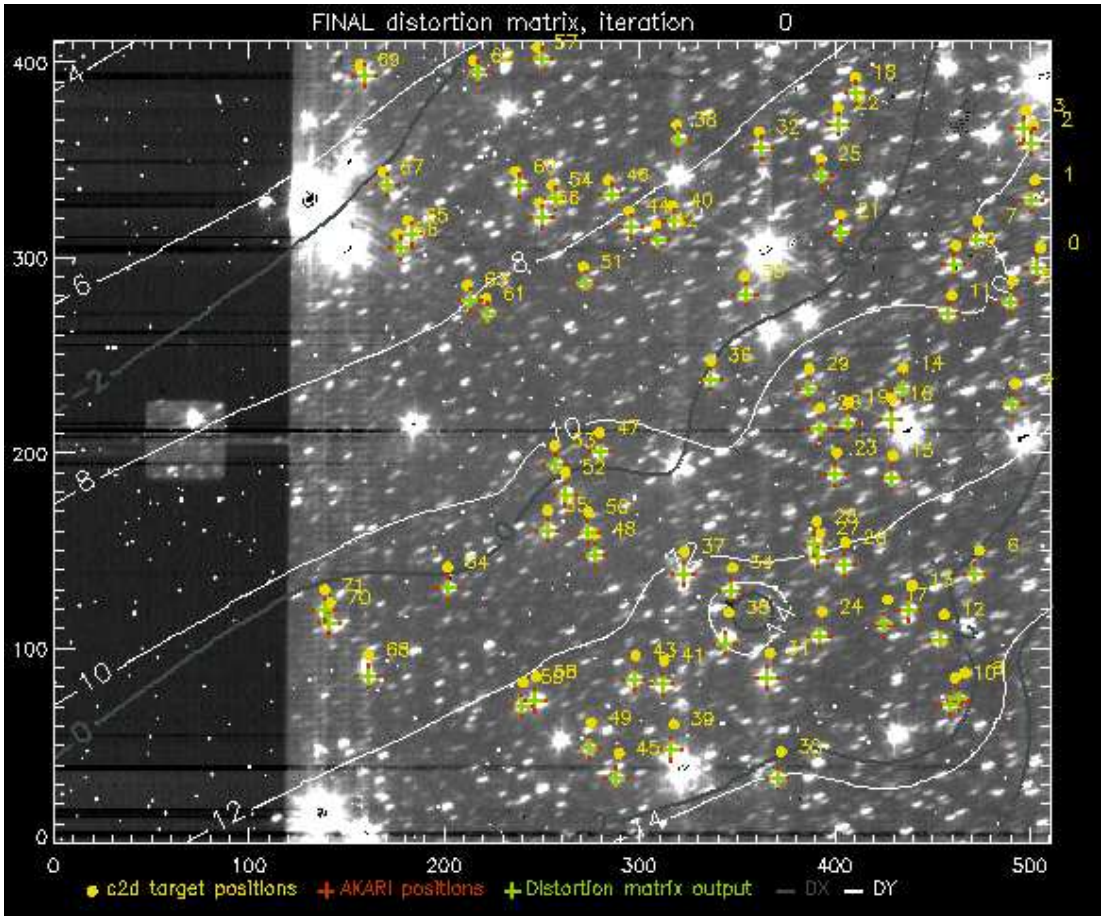

Figure 8.1. Calculated distortion matrix for 9.5′×10′ NP FoV. An AKARI N3 imaging frame is shown in greyscale. Overplotted are target positions in yellow (c2d catalogue), red (AKARI positions), and green (distorted c2d target positions). Also overplotted as grey contours is the calculated distortion matrix. See text for further details.

However, there are some more complicated aspects to the analysis of NP fields of view. The problem of distortion in the FoV, which was corrected in the significantly smaller 1′×1′ NG FoV by manual shifting of target positions, as described in § 3.5.4, is much more critical in the 9.5′×10′ FoV. While it was possible to manually correct for target position distortion in the 1′×1′ FoV, this would take an unreasonably long time in the 9.5′×10′ fields of view, where there are typically 100 – 200 objects observed in each pointing. Thus, a method of target position distortion correction must be developed.

Some work has already been done on this issue, with an example of a calculated distortion matrix presented in Figure 8.1. This figure includes an AKARI

N3 imaging frame (including both $9.5' \times 10'$ and $1' \times 1'$ fields of view) in greyscale. Overplotted on the image are three sets of target positions: firstly, target positions from the c2d catalogues are plotted as yellow circles- these data have been corrected for any distortion in the *Spitzer* optics, and thus represent the actual positions of objects on the sky; secondly, the positions of the corresponding AKARI objects are plotted as red crosses - these represent the central position of objects in the AKARI FoV, as hand-selected during the distortion calculation; thirdly, the green crosses represent the position of the c2d targets distorted to match the AKARI object positions by a distortion matrix calculation. This calculation involves the user individually correcting a selection of target positions across the FoV, and from the difference between the original (yellow) positions and the selected (red) positions, a distortion matrix is calculated, and convolved across the whole FoV. This distortion matrix is automatically iterated until all distorted c2d targets lie within a threshold distance of the AKARI objects. The distortion matrix itself is illustrated by contours overplotted on the imaging frame in Figure 8.1. Dark grey contours represent distortion in the X direction (left to right) and light grey contours represent distortion in the Y direction (top to bottom). The complex system of contours calculated across the FoV indicates that the distortion is not constant, and is more severe in some areas, rather than others.

The principle of distorting the c2d target positions by the distortion in the AKARI FoV is that all objects in the c2d catalogues are known objects, with associated photometric data. By identifying all extracted AKARI objects with a known c2d object, the extraction of spectra, stellar type assignment, and comparison with photometry can all be automated. Figure 8.1 represents an early attempt at quantifying and correcting for the distortion in the FoV. Another consideration is the possibility that the dispersed spectra are also subject to distortion along their length. This possibility was allowed for in the $1' \times 1'$ FoV by allowing the target position of each object to alter ± 1 pixel during PSF fitting, as detailed in § 3.5.4.3. As the fields of view were small, it was possible to manually check the fit of each object and each row, to confirm that this approach accounted for any small distortions. However, on the scale of the $9.5' \times 10'$ fields of view, this is not a realistic approach.

Other problems to address include the presence of excess emission in the fields

of view. This issue was addressed to a certain degree by backgrounding in the 1′×1′ fields of view, but there were still some spectra which were affected by excess light (e.g. Object 2, Figure 3.3a). In the 9.5′×10′ fields of view, the problem is more widespread, as the pointings map larger areas of molecular clouds, and more light is reflected and scattered from the dust in the FoV. A code has been written to generate a model dispersed image of the emission in the imaging frame, and this modelled dispersion could be subtracted from the spectral frames to remove some or all of the excess emission in these fields of view [Itsuki Sakon, *private communication*]. Extensive testing will be required in order to utilise this method on all 9.5′×10′ fields of view. In addition, the PSF of the NP dispersion element is different to that of the NG, and tests have suggested that it changes along the length of the dispersion (unlike the NG). Further work is required to find the best fitting model PSF to extract spectra from the 9.5′×10′ NP data.

A longer term aim of the ice mapping programme is to analyse MIR data towards the same clouds, also observed during the IMAPE observations in Phase 2 of AKARI's mission. Although the 15 μm CO_2 bending mode is not available, other spectral bands are found in this region, and interesting comparisons should be possible with *Spitzer* data in the same spectral region.

Ultimately, ice mapping on a 9.5′×10′ scale will test many factors, principally the A_V critical across an unbiased survey of background stars towards the edge of molecular clouds. Some tentative evidence was found in the 1′×1′ data for CO present on dust grains at extinctions lower than the critical A_V for CO freeze-out. This possibility can be more extensively studied in the 9.5′×10′ fields of view. Although the NP resolution will not allow for detailed component analysis, large ice maps of the relative abundances of H_2O, CO_2, and CO ices can be constructed based upon modification of the ARF pipeline.

Despite the problems with distortion and excess emission, some initial attempts at ice mapping have been made, and are shown in Figure 8.2. The left hand plot shows the AKARI 9.5′×10′ N3 imaging frame of B 35A, overplotted with target positions in orange, while the right hand plot shows a H_2O ice map in grey, convolved to the dimension of the two closest objects extracted in the FoV. The four objects clustered at the highest H_2O abundance are Objects 2, 3, 4 & 5 observed in the 1′×1′ observations in Chapters 3 & 4.

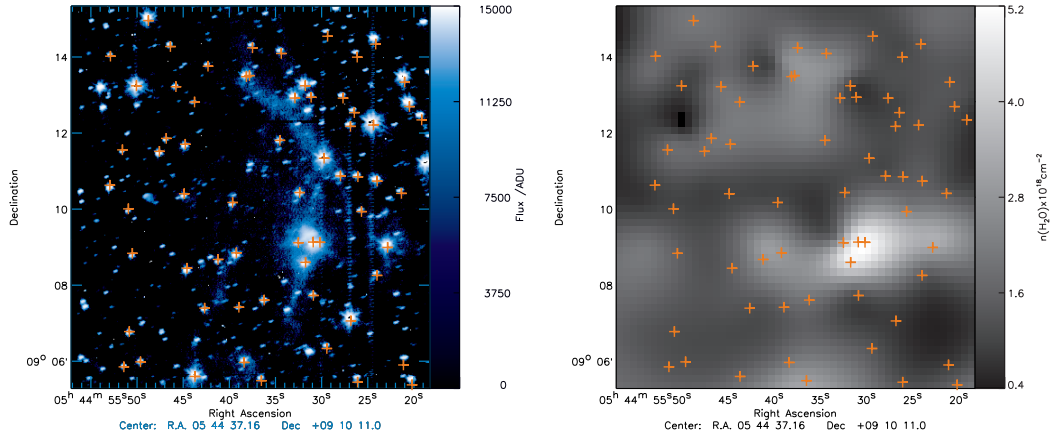

Figure 8.2. Initial ice maps of the 9.5′×10′ NP FoV. On the left is the AKARI 9.5′×10′ N3 imaging frame of B 35A, overplotted with target positions in orange. On the right is a H_2O ice map in grey, convolved to the dimension of the two closest objects extracted in the FoV. The four objects clustered at the highest H_2O abundance are Objects 2, 3, 4 & 5 observed in the 1′×1′ observations in Chapters 3 & 4.

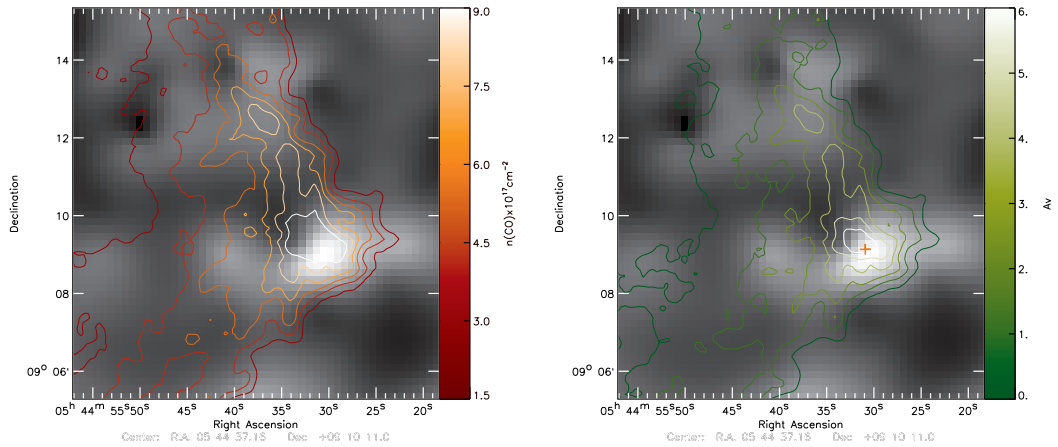

Figure 8.3. Initial combined ice and gas maps of the 9.5′×10′ NP FoV. The left hand plot shows gas phase CO abundance, calculated from gas phase observations of the CO 2-1 rotational transition, and the right hand plot shows A_V calculated from the gas phase data. Gas phase maps from Alison Craigon [*private communication*].

Figure 8.3 shows the first attempts at combining the 9.5′×10′ ice map with gas phase observations [Alison Craigon, *private communication*]. The left hand plot shows gas phase CO abundance, calculated from gas phase observations of the CO 2-1 rotational transition, and the right hand plot shows A_V calculated from the gas phase data. The orange cross represents the position of Object 3, an embedded YSO in B 35A. Already at this early stage of mapping, the data show that the highest abundances of H_2O ice are seen towards the most dense region

of the cloud (where the CO gas is most abundant). With further work, and the creation of more accurate ice maps, it is likely that many more interesting connections will be extracted from these data.

8.2.2 Experimental

The experiments presented in Chapter 7 only represent the first stage of quantifying the reaction network surrounding CO_2 formation by non-energetic routes. As discussed previously, this is likely to be a very important route for explaining CO_2 formation at early times (concurrent with H_2O formation on grain surfaces) as well as, potentially, CO_2 formation in a CO-rich ice, sometime after critical freeze-out of CO onto grains at high A_V. Some preliminary experiments have already been carried out to quantify the H_2O formation route alone, and it is envisaged that future experiments will be performed on the competition between H_2O and CO_2 formation at sub-monolayer grain coverages. Results in Chapter 6 have proven how important the sub-monolayer regime could possibly be to chemistry over long timescales in molecular clouds.

Further reactions using D, rather than H, to provoke OD formation on the surface could also be useful in quantifying the OH production rate and reactions on a H_2O surface, as the HDO produced by the water formation will be distinguishable from the H_2O of the water ice surface during TPDs. In the results presented in Chapter 7, the H_2O production was not highly constrained in the model, as only H_2O formed on the silicate surface could be quantified. The question of the product abundances must be resolved to obtain a more accurate model and thus more accurate reaction rates. Finally, the potential desorption of reactants observed during the experiment must be further investigated.

Ultimately, a pure OH beam is required to fully test the CO + OH reaction mechanism and OH radical chemistry under conditions as close as possible to the ISM. As discussed in Chapter 7, it is difficult to generate a pure OH beam. During preparations for the study in Chapter 7, some months were spent trying to produce such an OH source on FORMOLISM, but it did not prove possible by the methods attempted. If a pure, well characterised OH beam could be produced using H_2O:He mixtures, it would open up the possibility of investigating OH reactions with many other molecular species, for example NO, NH,

NH_3, SO_2, but more importantly, could ultimately lead to the study of other radical and ion species in standard surface science experiments, providing the opportunity to really test some of the key gas-solid interactions in molecular clouds.

8.3 Concluding remarks

This thesis has detailed observational and experimental results pertaining to the complex chemical network present in ices on the surface of dust grains. It has been shown that both laboratory and observational studies can provide much information on ice mantle compositions and grain surface chemical reactions, but that ultimately, the combination of both approaches is the only way to derive real insights into interstellar chemistry.

Acknowledgements

Helen, thanks for always wanting more from me but, more importantly, for me. Alison, for teaching me astronomy, and for so much more.

To Tom and Dave for greatly improving this manuscript and being kind and considerate while doing so.

Klaus, for your patience as I got to grips with IDL and astronomy. Yuri, for your generosity during my time in Kobe. To Itsuki, for all of your inspirational ideas and Takashi, for introducing me to the best sushi in Tokyo. I really appreciate all of the time and help you gave me.

To everyone at LAMAp for making me feel so welcome and for a memorable year. Especially, to Linda for our English days and jours français, François for teaching me so much about experiments, French life and Harry, and most of all to SS, thank you for everything chéri.

To all of my office mates, Ross, Scott, Alex, Ian, Mariana, Amy, Rafal, Yinan, Gregor, Leanne, Elie, Mario, Craig, Lawrence, James, Aleksi, and Pavel, for putting up with my occasional craziness. To the new friends I've made along the way for making my PhD more enjoyable, particularly Kirsten, Linus, Daniel, Paul, Davy, Farah, Julia, Will, John, John, John, Jane, Mark, Paul, Dave, Duncan, Lars, Edith, Stefan, Nadya, and Sharon.

I wouldn't have made it through these four years without the support of good friends. Special thanks to Sheona, Ben, Susan, Alex, Leah, Rhian, and Laura. Claire, for all of our adventures in Scotland, France and Japan - you were there for all three! To Leif for the all-night karaoke, Ryan and Sean for wearing bowling pin suits and Atanas for introducing me to Yodabashi. Ana, for all the beards we have taken and will take in the future. Les mecs et filles de Neuville for some great parties, pétanque and friendship. Special thanks to Val for taking pity on a Scot abroad, Lulu for always smiling, Eric for the French lessons, and Lyd for our volcano weekend. Hannah, Roy and Emily, I can never thank you enough for filling this last year with so much tea, Tim, jamming, Panique, tuna bake, glove horn, massages, and especially, you, your faces and your mums.

My final thanks are to my family. Pam, Derek, Emma and Callum, thank you for being there. Always.

Ce qui est admirable, ce n'est pas que le champ des étoiles soit si vaste, c'est que l'homme l'ait mesuré.
Anatole France